University of Sussex

# The XMM Cluster Survey: A new cluster candidate sample and detailed selection function

**Mark Hosmer**

Submitted for the degree of Doctor of Philosophy
University of Sussex
September 2009

# Declaration

I hereby declare that this thesis has not been and will not be submitted in whole or in part to another University for the award of any other degree.

Signature:

Mark Hosmer

UNIVERSITY OF SUSSEX

Mark Hosmer, Doctor of Philosophy

# The XMM Cluster Survey:

## A new cluster candidate sample and detailed selection function

## Summary

In this thesis we present the XCS DR3 cluster candidate list. This represents the first major update of the XMM Cluster Survey since 2005. The candidate list comprises of 1365 entries with more than 300 detected counts distributed over 229 deg$^2$. We note that a larger area (523 deg$^2$) is available for the study of X-ray point sources and that the new XCS point source sample has more than 130,000 entries. After redshift follow-up and X-ray spectral analysis, these 1365 clusters will comprise the largest homogeneous sample of medium to high redshift X-ray clusters ever compiled. The future science applications of the XCS DR3 clusters include the study of the evolution of X-ray scaling relations and a measurement of cosmological parameters. In support of these science applications, we also present in this thesis detailed selection functions for the XCS. These selection functions allow us to quantify the number of clusters we didn't detect in our survey regions. We have taken two approaches to the determination of the selection function: the use of simple (circular & isothermal) $\beta$ models and the use of 'observations' of synthetic clusters from the CLEF N-body simulation. The $\beta$ model work has allowed us to explore how the selection function depends on key cluster parameters such as luminosity, temperature, redshift, core size and profile shape. We have further explored how the selection function depends on the underlying cosmological model and applied our results to XCS cosmology forecasting (Sahlen et al. 2009). The CLEF work has allowed us to explore more complex cluster properties, such as core temperature, core shape, substructure and ellipticity. In summary, the combination of the cluster catalogues and selection functions presented herein will facilitate field leading science applications for many years to come.

# Acknowledgements

This is not a simple section to write; there are too many people to thank individually.

The XCS collaboration have been a brilliant group to work with, particular thanks go to Kathy Romer for the proof reading of, and suggestions for the thesis, Ed Lloyd-Davies for all the help and input he's given, Michael Davidson for helping me continue some of his work, Scott Kay for providing the CLEF catalogue, and Nicola Merhtens for the support and slightly insane humour.

Amongst the other students in physics and astronomy I found a great group of friends and briefly, house-mates. The banter, beer, and games made the time alot less stressful.

A special thank you must go to my wife Sarah. She has very graciously put up with me being a perpetual student. Her love and support are invaluable.

The biggest thank you is for God, the creator of everything scientists study.

# Contents

# List of Tables

# List of Figures

# Chapter 1

# Introduction

Being able to understand and explain the world around us has been the major goal of scientists throughout history. In the present age, advances in knowledge and technology have enabled us to build a consistent, if incomplete, picture of how the Universe has come to be in the state we currently observe. In the now favoured ΛCDM cosmology (see Section 1.1.1), the structure we observe today grew from an initial set of density fluctuations in the early Universe. Regions of space that are overdense with respect to the mean density grow over time under the influence of gravity, merging together to produce larger and larger systems. In this hierarchical model of structure formation the universe develops a weblike topology with large voids seperated by filaments of matter (See Figure 1.1). It is at the intersections of these filaments that we find massive clusters of galaxies.

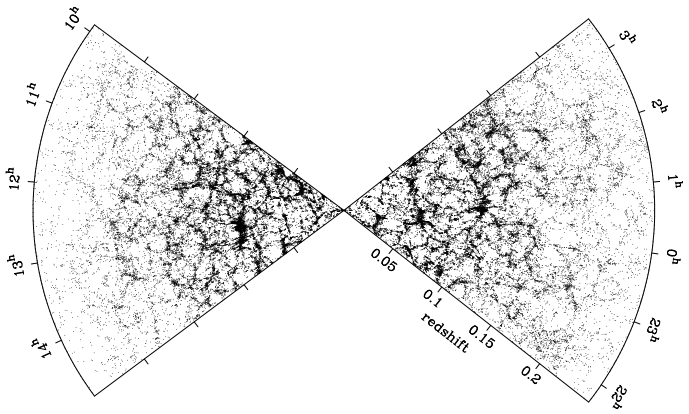


Figure 1.1: A map of the 2dFGRS (Colless et al., 2001) showing the weblike topology of the local universe

Clusters of galaxies are the largest gravitationally bound systems in the Universe with masses ranging from $10^{13} M_{\odot}$ for small groups to $10^{15} M_{\odot}$ for the richest clusters. It is largely due to their enormous size that clusters are interesting to study. They can reasonably be expected to reflect the mass content of the Universe as a whole, and are

key objects for studying cosmology, and structure formation (e.g. Rosati et al. (2002), Schuecker et al. (2003), Sahlén et al. (2009)).

Optical identification of galaxy clusters goes back as far as the late 1700's when it was recognised that 'nebulae' (galaxies) were more concentrated in certain regions of the sky (Messier 1784, Herschel 1785), these early discoveries were of what are now known as the Virgo and Coma clusters.

In the 1960's extended X-ray emission was detected from the direction of Coma (Boldt et al 1966). Felten et al. (1966) discussed the possibility of the X-rays being unresolved emission from galaxies. After ruling this out, on the grounds that the galaxies would need to be $10^4$ times brighter in the X-ray band than the Milky Way, the authors attributed the emission to thermal bremsstrahlung from hot ($\sim 10^8 K$) gas filling the cluster volume. Shortly thereafter this was observed to be the case for Coma, Virgo and Perseus (Forman et al. (1972), Gursky et al. (1971), Kellogg et al. (1972)). By now over a thousand clusters have been detected in the X-ray band (e.g Böhringer et al. (2001)).

Figure 1.2 shows the Coma cluster in both optical and X-ray wavebands. X-ray radiation is absorbed by the Earth's atmosphere, so X-ray observations must be taken from high altitude, often by satellite. X-ray astronomy is expensive, but is vital for cluster studies since, by mass, the X-ray emitting gas makes up a factor of $\sim 5-10$ more of the cluster than the galactic component (the dominant component by far is dark-matter, $\sim 90\%$).

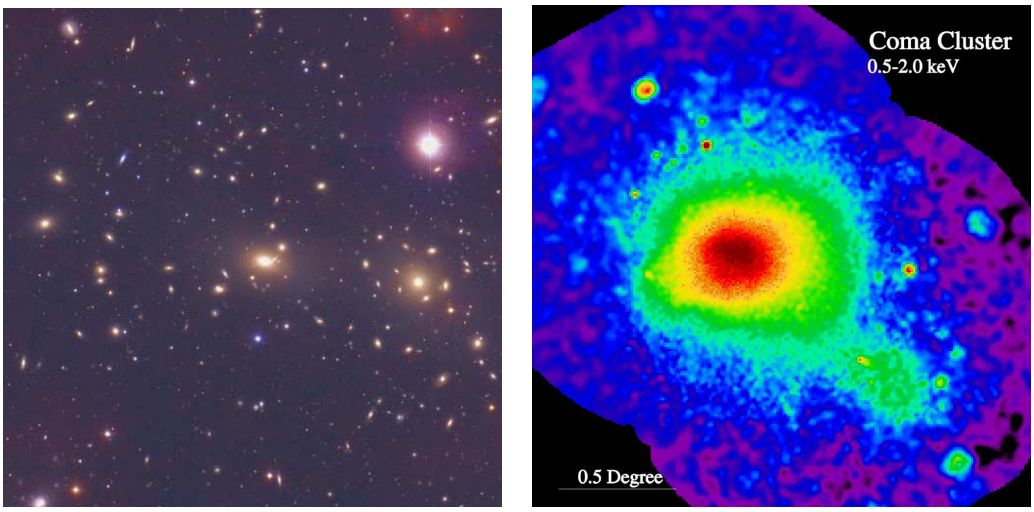


Figure 1.2: On the left, An optical image (Omar Lopez-Cruz & Ian Shelton NOAO/AURA/NSF), and on the right, an X-ray image (S. L. Snowden USRA, NASA/GSFC) of the Coma cluster of galaxies.[1]

This introductory chapter outlines some of the current understanding of clusters of galaxies, including their appearance in X-ray wavelengths and how they can be used to study

[1]The optical image was created from three separate exposures taken in three different bands, using the Kitt Peak National Observatory's 0.9-meter telescope. The X-ray image was taken by ROSAT.

cosmology. We will begin by looking at the theorectical framework within which this work sits. Then we will discuss the observational picture, and see where this agrees with theoretical predictions, and where it differs. Finally we will discuss the motivation and need for a new cluster survey, the XMM Cluster Survey (XCS).

## 1.1 Theoretical Framework

In this section we will discuss the theory behind the rest of the work in the thesis. While this is not a theoretical thesis, an understanding of the theory is important in order to motivate any observational work. We also use some the following equations in Chapters 5 and 6. We will begin with the cosmological model, and see how some of the parameters in this model can be constrained though observations.

### 1.1.1 Cosmological Framework

Over the past decade one cosmological model in particular has emerged that appears to be able to explain the current observations. In this model, the geometry of the universe is flat, and the energy density is made of two principal components, matter and dark energy. The baryonic matter (stars, gas, dust etc.) that we can observe only makes up a small percentage of the total matter density, the rest is made up of cold dark matter, which we can only detect via its gravitational interaction. It is the dark energy component of the universe that is driving the recently observed accelerating expansion (e.g Perlmutter and Schmidt (2003)).

Arguably the first person to notice and attempt to measure the expansion of the Universe was Edwin Hubble. In 1929 Hubble formulated the following expresion to explain the observed recession velocity of galaxies in the universe, $v = H(t)d$, where $v$ is the recession velocity between galaxies seperated by distance $d$. $H(t) = \dot{a}/a$ is the Hubble parameter, $a(t)$ is the scale factor, the present day value is $a_0 = 1$, $\dot{a}$ is the time derivative of $a$. $\dot{a}$ and $a$ are constant in space, but vary with time. Hubble made the measurement of recession velocities via the galaxy's redshift; this is a shifting of the galaxy's spectrum caused by its line of sight velocity. Redshift is defined in Equation 1.1, where $\lambda_{em}$ is the emitted wavelength of a particular spectral feature (e.g absorbtion line), and $\lambda_{ob}$ is the observed wavelength of the same feature.

$$z = \frac{\lambda_{\rm ob} - \lambda_{\rm em}}{\lambda_{\rm em}} \tag{1.1}$$

The cosmological redshift $z$ of radiation from distant objects is related to the scale factor of the universe when that radiation was emitted by $a = (1 + z)^{-1}$.

We can better understand the expansion of the universe using a model. The current favoured series of model for predicting the observed behaviour are known as Friedmann-Lemaitre models. There are many review articles and textbooks that go into this topic in great detail (eg. Peacock, 1999. Liddle and Lyth, 2000.). Here we will just discuss some of the key points.

The cosmological principle states that on large enough scales the universe is homogenous and isotropic, and that the expansion rate will be the same everywhere. Using this principle, in conjunction with laws of energy conservation, it is possible to derive Equation 1.2. This is the Friedmann equation which describes the expansion of the universe.

$$\left(\frac{\dot{a}}{a}\right)^2 = \frac{8\pi G}{3}\rho - \frac{k}{a^2} \tag{1.2}$$

where $\rho$ is the time dependant, but spatially invariant density. The constant $k$ describes the curvature of the universe and can have values of -1,0,1 relating to open, flat and closed geometry respectively.

To make use of the Friedmann equation we need to know how the density of the universe evolves with time. For this we use the fluid equation (Equation 1.3) which can be derived from the first law of thermodynamics.

$$\dot{\rho}c^2 = -3\frac{\dot{a}}{a}(\rho c^2 + p) \tag{1.3}$$

Where $p$ is pressure, and $c$ is the speed of light.

The Friedmann and fluid equations can be used to derive Equation 1.4 describing the acceleration of the scale factor, this is known as the acceleration equation.

$$\frac{\ddot{a}}{a} = -\frac{4}{3}\pi G\left(\rho + \frac{3p}{c^2}\right) \tag{1.4}$$

In order to see how the universe will behave we also require an equation of state, relating $\rho$ and $p$. If $p = w\rho c^2$, then density changes with the expansion as $\rho \propto a^{-3(1+w)}$, leading to Equation 1.5, which relates the rate of change in the scale factor to the equation of state.

$$\dot{a}^2 = \frac{8\pi G}{3}\rho_0 a^{-(1+3w)} + const \tag{1.5}$$

Where $\rho_0$ is the density at the present day.
It is common practice to express the energy density in terms of the critical density, $\rho_c = 3H^2/8\pi G$, (the density required for a flat, $k = 0$, universe dominated by a $w = 0$ component). The density parameter is defined such that $\Omega = \rho/\rho_c$. Using this definition we can now begin to express the behavour of the universe using Equation 1.6.

$$\left(\frac{\dot{a}}{a}\right)^2 = H_0^2[\Omega(1+z)^{3(1+w)} + (1-\Omega)(1+z)^2] \tag{1.6}$$

It is possible, and indeed is the case for our universe, that several different components each with its own equation of state, will influence the dynamics of the expansion. The key components of our universe are non-relativistic particles, e.g dark matter and baryons ($\Omega_m; w = 0$), photons and relativistic particles e.g. neutrinos ($\Omega_r; w = 1/3$), and 'dark energy' ($\Omega_{DE}; w < -1/3$). Below we assume a more specific type of dark energy, the so called 'cosmological constant' ($\Omega_\Lambda; w = -1$).

A dynamical description of the universe is therefore given by Equation 1.7, in which $\Omega_{total} = \Omega_m + \Omega_\Lambda + \Omega_r$.

$$H^2(z) = \left(\frac{\dot{a}}{a}\right)^2 = H_0^2[\Omega_m(1+z)^3 + \Omega_r(1+z)^4 + \Omega_\Lambda + (1-\Omega_{total})(1+z)^2] \tag{1.7}$$

which can be reduced to $H(z) = H_0 E(z)$. It is clear from Equation 1.7 that measurements of the density parameters ($\Omega_x$) will give an understanding of the expansion history of the universe.

Measurements of the Cosmic Microwave Background (CMB), combined with those from Supernovae and Galaxy Cluster studies, have shown that the likely make up of the Universe is $\Omega_\Lambda = 0.726 \pm 0.015$, $\Omega_{DarkMatter} = 0.228 \pm 0.013$, $\Omega_{Baryons} = 0.0456 \pm 0.0015$, $\Omega_r = 2.469 \times 10^{-5}$ (for $T_{CMB} = 2.725\text{K}$)[2], this is often called the $\Lambda$CDM cosmology in reference to the principal components. See Figure 1.3 for a pictoral representation of values of the dominant components.

$\Omega_r$ is measured from the temperature of the CMB blackbody radiation and is known to a high precision. The parameters $\Omega_\Lambda$ & $\Omega_m$ can be determined in combination (i.e. $\Omega_\Lambda + \Omega_m$) from the CMB anisotropy power spectrum or the luminosity of distant supernovae. In order to gain an estimate of $\Omega_m$ (rather than $\Omega_\Lambda + \Omega_m$), the traditional approach is to use the evolution in the number density of clusters of galaxies, $(n(m,z))$ . The driving science motivation behind the development of the XCS is the measurement of $\Omega_m$. The cluster abundance has some sensitivity to $\Omega_\Lambda$ and we hope to exploit that in XCS also. For completeness we also define here the parameter $\sigma_8$. This is the normalisation of the matter power spectrum at cluster scales ($8h^{-1}$Mpc).

### 1.1.2 Cosmological distances

In this subsection we define three distance measurements used in this thesis.

**Comoving distance.**
The comoving distance ($d_C$) between two objects is defined in such a way that it remains

[2]parameter data taken from Komatsu et al. (2009).

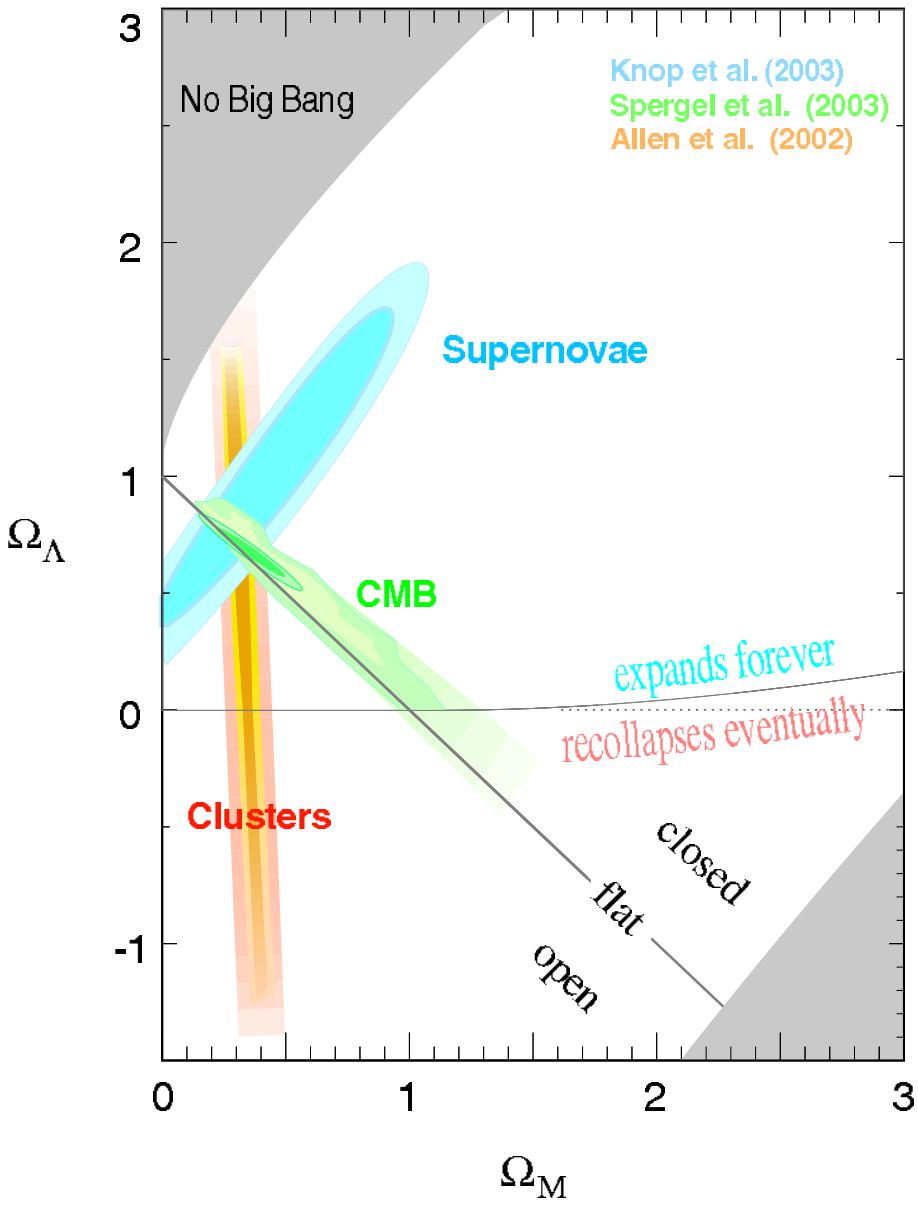


Figure 1.3: Cosmological parameters as measured from three complementary methods. Figure courtesy of the Supernova Cosmology Project (Knop et al., 2003).

constant with time if the only motion is that caused by the universal expansion.

$$d_C = \frac{c}{H_0} \int_0^z \frac{dz}{E(z)} \tag{1.8}$$

This is actually the line-of-sight co-moving distance to an object at redshift $z$. For cases where $k = 0$ this is equal to the transverse co-moving distance ($d_M$).

**Luminosity distance.**
A method of measuring distance is via the 'standard candle' method. A standard candle is an object with a known luminosity. By measuring the flux (energy received per area, in Watts/m$^2$) received from an object, the distance can be calculated.

Due to the expansion of the universe, the flux (S) received from an object does not relate to its luminosity (L) and distance in the same way as expected in flat, static space. The luminosity distance ($d_L$) is defined as the apparent distance to an object, i.e. the proper distance assuming static flat space. $d_L$ is given by Equation 1.9.

$$d_L = \sqrt{\frac{L}{4\pi S}} \tag{1.9}$$

The expansion in fact causes the measured flux to be reduced by a factor of $1/(1+z)^2$ from the Euclidean expectation.

**Angular-diameter distance.**
Another method of measuring distance is using a 'standard ruler'. If you know the physical size ($l$) of an object, the distance to it can be calculated by measuring its angular size ($\theta$) on the sky.

The Angular-diameter distance ($d_A$) is a measure of how large an object appears to be. It is defined as the apparent distance to an object under the assumption of static Euclidean geometry, $d_A \sim l/\theta$.

Like $d_L$, $d_A$ is also affected by the expansion and geometry of the universe.

$d_L$, $d_C$ and $d_A$ are related via Equation 1.10.

$$d_L = (1+z)d_c = (1+z)^2 d_A \tag{1.10}$$

As seen in Equation 1.8, $d_C$ is dependent on cosmological parameters via $E(z)$, and therefore so are $d_L$ and $d_A$ (Equation 1.10). This enables different projects to measure cosmological parameters using very different methods: Supernovae can be used via $d_L$ since type Ia supernovae are standard candles (e.g. Perlmutter and Schmidt (2003)); Baryon acoustic oscillations (BAO) can be used via $d_A$ since they are standard rulers (e.g. Percival et al.

(2007)); The gas mass fraction ($f_{gas}$) in clusters is also a type of standard candle, as it is thought to be invariant with $z$ (e.g. Allen et al. (2002), see the orange section in Figure 1.3). It is to be noted that the $f_{gas}$ method is not the mechanism XCS plans to use to measure parameters.

In Chapters 5 and 6, $d_L$ and $d_A$ must be calculated for our simulated clusters, in order to do this $d_L$ is computed via numerical integration (See Appendix A).

## 1.2 From cluster observables to halo masses

The evolution of the mass function of clusters can be used to place constraints on cosmological parameters (See Press and Schechter (1974),Viana and Liddle (1996), Linder and Jenkins (2003) and Sahlén et al. (2009) for theory and arguments.). However we cannot measure masses directly, instead masses have to be infered from an observable. Here we will discuss how halo masses can be measured from cluster observables.

### 1.2.1 Cluster galactic component

For a bound system of particles, the virial theorem relates the potential energy (PE) to the kinetic energy (KE) as follows,

$$\langle PE \rangle / 2 = -\langle KE \rangle. \tag{1.11}$$

For a bound cluster of galaxies, its member galaxies would have a Gaussian velocity distribution. This is distribution is often characterised by the dispersion of the velocities about the mean, as in equation 1.12:

$$\sigma_r = \langle (v_r - \langle v_r \rangle)^2 \rangle^{1/2} \tag{1.12}$$

where $v_r$ is the radial velocity. With a measurement of the velocity dispersion ($\sigma_r$), it is possible, via the use of the virial theorem, to determine the mass of an isolated cluster.

$$M = \frac{R \langle v^2 \rangle}{G} \tag{1.13}$$

Where $\langle v^2 \rangle = 3\sigma_r^2$, and $R$ is the radius enclosing mass M.

Zwicky (1933,1937) was first to measure the velocity dispersion and mass of a cluster in such a way. Zwicky's study of the Coma cluster yielded $\sigma_r \sim 700 \mathrm{kms}^{-1}$, inferring a mass far in excess of the observed mass seen in stars. A similar study (Smith, 1936) showed that the same was true of the Virgo cluster. This mass excess in clusters was is the

earliest evidence suggesting the existence of dark matter. Dark matter in clusters has more recently been confirmed by mass estimates from weak lensing (see Bartelmann and Schneider (2001) for a review).

King (1962) demonstrated that under the assumptions of a cluster being spherically symmetric, isothermal, isolated, and in equilibrium, the galaxy density in clusters is well fit to a profile of the form:

$$n(r) = n_0 \left[ 1 + \left( \frac{r}{r_c} \right)^2 \right]^{-3/2} \tag{1.14}$$

where $n_0$ is the central number density (i.e at $r = 0$), and $r_c$ is the core radius.

### 1.2.2 Cluster gas component

A simple and popular gas model proposed by Cavaliere and Fusco-Femiano (1976) is one of an isothermal gas, in the same potential as the galaxies in Equation 1.14. This is the known as the isothermal $\beta$ model. The gas density is given by:

$$\rho(r) = \rho_0 \left[ 1 + \left( \frac{r}{r_c} \right)^2 \right]^{-3\beta/2} \tag{1.15}$$

where

$$\beta \equiv \frac{\mu m_p \sigma_r^2}{kT} \tag{1.16}$$

where $m_p$ is the proton mass, and $\mu$ is the mean molecular weight ($\mu = 0.6$ for typical Intracluster Medium (ICM) predominantly comprised of hydrogen), $k$ is the Boltzmann constant, and $T$ is the Temperature.

The X-ray surface brightness is given in Equation 1.17 (eg. Sarazin and Bahcall (1977), Gorenstein et al. (1978)),

$$S(r) \propto \left[ 1 + \left( \frac{r}{r_c} \right)^2 \right]^{-3\beta+1/2}. \tag{1.17}$$

The gas trapped in the potential well of a halo could reasonably be expected to be in thermal equilibrium with the galaxies, $\beta = 1$. Equation 1.16 then gives us a relation for the gas temperature, which is proportional to the depth of the potential well (Equation 1.18). Therefore, based on these assumptions, a temperature measurement will in turn lead to a mass measurement (Equation 1.19). (Note that $\beta$ is actually measured to be $\neq 1$, see Section 1.3.2)

$$kT = \mu m_p \sigma_r^2 \tag{1.18}$$

$$M = \frac{3RkT}{G\mu m_p} \tag{1.19}$$

### 1.2.3 From self-similarity to cluster scaling relations

A typical cluster will have a gas temperature of $\sim 10^8 K$ or $0.5 - 15$keV. At temperatures of $kT \geq 2$keV Hydrogen and Helium are fully ionized, causing the intracluster medium (ICM) to be largely a hot plasma of free ions. The principal mechanism for emission from this type of system is in the X-ray wavebands via thermal Bremsstrahlung or 'braking' radiation, the emissivity of which can be quoted as:

$$\epsilon \propto g(\nu, T) T^{1/2} n_e^2 e^{-h\nu/kT} \tag{1.20}$$

where the Gaunt factor $g(\nu, T) \sim 1 + \log(kT/h\nu)$.
As can be seen from equation 1.20, the emission from the ICM scales as density squared ($n_e^2$) making the measurement of this emission a very powerful tool for probing the 3 dimensional structure of clusters. The X-ray luminosity $L$ of a cluster is given by Equation 1.21.

$$L = \int n_e^2 \Lambda(T) dV \tag{1.21}$$

Where $\Lambda(T)$ is the so-called cooling function. If the emission is purely Bremsstrahlung then $\Lambda(T) \propto T^{1/2}$.

Under the assumption that the thermodynamics of the ICM are determined by gravity only, Kaiser (1986) showed that all virialised clusters will be scalable or self-similar. Meaning that there are scaling relations between cluster properties $(M, L, T)$, that will be true regardless of the mass of the system (See Equations 1.22 and 1.23).

$$T \propto M^{2/3} (1+z)^{2/3} \tag{1.22}$$

$$L \propto M^{4/3} (1+z)^{7/2} \propto T^2 (1+z)^{3/2} \tag{1.23}$$

If these relations hold true, then it would be easy to make a measurement of either $L$ or $T$ and directly infer the halo mass.

## 1.3 Observational Framework

Observationally clusters are not all spherically symmetric and isothermal, but have a wide range of morphological and physical properties. They do exhibit some of the behaviour discussed in the previous section, but they do not exactly follow the predicted relations (Equations 1.15, 1.17, 1.22 and 1.23). In this section we will discuss the properties of the observed cluster population and see how this differs from the theoretical picture laid out in Section 1.2.

### 1.3.1 $\beta$ model: success

As the X-ray emission is very sensitive to changes in the gas density it is relatively easy to derive the gas distribution from a surface brightness profile. Studies of this type have shown that in the outer regions of a cluster the density profiles are reasonably fitted by a $\beta$ model (Equation 1.15) with $\beta = 2/3$ and $r_c \sim 0.12R_{200}$ (Arnaud et al., 2002). In Figure 1.4 are density and emission measure profiles for clusters from the REXCESS survey (Croston et al. (2008), Pratt et al. (2008)), the profiles in the figure show very similar behaviour outside of the core regions.

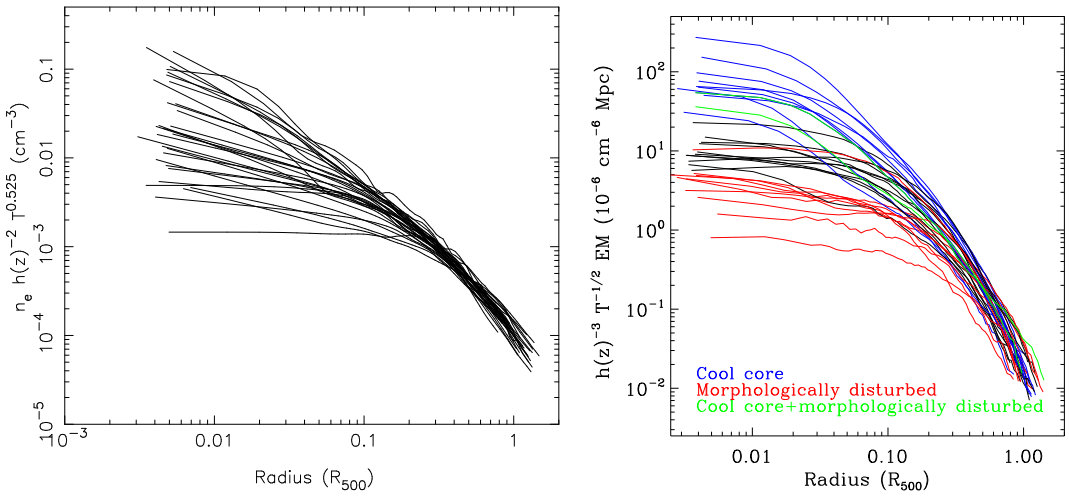


Figure 1.4: Left) Figure 1d from Croston et al. (2008), Gas density profiles for the REXCESS sample, profiles of density scaled for redshift evolution and according to $T^{0.525}$ as implied by modified self-similar S-T scaling. Right) Figure 1c from Pratt et al. (2008), *"Emission measure profiles of the REXCESS sample, scaled according to the standard dependence on temperature and expected evolution with redshift. Systems classified as cool core and as morphologically disturbed are indicated."*

The simplicity of the $\beta$ model, and general agreement with a large number of cluster observations, has caused this model to remain popular despite the problems discussed in Section 1.3.2.

### 1.3.2 $\beta$ model: departures

Comparisons of optical and X-ray observations of clusters of galaxies led to the so-called '$\beta$ discrepancy'. The standard hydrostatic-isothermal model for clusters predicts that the parameter $\beta_v = \sigma_r^2/(kT/\mu m_p)$ , which describes the ratio of energy per unit mass in galaxies to that in the gas, should equal the parameter $\beta_{fit}$ where $\rho_{gas}(r) \propto \rho_{gal}^{\beta_{fit}}$ determined from the X-ray surface brightness distribution. The observations suggest an apparent discrepancy : $\beta_v \sim 1.2$ (i.e. the galaxies are hotter than the gas) while $\beta_{fit} \sim 0.65$ (i.e. the gas is hotter and more extended than the galaxies). It has been shown however that this discepancy may disappear if the assumption that the galaxies follow a King profile is dropped (Bahcall and Lubin, 1994).

As well as showing the self-similarity in the outer regions of cluster profiles, Figure 1.4 also highlights that this is not the case in the inner regions. Some clusters exhibit cores of near constant density, and surface brightness profiles that show a similar flattening, others have density and surface brightness profiles that continue rising well into the core, this variation is attributed to variations in amount of cooling of the core gas, resulting in the clusters being called non-cool-core and cool-core respectively.

### 1.3.3 Self-similarity: success

As predicted by the self-similar theory, clusters of galaxies do not occupy all areas in the $L-T$ and $M-T$ planes, there are strong correlations between the parameters. Figure 1.5 shows $L-T$ and L-M relations as measured by Pratt et al. (2008). It is clear that scaling relations between the parameters do exist.

The fact that there are indeed scaling relations between observables and mass, means that surveys like XCS will be useful for cosmology.

### 1.3.4 Self-similarity: departures

The measured scaling relations between cluster properties do not follow the predicted relations (Equations 1.22 and 1.23), the slope in the $L-T$ and $M-T$ relations are steeper than self-similar, see Table 1.1.

These departures from the self-similar scaling are even more pronounced in lower mass systems. Studies of galaxy groups ($T \sim 1$keV) show that groups have significantly different scaling trends than clusters. In particular groups are seen to have lower $\beta$ values, i.e flatter surface brightness profiles, and much steeper scaling between $L-T$, with measured slopes of $\sim 5$ (e.g, see Helsdon and Ponman (2000), Davé et al. (2002)).

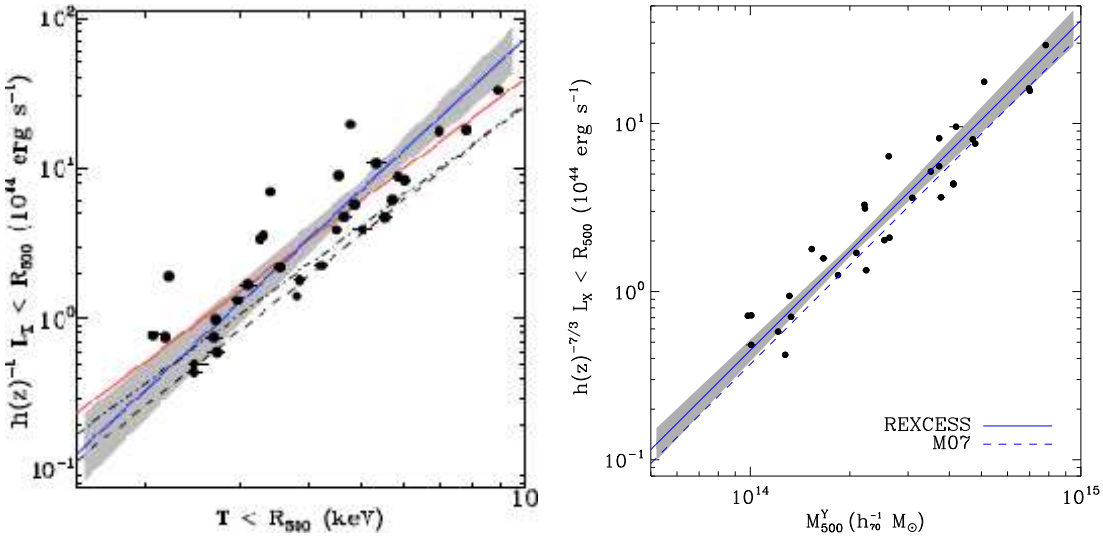


Figure 1.5: Figures 2a and 6a from Pratt et al. (2008). Left) *"The $L-T$ relation for the REXCESS sample (quantities derived from all emission interior to $R_{500}$). The error bars are smaller than the points in many cases. The best fitting power law relation derived from the BCES (Y—X) (red line) and BCES orthogonal (blue line) are overplotted; the shaded region corresponds to the $1\sigma$ uncertainty on the latter. The dashed and dot-dashed lines are the relations of Arnaud & Evrard (1999) and Markevitch (1998), respectively."* Right) *"The $L-M_{500}$ relation for the REXCESS sample, with the mass estimated from the $Y_X - M$ relation of Arnaud et al. (2007). Relation for all emission interior to $R_{500}$."*

In order to understand the physical origin of the deviation from the self-similar model it is more useful to consider the gas entropy rather than its density. In X-ray studies of galaxy clusters the term entropy is often used to describe a characteristic property of the ICM that is related to the true entropy, we define it here in Equation 1.24.

$$S = kT/n_e^{2/3} \tag{1.24}$$

The shape of a clusters potential well and the entropy profile of the gas fully define the X-ray properties of a relaxed cluster. Ponman et al. (1999) demonstrated that the entropy measured at $0.1r_{virial}$ is greater than the level that can be generated through gravitational heating alone (See Figure 1.6), we shall discuss some of the possible causes of this increase in entropy in Section 1.3.5.

### 1.3.5 Self-similarity departures: Understanding through simulations

Understanding this departure from self similarity has become an area where numerical simulations can play a major role. Hydrodynamical simulations have shown that in the absence of complex heating and cooling mechanisms, the self similar predictions are well recovered (Navarro et al. (1995), Eke et al. (1998)). The inclusion of additional physics has been shown to break this self-similarity and recover scaling relations that are much

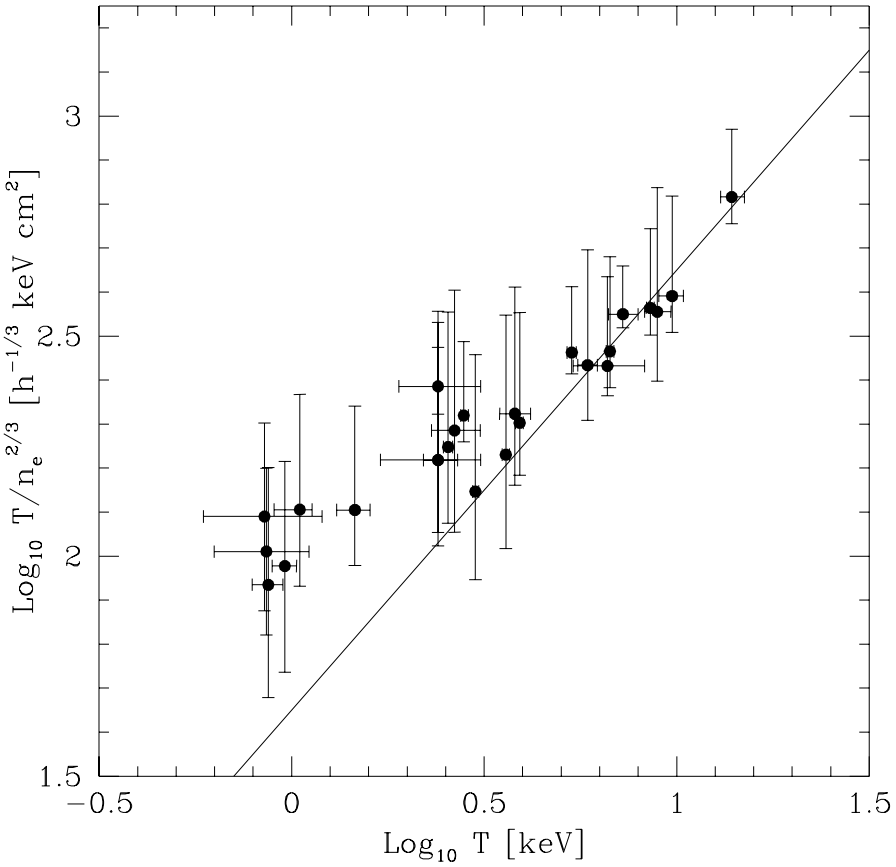


Figure 1.6: Figure 2 and caption from Ponman et al. (1999). *"The gas 'entropy' (defined as $S = T/n_e^{2/3}$ , where $T$ is the mean temperature and $n_e$ is the electron number density) at a fiducial radius $r = 0.1r_v$ is shown as a function of temperature for the 25 systems in our sample. Entropies are computed by fitting isothermal-$\beta$ models to the surface brightness profiles shown in Figure 1."* [NB. Figure 1 not shown here]. *"Error bars indicate* 90% *confidence levels in temperature, and span the variation in entropy from* 0.05 *to* $0.2r_v$*. The solid line shows the similarity relation obtained from numerical simulations including non-radiative gas dynamics, $S(0.1r_v) \sim 45(T/keV)(f_{gas}/0.06)^{-2/3}h^{-4/3}$ $keV$ $cm^2$, where Hubble's constant is $H_0 = 100$ $h$ $km$ $s^{-1}$ $Mpc^{-1}$. The numerical results depend only weakly on the assumed cosmological model, and provide a very good match to the central entropy of hot ($T > 4$ $keV$) systems for $f_{gas} \sim 0.06h^{-3/2}$. However, poor clusters and groups have apparently been heated to higher entropy than achievable through gravitational collapse."*

| *Sample* | *Slope* |
|---|---|
| Markevitch, 1998 | $2.64 \pm 0.27$ |
| Arnaud & Evrard, 1999 | $2.88 \pm 0.15$ |
| Pratt et al, 2008 | $2.73 \pm 0.23$ |

| *Sample* | *Slope* |
|---|---|
| Finoguenov et al, (2001 | $1.89 \pm 0.15$ |
| Sanderson et al, (2003) | $1.84 \pm 0.06$ |
| Vikhlinin et al, (2006) | $1.58 \pm 0.11$ |

Table 1.1: Top) $L - T$ slopes from the literature (Self-similar theory predicts a slope of 2). Bottom) $M - T$ slopes from the literature (Self-similar theory predicts a slope of 1.5). Note that the Vikhlinin et al, (2006) value is measured with cores excised.

nearer to the observed population. In particular Ponman et al. (1999) and Kaiser (1991) have shown that much of the effect is due to an excess of entropy in the core.

A few popular mechanisms for raising the entropy of the core gas via heating and/or cooling are discussed below:

**Radiative Cooling**
If a model of the intra-cluster medium contains a cooling mechanism, one may expect the entropy of the gas to decrease. However, cooling mechanisms have been suggested that may produce large constant-density gas cores, raising the entropy of the gas in the centre of the cluster.

Thomas and Couchman (1992), suggested that radiative cooling removes the lowest entropy gas, causing a loss of pressure support, this in turn causes the remaining gas of higher entropy to flow in from more external regions to form a core. Early studies into this effect (Katz and White (1993), Lewis et al. (2000)) were able to produce synthetic clusters that, in terms of their luminosity and temperature, more closely resemble those we observe. However in this regime there is nothing to prevent excessive overcooling of the gas, resulting in $40 - 50\%$ of the baryons in the cluster forming stars, thus causing large amounts of cool gas to condense onto enormously bright central galaxies (Suginohara and Ostriker, 1998). This is a picture not supported observationally, where we see only $\sim 10\%$ of the baryons in stars (e.g Balogh et al. (2001)). This cooling mechanism was examined further by Pearce et al. (2000), using a more sophisticated multiphase gas model and artifically limiting the amount of gas that is allowed to cool, thus preventing large, bright cooling flows. They found the predicted entropy rise in the core, lowering the overall density; however this did not produce a constant density core as expected. The general effect of their cooling model is to increase the temperature and lower the luminosity of the gas, returning an $L - T$ relation more like the self-similar model, thus returning to the same problem (of not matching the simulations to the observations) as before cooling

was incorporated. In small halos radiative cooling is very efficent as the cooling time is less than the dynamical time (White and Rees, 1978). Pearce et al. (2000) discuss that the lowering of the luminosity will therefore be much more dominant in low mass systems, concluding that in a larger simulation, with a wider mass range, the overall effect will be a steepening of the $L-T$ relation. Models of this type have more recently been shown to be able to recover the $z=0$ scaling relations (e.g Muanwong et al. (2002)).

**Pre-heating**

A period of energy injection prior to cluster formation has been suggested to break self-similarity without causing over-cooling. Pre-heating usually involves a uniform heating of the gas at a redshift of 4 or 5, this is scaled to an amount that correctly recreates the observed $z=0$ scaling. (Kaiser (1991), Ponman et al. (1999)). This pre-heating scheme still lacks a clear physical origin; many authors have tried to attribute the heating to early supernovae. Studies of the entropy available from supernovae, Wu et al. (2000), and Kravtsov and Yepes (2000), have shown that this is unlikely, as the number of supernovae and the heating efficiency required are quite extreme. A more satisfactory, highly energic process that could cause this pre-heating has yet to be found.

**Feedback**

A more realistic picture that may be able to explain the observed properties of clusters is a class of model known as feedback models. The regions of dense cold gas in the core regions of a cluster can reasonably be expected to collapse and form stars ( Katz (1992), Navarro and White (1994)). This star formation ultimately leads to supernova explosions, thus feeding energy back into the interstellar medium. Although this alone may not provide enough energy, when coupled with AGN feedback this will act to increase the entropy of the gas, preventing it from settling in the centre of the halo. Many models in the literature generally mimic feedback by artificially injecting energy into the densest regions of the IGM (e.g Kay et al. (2004)). The models can also reproduce the observed departure from self similarity. A recent set of simulations (Puchwein et al., 2008) have investigated the feedback associated with AGN and black hole growth in a more detailed and realistic way than previous studies, and included its effects within a cooling model. The simulations show that feedback from AGN may be a good candiate for bringing theoretical studies into agreement with the observations without resorting to preheating.

These three different possible solutions (Radiative Cooling, Pre-heating, Feedback) to the observed non-self-similarity present us with a problem, i.e which of them is correct? It is more likely that it is a combination of the above processes that produce the observed properties. In order to make progess it is desirable to be able to make some testable predictions about the effects of each of these processes. For example Muanwong et al. (2006) have used three different cosmological hydrodynamical simulations, each with a different model for the gas physics (Radiative, Preheating and Feedback), all of which are able to reproduce the observed local $L-T$ relation. Each of the models do however show very different evolution in the $L-T$ relation. Looking at the $L-T$ relation in the form

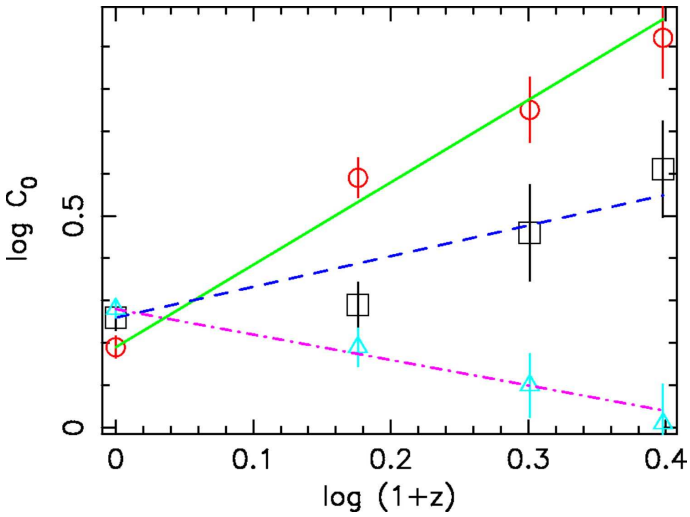


Figure 1.7: figure 8 from Muanwong et al, 2006: The normalistaion of the $L_X - T$ relation as a function of redshift, for clusters in the Radiative (solid line), Preheating (dashed) and Feedback (dot-dashed) simulations.

of equation(1.25)

$$\log C_0 = \log L_0 + A \log(1+z) \tag{1.25}$$

(where $C_0$ is the normalisation, $L_0$ is the best fit Luminosity at $z = 0, T = 1$keV, and $A$ describes the redshift evolution of the relation) the simulations give $A$ values of $1.9, 0.7$ and $-0.6$ respectively (See Figure 1.7). All of which differ from the self similar value of $A = 1.5$.

The difference in evolution between these models allows a potential way of discriminating for or against a model. Muanwong et al. (2006) tentatively suggest that a comparison with observations indicates that their feedback model is generating too much entropy at $z < 1.5$, and that the bulk of heating must have occurred at higher redshift.

The predictions from simulations are becoming more sophisticated all the time (e.g Short and Thomas (2009)). Another major goal of XCS is to measure $L - T$ as a function of lookback time, and to help constrain some of the rival theories.

## 1.4 Motivation for the XMM Cluster Survey

Clusters of galaxies are very interesting objects. The physics that determine their properties is not yet fully understood, and increasing this understanding is reason enough to want to study them further. However they also can be used for cosmology. Constraining cosmological parameters via the cluster abundance is reliant on both well understood scaling relations, and having a large cluster sample over a range of masses and redshifts. A real key to cluster studies is having a good understanding of any biases in the selection processes. To do cosmology, the completeness of a catalogue must be known. To meas-

ure accurate scaling relations, particularly their evolution, the detection dependences on $L, T, z$ and morphology must be understood. With these things in mind many authors have sought to build better catalogues, some of which will be discussed in this section.

### 1.4.1 Optical cluster surveys

The Abell catalogue contains $\sim$ 4000 clusters identified by visual inspection of photographic plates. The original catalogue of clusters in the northern hemisphere was published in 1958 (Abell, 1958). The extended catalogue, including clusters in the southern hemisphere, was published posthumously in 1989 (Abell et al., 1989). The clusters identified by Abell are still being studied, with work based on them being published $\sim$ 50 years after the release of the first catalogue. Optical cluster identification is now automated, with many different methods and algorithms being implemented. The most successful use a combination of finding spatial clustering, and looking for correlations in galaxy properties (often colour), e.g. The Red-sequence Cluster Survey (RCS) (Gladders and Yee (2005); 429 clusters between $0.0 < z < 1.5$ in an inital 10 deg$^2$), The C4 Cluster catalogue (Miller et al. (2005); 748 $M > 10^{14} M_{\odot}$ clusters between $0.02 < z < 0.17$ in 2600 deg$^2$), MaxBCG (Koester et al. (2007); 13823 $M > 10^{14} M_{\odot}$ clusters between $0.1 < z < 0.3$ in 7500deg$^2$). The use of additional information along with spatial correlations is vital to help reduce the effect of superpositions, and fluctuations in the background field of galaxies.

These optical catalogues can also be used to constrain cosmology via the cluster abundance, with the calibration of the mass estimates coming from either weak lensing or X-ray follow-up. For example, a joint analysis of the MaxBCG catalogue with WMAP five year data produces the following : $\sigma_8 = 0.807 \pm 0.020$ and $\Omega_m = 0.265 \pm 0.016$ (Rozo et al., 2009).

### 1.4.2 X-ray cluster surveys I (before XMM/Chandra)

There are numerous X-ray cluster surveys in the literature. Here we will give a very brief summary of some of the surveys carried out before the launch of XMM and Chandra.

The Einstein-Observatory Extended Medium-Sensitivity Survey (EMSS) (Gioia et al., 1990) serendipitously detected 98 clusters in 778 deg$^2$ in a $0.3 - 3.5$keV band, about 40% of which were at $z > 0.2$ and were previously unknown. Although known clusters had been detected in X-ray bands before, work with Einstein highlighted the relative ease with which clusters could be serendipitously detected with X-ray instruments.

The ROSAT Brightest Cluster Sample (BCS) (Ebeling et al., 1998) is a sample of the 201 X-ray-brightest clusters of galaxies (dec $> 0$, $|b| > 20^{\circ}$), at $z \leq 0.3$ with fluxes higher than $4.4 \times 10^{-12}$ erg cm$^{-2}$ s$^{-1}$ in the $0.1 - 2.4$ keV band. Selected from the ROSAT All Sky Survey (RASS) the BCS was the largest X-ray selected cluster sample compiled at the

time.

The ROSAT-ESO Flux-Limited X-ray (REFLEX) (Böhringer et al., 2001) cluster sample was also produced from the RASS. It has a flux limit of 3 $\times 10^{-12}$ erg s$^{-1}$ cm$^{-2}$ in the $0.1 - 2.4$ keV band and comprises 452 clusters at $z \leq 0.3$. The selection function of the survey gave an understanding of the catalogue completeness ($\sim 90\%$), enabling its use for cosmology, resulting in constraints of $\Omega_m = 0.16 \pm 0.06$ $\sigma_8 = 1.2 \pm 0.3$.

The ROSAT Deep Cluster Survey (RDCS) (Rosati, 1998) is, in contrast to the majority of ROSAT surveys, comprised of only the deepest observations in the pointing archive. The RDCS covered $\sim 50$ deg$^2$. About 100 clusters were detected and confirmed, $\sim 25\%$ of which are at $z > 0.5$. The large redshift range of the sample enabled a study of evolution in the cluster population via the X-ray luminosity function (XLF). Rosati (1998) demonstrate that the RDCS sample, in comparision with the EMSS, shows no significant evolution in the XLF at $z \leq 0.8$.

Two more pre-XMM surveys of particular relevance are the 400 Square Degrees ROSAT PSPC Galaxy Cluster Survey (Burenin et al., 2007) and The Bright Serendipitous High-redshift Archival ROSAT Cluster survey (Bright SHARC) (Romer et al., 2000). Like RDCS both used the ROSAT pointing archives to find serendipitous detections of clusters. Due to their similarities with XCS and detailed selection function work they are discussed in more detail in Chapter 5.

In summary, ROSAT surveys covering more than $10^4$ deg$^2$ have yielded over 1000 clusters, out to redshift $z \sim 0.5$ (RASS), or $z \sim 1.0$ (pointed archives). A large fraction of these were new discoveries, although about a third were previously identified as clusters in the Abell or Zwicky catalogues. The ability to determine the selection function for a number of these surveys, and the presence of good optical follow-up, have led to investigations of individual clusters, scaling relations, and cosmological studies.

### 1.4.3 X-ray cluster surveys II (after XMM/Chandra)

The majority of cluster surveys being undertaken with the current generation of X-ray satellites (XMM and Chandra) are using the new, higher quality instruments to follow-up clusters detected with ROSAT. The Reprentative XMM Cluster Structure Survey (REXCESS) (Böhringer et al., 2007), is based on the REFLEX sample, the largest statistically understood sample of clusters available at the time. Böhringer et al. (2007) use the higher sensitivity and spectroscopic ability of XMM to study 31 of the REFLEX clusters in more detail, this has led to a greater understanding of cluster structure, scaling relations, and provides a low-redshift benchmark with which to study cluster evolution.

The Chandra Cluster Cosmology project (Vikhlinin et al., 2009) is based on a complete

high-redshift subsample of the 400 Square Degree clusters, 37 objects at $z = 0.35-0.9$ with $\langle z \rangle = 0.55$. These clusters have been re-observed with Chandra to provide more accurate mass measurements, particularly at higher redshift, for use in measuring the evolution in the cluster mass function. In conjuction with 49 $z \sim 0.05$ clusters from the ROSAT All Sky Survey, the WMAP five year data, and BAO and SN data,Vikhlinin et al. (2009) measure $\Omega_m = 0.225 \pm 0.043$. Depending on the assumptions used, Vikhlinin et al. (2009) also find $\Omega_\Lambda = 0.83 \pm 0.15$ in non-flat $\Lambda$CDM or $w_0 = -1.14 \pm 0.21$ in a flat universe.

There are very few surveys in the literature using XMM and Chandra for serendipitous cluster searching. The XMM-LSS (Pacaud et al., 2007) is a serendipitous survey of an $8 \times 8$ deg$^2$ contiguous region. The depth of these pointings results in a flux limit of $\sim 5 \times 10^{-15}$ erg cm$^{-2}$ s$^{-1}$ in the 0.5-2 keV band. The processing of the first 5 deg$^2$ of data produced a sample of $\sim 30$ clusters. The XMM-Newton Distant Cluster Project (Lamer et al., 2006) are using XMM archival data with exposure times $> 20$ks for cluster searching, with the aim of increasing the known population at $z > 1$, this has led to the discovery of one of the most distant clusters known to date (Mullis et al., 2005).

There is clearly a need for a survey to complement these existing studies. The surveys discussed tend to fall into two categories: large-area low-redshift, or small-area high-redshift. In order to study evolutionary effects (e.g. for the mass function, or scaling relations) it is necessary to cover a wide range of redshifts, which often means comparing two or more different samples. This can be difficult, as each will have its own biases, and only some have detailed selection functions. The data in the XMM archive will allow a serendipitous survey to fully cover the redshift range already sampled (and even extend it), and do so in a homogenous manner in order to provide a large cluster sample with which to study many areas of cluster science. This is the gap in the field that the XCS (Romer et al. (2001), see Chapter 3) aims to fill (See Figure 1.8).

## 1.5 Overview of the rest of the thesis

The rest of this thesis concentrates on the XMM Cluster Survey (XCS). Chapter 2 will give an overview of XMM-Newton, the instrument used by XCS. Chapter 3 reviews the XCS survey, and introduces the candidate and confirmed cluster samples being produced. Chapter 4 presents an entirely new cluster candidate sample, some of which has already had redshifts determined by the collaboration. Chapter 5 presents the XCS selection function as applied in Sahlén et al. (2009), and tests the assumptions made therein. Chapter 6 compares the Chapter 5 selection function to one determined using profiles from Cosmological Hydrodynamical simulations. The use of these simulated clusters also enable us to determine the selection function dependencies on more realistic cluster properties, such as cool cores and substructure.

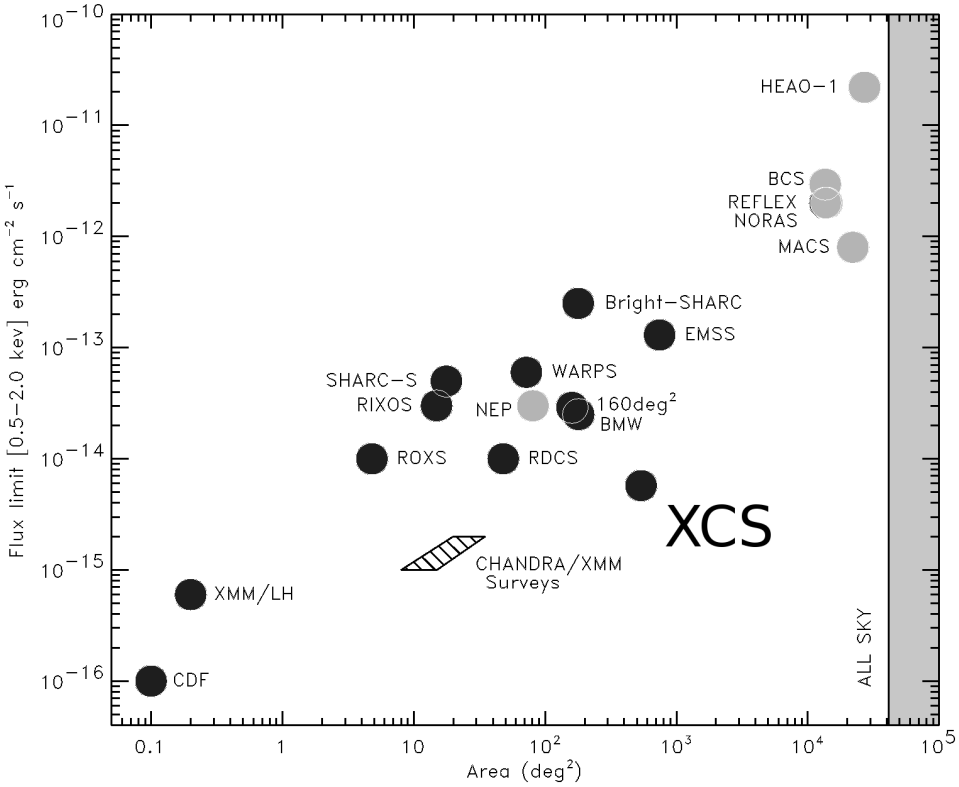


Figure 1.8: Figure 1.3 from Davidson (2005), adapted from Rosati et al. (2002). A flux vs area summary of pre 2002 serendipitous and pointed X-ray cluster surveys (dark and light circles respectively). The likely position for XCS, when it is complete, is also shown.

# Chapter 2

# XMM-Newton

This chapter will give an introduction to the X-ray Multi-Mirror (XMM) Newton observatory satellite. This is a review chapter, with figures drawn from the XMM users handbook, with the exception of Figure 2.4 which was generated by the author.

XMM-Newton is the second of ESA's four cornerstone missions defined in the Horizon 2000 Programme. It was launched on December 10th, 1999 and carries two distinct types of telescope: three Wolter type-1 X-ray telescopes, with different X-ray detectors in their foci, and a 30-cm optical/UV telescope with a pre-amplified CCD detector in its focal plane. The three main types of science instrument onboard are as follows:

- European Photon Imaging Camera (EPIC): 3 CCD cameras for X-ray imaging, moderate resolution spectroscopy, and X-ray photometry; there are two different types of EPIC camera, MOS and pn. XMM-Newton carries 2 MOS cameras and one pn.

- Reflection Grating Spectrometer (RGS): 2 essentially identical spectrometers for high-resolution X-ray spectroscopy and spectro-photometry.

- Optical Monitor (OM): for optical/UV imaging and grism spectroscopy.

Unless prohibited for some unusual reason, all six of the science instruments on board operate simultaneously. However little more will be said of the optical monitor or RGS, as this thesis is primarily concerned with the images produced from the three X-ray cameras. The simultaneity of the data collection means that regardless of the pointing type, the EPIC cameras will be collecting serendipitous data. A pictoral representation of the satellite is given in Figure 2.1.

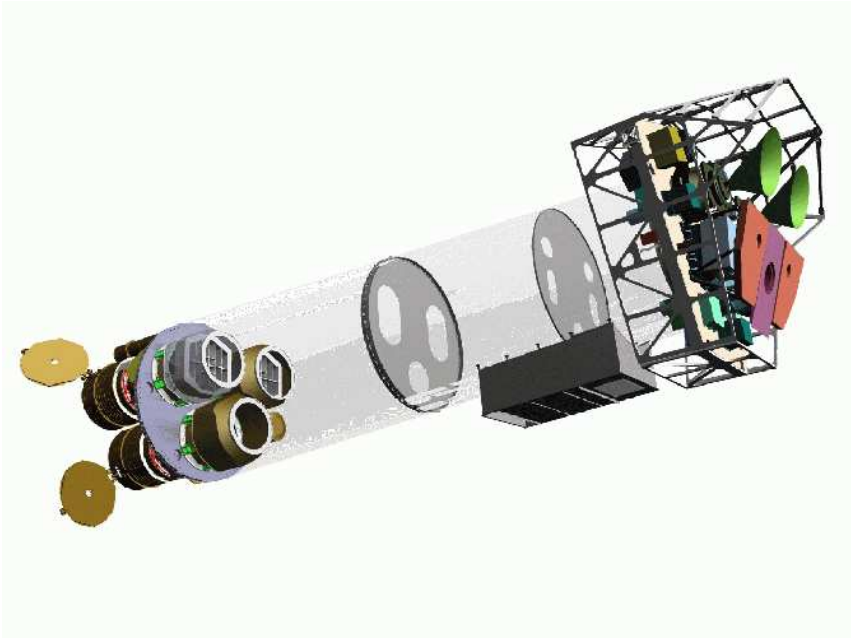

Figure 2.1: Caption and figure from the XMM users handbook, figure 1. *"Sketch of the XMM-Newton payload. The mirror modules, two of which are equipped with Reflection Grating Arrays, are visible at the lower left. At the right end of the assembly, the focal X-ray instruments are shown: The EPIC MOS cameras with their radiators (black/green "horns"), the radiator of the EPIC pn camera (violet) and those of the (light blue) RGS detectors (in pink). The OM telescope is obscured by the lower mirror module. Figure courtesy of Dornier Satellitensysteme GmbH."*

## 2.1 X-ray Mirrors and Cameras

Due to the high energy of X-ray photons, it is difficult to use them for imaging. Their tendancy to pass through material is well known and so they must by focused by grazing incidence reflection. The solution found to maximize the collecting area of the telescope was to use a set of 58 co-aligned concentric nested mirrors (See Figures 2.2 and 2.3). There are three such sets of mirrors, each of which has a focal length of 7.5m. Each mirror has a nickel substrate and a reflective gold coating to ensure efficient focussing of X-rays with energies up to 10 keV. The mirror nests were constructed and aligned with very high precision. However, the launch of the satellite caused a small amount of misalignment, which was expected. The three X-ray telescopes are co-aligned with a relative astrometry between the three EPIC cameras calibrated to better than 1-2" across the full FOV. The light paths of the telescopes can be seen in Figures 2.2 and 2.3, the two telescopes fitted with the MOS cameras have grating assemblies in their light paths, diffracting part of the incoming radiation onto their secondary focus.

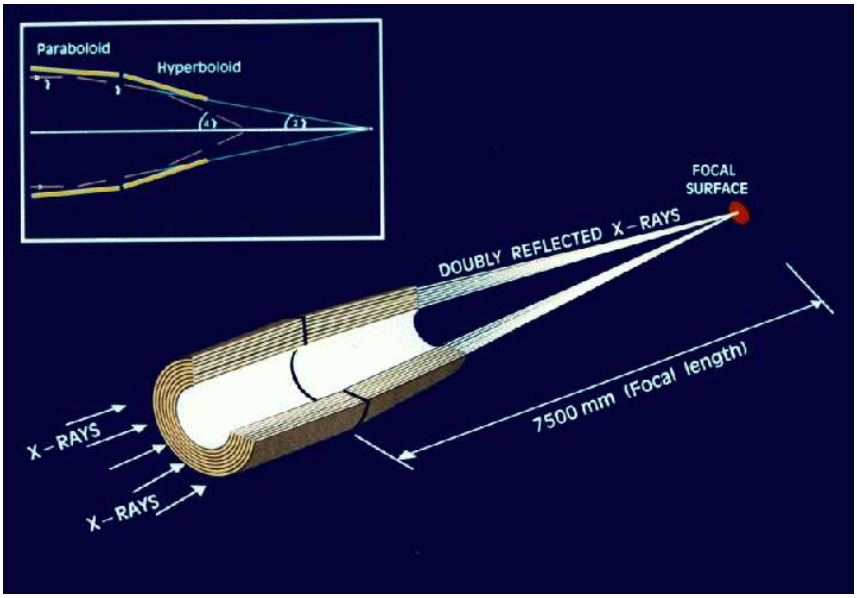


Figure 2.2: Caption and figure from the XMM users handbook, figure 2. *"The light path in XMM-Newton's open X-ray telescope with the pn camera in focus (not to scale)."*

### 2.1.1 European Photon Imaging Camera (EPIC)

Two of XMM-Newton's X-ray telescopes are equipped with EPIC MOS (Metal Oxide Semiconductor) CCD arrays rotated by 90° with respect to each other, the third carries a different CCD camera called EPIC pn. The two types of EPIC camera are fundamentally different, not only in their array geometry but other properties as well, e.g their readout times. The readout of the pn chips is much faster than that of the MOS cameras, because each pixel column has its own readout node. The MOS chip arrays consist of 7 individual

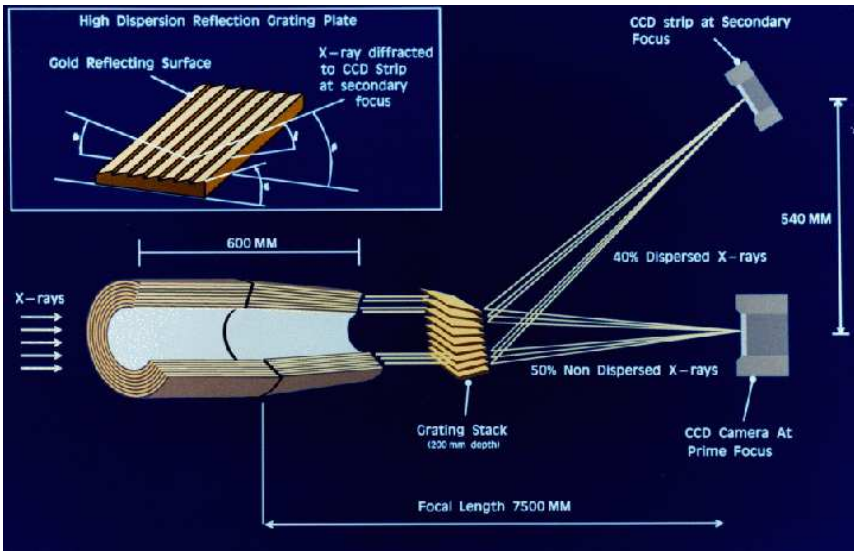


Figure 2.3: Caption and figure from the XMM users handbook, figure 3. *"The light path in the two XMM-Newton telescopes with grating assemblies (not to scale). Note that the actual fraction of the non-intercepted light that passes to the primary MOS focus is 44%, while 40% of the incident light is intercepted by grating plates of the RGA."*

identical, front-illuminated chips, the pn camera is a single Silicon wafer with 12 rear-illuminated CCD chips integrated.

The three cameras can operate in a number of different science modes, examples of which can be seen in Figure 2.4. The outer 6 MOS CCD's remain in standard imaging mode while the central MOS CCD can be operated separately. Shown within Figure 2.4 is an example of an exposure with MOS1 CCD6 switched off, this is due to an event on 09 March, 2005, during XMM-Newton revolution 961, registered in the focal plane of the EPIC MOS1 instrument. The characteristics of the event might be attributed to a micrometeorite impact scattering debris into the focal plane. The chip has not responded properly since, and at the time of writing remains switched off [1].

## 2.2 Point Spread Function

Of crucial importance is an understanding of XMM's ability to focus photons, this is defined by the Point Spread Function (PSF). The PSF details how the photons from a perfect point source are focused by the mirrors and registered on the CCDs. The shapes of the on-axis PSF of the XMM X-ray telescopes are shown in Figure 2.5. This on-axis PSF has a narrow core and varies little between $0.1 - 6$keV, the azimuthally averaged MOS1 PSF is shown in Figure 2.6 with the best fit king-profile.

However the PSF has some off-axis angle dependence and becomes elongated at large

[1] http://xmm.esac.esa.int/external/xmm news/items/MOS1-CCD6/

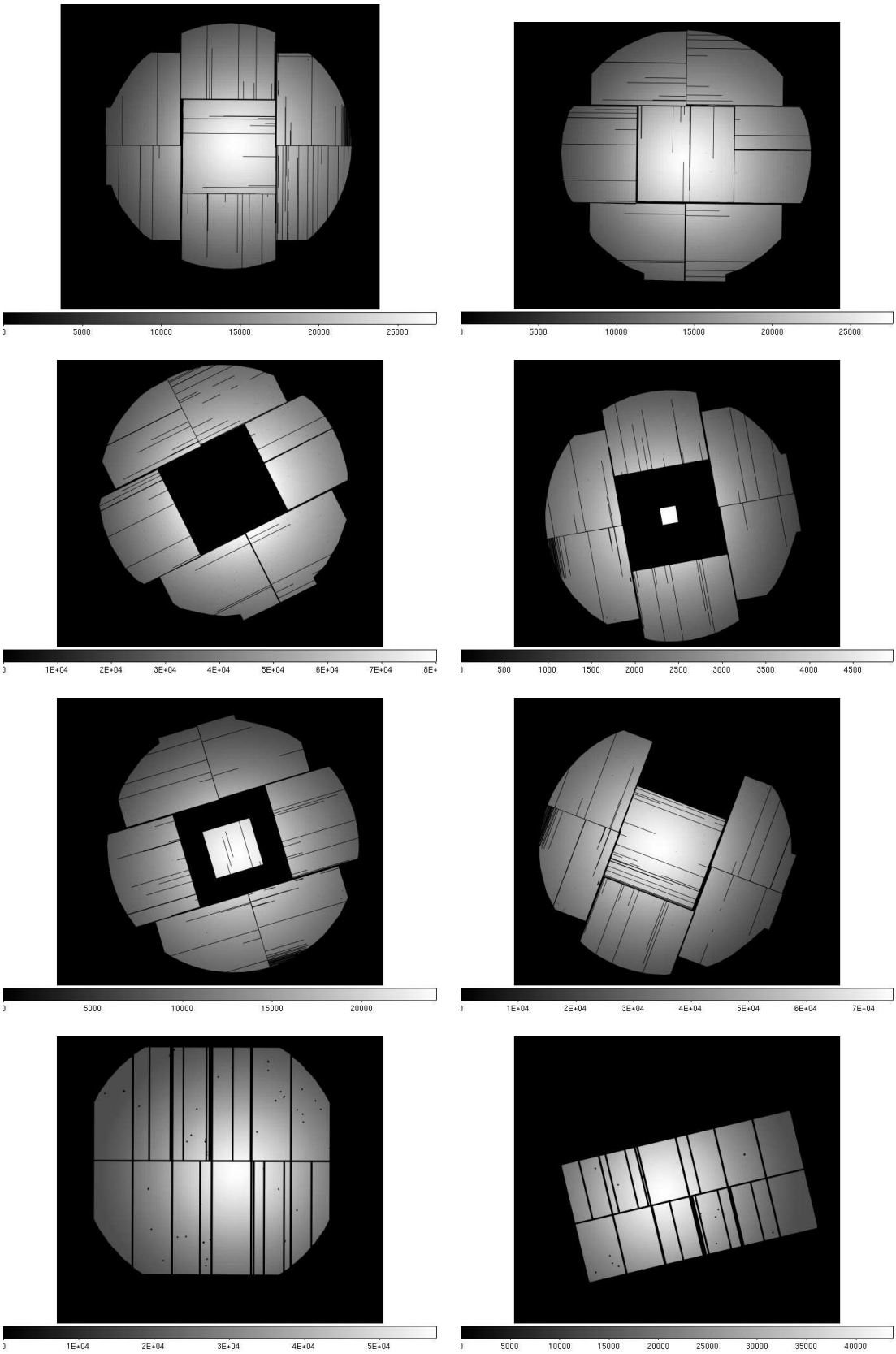


Figure 2.4: Typical sky footprints of differing observing modes. In order from top left: MOS1 full window mode, MOS2 full window mode, MOS fast uncompressed, MOS partial window W2 or W4 mode, MOS partial window W3 or W5 mode, MOS1 full window mode with CCD6 switched off, pn full window mode, pn large window mode.

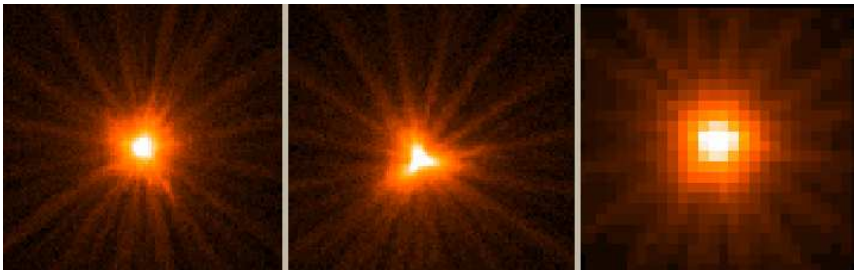

Figure 2.5: Caption and figure from the XMM users handbook, figure 4. *"On axis point spread function of the MOS1, MOS2 and pn X-ray telescopes (left to right) registered on the same source with each MOS camera in Small Window Mode, and the pn camera in Large Window mode. The pixel size is 1.1 arcsec square for the MOS, and 4.1 arcsec square for the pn. The images are 110 arcsec wide. A square root scale has been used to visualise the wings of the point spread function. The core of the PSF is piled-up for this source, with a different factor for the MOS and the pn. The star-like pattern is created by the spider which supports the 58 co-axial Wolter I mirrors of the telescope. The shape of the point spread function core is slightly different for all cameras, with MOS2 having a somewhat more pronounced shape."*

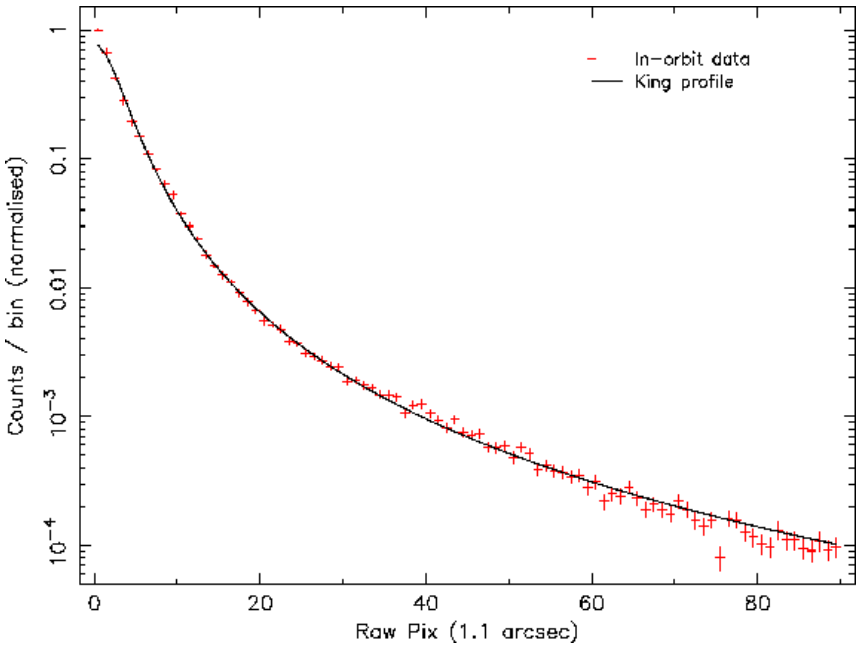


Figure 2.6: Caption and figure from the XMM users handbook, figure 5. *"Radial count distribution for the on-axis PSF of the MOS1 X-ray telescope in the 0.75-2.25 keV energy range. A King profile (solid black line) best fit to the in-orbit measurement (red crosses) is shown for comparison."*

off-axis, to make matters more complicated the shape of the PSF is not azimuthally symmetric as seen in pre-launch tests (see Figure 2.7), in addition the PSF becomes more energy dependent at increasing off-axis angles.

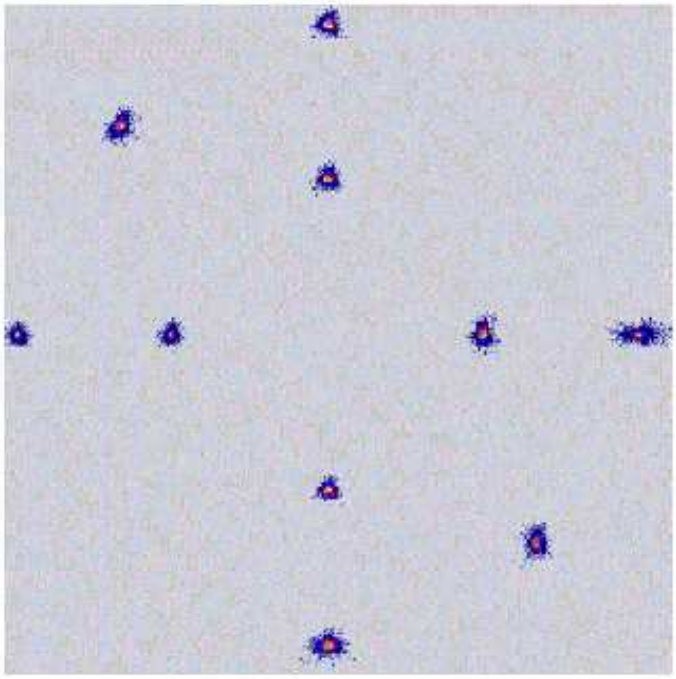

Figure 2.7: Pre-launch test showing the shape of the PSF across the field of view (at off-axis angles of $7'$ and $14'$), from the XMM Users Handbook.

### 2.2.1 Modelling the PSF

There are four main PSF models in the XMM calibration documents. These have their different merits, and are summarised here.

1. **Low Accuracy.** This model consists of a Gaussian, that is dependent on off-axis angle and energy. The simplicity of this model is appealing; however it fails to take into account the ellipticity of the off-axis PSF or its azimuthal variation.

2. **Medium Accuracy.** This model is based on a library of PSF images created through numerical simulations of the mirrors. For a given energy and off-axis angle an image can be produced by interpolation of the library images. In the Science Analysis System (SAS) task CALVIEW the model PSF for any azimuthal angle can be obtained. This however is just a rotated version of the library image at the same off-axis angle and so does not reproduce any azimuthal variation in structure. Also, at high off-axis angle there is evidence that the true PSF develops twin peaks with extensive wings, which is also not accounted for in the model (See Figure 2.8). This is the only two-dimensional PSF model available.

3. **High Accuracy.** This is an analytical model comprised of three Gaussian profiles combined in an attempt to model both the core and wings of the PSF. It has been superseded by the Extended Accuracy model.

4. **Extended Accuracy.** Through studying a sample of real detected point sources Ghizzardi (2001) parameterised the in-flight PSF for all three cameras. The model consists of an analytic King Model, plus background.

$$PSF = A\left[1 + \left(\frac{r}{r_c}\right)^2\right]^{-\alpha} + B \tag{2.1}$$

where the core radius, $r_c$, slope, $\alpha$, normalization, A, and a constant background, B, are all fitted for each camera as a function of off-axis angle. This provides a more reliable fit than a Gaussian to both the core and the wings, but despite this there are still some inadequacies of the model. The fits are limited to low energies ($\leq$ 5keV) and low/moderate off-axis angles ($\leq 7'$). Also the fit is made to azimuthally averaged profiles, leading to a lack of structure and crucially ellipticity.

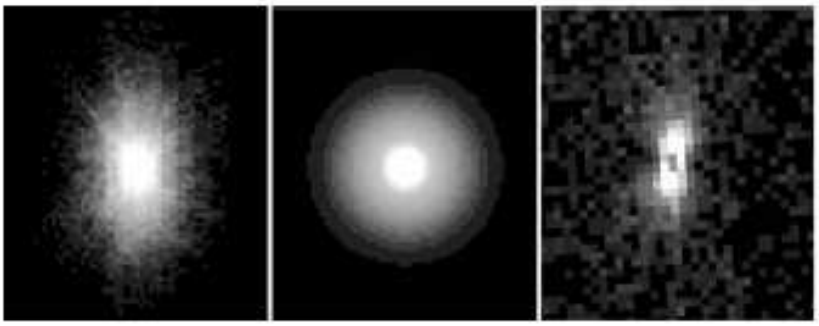

Figure 2.8: Figure 3.2: from Davidson (2005). Left) The model PSFs from CALVIEW for an off-axis angle of $10'$, azimuthal angle= $90^\circ$ using the Medium accuracy model; middle) likewise for the Extended accuracy model; right) real twin-peaked source at an off-axis angle of 14'.

## 2.3 Summary

A summary of the important characteristics of XMM is given in Table 2.1. The energy range of EPIC cameras is $0.15 - 12$ keV, with a Field of View of $30'$ diameter. The spatial resolution is determined by the size of the PSF, which has on-axis values of $5 - 6''$ (FWHM).

| Instrument | EPIC MOS | EPIC pn | RGS |
|---|---|---|---|
| Bandpass | $0.15 - 12$ keV | $0.15 - 15$ keV | $0.35 - 2.5$ keV |
| Sensitivity* (erg $s^{-1}$ $cm^{-2}$) | $\sim 10^{-14}$ | $\sim 10^{-14}$ | $8 \times 10^{-5}$ |
| Field of view (FOV) | $30'$ | $30'$ | $\sim 5'$ |
| PSF (FWHM) | $5''$ | $6''$ | N/A |
| Pixel size | $40\mu m(1.1'')$ | $150\mu m(4.1'')$ | $81\mu m(9 \times 10^{-3}A)$ |
| Timing resolution | 1.75ms | 0.03 ms | 0.6 s |
| Spectral resolution | $\sim 70$ eV | $\sim 80$eV | $0.04/0.025A$ |

Table 2.1: A summary of the important characteristics of XMM. Table information from the XMM Users Handbook. * Sensitivity is quoted after 10ks of exposure.

# Chapter 3

# XCS and XCS DR1 & DR2

In this chapter we shall give an outline of the XMM Cluster Survey (XCS), including its current status and long-term science goals. This will include a review of previous published XCS papers and the PhD thesis of Michael Davidson (Davidson, 2005). Although most of this chapter is review, note that Figure 3.6 and the DR2 catalogue are the work of the author.

## 3.1 Survey overview, motivation and goals

The XMM Cluster Survey (XCS) (Romer et al., 2001) is a serendipitous X-ray galaxy cluster survey using data from the XMM archive. Since its launch in 1999, XMM-Newton has taken over 4000 observations covering more than 500 square degrees, and much of this data is publicly available. The main aim of XCS is to exploit this large archive for cluster searching, in order to provide a cluster catalogue suitable to study cosmology. To achieve the goal of constraining cosmological parameters the cluster catalogue must have the following attributes: the catalogue must cover a redshift range large enough to be able to measure evolution in the cluster number density; likewise the catalogue must contain enough clusters so that each redshift bin contains a significant number of objects; each object must have a known mass (measured via its X-ray temperature) and redshift; in addition the catalogue must be accompanied by a detailed selection function.

Alongside the main cosmology goal of XCS there are numerous other results that will come out of the project, many of which will in themselves be field-leading results. The final catalogue is expected to be an order of magitude larger than any other homogenous sample so-far compiled, thus the $L-T$ relation from this sample will be able to place constraints on deviations from the self-similar model, and so assist in studies of non-gravitational heating (See Section 1.3.5). With its detailed selection function (Chapter 5) the XCS sample will also be a key tool for morphological studies. XCS expects to detect many clusters at

$z > 1.0$, XMMXCS J2215.9 − 1738 (hereafter XMMXCS J2215) for example remains the most distant spectroscopically confirmed X-ray selected cluster currently known, and so offers important information regarding star formation rates, galaxy morphology, and colour-magnitude relations (Hilton et al., 2009). In addition studies of BCGs in these high redshift clusters can place constraints on mass build-up and galaxy evolution (Collins et al., 2009). One of the by-products of the XCS cluster sample is a large point source catalogue, which is currently being exploited for finding X-ray spectra of SDSS Quasars, and also hunting for Isolated Neutron Stars.

The collaboration currently consists of 19 full members plus additional affiliates from a range of intitutions based in 5 different countries (see Table 3.1)

| Name | Institution | Country |
|---|---|---|
| Chris Collins | Liverpool John Moores University | UK |
| Michael Davidson | Royal Observatory Edinburgh | UK |
| Matt Hilton | University of KwaZulu-Natal SAAO | South Africa |
| Mark Hosmer | University of Sussex | UK |
| Ben Hoyle | University of Portsmouth | UK |
| Scott Kay | University of Manchester | UK |
| Andrew Liddle | University of Sussex | UK |
| Ed Lloyd-Davies | University of Sussex | UK |
| Robert Mann | Royal Observatory Edinburgh | UK |
| Nicola Mehrtens | University of Sussex | UK |
| Chris Miller | Cerro-Tololo Inter-American Observatory NOAO | Chile |
| Robert Nichol | University of Portsmouth | UK |
| Kathy Romer (PI) | University of Sussex | UK |
| Kivanc Sabirli | University of Sussex | UK |
| Martin Sahlen | University of Sussex | UK |
| Adam Stanford | Lawrence Livermore National Laboratory | USA |
| John Stott | Liverpool John Moores University | UK |
| Pedro Viana | Universidade do Porto | Portugal |
| Mike West | European Southern Observatory | Chile |

Table 3.1: The XCS collaboration

## 3.2 Review of published XCS papers

*A serendipitous galaxy cluster survey with XMM: Expected cluster catalog properties and scientific applications* (Romer et al., 2001).
Romer et al. (2001) predicted the properties of XCS based on simulations of cluster population models as a function of cosmology, the charactistics of the EPIC PN camera, and a generic model for cluster profiles. While XCS itself had not yet been built, and the XMM archive was still in its infancy, Romer et al. (2001) demonstrated how a serendipitous survey with archival XMM data had the potential to place strong constraints on $\Omega_0$ and to a lesser extent $\Omega_\Lambda$, while also producing a cluster catalogue, with luminosities and temperatures, that would be at least an order of magnitude larger than any other in the literature at the time.

*Apparent and actual galaxy cluster temperatures* (Liddle et al., 2001).
Liddle et al. (2001) investigate how far the XCS X-ray data alone could be exploited in terms of cosmology. The authors show that without redshifts, the apparent temperature function of clusters can be used to make constraints on a combination $\sigma_8$ of $\Omega_m$, but to break the degeneracy redshift information is required. Liddle et al. (2001) investigate how well the redshifts can be estimated from the X-ray data, given enough counts this may be possible based upon the continuum emission or spectral features, however this will not be possible in the majority of cases, so the authors test some other estimators. A combination of X-ray flux with the apparent temperature may be able to provide redshifts, but only if the evolution in the $L-T$ relation is well understood. They conclude stressing the need for redshift measurements, and indicate the use of optical data to meet this need.

*The XMM Cluster Survey: A massive galaxy cluster at* $z = 1.45$ (Stanford et al., 2006).
Stanford et al. (2006) report the discovery of XMMXCS J2215, a massive galaxy cluster found as part of XCS. Optical spectroscopy shows that six galaxies within a $60''$ diameter region lie at $z = 1.45 \pm 0.01$, making this the most distant X-ray spectroscopically confirmed cluster. Model fits to the X-ray spectra yield a temperature of 7.4keV. The authors discuss the possibility of a central point source contaminating the cluster emission, accounting for this would lower the temperature to 6.5keV. The measured temperature was the highest for any known cluster at $z > 1$ indicating a relatively massive cluster for this redshift.

*The XMM Cluster Survey: The Dynamical State of XMMXCS J*2215.9$-$1738 *at* $z = 1.457$ (Hilton et al., 2007).
Hilton et al. (2007) increased the number of galaxies with spectroscopic redshifts within the virial radius of XMMXCS J2215 to 17. Using this data the authors make a measurement of the line of sight velocity dispersion, $\sigma_v = 580\mathrm{kms}^{-1}$, and note that given the temperature measured in Stanford et al. (2006) this is inconsistant with the hypothesis of equipartition of energy between the gas and galaxies, $\beta = \sigma_v^2 \mu m_p / kT = 1$, indicating that the intracluster medium contains 2-3 times the kinetic energy of the galaxies. The cluster is also significantly under-luminous compared to the expectation from self-similar

$L-T$ evolution. Hilton et al. (2007) investigate the possiblity of a recent merger causing this behaviour, and find only mild evidence for a line of sight merger. The alternative mechanism may be heating due to supernova and/or AGN.

*Early assembly of the most massive galaxies* (Collins et al., 2009).(Hosmer is a co-author). Collins et al. (2009) use a sample of 5 high redshift ($1.2 \leq z \leq 1.5$) clusters including XMMXCS J2215 to investigate stellar mass evolution in brightest cluster galaxies with respect to a local sample of clusters of similar mass. Using a range of stellar evolution models the BCG stellar masses are estimated and are found to show much less evolution than expected from hierarchical models. The BCGs appear to have already assembled $\geq 90\%$ of their mass by $z \sim 1.5$, where as current models predict $z \sim 0.2$ before this mass level is reached.

*The XMM Cluster Survey: Galaxy Morphologies and the Color-Magnitude Relation in XMMXCS J*$2215.9-1738$ *at* $z = 1.46$ (Hilton et al., 2009).(Hosmer is a co-author).
Hilton et al. (2009) conducted a study of the morphological fractions and colour-magnitude relation in the galaxy cluster XMMXCS J2215. This is the 1st such study of an X-ray selected cluster at $z \sim 1.5$. The morphological fractions are similar to other clusters at $z \sim 1$. Thus, the dominant component of the galaxy population observed in clusters at low redshift was already in place $\sim 4.5$Gyr after the Big Bang. The colour-magnitude relation is found to be consistent with that from Coma, implying little evolution over the last $\sim 9$ Gyr. XMMXCS J2215 is also found to show evidence of 'downsizing', with a deficit of faint red sequence galaxies in comparison to observations of clusters at low redshift.

*The XMM Cluster Survey: Forecasting cosmological and cluster scaling-relation parameter constraints* (Sahlén et al., 2009).(Hosmer is a leading co-author).
As discussed previously, XCS aims to use the abundance of galaxy clusters as a function of mass and redshift to place constaints on cosmological models. The ability of XCS to achieve this goal is assessed in Sahlén et al. (2009). The paper forecasts the expected cluster samples from the XCS, and based on those, its ability to constrain cosmology and cluster scaling relations using self-calibration, specifically the expected constraints on $\Omega_m$,$\sigma_8$ and the $L-T$ relation for a flat universe. Sahlén et al. (2009) details the way in which errors in cluster observables ($L$, $T$, $z$), and the assumptions made in their scaling, can influence the accuracy of the measured $n(M,z)$. This in turn can increase the statistical errors in the cosmological parameters, or in some cases cause systematic offsets.

Figure 3.1 (Figure 14 from Sahlén et al. (2009)) shows the expected constraints on $\Omega_m$ and $\sigma_8$ from the XCS500 (see Section 3.6.1). These are the result of exploring the likelihood function for the observed cluster catalogue through Monte Carlo Markov Chain techniques. Figure 3.1 demonstates the effect of temperature and/or redshift measurement errors on the expected cosmological constraints. Figure 3.1a shows that if the scaling relations are known, and the measurement errors accounted for, the constraints are centred around the fiducal value. Figure 3.1b and Figure 3.1c show that if these measurement errors are not

accounted for in the analysis, then the constraints can be systematically offset from the fiducal values. $\Omega_m$ is expected to be measured to $\pm 0.03$, and assuming flatness, $\Omega_\Lambda$ to the same accuracy. $\sigma_8$ is expected to be measured to $\pm 0.05$. We also expect to measure the slope and normalisation of the $L - T$ relation to $\pm 13\%$ and $\pm 6\%$ respectively.

Figure 3.2 (Figure 15 from Sahlén et al. (2009)) shows how the incorrect assumptions in the $L-T$ relation can cause considerable difficulties for cosmological parameter estimation, futher highlighting the importance of well understood scaling relations. If we consider as an example the light blue data in Figure 3.2; here we have self-similar $L-T$ evolution, with scatter in the data, however in the analysis constant evolution and no scatter have been assumed. This example returns very tight constraints on both $\Omega_m$ and $\sigma_8$, these constraints are however misleading as the fiducal model is offset by a considerable amount.

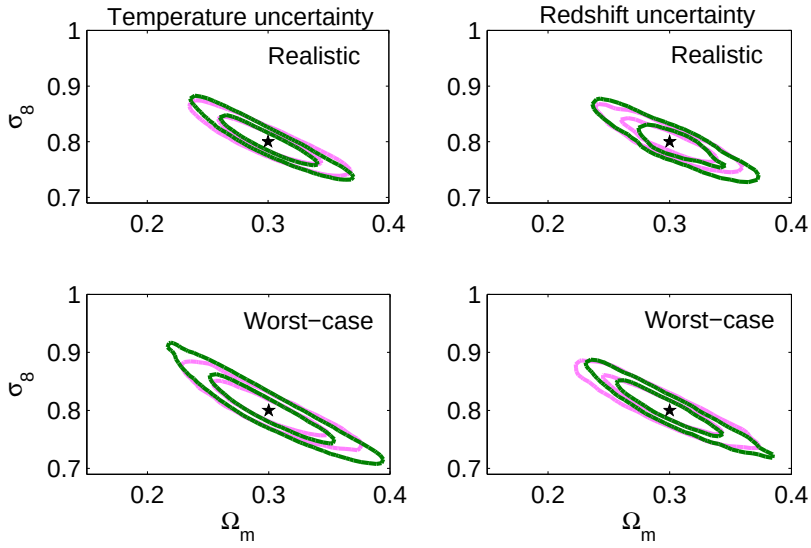


(a) Accounted for single measurement errors

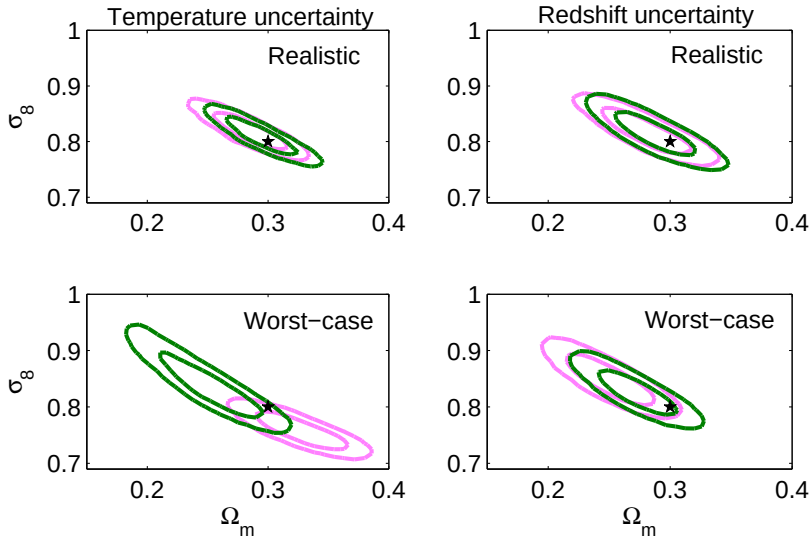


(b) Unaccounted for single measurement errors

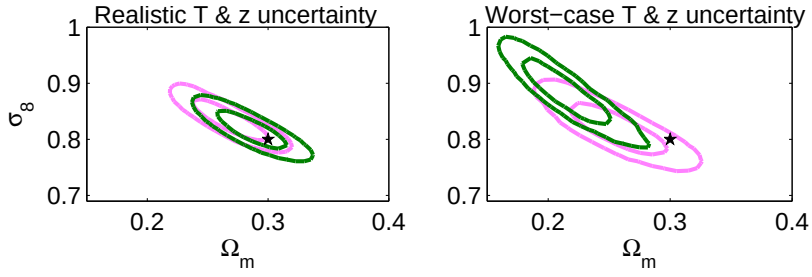


(c) Unaccounted for combined measurement errors

Figure 3.1: Figure 14 from Sahlén et al. (2009). Expected 68 and 95 per cent parameter constraints for XCS500, for known scaling relations, no scatter, and with measurement errors. Stars denote the fiducial model assumed. Green = Self-similar $L - T$ evolution, Pink = No $L - T$ evolution.

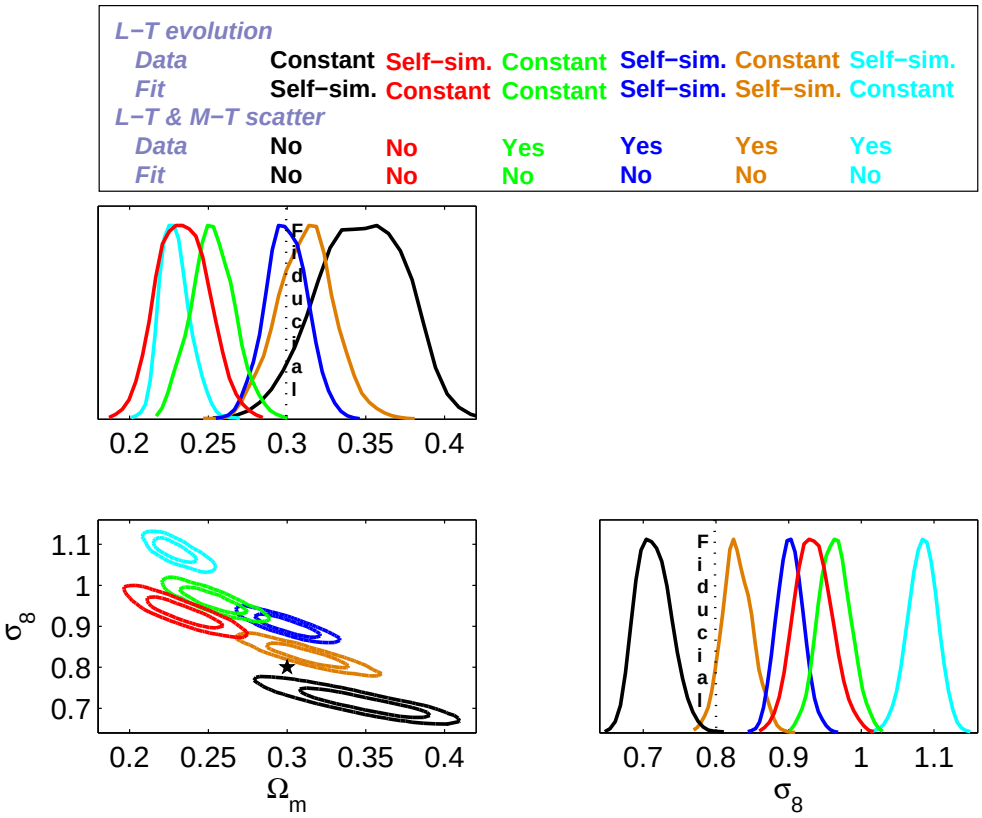


Figure 3.2: Figure 15 from Sahlén et al. (2009). Expected 68 and 95 per cent parameter constraints from the XCS500, for various cluster scaling relation assumptions inconsistent with the fiducial model used for generating the data.

## 3.3 XCS Source Detection

This section will describe the processes undertaken by XCS to extract source lists from XMM images. The steps taken are first summarised, followed by a more in-depth description of the key elements.

- **Data retrival.** All of the public data available in the XMM archive is downloaded to local disks. The data has so far been downloaded on three occasions to account for the growth of the archive, February 2005 (undertaken by K. Sabirli), April 2006 (K. Sabirli) and May 2009 (E. Lloyd-Davies). These downloads define three sets of XCS data, refered to as DR1, DR2, and DR3 respectively. Note that DR3 is a complete re-download and analysis of all previous data to maintain the homogeneity of the data following some changes to the image generation, XAPA and the optical follow-up (See Chapter 4). The remaining sections of this Chapter primarily regard the data in DR1 and DR2.
- **Image creation.** Various inputs to the XCS detection pipelines are created from the raw data. Each observation commonly consists of images from each of the three cameras onboard XMM, and in some cases each camera has multiple exposures. These exposures are merged to create a single image per camera, and also to boost the detectability of faint clusters the three individual camera images are coadded. Images are created in this way for two energy bands: a 'soft' band, $0.5-2.0$keV, and a 'hard' band, $2.0-10.0$keV. The creation of a merged exposure map to accompany the merged image is detailed in Lloyd-Davies (in prep). Also included at this stage is the creation of accompanying ECF's (Energy Conversion Factor) to convert between count rates and fluxes. This ECF calculation was undertaken by the person doing the respective download, i.e. DR1,DR2 (K. Sabirli), DR3 (E. Lloyd-Davies). See Appendix G for details.
- **Image inspection.** Each image is visually inspected for its suitability for cluster finding. At this stage Masks are created by hand to remove any unwanted features of the images (See 3.3.1). DR1 masks were made by M. Davidson, DR2 (by M. Hosmer), DR3 (by M. Hosmer and E. Kuwertz).
- **Source detection** The images are run through XCS Automated Pipeline Algorithms (XAPA) (Davidson, 2005), to create a detection list for each observation. XAPA was run on DR1 by M. Davidson , and on DR2 and DR3 by M. Hosmer (See Section 3.3.2).

### 3.3.1 Image inspection and Mask creation.

Since XMM is used for a wide range of projects in a variety of different areas in astronomy, the observations in the XMM archive contain a large number of target types. As a result

not all of the XMM observations are suitable for XCS. To assess the suitability of the observations, each one is examined by eye. Only if there exists significant area where a new extended source could be discovered is the observation kept in XCS. On this basis, observations of large supernova remnants, crowded star clusters, large nearby galaxies or galaxy clusters, and observations of very bright point sources are not suitable for source detection and are not processed further. Also, if the exposure time of the observation is extremely low or the camera mode is unusable the observation is removed from the XCS list. Some examples of excluded observations are shown in Figure 3.3.

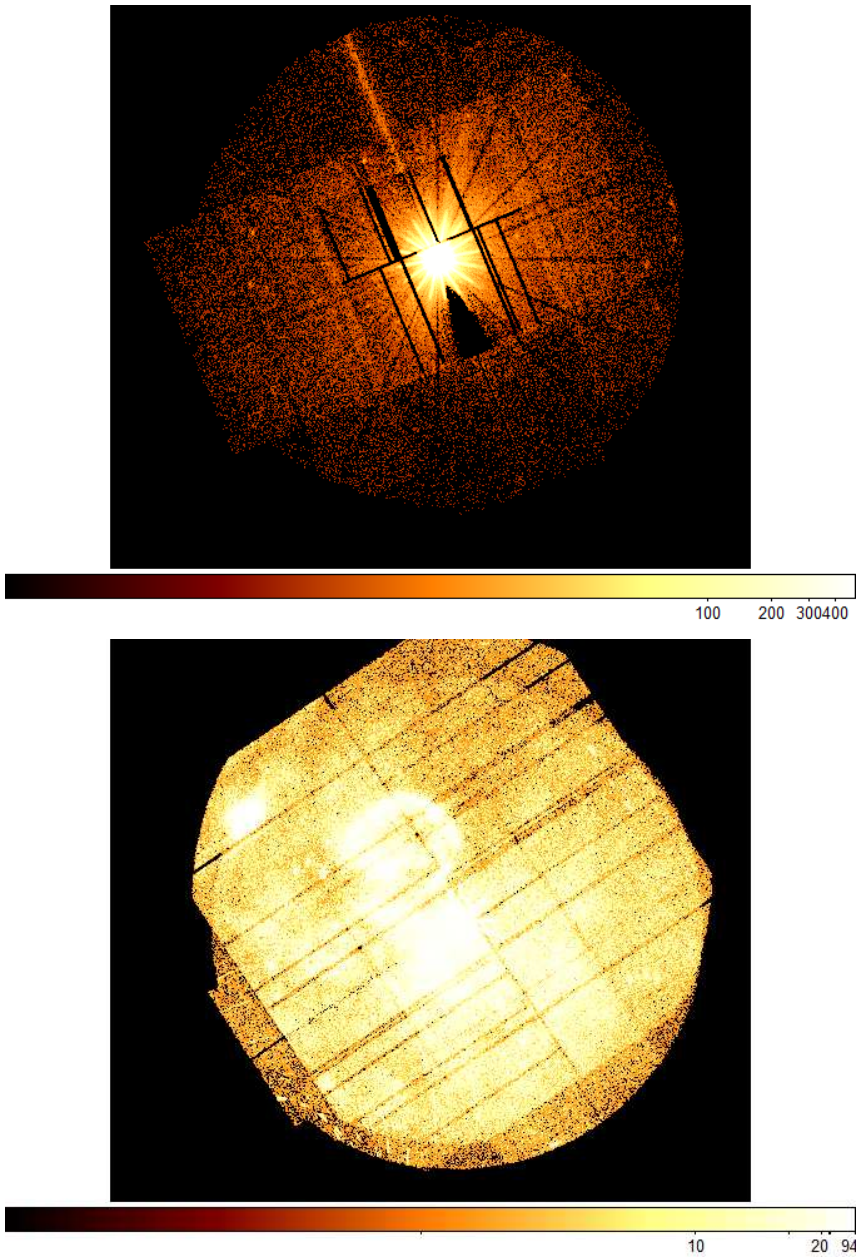


Figure 3.3: Obsids 0411082701 and 0406840301, two examples of observations that are not suitable for XCS. Top: Field dominated by a large point source, showing out-of-time events and artifacts caused by the mirror supports. Bottom: Field entirely covered by a SNR.

For the observations that remain, a mask is made by hand, to remove a range of objects and artefacts that would result in spurious detections. Mask regions include those with bright point sources displaying prominent diffraction spikes; hot pixels; streaks due to Out-of-Time events (when photons are registered as the CCD is being read out, creating a line of counts between the source and the read-out node); and areas containing ghost images (caused by sources outside of the field of view). Both the image and exposure image are multiplied by the mask before being passed on to the detection pipeline. Examples of these artifacts are shown in Figure 3.4. The removal of unsuitable observations reduced the inputs to the source detection processes to 1847 (of 2413) for DR1.

### 3.3.2 Source Detection

The XCS Automated Pipeline Algorithm (XAPA) was first presented in detail in the Ph.D thesis of Michael Davidson (Davidson, 2005). Here we will only summarize the key features of XAPA. An overview of the algorithms is given in Figures B.1 to B.4 of Appendix B, the figures are a set of flow charts from Davidson (2005) showing the steps taken in detection, reconstruction, recovery of source properties and source list cleaning.

XAPA makes use of the WTRANSFORM part of the wavelet transform package WAVDETECT, this uses wavelets to detect sources on given scales in an image. Nine wavelet scales are used (numbered according to increasing size, corresponding to $\sqrt{2}$, 2, $2\sqrt{2}$, 4, $4\sqrt{2}$, 8, $8\sqrt{2}$, 16 and 32 image pixels). These scales are run in 2 separate stages, scales $1-3$ (Run1) are used first, some of the sources detected here are masked out before continuing with scales $4-9$ (Run2). This is to prevent very bright small sources from contaminating the larger scales.

Occasionally, extended sources do present a large central first scale signal, for instance if they contain a point source or the density profile is cuspy. If this happens then the central source can cause the Run2 detection of the larger extent to be removed as a likely lobe around a bright Run1 source (see Davidson (2005) for details). Thus, the true extent of the source is underestimated. To prevent this a simple test is performed:

A grid of 5 by 5 pixels, Q, centred on the source is extracted from the image. The quantity representing the 'cuspiness', C, of the central region is calculated:

$$C = \frac{Q_{max} - Q_{min}}{Q_{max}} \tag{3.1}$$

If $C < 0.85$, then the source is removed from the Run1 list as it is flatter than a real point source.

After both detection runs, XAPA then reconstructs the sources into multi-scaled structures and objects, after which an initial set of source properties is calculated. All sources

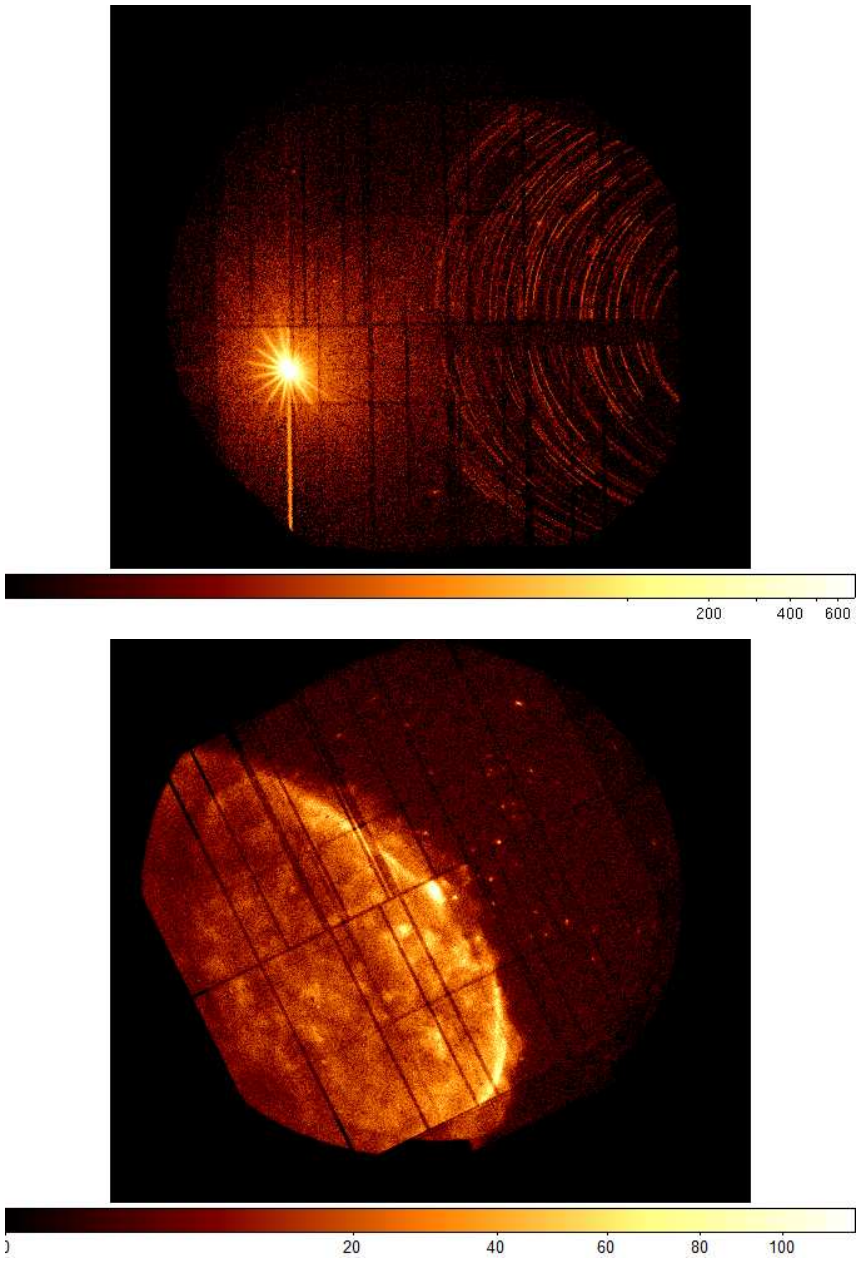


Figure 3.4: Examples of observations containing areas that must be masked out to avoid unnecessary spurious detections. Top: Bright point source with spikes and OOT events, also ringing caused by single reflections from a bright source outside the FOV. Bottom: A large supernova remnant covering half of the FOV.

detected with a significance of less then $4\sigma$ above the background level are removed from the source list. After cleaning of the source list the properties of the remaining sources are re-calculated.

The reconstructed objects are classified based on a comparison of the Encircled Energy Fraction (EEF) of the source to the EEF of the Point Spread Function (PSF) at the source position. The comparison uses a Kolmogorov-Smirnov (K-S) test to determine the probability of a source being pointlike.

The PSF model employed is the Extended model (see Section 2.2). This model is radially averaged, and has limited validity across the field of view. Despite the variation in the shape of the PSF as a function of position, the PSF EEF varies only weakly with off-axis angle. The current PSF model is not ideal, it would be preferable to have a model that re-creates the structure that is seen in the true PSF at large off-axis angles. Due to potential misclassification caused by inadequacies in the model, XAPA assigns certain flags to those sources that maybe classified incorrectly (see Section 3.3.3).

Because we use the actual data in our estimation of the PSF EEF model (by measuring the background component) we cannot strictly use the analytical expression for the K-S confidence threshold. The only option in this case is to perform a set of MonteCarlo (MC) simulations for every source. Although this is computationally expensive it is vital to prevent misclassification. The bootstrap resampling process involves generating 200 realisations of the PSF EEF model and populating them with the same number of counts as measured in the data. Each of these realisations can be compared to the model and an empirical distribution of the K-S $d$ values found ($d$ is the maximum deviation between two sets of cumulative data). If none of the simulated distributions returns a $d$ value as great as the measured value then an approximate upper limit on the probability of the source being truly a point is 0.005.

The extent determination algorithm in XCS is one of its key features. It works well across the field of view, but we do hope to improve the PSF model in time for DR4.

### 3.3.3 XAPA warning flags

Due to various uncertainties, e.g the PSF and the background level, there is still some potential for artifacts in the source lists generated by XAPA. These are flagged in the source list as follows:

- PSF-SIZED FLAG. Due to the flaws in the PSF model, there is a large potential for the mis-classification of point sources as extended (and vice-versa) that are of comparable size to the PSF. In light of this any extended objects that are PSF-sized are flagged as such.

- RUN1 CONTAMINATED FLAG. It is also possible for the wings of the true PSF around bright point sources to be detected as extended emission. To account for this, any extended sources where 50% or more of the flux is coming from internal sources detected in Run1, are flagged as being potential artifacts.

- POINTSOURCE CONTAMINATED FLAG. In addition a final flag is applied to extended objects that are detected with internal pointsources, where the pointsource flux is $\geq 1.3\times$ the extended source flux. This also helps prevent the mis-classification of groups of point sources as a single extended source.

## 3.4 Creation of a source list

XAPA produces a source list for each of the input observations, then these lists are concatenated to form a master detection list. Present in the XMM archive are many areas that have been observed multiple times. As a result some of these entries in the master list will be duplicate detections of the same sources. In order to remove these it is necessary to set an appropriate matching radius. The positional accuracy of the survey is higher for point sources than for extended sources, so it makes sense to use a different radius for each type. The accuracy for point sources varies as a function of off-axis and azimuthal angles (amongst other parameters). However, for simplicity we use a single value for the radius of 5". The case for extended sources is less straightforward because of the variety of source types and morphologies. The positional accuracy for large diffuse objects, such as low redshift clusters, can be very poor, making it very hard to pick an appropriate radius. Fortunately, the largest diffuse sources should have already been masked and removed entirely from their host observation. So, for XCS we use a fixed matching radius of 2' for extended sources (Davidson, 2005). (See Chapter 4 for the matching radius used in DR3). When duplicates are found, the detection with the most soft band counts is kept and a Source list is produced. A final summary of the XCS DR1 and DR2 is given in Table 3.2.

| | Obsids | Detections | Sources |
|---|---|---|---|
| DR1 | 1847 | 74295 | 63327 |
| DR1+DR2 | 2395 | 95694 | 81528 |

Table 3.2: Summary of the XCS DR1 and DR2.

## 3.5 Comparison of XCS DR1 & DR2 point sources to those in the public archives.

It is desirable that the XCS catalogues be of value to the wider X-ray community, not just those working in the field of clusters of galaxies. To this end it is important to undertake

comparisons of the XCS source lists with the data available in the literature. An obvious study with which to make such comparisons is the XMM-SSC's (XMM-Survey Science Centre), XMM-Newton Serendipitous Source Catalogue, known as 2XMM (Watson et al., 2009). Released in 2008, the 2XMM catalogue was the largest X-ray source catalogue ever produced, containing almost twice as many discrete sources as either the ROSAT All Sky Survey or pointed catalogues. Based on 3491 XMM observations, 2XMM contains 246897 X-ray source detections which relate to 191870 unique X-ray sources.

Davidson (2005) included a cross match of the point sources in the DR1 detections list to the first catalogue produced by the XMM-SSC. In general the source properties were in very good agreement, however a comparison of the fluxes showed a $\sim 10\%$ offset in the MOS fluxes, and $\sim 20\%$ in the PN (see the histograms in Figure 3.5). Since Davidson (2005), XMM-SSC have made alterations to their reduction and re-released the data (now included as part of 2XMM). So we have re-done this comparison as follows.

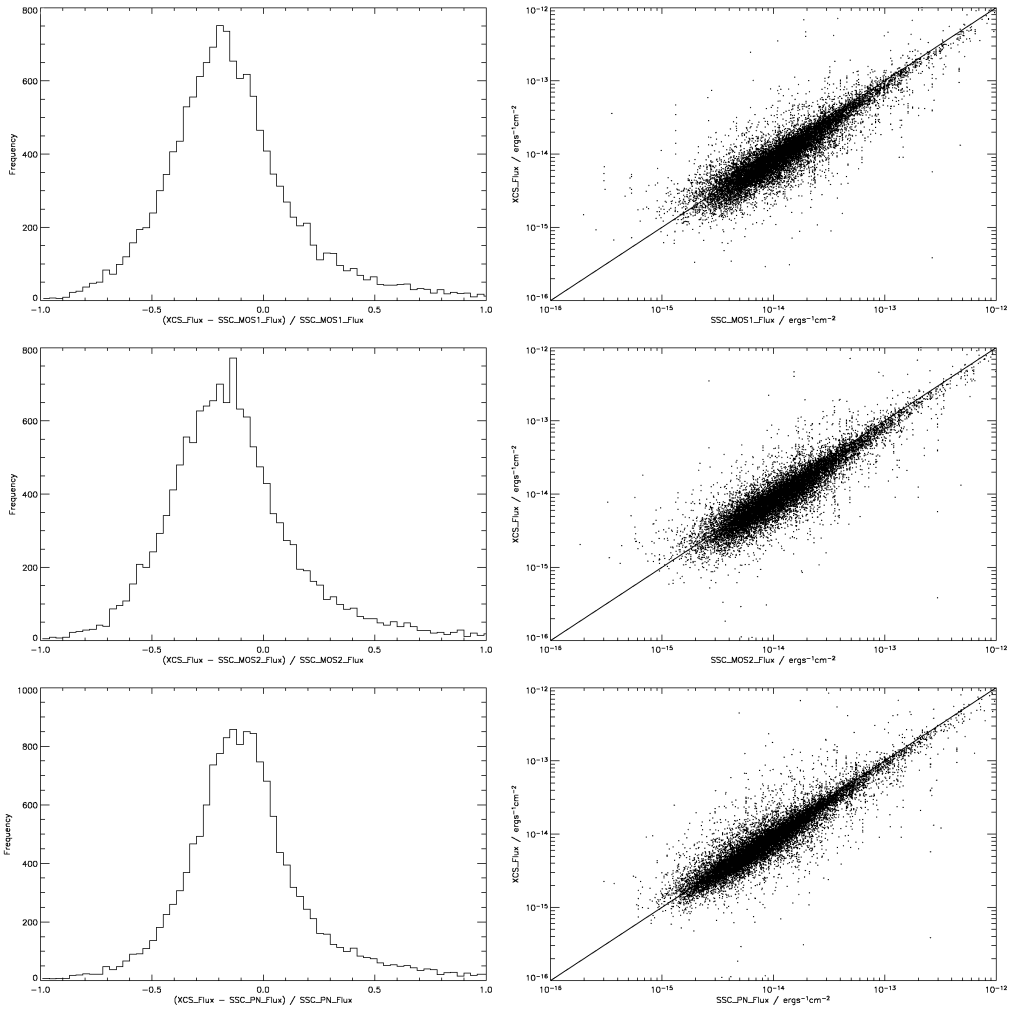


Figure 3.5: Figure 5.7 from Davidson (2005). A comparison of the individual camera fluxes of XCS point sources vs their matches from the XMM-SSC.

Using a 10" matching radius, a comparison between the DR1+DR2 detections and the 2XMM catalogue returns 84283 matches, from a total of 95694 XCS detections. The

difference in the number of detections contained in the two catalogues (246897 vs. 95694) is the result of two factors

- There are less pointings in the combined DR1+DR2 than in 2XMM (2395 vs. 3491)
- Different methods are employed to clean the lists of spurious detections. The 2XMM authors note that: *'About half of the observations have features that may cause spurious detections (mainly the wings of bright sources and large extended emission), and it is strongly recommended to use a filter'* [1]. As outlined in Section 3.3.2, a large amount of filtering of such sources is done on the XCS source lists as part of the detection process.

An updated comparison of the XCS fluxes and their 2XMM counterparts is shown in Figure 3.6. The offset between the 2XMM fluxes and the XCS fluxes remains. The level of the offset is larger than before, it is now consistent across the three cameras, but exists at the $\sim 30\%$ level (vs. previous levels of 10% for MOS and 20% PN). The XMM-SSC have improved the calibration between their PN fluxes and those from the MOS cameras, however this has also caused a greater difference to appear between their data and that of DR1 and DR2. The problems with the 2XMM flux calibration are well documented [2], although this difference may also be an indication of problems with the DR1 and DR2 fluxes. This comparison is repeated in Chapter 4 for the DR3 fluxes and the offset is seen to be significantly reduced. This indicates the majority of the offset may be caused by the use of different calibration. The XMM calibration files are ever changing; the comparision in Figure 3.6 may be comparing data at a time when 2XMM were using more up to date calibration than was used in DR1 and DR2, hence the improvement when using the updated DR3. A small systematic offset is not unexpected, the fluxes are dependent on the ECF's, which assume a spectral model (see Appendix G).

Davidson (2005) made additional checks against optical catalogues and verified the positional accuracy such that 95% of the matches to the optical data are within $7.8''$. These position checks are repeated for DR3 in Section 4.3.1.

The quality of the point source catalogue produced by XAPA has enabled XCS spin-off projects to make specific use of this data; these include a search for Isolated Neutron Stars and projects matching XMM data to SDSS Quasars.

## 3.6 Statistical Sample of cluster candidates

To achieve the cosmology goals of XCS we require an unbiased sample of clusters. Selecting our cluster candidates from the XCS source list is not as simple as just selecting all of the

[1] http://xmmssc-www.star.le.ac.uk/Catalogue/2XMM/

[2] http://xmm.vilspa.esa.es/docs/documents/CAL-TN-0018.pdf

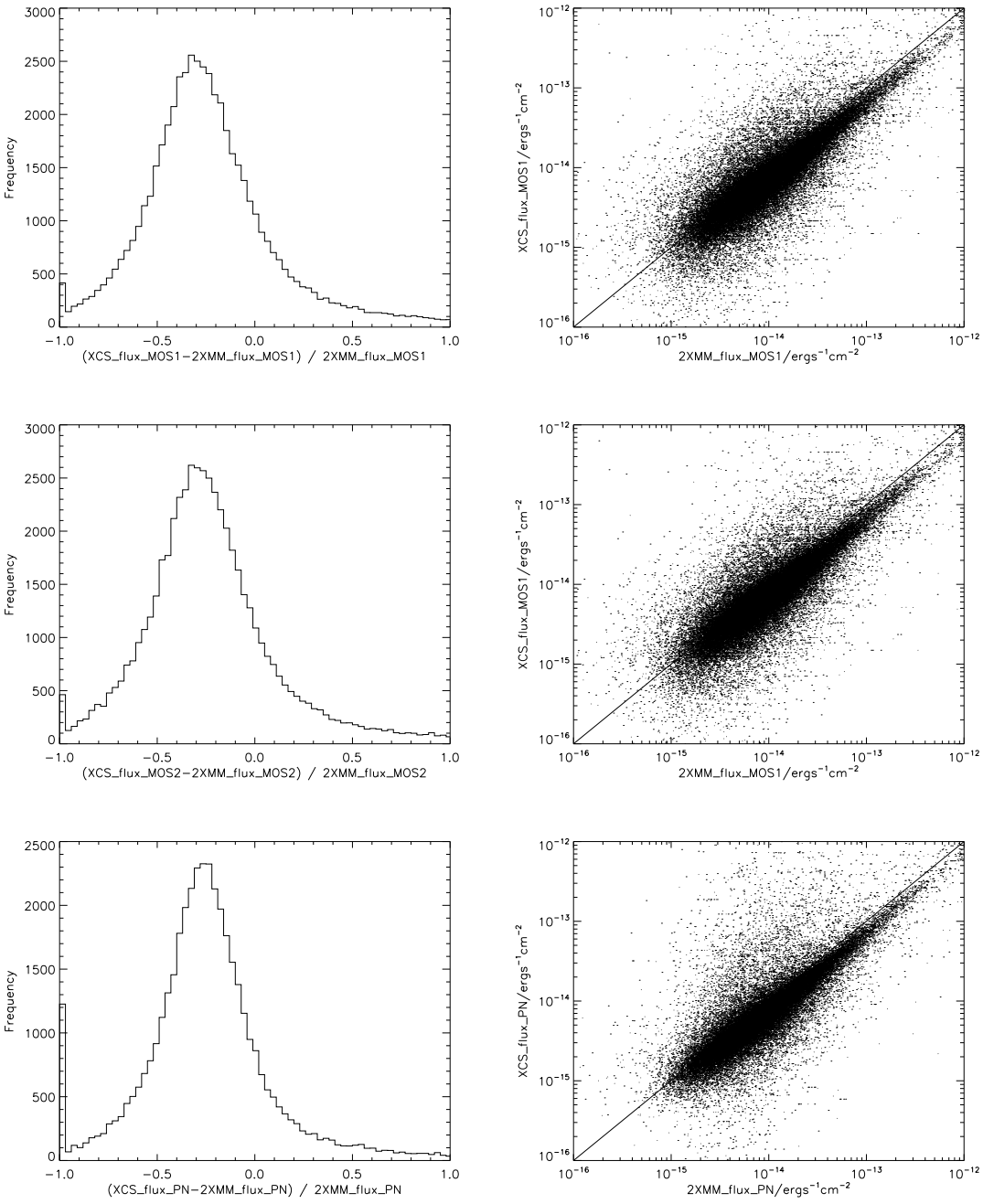


Figure 3.6: An updated comparison of the individual camera fluxes of XCS point sources vs their matches in 2XMM (Watson et al., 2009).

extended objects, as the list must be extensively filtered. The filtered list is known as the Statistical Sample (StatSam).

- Any candidates that are the pointing targets are not serendipitous and so need to be removed. A $2'$ radius from the pointing centre is used for this purpose.
- Since clusters have a certain amount of clustering, all candidates in targeted cluster pointings are excluded from the sample.
- To ensure a minimal level of contamination in the sample any source which is flagged as potentially suspicious is removed, i.e PSF-SIZED FLAG, POINTSOURCE CONTAMINATED FLAG or RUN1 CONTAMINATED FLAG (see Section 3.3.2).
- There are a considerable number of published source catalogues available to the community. These can be used to clean the candidate list of non-cluster extended objects such as supernovae that were not already removed by the masking (See Section 3.3.1). Objects already classified in NED (NASA/IPAC ExtraGalactic Database[3]) or SIMBAD [4] as one of the following: HII cloud, Supernova Remnant, Planetary Nebula, or low Redshift Galaxy ($z < 0.04$) are removed from the candidate list (using a $2'$ matching radius).
- To assist in the optical follow-up, candidates in the Galactic plane, or within either of the Magellanic clouds, are also removed (See Table 3.3). This has been added by the author as it was neglected in Davidson (2005).

This filtering produces a DR1 StatSam containing 1411 cluster candidates, and a DR1+DR2 StatSam containing 1874 cluster candidates.

| Name | Cut |
|---|---|
| Galaxy | $\|b\| < 20°$ |
| LMC | RA:$5h23'35''$, Dec:$-69°45'$, Radius:$6°$ |
| SMC | RA:$0h52'44''$, Dec:$-72°50'$, Radius:$3°$ |

Table 3.3: Details of sky cuts applied to the XCS StatSam. All candidates are excluded if they are within the specified regions.

### 3.6.1 The XCS500 and XCS300 subsamples

Here we outline the definition of the XCS500 and XCS300 sub-samples of clusters referred to throughout this thesis. The XCS500 and XCS300 are defined based on the number of counts a cluster is detected with in the soft band. The requirement that the final

[3]http://nedwww.ipac.caltech.edu
[4]http://simbad.u−strasbg.fr/simbad

cluster sample have known temperatures has led to this necessity. The count limit has been set in such a way that the cluster spectrum can be fitted to a model spectrum of a known temperature. To produce reliable fits, enough counts have to be present such that the shape of the bremsstrahlung continuum is well sampled. The minimum count limit has initially been set at 500 (counts from XAPA, not aperture corrected), and this number has been used in Sahlén et al. (2009) for XCS's cosmologal forecasting (See 3.2). To remain consistent with this work a count limit of 500 is used where appropriate in this thesis; however a reduction in the limit is being considered based on the temperature measurement work undertaken by E. Lloyd-Davies. With this in mind Chapter we also provide candidate numbers for the XCS300 subsample.

## 3.7 DR1 and DR2 StatSam redshift follow-up

### 3.7.1 Online archives

In addition to their use in removing non cluster extended sources, NED and SIMBAD are also used to identify serendipitous re-detections of known clusters (to avoid unnecessary follow-up). However these are not dedicated cluster catalogues and so it should not be expected that they contain all known clusters. The X-Rays Galaxy Clusters Database[5](BAX) is a dedicated cluster project with the aim of gathering cluster data into one resource, and so this database was used also for completeness. These literature searches identify 222 known clusters and groups in the DR1+DR2 StatSam (Literature search Feb 2008) leaving 1652 new DR1+DR2 candidates.

### 3.7.2 The NOAO-XCS Survey

The following subsection contains a description of the NOAO-XCS survey, the text has been edited from that provided by N. Merhtens (Private communication). M. Hosmer was an observer during one of the 6 night runs at the CTIO, Chile; however all of the data reduction and redshift fitting has been undertaken by N. Merhtens.

The NOAO-XCS Survey (NXS) is the optical follow-up survey to XCS providing photometric redshifts for DR1 and DR2 XCS cluster candidates. NXS uses a method of cluster detection inspired by Gladders and Yee and the Red-Sequence Cluster Survey (RCS) Gladders and Yee (2000). The main assumption is that all clusters are made up of a centrally concentrated clump of homogeneous, old, red, passively evolving elliptical galaxies. These galaxies, having formed at similar times from the same constituent gas, have similar metalicities and therefore colours, allowing them to exhibit a tight relation in colour-magnitude space -the red sequence. By taking imaging photometry of a cluster in

[5]http://bax.ast.obs-mip.fr

two filters sampling either side of the 4000Åbreak of cluster elliptical galaxies, one can use the colour of the red-sequence as a redshift estimator. As the 4000Åbreak migrates with increasing redshift the observed colour becomes redder providing a redshift estimate. The NXS survey therefore identifies clusters and assigns photometric redshifts and richness estimates (i.e. the number of cluster galaxies) by exploiting the ubiquitous red sequence observed in most galaxy clusters.

The NXS redshift algorithm (See Appendix C) was run on 220 XCS DR1 and 34 XCS DR2 cluster candidates imaged by NXS under photometric conditions (the results of which are shown in H.1. Of these candidates, 163 XCS DR1 clusters were detected with at least 5 member galaxies (including 54 XCS300 clusters) with redshift estimates between $0.1 \leq z \leq 1.0$; and 22 XCS DR2 clusters were detected with at least 5 member galaxies with redshift estimates between $0.1 \leq z \leq 0.74$.

## 3.8 Summary & Future work

### 3.8.1 Cluster catalogue

The DR1+DR2 StatSam will produce the first XCS catalogue of clusters (E. Lloyd-Davies, (in prep)). The DR2 clusters which comprise $\sim 25\%$ of this catalogue are a result of the work done by the author.

### 3.8.2 Summary

Using images, exposure maps and ECF's produced by K. Sabirli, and the XAPA pipeline designed by M. Davidson, we have been able to produce a source list of 81528 entries, and a StatSam cluster candidate list of 1874. Of these 1874, 250 already have redshifts. The author had responsibility for the DR2 extension of XCS, representing a 25% increase in the number of sources, cluster candidates, and confirmed clusters. The confirmed clusters from the XCS300 sample have now been subjected to X-ray spectroscopy and morphological analysis by E. Lloyd-Davies, see Appendix I.

# Chapter 4

# The XCS DR3

This chapter presents the XCS DR3. Discussed within are any changes made since DR1 and DR2, and the validation of the catalogue via cross checks with optical and X-ray data sets. Finally the catalogue itself is described and presented in detail. The delivery of DR3 has been the responsibility of the author, and consitutes one of the major results in the thesis. It has extended the area covered by XCS (from the DR1+DR2 area) by $\sim 70\%$, and the increased the number of StatSam cluster candidates by a factor of 2.

## 4.1 Modifications since Davidson (2005)

Since the reduction and compilation of DR1 and DR2 some corrections and modifications have been made (by the author) to XAPA and to the processes used to generate the final source list.

- **Off-axis angles** A small fraction ($\sim 1\%$) of the sources in DR1 and DR2 were seen to have off-axis angles that would put them well outside of the FOV. A closer inspection of this revealed that these cases were the extreme end of a more systematic problem. The error was caused by use of an incorrect pointing centre. In the majority of cases this offset was minor; however the potential for additional effects required not only correction of the off-axis values, but a complete re-running of XAPA. This is because, as part of the classification process (See Section 3.3.2), the source is compared to a PSF model, and this model is dependent on the off-axis position of the source. Errors here may result in misclassification, in turn leading to incorrect apertures being used for flux measurement. This correction was not available for the DR1 and DR2 samples described in Chapter 3.

- **Azimuthal angle** Inconsistent conversion from physical image position (x,y) to azimuthal angle, $\phi$, in DR1 and DR2 has also been corrected in DR3. The impact

of this conversion is less important than the off-axis issue, since there are no catalogue properties that are directly dependant on $\phi$. However this would have caused problems for some uses of the data, e.g. modelling the PSF as a function of $\theta$ and $\phi$.

- **Duplicate source removal** In DR1 and DR2, a matching radius of $2'$ was used to check for extended source duplicates (See Section 3.4). Extended sources within this radius were considered duplicates, and the one with the highest number of counts was used as the master detection and so appears in the final source list. Experience has shown that this radius is too large. An example clearly highlights the problem. XMMXCS J2215 was originally detected in obsid 0106660101, and this area has since been re-observed with longer exposure time in obsid 0106660601 (Figure 4.1). The greater exposure has caused 2 nearby point sources to blend, and be detected as extended, this 'extended' object has a greater number of counts than XMMXCS J2215 and so XMMXCS J2215 is removed from the source list in favour of this blend. This object is clearly not a good cluster candidate, and so would not be followed-up, thus XMMXCS J2215 would likely be not considered further. While for nearby clusters this radius of $2'$ may be suitable, with increasing redshift this quickly corresponds to an unnecessarily large distance. Ideally a radius as a function of redshift would be implemented, but at this stage we would not have any redshift data, so a fixed radius is the only option. To avoid cases like the given example, the match radius used for DR3 extended sources has been reduced to $30''$. This radius is large enough to allow reliable source matching, but small enough to minimise removal of genuine cluster candidates. The chosen value of this radius is somewhat arbitrary, the implications of this choice are discussed in Section 4.1.1. The matching radius for point sources remains $5''$.

- **Image and exposure map creation** As mentioned in Section 3.3 the images and exposure maps for DR3 have been created by E. Lloyd-Davies, where as for DR1 and DR2 they were made by K. Sabirli. The image and exposure map generation pipelines were re-written from scratch by E. Lloyd-Davies for DR3. So even for pointings previously analysed for DR1 and DR2, we can expect the source lists and their respective properties to have changed slightly.

### 4.1.1 Implications for Source lists.

The modifications to the $\theta$ and $\phi$ values detailed above improve the quality of the source catalogues, and little more need be said about them. The change to the extended source matching radius however warrants further discussion. The reduction in this radius increases the number of candidate objects in fields processed in DR1 and DR2, and makes the relative size of the cluster candiate list for DR3 considerably larger than would be expected simply from the increase in the number of pointings analysed. There are two main points that must be noted here. The extended source list will now more closely match the completeness levels expected from the selection functions presented in Chapters 5 and 6,

having a knock-on effect of improving the quality of other science results from the survey. The other point to consider is that the increase in the number of extended objects will undoubtedly affect the contamination level of the candidate list. The candidates are all examined by eye before follow up, so the level of contamination in the initial source list has little influence on the final XCS cluster sample.

## 4.2 Initial problems with DR3

After the creation of DR3 some errors became apparent, as shown in Figure 4.2. Plotted in Figures 4.2(a), 4.2(c), 4.2(e) are a comparison of the individual camera fluxes from DR3 and the counterpart sources found in the 2XMMi catalogue, an incremental update of 2XMM (Watson et al., 2009), it is clear that two subsets of the sources have distinct flux offsets of a factor of $10 - 100$ in the MOS cameras. Figure 4.2(b) is a comparison of the DR3 MOS1 fluxes and those from DR1. It is clear from this that the problem is in the DR3 data rather than 2XMMi, Figure 4.2(d) shows that the offset is not even consistent between MOS1 and MOS2. This problem does not affect the PN data (See Figures 4.2(e), 4.2(f)). In addition to the flux issue, there were a small number of obsids that featured spurious sources, generally within chip gaps and regions of low exposure (See Figure 4.3). The symptoms shown in Figures 4.2 and 4.3 point to errors within the exposure maps. Indeed the MOS cameras in the affected obsids were all in one of the partial window modes (See Section 2.1.1). The original merging of the exposure maps and images had not properly taken into account the different mode of the central chip, and this affected the relative weighting of all regions in the maps and caused the ECFs to be artifically boosted. This particular problem has now been corrected. Figure 4.4 shows that there is now a very tight agreement between the fluxes from both of the MOS cameras, and that the DR3 MOS1 fluxes now show a much better match with those from 2XMMi (See Section 4.3.2 for futher details).

It is noted that in Figure 4.4(a) there are still a small fraction of detections (1112 of 179530) where the MOS1 and MOS2 fluxes still show a systematic offset. The detections which show an offset of more than 15% are all from the same 115 obsids. The reason for this is offset is yet to be determined, but is expected to be of similar origin to the above, and at the time of writing was being corrected by E. Lloyd-Davies.

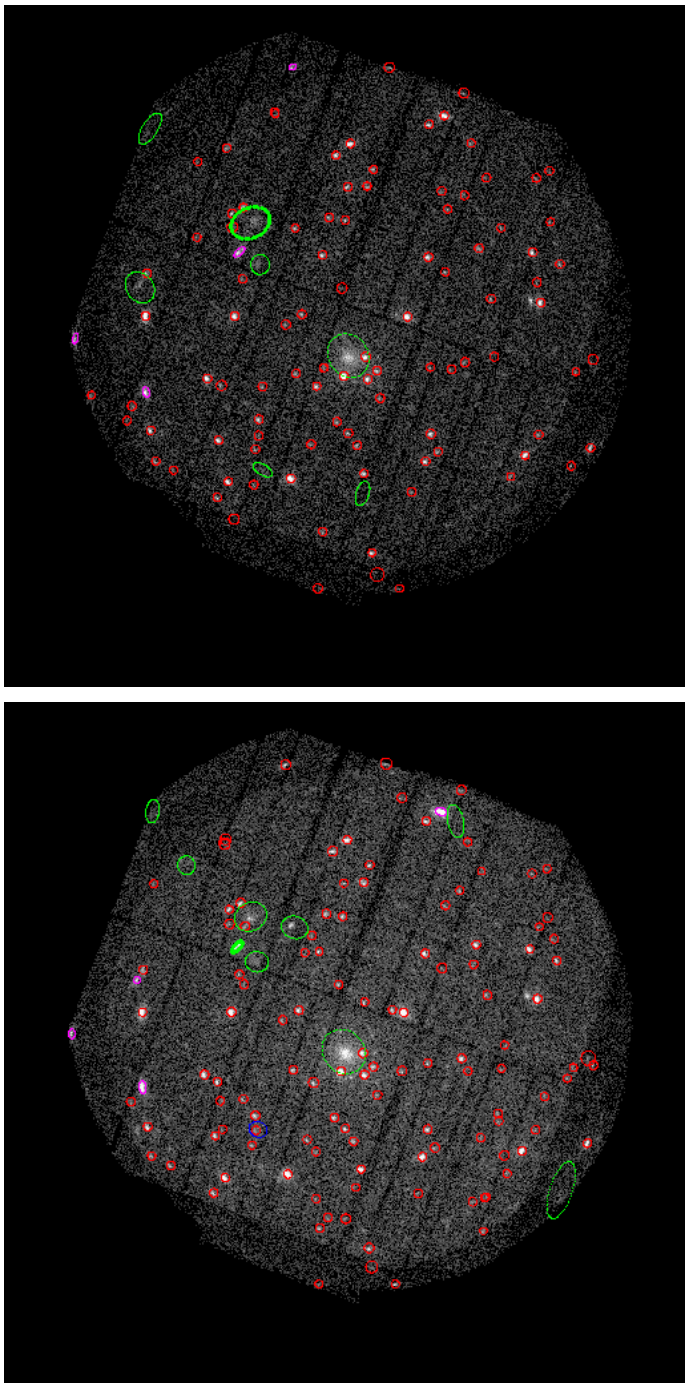

Figure 4.1: Top: Obsid 0106660101, XMMXCS J2215 is highlighted by a bold green ellipse. Bottom: Obsid 0106660601, the bold green ellipse denotes the blended point sources chosen as the master source detection by the old DR1 & DR2 method.

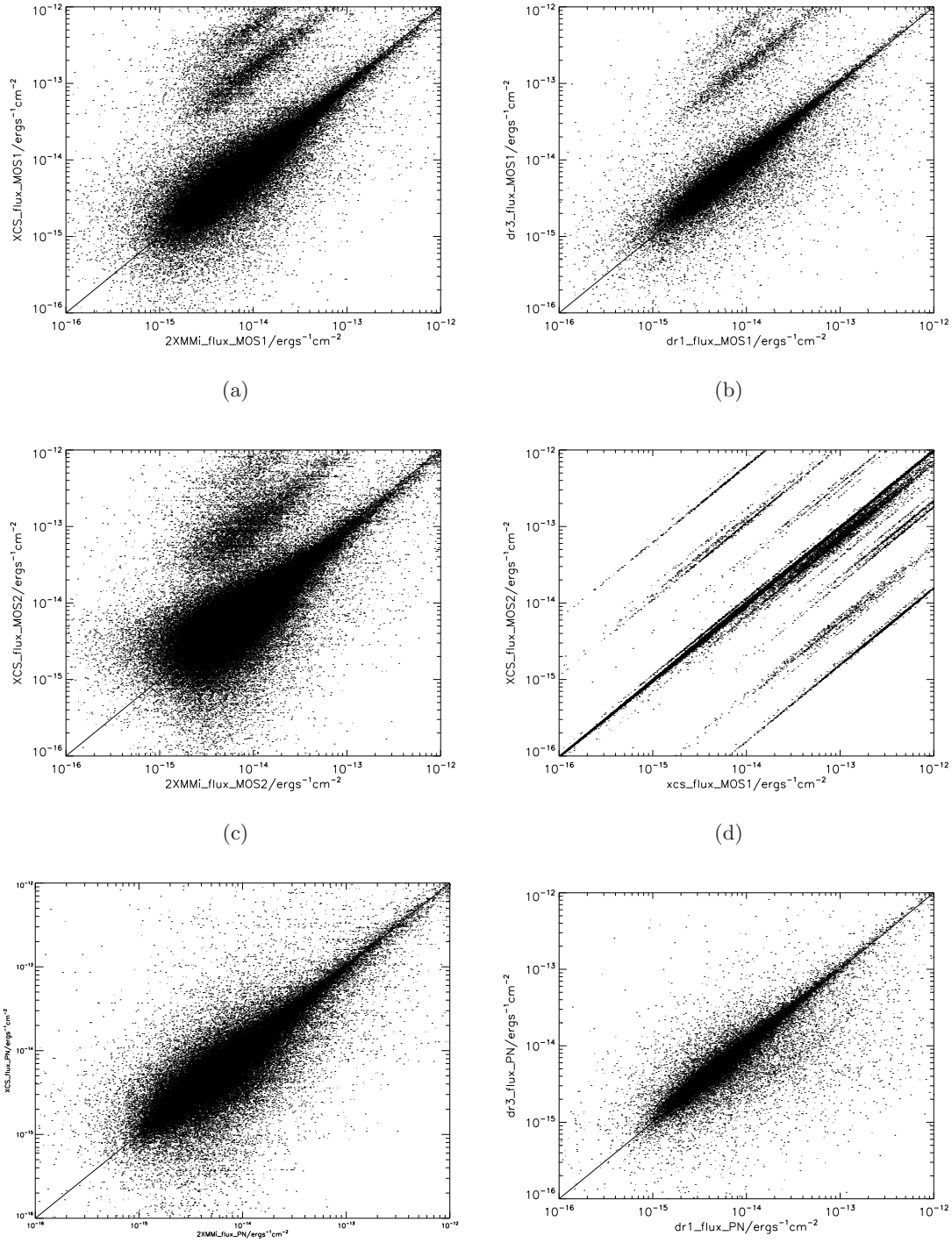


Figure 4.2: A comparison of initial DR3 individual camera fluxes to 2XMMi (a,c,e), DR1 (b,f), and another DR3 camera (d) (See text for details).

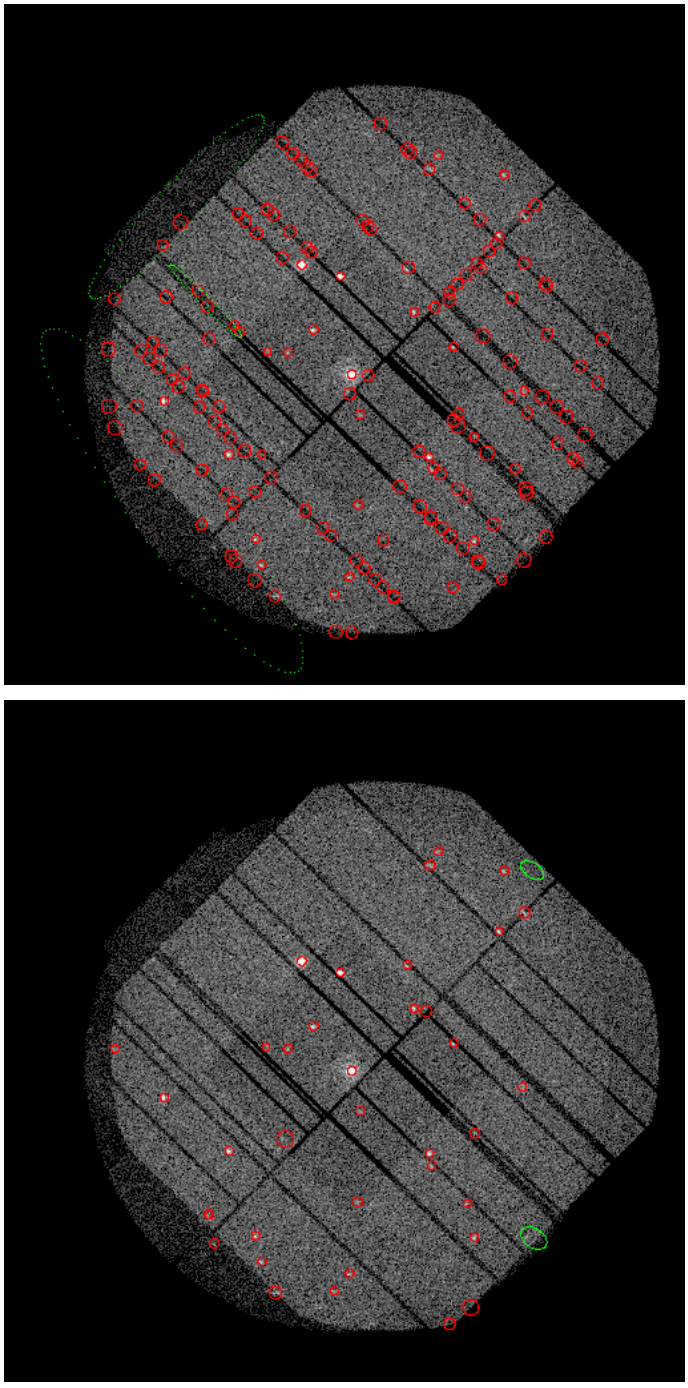

Figure 4.3: Obsid 0142970101, before (top) and after (bottom) diagnosis and correction of the exposure map error.

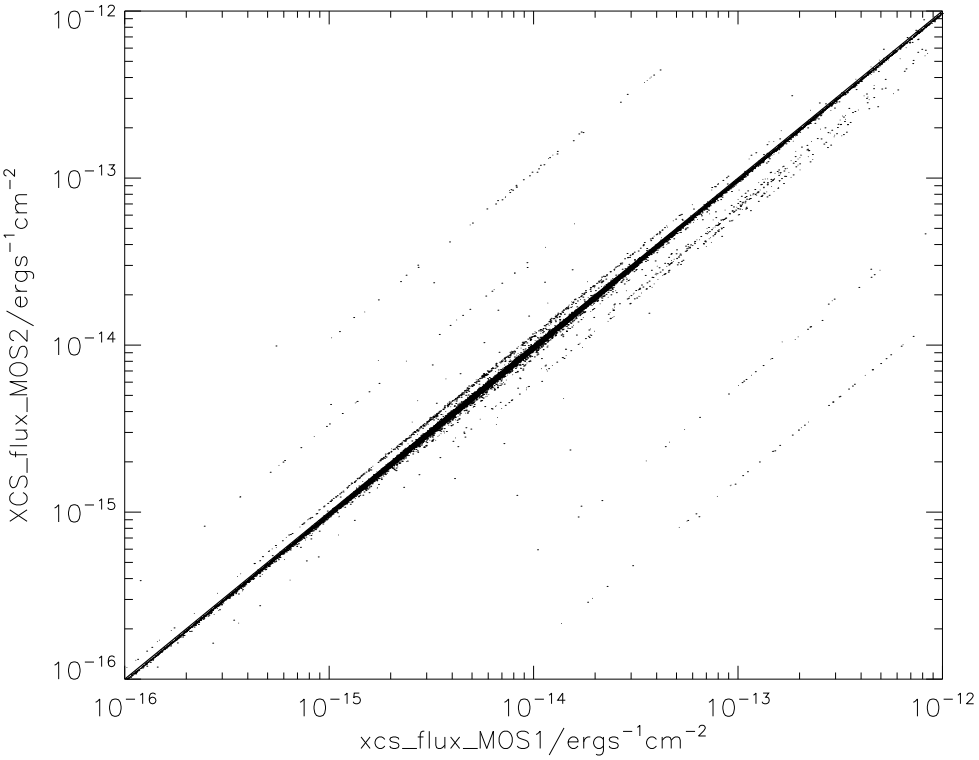


(a)

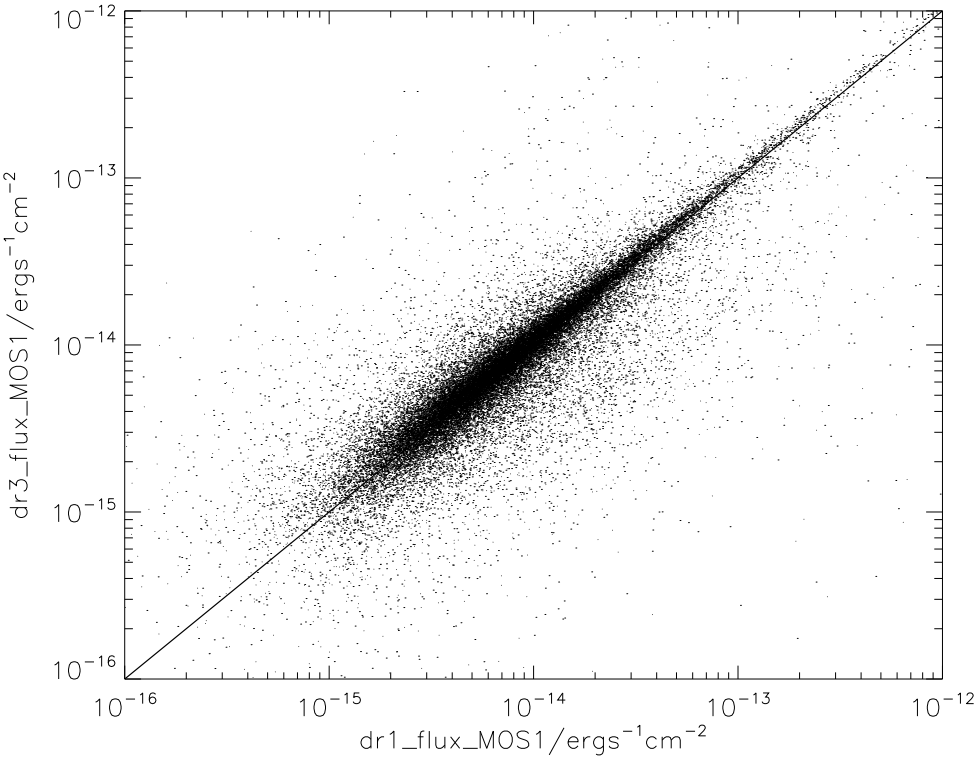


(b)

Figure 4.4: Same as Figures 4.2(d) and 4.2(b), but after the exposure map correction.

## 4.3 Comparison to Literature samples

With the internal calibration and quality checks complete it is necessary to assess DR3 in light of the literature data. We will first check the accuracy of the source positions with a comparison to optical data, and then compare the DR3 X-ray properties to some relevant samples.

### 4.3.1 Determination of the DR3 positional accuracy using optical quasar catalogues

To determine the positional accuracy of DR3 it is desirable to use as a comparison a catalogue that has high spatial resolution and precision, and significant overlap with the XMM data. A natural choice for this is SDSS; the data is of high quality and contains many objects that would be expected to have X-ray counterparts, e.g quasars and AGN. A cross match against the SDSS Quasar Catalog IV (Schneider et al., 2007) using a radius of $10''$ produces the results in Table 4.1 and plotted in Figure 4.5. There are 1131 matches, 95% of which are within $5.723''$. The mean matching distance is approximately the size of 2 MOS pixels. Given the uncertainty in the PSF, and the fact that the XMM cameras are only calibrated to $1-2''$ relative to each other, this level of precision is as good as could be expected. However there does appear to be a small systematic offset in both RA and Dec directions at the $0.5''$ level, and this is yet to be diagnosed.

| number of matches in $10''$ | 1131 |
|---|---|
| 95% matching radius | $5.72''$ |
| Mean distance | $2.36''$ |
| Median distance | $1.94''$ |
| Standard deviation | $1.65''$ |
| mean(XCS RA -SDSS RA) | $0.53''$ |
| mean(XCS Dec - SDSS Dec) | $-0.50''$ |

Table 4.1: A summary of the results of the cross match between DR3 and The SDSS Quasar Catalog IV.

As an aside we note that the XCS-SDSS quasar sample is being exploited by Miller et al. (in prep) to determine X-ray spectral properties of optical quasars. See also Young et al. (2009) for a complementary SDSS-XMM quasar survey. Young et al. (2009) find 792 SDSS QSO's with matches in the XMM data, we find 1131.

To improve the number statistics in the above results we can extend this further by using the catalogue of Véron-Cetty and Véron (2006) (hereafter VeronCat). This catalogue is a compilation of all known AGN and QSOs. The results are in Table 4.2 and Figure 4.6.

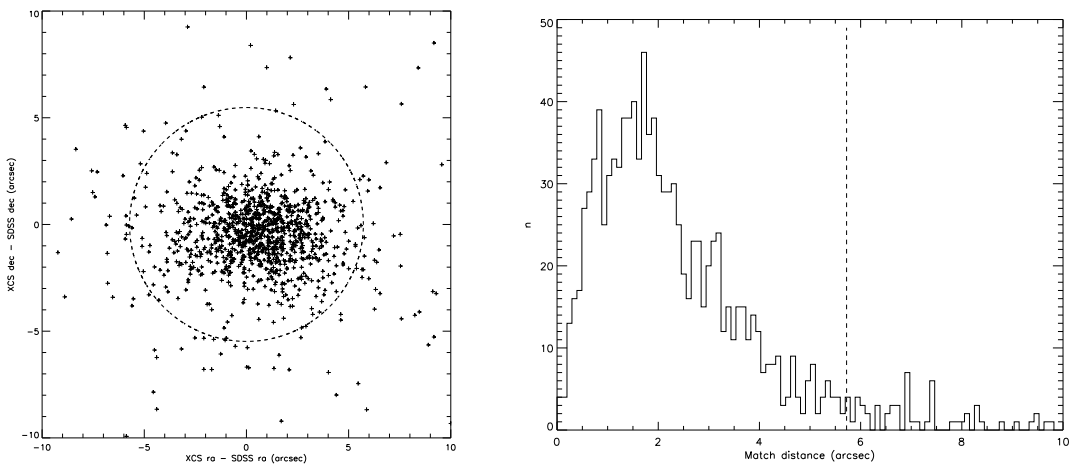


Figure 4.5: The relative position of the matches between DR3 and The SDSS Quasar Catalog IV. The dashed line represents the 95% matching radius

This cross match was also done in Davidson (2005) for the DR1 catalogue, and he found a 95% matching radius of 7.8″.

| Number of Veroncat AGNs+QSOs | 106958 |
|---|---|
| Total number of matches in 10″ | 2807 |
| AGN matches | 947 |
| QSO matches | 1860 |
| 95% matching radius | 6.56″ |
| Mean distance | 2.62″ |
| Median distance | 2.17″ |
| Standard deviation | 1.80″ |
| mean(XCS RA - VeronCat RA) | 0.37″ |
| mean(XCS Dec - VeronCat Dec) | −0.20″ |

Table 4.2: A summary of the results of the cross match between DR3 and VeronCat.

The use of VeronCat gives 2807 matched sources, the mean, median, and standard deviation of which indicate a slightly larger amount of scatter in the match distribution compared to the SDSS quasars, this can be seen in Figure 4.6. The systematic offset in RA and Dec is still present, although it is reduced in both directions.

The above work confirms the positional accuracy of the DR3 source list to within that expected from the instrument. The number of matches with the SDSS data is also encouraging, being significantly larger in number than that already in the literature.

When cross matching two catalogues there will be a certain number of matches that occur purely by chance. For example, a randomly placed source will always be associated with a real source given a large enough matching radius. The radius at which this random matching begins to dominate any genuine matching is dependent on the source density,

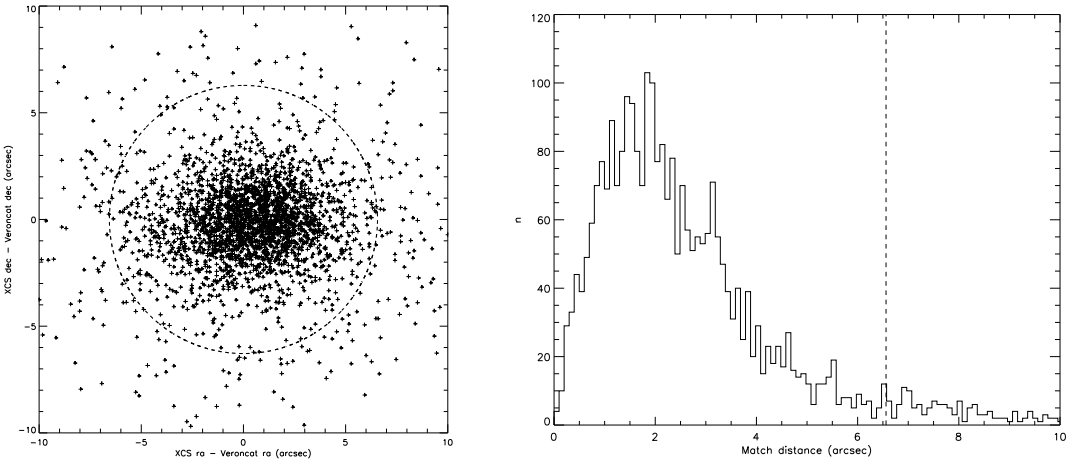


Figure 4.6: The relative position of the matches between DR3 and VeronCat. The dashed line represents the 95% matching radius

and the footprint of the catalogues in question. For catalogues such as XCS and VeronCat this is complicated further as neither catalogue is contiguous, however we can still get a reasonable estimate of the number of random matches. In order to do this we can offset the VeronCat sources in a random direction by a large enough amount to remove any possibility of genuine association. This was done 5 times, with offsets of $0.02, 0.1, 0.25, 0.5,$ and 1.0 degrees. The number of matches with these 5 realisations, with a $10''$ radius, is an average of 31. Figure 4.7 shows how both the number of false matches and the number of matches against the real catalogue vary with radius. As expected the number of false matches is an increasing function of radius, however the number of matches obtained from the real data has already begun to level off at $10''$. The desire to generate as many matches as possible, while mimimising the number of false matches, means that $10''$ is the natural choice of match radius; it returns a large number of matches, while keeping the probability of any given association being false low ($\sim 0.1\%$).

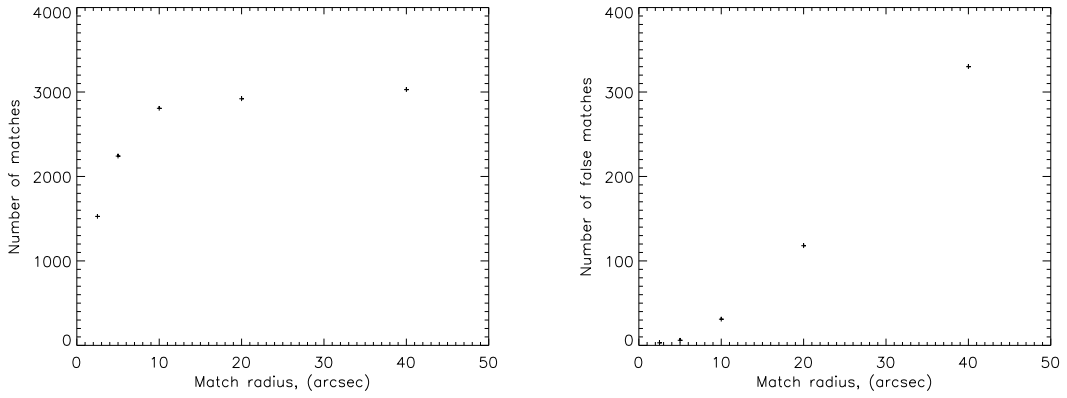


Figure 4.7: Left: The number of matches between XCS and VeronCat as a function of match radius. Right: The number of matches between XCS and the offset VeronCat as a function of match radius.

### 4.3.2 X-ray point source catalogues

#### 2XMMi

Having assesed the quality of the source positions, we can now look in more detail at the source properties. As discussed in Section 3.5, the 2XMM catalogue of Watson et al. (2009) is a natural choice of comparison project, and as in Section 4.2 we used the updated version, 2XMMi here. A summary of the catalogue sizes is shown in Table 4.3. In Section 3.5 we discussed the difference in the number of sources between DR1+DR2 and 2XMM, and the same reasons for this are true here. As before, a 10″ matching radius has been used to produce the flux comparisons in Figure 4.8. The flux offsets seen in Figure 3.6 are now much smaller, below 10% for MOS1 and PN. The MOS2 offset is not only larger than for the other cameras, but also has a larger amount of scatter, however as seen in Figure 4.4(a) the DR3 MOS camera fluxes are in very good agreement with each other, and so the offset is likely a result of the 2XMMi calibration (See Section 3.5) rather than of any undiagnosed issue with XCS.

The improvement seen in Figure 4.8 compared to Figure 3.6 demonstrates that the work by E. Lloyd-Davies that has gone into making new images, exposure maps, and ECF's for DR3 has been worthwhile.

| Name | Obsids | Detections | Sources |
|---|---|---|---|
| DR3 | 4214 | 179530 | 146842 |
| 2XMMi | 4653 | 289083 | 221170 |

Table 4.3: A summary of the DR2, DR3 and 2XMMi catalogue sizes.

#### CDFN and CDFS

To understand the flux calibration of XCS in a more meaningful manner it is necessary to see how the results compare to a project using a different instrument. Due to its excellent resolution, Chandra should produce well-calibrated fluxes, and so is the ideal instrument for this purpose. The 2 deep fields, Chandra Deep Field North (CDFN) (Alexander et al., 2003) and Chandra Deep Field South (CDFS) (Giacconi et al., 2002), provide large areas that have been analysed in a consistent manner. Both projects also publish fluxes which can be expected to be of high accuracy due to the depth of the observations. Using a 10″ radius there are 102 and 114 matches with the CDFN and CDFS respectively, and the fluxes here are also in good agreement (See Figure 4.9).

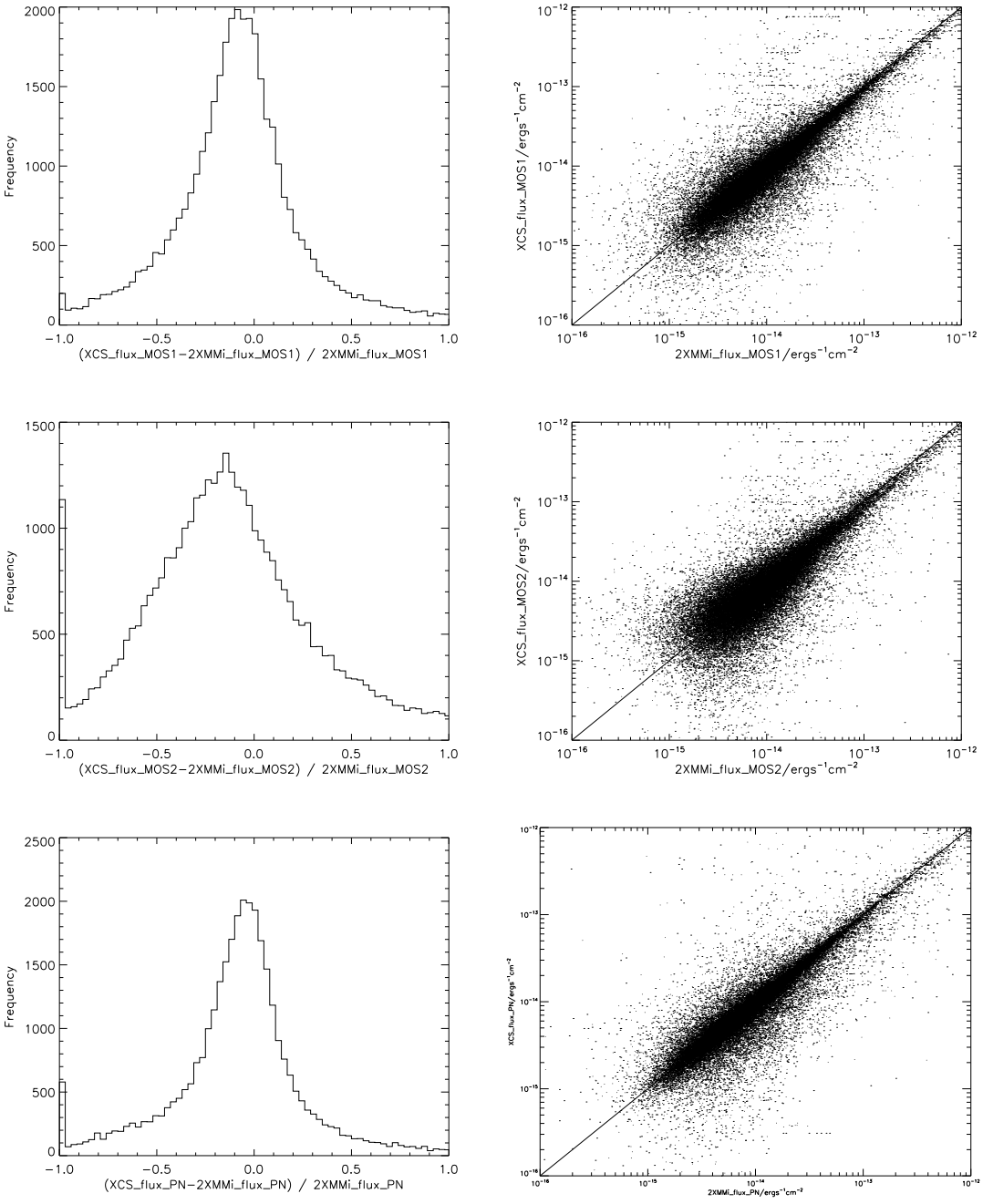


Figure 4.8: A comparison of the individual camera fluxes of DR3 Sources vs their matches in 2XMMi.

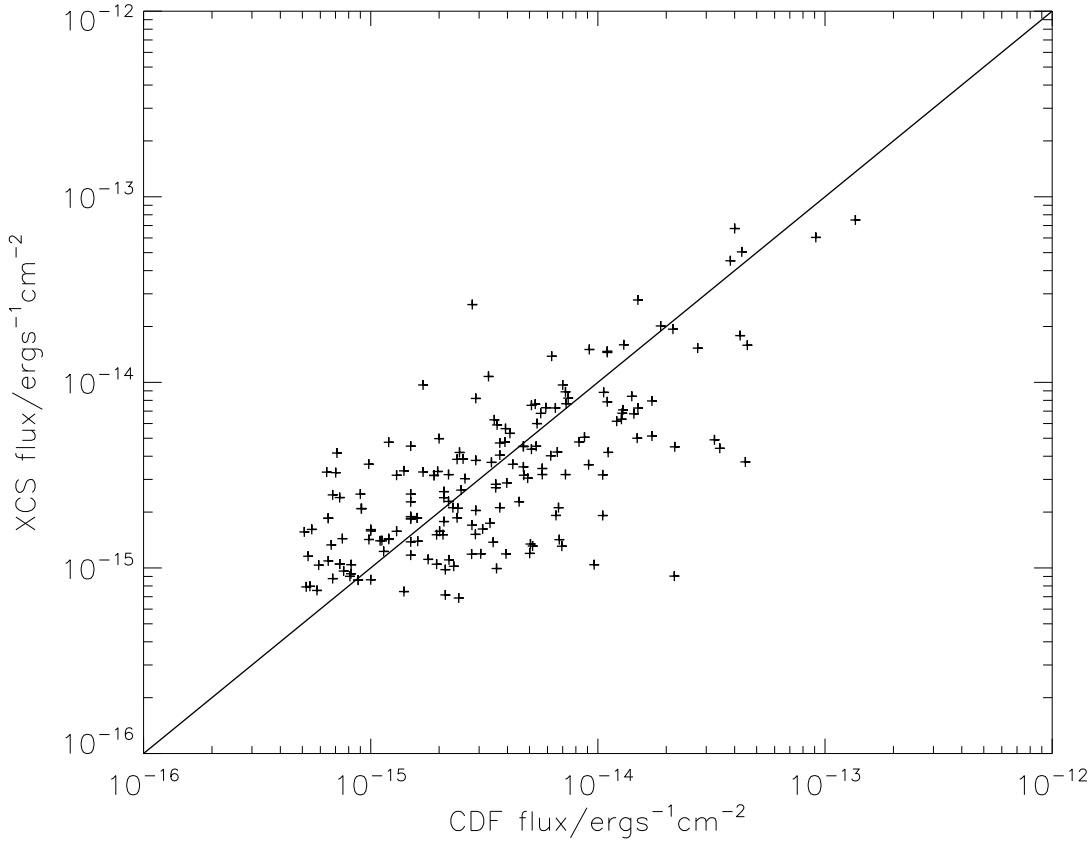


Figure 4.9: A flux comparison of DR3 and the Chandra deep fields. This includes matches for both CDFN and CDFS.

### 4.3.3 X-ray cluster catalogues: XMM-LSS

In Sections 4.3.1 and 4.3.2 we have compared the XCS DR3 point sources with samples taken from the archives. The situation for extended sources is less straight-forward. There is no equivalent extended source catalogue that is both homogenous and large enough to be of use in validating a significant amount of DR3. The employed alternative is make use of extensive simulations (See Chapters 5 and 6). These assess XAPA's reliability in detecting and correctly classifying the extended emission from clusters of galaxies. However there are smaller XMM cluster surveys with which XCS has overlap, e.g the XMM-LSS.

The XMM Large Scale Structure (XMM-LSS) Survey is reported in Pierre et al. (2007) and Pacaud et al. (2007). It covers a single contiguous region of roughly 6 $\deg^2$, comprised of 51 XMM pointings, in which the authors have undertaken a dedicated cluster survey, accompanied by a detailed selection function. In this region they detected 33 'Class 1' extended objects (Pierre et al., 2007), a class designed to be uncontaminated by mis-classified point sources. A more detailed look at these objects (including optical overlays, photometry and spectroscopy) has confirmed 28 of these to be genuine clusters (Pacaud et al., 2007); the remaining 5 were shown to be nearby X-ray emitting galaxies. 29 of the 33 Class 1 objects have matches in DR3 that are classified as extended. This includes 2 of the non-cluster objects, the other 3 of which XAPA classified as pointlike (See Figure 4.10). There remains one XMM-LSS Class 1 cluster (XLSS J022210.7-024048) that is not recovered by XCS; XAPA detects a source at this location but it is removed from the final list as it does not meet the $4\sigma$ significance requirement (See Figure 4.11).

The radius used in the matching of DR3 to the XMM-LSS was typically 10". However for XLSS J022433.8-041405 a radius of 24" was required to get a match; this source is large and elliptical, hence there is some uncertainty in the source centre, though the extent of the XCS source and its XLSS counterpart are overlapping.

The XMM-LSS also have a C2 class of clusters with slightly less conservative selection criteria. This sample is yet to be published, but the authors report this class to contain $\sim 60$ sources. Within the XMM-LSS obsids, XCS detects 82 extended objects that pass the usual filtering (See Section 3.3.3), and after applying a 300 count cut (see Section 3.6.1) 17 remain.

Although XAPA does measure fluxes for extended sources they are not suitable for scientific application. The difficulties inherent with extended sources (PSF correction, background subtraction etc.) necessitate a separate analysis of the detected objects to measure fluxes, luminiosities and temperatures. This is being undertaken by E. Lloyd-Davies (see Appendix I). At the time of writing the XCS determination of the XMM-LSS Class 1 luminosities and temperatures are not available for inclusion in this thesis.

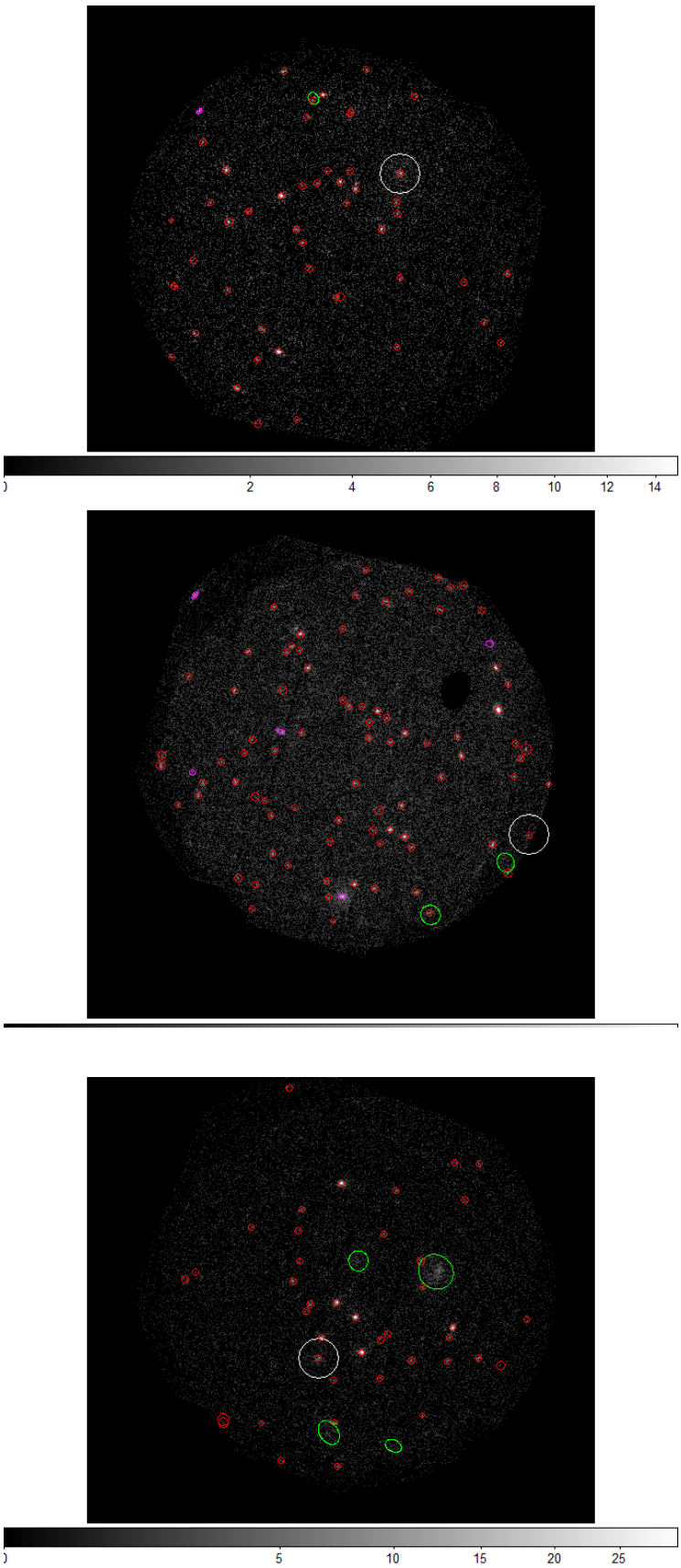


Figure 4.10: Circled in white are 3 XMM-LSS Class 1 objects shown to be nearby X-ray emitting galaxies, recovered as point sources by XAPA.

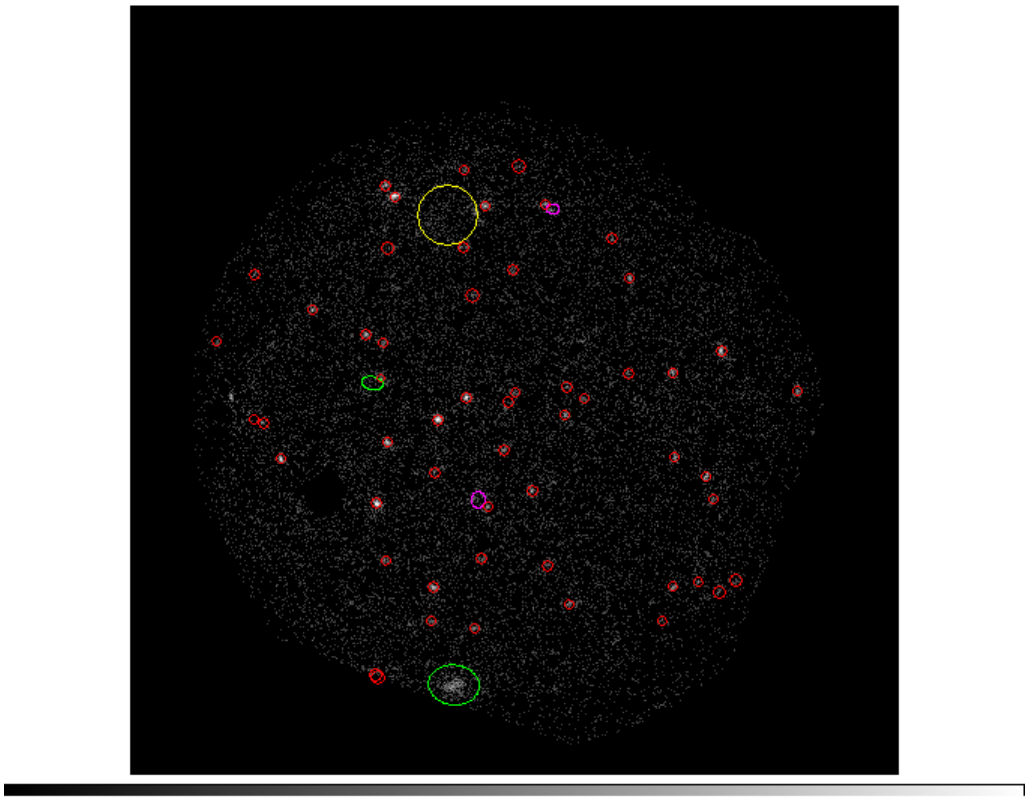

Figure 4.11: The yellow circle encloses the location of XLSS J022210.7-024048. The source was cleaned from the XCS source list as it is of low significance.

## 4.4 The DR3 Catalogue

### 4.4.1 Basic StatSam

A vast number of extended sources are detected in DR3, more than double that in DR1, this section will describe some of the properties of the catalogue with the aim of assisting future work reliant on the source lists (e.g redshift follow-up). Table 4.4 summarises the number of sources detected in the 4214 observations comprising DR3. The point source catalogue contains 131694 unique sources. After applying the same StatSam filters as before (See Section 3.6) to the extended source list there are 4092 cluster candidates, 1402 of which are detected with $\geq$ 300 counts. The sky positions of the DR3 obsids and the DR3 XCS300 are shown in Figure 4.12. The total, non-overlapping area[1] of DR3 is 522.29 deg$^2$, and the available StatSam area amounts to 229.73 deg$^2$.

| Obsids | Detections | Sources | Point Sources | StatSam |
|---|---|---|---|---|
| 4214 | 179530 | 146842 | 131694 | 4092 |

Table 4.4: A summary of DR3 catalogue properties.

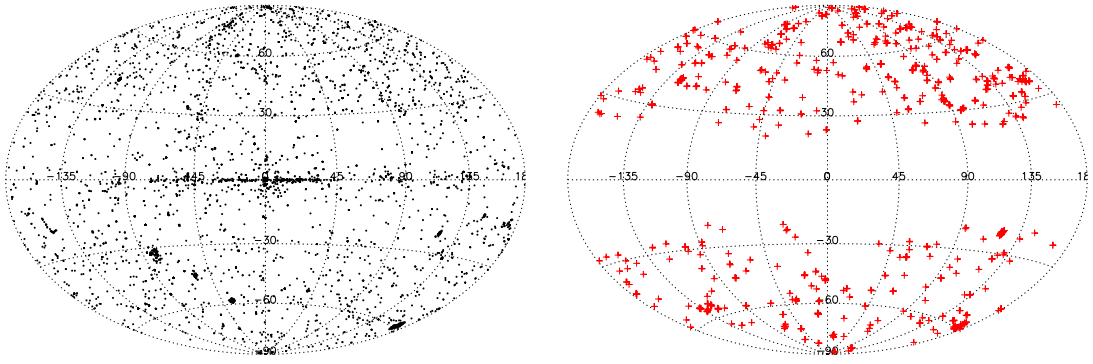

(a) (b)

Figure 4.12: Sky positions of (a) DR3 obsids and (b)DR3 StatSam XCS300 in Galactic co-ordinates (Aitoff projection).

[1]E. Lloyd-Davies, private communication

## 4.5 DR3 redetections of known clusters, and removal of non-cluster extended sources

As in Section 3.6 we can make use of the NED and SIMBAD databases to better understand the StatSam candidate list. Aside from galaxy clusters/groups there are other astronomical objects which may be detected as extended in the X-ray bands, these include Planetary Nebula (PN), HII regions (HII) and Supernova remnants (SN). Using the literature databases enables a removal of known sources of these types, thus cleaning the candidate list of unwanted objects. As before the catalogues are also utilised to determine the number of serendipitous re-detections of known clusters and groups. The difficulty in doing the above is the choice of matching radius. PN, HII and SN can all be incredibly large; however the largest regions will have been masked out of the DR3 footprint, so only small and/or distant regions need be considered, but still the choice of radius is not obvious. For clusters and groups the situation is also not clear. The literature positions of clusters and groups are in some cases defined by the optical positions of the galaxies, which are not always in exactly the same position as the X-ray emission from the gas. Taking these points into consideration suggests using a large matching radius, but this may cause mis-association of new candidates that are incidentally close (in terms of angular separation) to known objects. To fully assess the best way of cross matching inhomogenous catalogues from different wavebands would require an enormous amount of work, and is beyond the needs of this thesis. Table 4.5 contains the results of the cross matching for radii $1'$. What is clear is that DR3 contains numerous re-detections of known objects, and those objects with literature matches should be examined in more detail before committing follow-up resources, i.e. telescope time.

| PN + HII | SN | Groups | Clusters |
|---|---|---|---|
| 108 | 38 | 28 | 277 |

Table 4.5: NED and SIMBAD associations with DR3 extended sources using radii of $1'$

## 4.6 Removal of highly elliptical candidates

We have demonstrated XAPA's ability to detect and classify known clusters. The completeness of the sample is thoroughly assessed through simulations presented in Chapters 5 and 6, but experience with DR1 has shown that contamination of the candidate list is an issue. Section 3.3.1 details how image artifacts that may cause spurious detections are masked out of the images. However, despite this masking, spurious sources do remain. These are often apparent upon visual inspection as the majority are highly elliptical. Figure 5.16 demonstrates how well XAPA performs in detecting elliptical objects, this holds even if the sources are spurious. An appropriate ellipticity cut can help remove some of the contamination in the source list. Plotted in Figure 4.13 are the ellipticities of the XCS detection of the known clusters and groups. The ellipticities are defined based on the major and minor axis of the source ellipses given by XAPA (Equation 4.1). The source ellipse is constructed from the set of multi-scale WAVDETECT ellipses that make up the source (see Davidson (2005) for details).

$$e = 1 - (\text{minor axis}/\text{major axis}) \tag{4.1}$$

Table 4.6 contains StatSam numbers for known clusters and new candidates using the same matching radii as Table 4.5, also shown are the numbers after the application of a $\geq 300$ count cut, and an additional cut of $e \leq 0.6$. The ellipticity cut does exclude $3-4\%$ of the known clusters. However it removes $\sim 25\%$ of the new candidates, the majority of the remaining sources could reasonably be expected to be genuine, physical objects. A lower $e$ cut would improve this further, however it is important that as few genuine clusters are rejected as possible. Work by Mohr et al. (1995) found real clusters have $0.0 \leq e \leq 0.6$, and so this cut seems justified. A true quantification of the contamination levels will not be possible until follow-up has been undertaken, by which time the real clusters will have been confirmed.

| | Known Clusters & Groups | New Candidates |
|---|---|---|
| StatSam | 305 | 3701 |
| soft counts $\geq 300$ | 159 | 1206 |
| scts $\geq 300$, $e \leq 0.6$ | 152 | 895 |

Table 4.6: Known StatSam clusters/groups and new candidates, using matching radii of $1'$. DR3 StatSam matched against NED and SIMBAD.

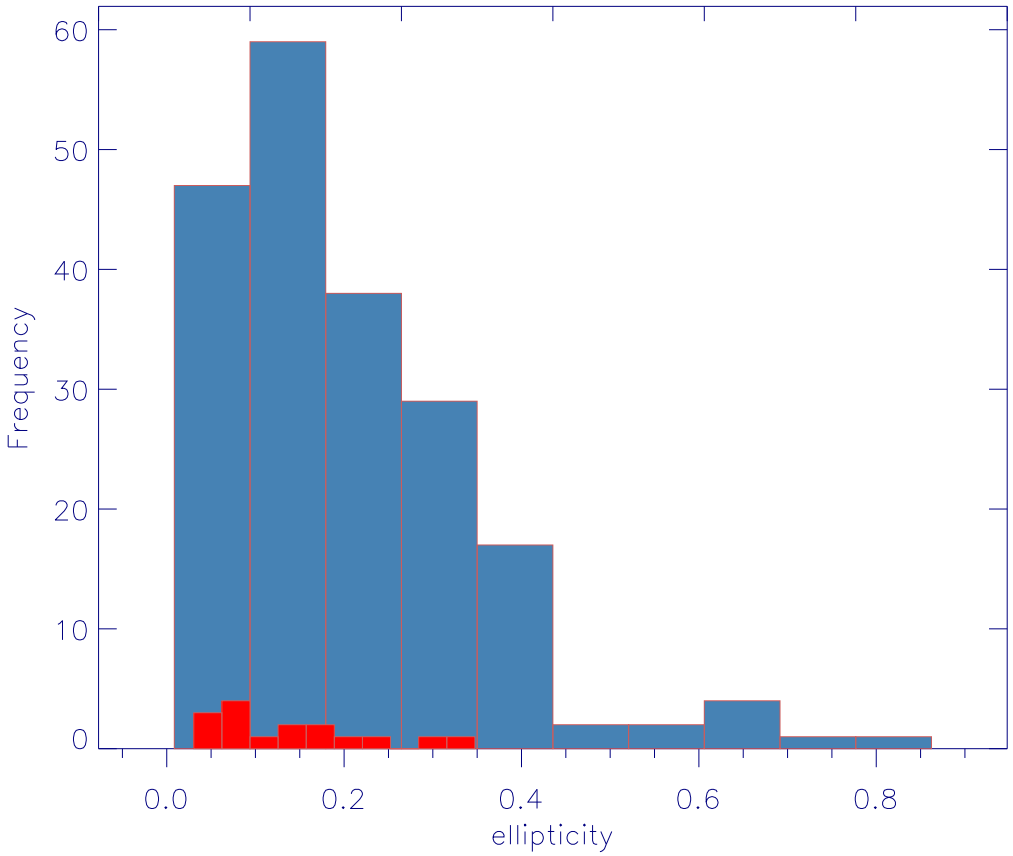


Figure 4.13: A histogram showing the ellipticities of the XCS detections of known clusters (blue) and groups (red) listed in NED and SIMBAD.

## 4.7 The DR3 StatSam cluster candidate list

The DR3 StatSam is presented in Appendix D. Tables D.1 and D.2 contain the re-detections of known clusters and the new candidate objects respectively. The literature matching radius to define this sample is $30''$.

The table columns are named as follows:

- **XCS Name** XCS name of the source.
- **Obsid** XMM observation in which the source was found.
- **RA** Right Ascension of the source (J2000.0).
- **Dec** Declination of the source (J2000.0).
- **Counts** Source counts in $0.5 - 2.0$ keV band.
- **Flux** Flux in $0.5 - 2.0$ keV, using Point Source ECF.
- **Literature Name** Literature name of the source.
- **Match Distance** Distance to Literature position ($''$)
- **Literature Redshift** Literature redshift *.
- **Sig** Significance of source, $-\log(P)$, where P is the probability of the source being a background fluctuation. 'NaN' indicates that P is so close to zero that $-\log(P)$ is undefined using the current machine accuracy, i.e. the source is extremely significant.

* The XCS measured redshifts are tabulated separately, see Section 4.9.

Two example objects from the DR3 New candidates can be seen in Figures 4.14 and 4.15. Shown in Figures 4.16 and 4.17 are serendipitous DR3 re-detections of Abell clusters 2634 and 0150.

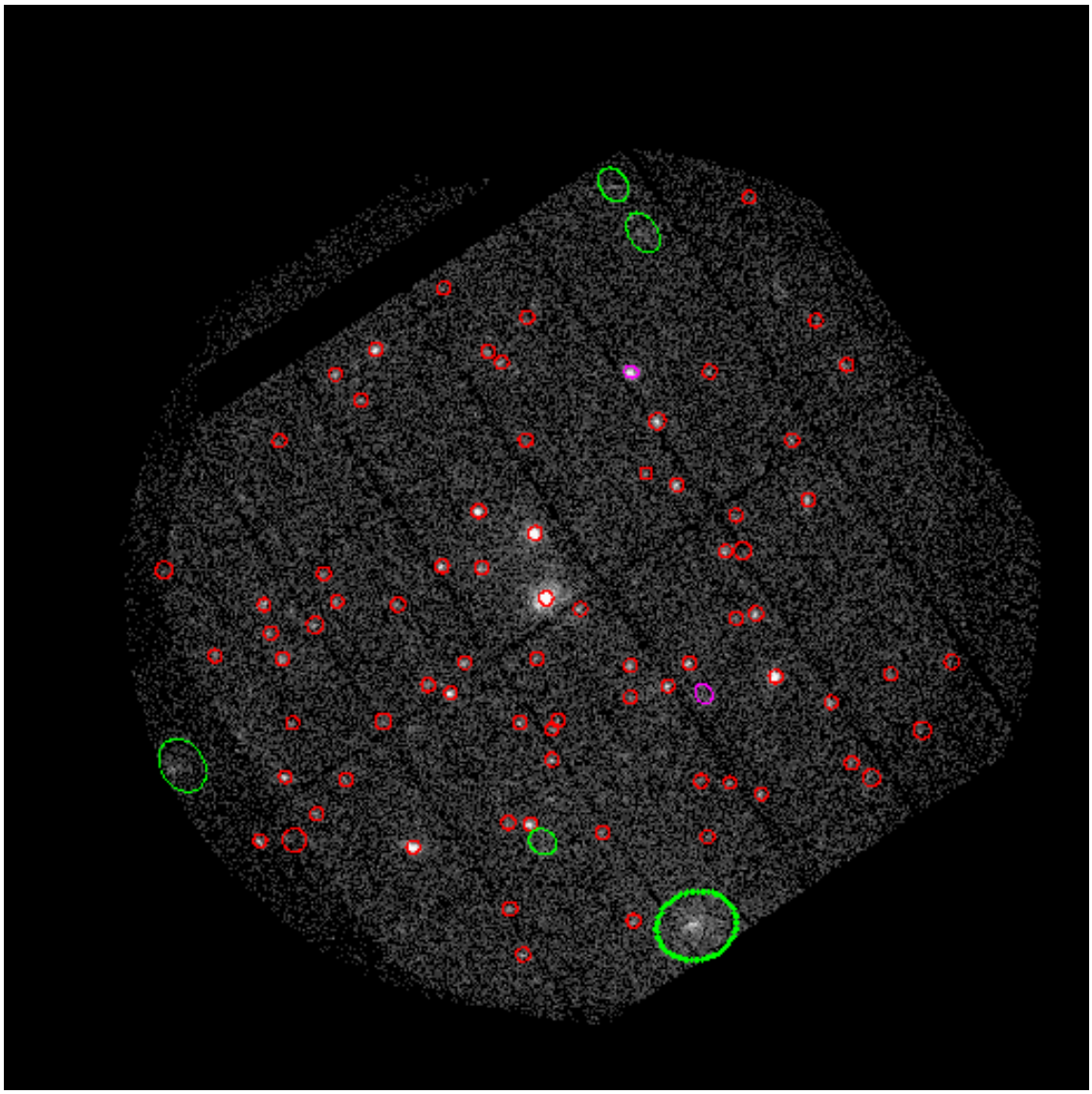

Figure 4.14: XMM observation 0200250101, with detected sources circled. Red circles are pointsources, Magenta ellipses denote PSF-sized sources, Green ellipses are extended sources. The bold green ellipse is XMMXCS J091820.8+690101.1, a DR3 StatSam New candidate detected with 2070 counts in the 0.5-2.0keV band.

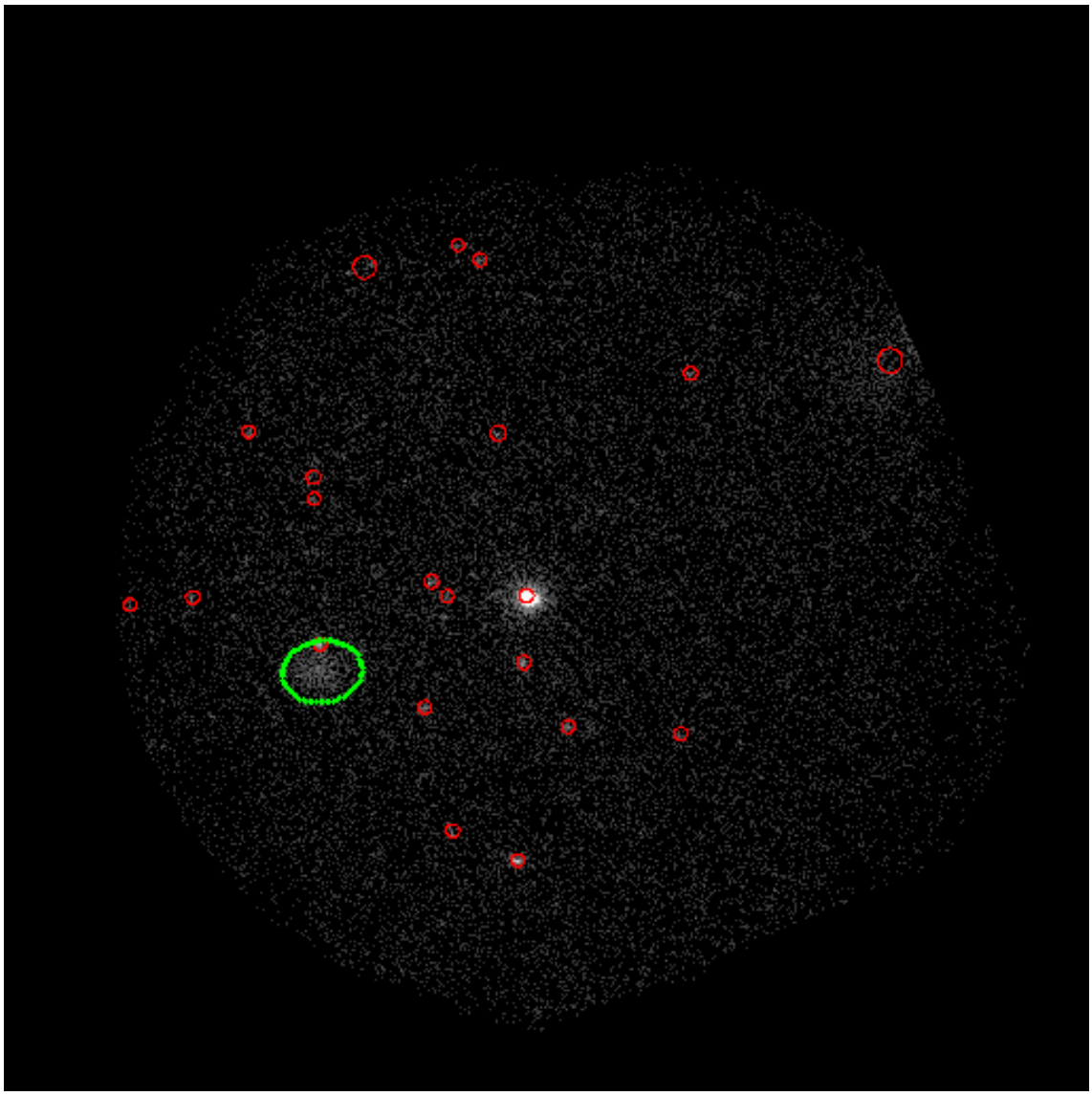

Figure 4.15: XMM observation 0200430801. Ellipse colour definitions are the same as in Figure 4.14. The bold green ellipse is XMMXCS J133511.8-232920.9, a DR3 StatSam New candidate detected with 1068 counts in the 0.5-2.0keV band.

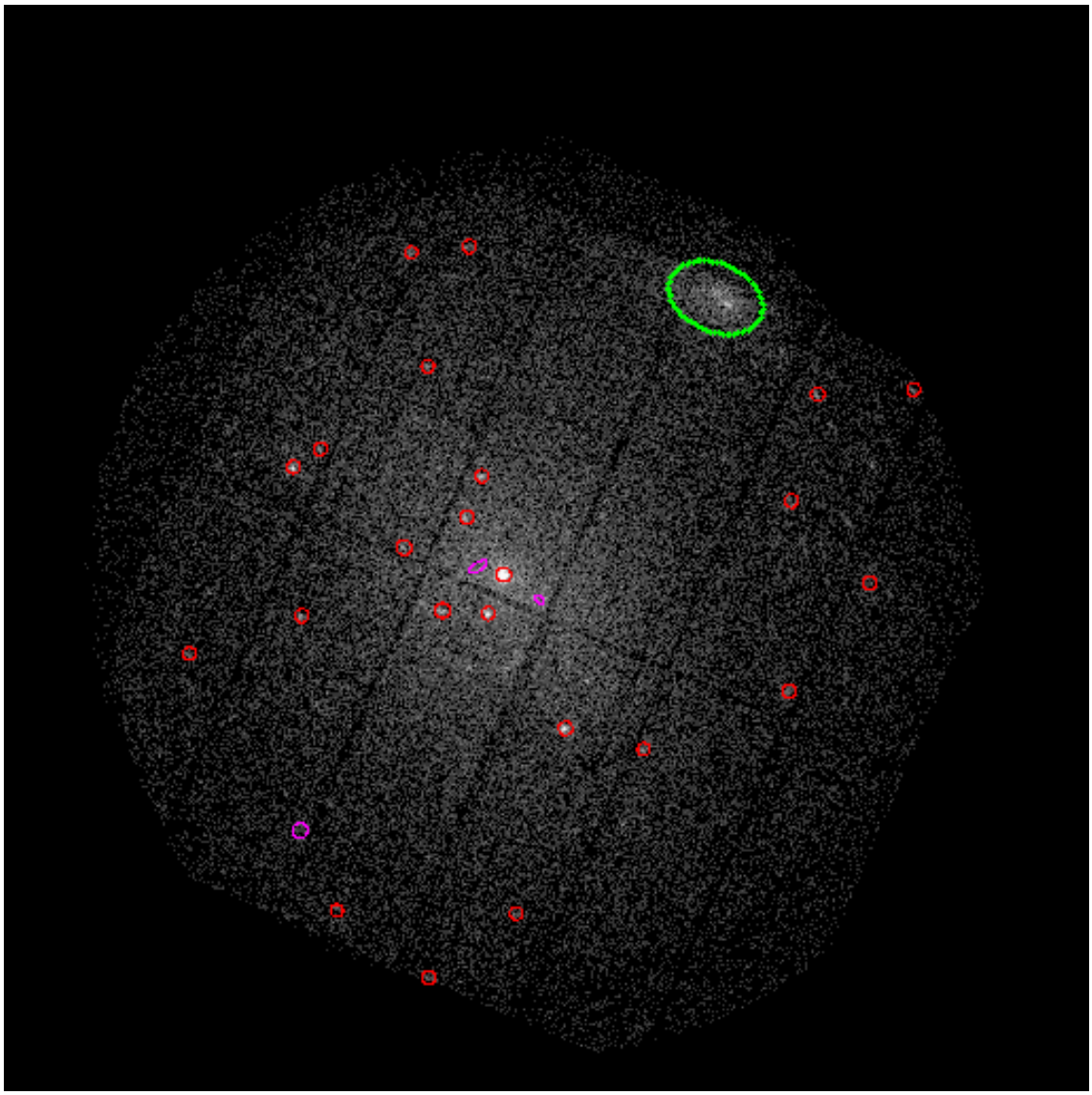

Figure 4.16: XMM observation 0002960101. Ellipse colour definitions are the same as in Figure 4.14. The bold green ellipse is a serendipitous re-detection of Abell 2634 at z=0.03, detected with 2386 counts in the 0.5-2.0keV band.

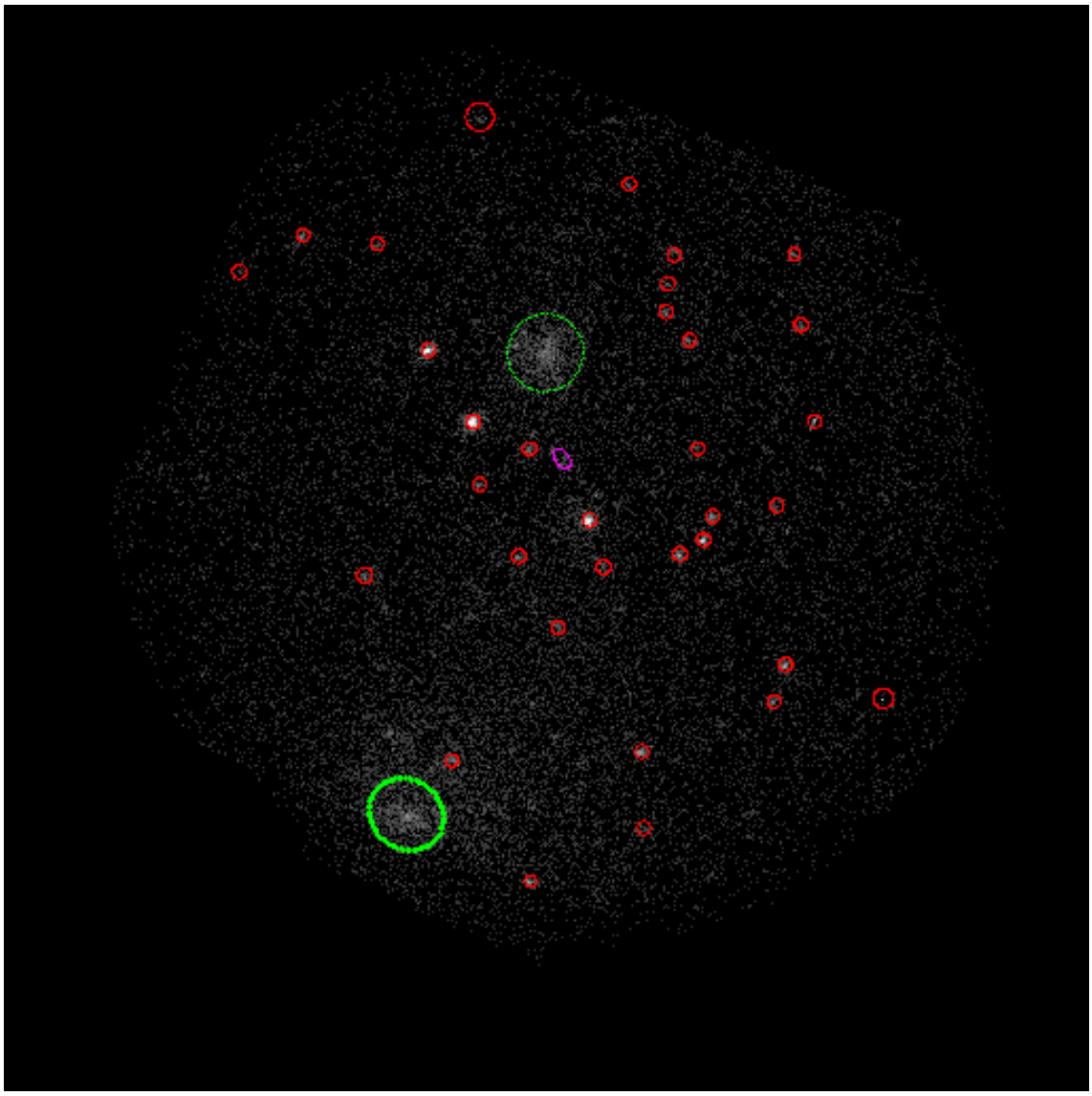

Figure 4.17: XMM observation 0203280301. Ellipse colour definitions are the same as in Figure 4.14. The bold green ellipse is a serendipitous re-detection of Abell 0150 at z=0.06, detected with 1549 counts in the 0.5-2.0keV band.

## 4.8 Online Database

The tables of data presented in this thesis are only a small representation of the vast amount of data produced by XCS. It has always been a stated aim of the project to make as much of the data as possible accessible to the astronomical community. Naturally, the best way to do this is via an online database.

A series of tables were designed in Davidson (2005) with this in mind. To maintain consistency this design has been kept.

- **Observation Table** Describes each of the XMM observations that make up the XCS archive.
- **Detection Table** Contains information on every detection in the merged images.
- **IndivExpProp Table** More detailed detection information from each individual camera
- **Source Table** Contains only unique sources

(See Appendix E for a description of the table columns). As part of this thesis work, the tables have been compiled into a relational MYSQL database to enable fast crossmatching and infomation retrieval. In addition the author has also designed and created webpages for each cluster candidate enabling visual inspection of the data (see Figure 4.18). The pages include relevant information from the database, literature and XCS redshifts, multi-band images with overlaid X-ray contours, and links to any likely matches in NED. These pages will all be linked into the database when it goes online. In the mean time it is possible to sort the data by ra, dec, counts, flux, and redshift via a series of summary pages.

These resources are currently only available to the XCS collaboration and affiliates, however a wider release is expected to happen as part of the natural progession of the project.

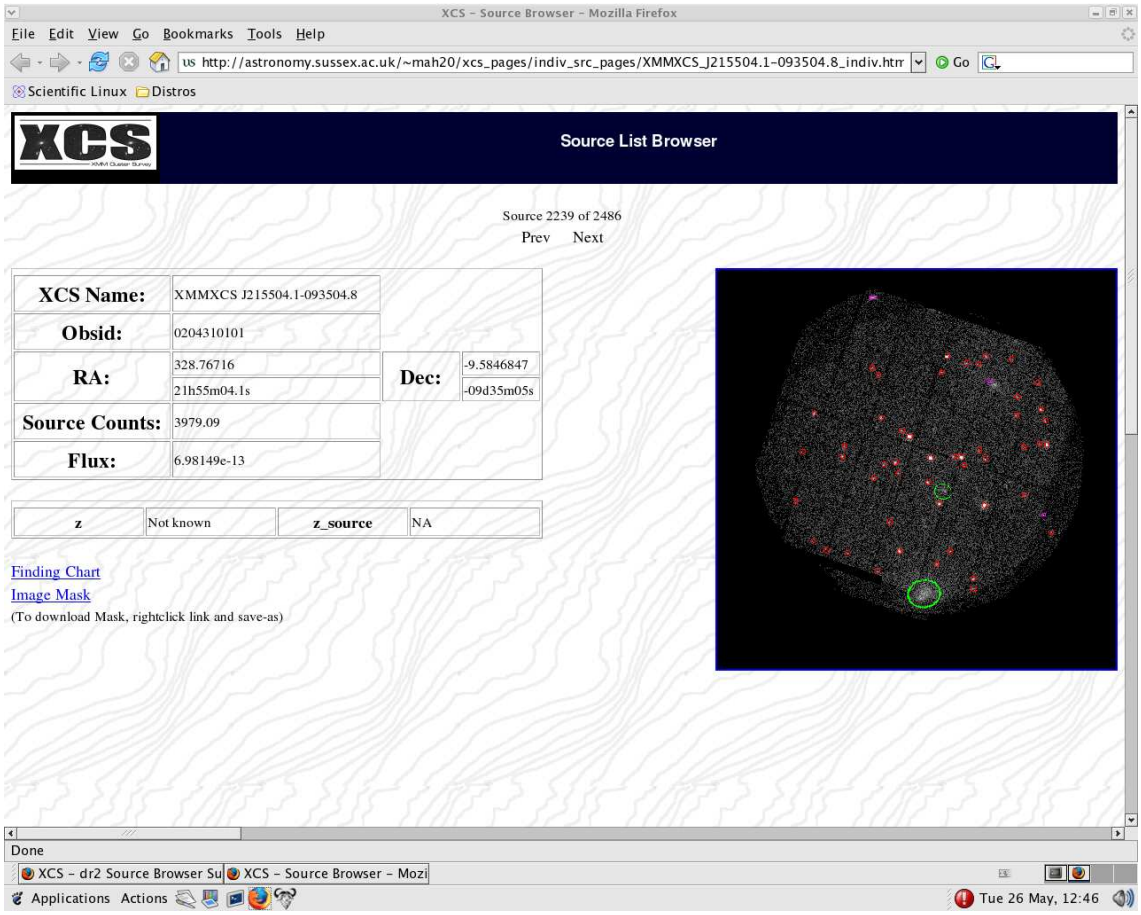


Figure 4.18: An example from the XCS Source Browser pages. Each page also contains multi-waveband images of the source (eg. SDSS, DSS, NVSS, 2MASS) and any likely matches from NED.

## 4.9 DR3 StatSam redshift follow-up

### 4.9.1 NXS and literature redshifts

The NXS survey was completed prior to the construction of DR3. However, since DR1 and DR2 are both fully contained within DR3, all of the DR1 and DR2 sources with NXS redshifts are also part of DR3. This amounts to 185 clusters with $0.1 \leq z \leq 1.0$ (See Section 3.7)

The search of the NED and SIMBAD archives described in Section 4.4 has also produced a list of up to 406 known clusters and groups (406 matches with a $2'$ search radius), many of which already have redshifts. The retrieval of reliable redshifts from such archives is complex: the archives are drawn from multiple sources, meaning that some quoted redshifts are of lesser quality than others. A variable radius to match XCS candidates to the known objects should also be used; for example, the radius suitable at $z = 0.1$ will not be appropriate for sources at $z = 1.0$. The archives may also contain galaxies with known redshifts, where we detect X-ray emission, these galaxies may not have been associated with a cluster before and so a more complex method than simply searching for known clusters must be implimented. This work is on going (E. Lloyd-Davies).

### 4.9.2 DR3 XCS300 redshifts using SDSS DR7

This section of text has been edited from that provided by N. Merhtens (Private communication), describing part of her follow-up work on the candidates presented in this thesis.

XCS DR3 contains 1513 cluster candidates (This number is before any literature checks were done) detected with at least 300 measured soft counts. Therefore with a measured redshift for each of these clusters an a X-ray temperature estimate can be derived. Of these 1513, candidates 827 fall within the survey regions of the latest public Sloan Digital Sky Survey (SDSS) data release DR7 (Abazajian et al., 2009).

Galaxy catalogs were downloaded from the public SDSS data archive [2] containing dereddened model $r'$- and $z'$- band magnitudes for all galaxies within a $20'$ radius of each cluster candidate. The NXS redshift algorithm (See Appendix C) was then run on these SDSS galaxy catalogs with the slight modification that a fixed external field sample was used as opposed to a local field sample around each candidate. A field sample was created using all galaxies within a $0.5^\circ$ radius centered on the coordinates ($22^h00^m$, $00^\circ00'$). Once again, potential cluster galaxies were chosen from within twice the X-ray extent of each cluster candidate.

[2] http://www.sdss.org/dr7/

As a result, 524 clusters (shown in H.2) were detected with at least 5 member galaxies with redshift estimates ranging between $0.1 \leq z \leq 0.75$, 437 of which are new cluster candidates to DR3.

## 4.10 Future work

### 4.10.1 New PSF model incorporation: DR4

The DR3 point source catalogue is being used by Dubois & Lloyd-Davies et al. (in prep) to create a better PSF model than those currently available. When complete this model will be incorporated into XAPA for the production of DR4.

### 4.10.2 Point-Source selection function & log$N$-log$S$

The large number of point sources in DR3 will enable us to put together a sample population with which to measure the point source selection function. With this we will then be able to determine the XCS measurement of the point source log$N$-log$S$.

## 4.11 Summary

The total, non-overlapping area of DR3 is 522.29 deg$^2$, and the available StatSam area amounts to 229.73 deg$^2$. DR3 has extended the total area covered by XCS (from the DR1+DR2 area) by $\sim 70\%$, and increased the number of StatSam cluster candidates by a factor of 2. Using a $1'$ radius to search the literature: there are 1365 StatSam cluster candidates with $> 300$ counts, 159 of which are already listed in NED as being known clusters/groups. This corresponds to $\sim 6$ serendipitous $> 300$ count candidates per deg$^2$. This is greater than the source density in DR1+DR2 due to the improvements made in the source list creation (see Section 4.1). For comparison the 400d survey find $\sim 0.75$ candidates per deg$^2$ with fluxes $> 1.4 \times 10^{-13}$ergs s$^{-1}$ cm$^{-2}$. The XMM-LSS find 5.4 'C1' clusters per deg$^2$ and estimate $\sim 12$ 'C2' per deg$^2$ (the C2 clusters have not yet been published).

We can potentially measure temperatures for all these DR3 XCS300 candidates, once redshifts are known. 709 redshifts have already been obtained from NXS and SDSS and other literature data. The temperature fitting is currently underway (E. Lloyd-Davies), and at present there are 227 DR3 clusters with both temperature and redshift measurements (See Table H.3 in Appendix H), although most of these have come from DR1+DR2. This is already a significant improvement over the samples in the literature, see Table 4.7. A

preliminary XCS $L-T$ relation is shown in Figure 4.19.

| Survey | Data | Clusters | z range |
|---|---|---|---|
| HIFLUGS | Rosat | 63 | 0.005 - 0.2 |
| Maughan et al. | Chandra | 115 | 0.1 - 0.3 |
| O'Hara et al. | Chandra | 70 | 0.18 -1.24 |
| 400SD | Chandra | 36 | 0.35 - 0.9 |
| XMM-LSS | XMM | 29 | 0.05 - 1.05 |
| XCS300 | XMM | 227 | 0.003 - 1.457 |

Table 4.7: Literature cluster samples with measured temperature and redshifts. Also added is the current size of the XCS300 sample with temperatures and redshifts.

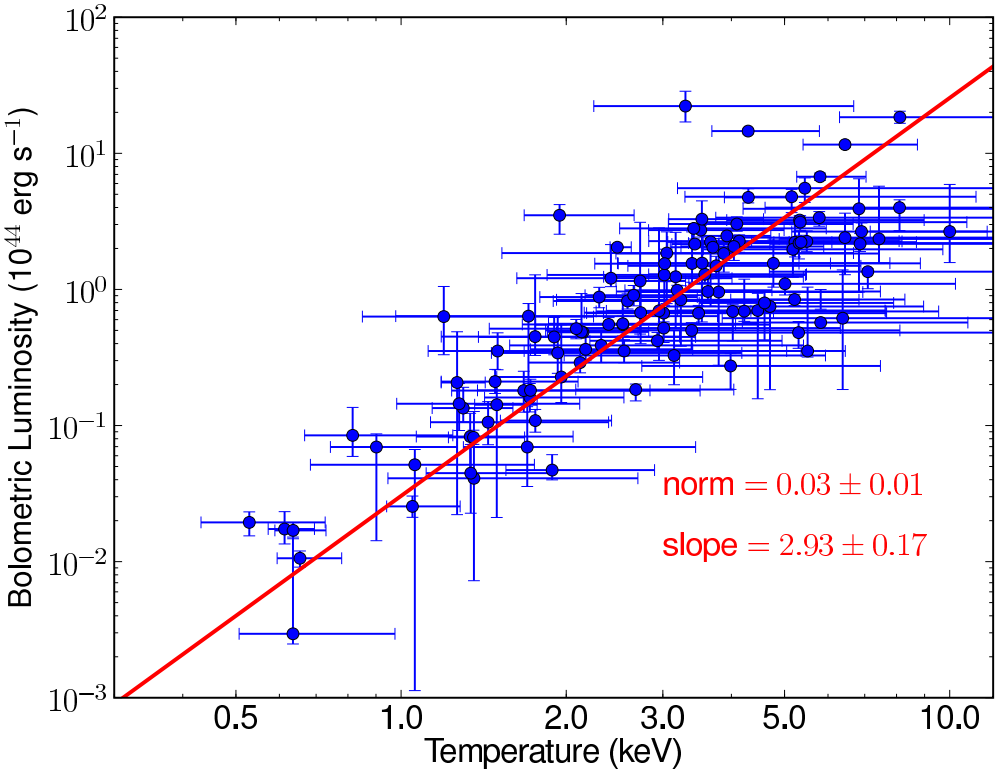


Figure 4.19: A preliminary XCS $L-T$ relation. Figure courtesy of E. Lloyd-Davies.

In addition to the large cluster sample that will come from DR3, Campbell et al. (in prep) have used the DR3 point source catalogue to find 11 high-quality isolated neuton star candidates. These candidates are mostly new to DR3.

With the constuction of DR3 the XCS expect to have a sample of $\sim$ 1000 clusters with redshifts, and the potential to measure temperatures for the majority of these. This will be significantly larger than any other homogenous sample of clusters.

The current distribution of the DR3 cluster redshifts is displayed in Figure 4.20.

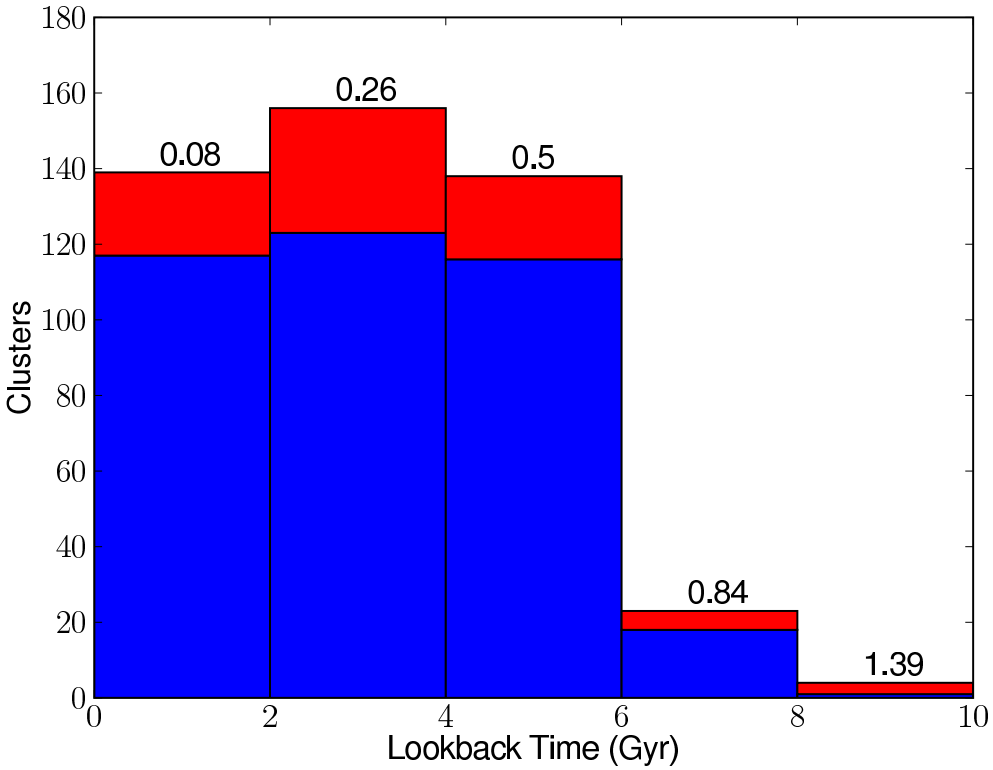


Figure 4.20: A histogram of the lookback time of DR3 clusters with measured redshifts. The red histogram is for spectroscopic redshifts, the blue histogram is for photometric redshifts. The numbers above the bins are the centre of the bin in redshift space. Figure courtesy of E. Lloyd-Davies.

# Chapter 5

# XCS Selection Function with Two-Dimensional $\beta$ profiles.

In this chapter we will discuss the XCS selection function as measured using isothermal $\beta$ profile clusters. The method was first laid out in Davidson (2005), but the work presented here represents the first full test and application of that method.

We will discuss the selection function applied to the cosmological prediction analysis presented in Sahlén et al. (2009), then look at the effects of the simplifications made in some of the assumptions used therein. Finally we will see how the methods used in this chapter can assist the planning of future studies.

As discussed in the preceeding chapters, many authors are attemping to use the abundance of clusters of galaxies to constrain cosmological parameters. In order to achieve this it is important to realise that it is not currently possible to detect and analyse every cluster in a survey region. Some will not be found, either because they fall below the flux limit of the survey in question, or maybe due to some particular bias in the detection methods. The selection function is a quantitative description of these effects. In addition to cosmological studies, an understanding of the selection function is vital to studies of cluster scaling relations, for example in measuring an $L - T$ relation a survey will preferentially select more luminous clusters, i.e. those above the mean relation. This bias is especially large at high redshift where less luminous clusters are even harder to detect. It has recently been shown that the selection function must be accounted for when studying $L - T$ evolution (Pacaud et al., 2007). The popular way of determining the selection function of a survey is by running a series of fake images through the detection processes, which is the general procedure employed below.

The work in this chapter is split into three main sections:
In Section 5.3 we assume a fixed profile, and vary the cosmology, luminosity, temperature and redshift of our input clusters, within random exposures from the archive. In Section

5.4 we assume a fixed $\Omega_m = 0.3$ and $\Omega_\Lambda = 0.7$ cosmology, and fixed $L$ and $T$. We then vary the morphological parameters $r_c$ (Section 5.4.1), $\beta$ (Section 5.4.2), and $e$ (Section 5.4.4), at various redshifts within random exposures from the archive. In Section 5.6 we assume a fixed profile and cosmology, and vary $L$, $T$, $z$ selecting the pointings based on exposure time.

## 5.1 Review of some Selection Function studies in the literature

### 5.1.1 The 400 Square Degrees ROSAT PSPC Galaxy Cluster Survey

The 400 Square Degrees ROSAT PSPC Galaxy Cluster Survey (hereafter: 400d) (Burenin et al., 2007) has some similarities to XCS, and so we will review their selection function approach here. The 400d survey uses all archival ROSAT PSPC fields that meet the following criteria: Galactic latitute $|b| > 25°$; Galactic absorption $N_H < 10^{21} cm^{-2}$; total clean exposure $t_{exp} > 1000s$, and at least 10° away from both of the Magellanic clouds. The 1610 ROSAT fields that remain cover 397deg$^2$ and are searched for sources using the same algorithms as used for the 160d survey (Vikhlinin et al., 1998). This implements wavelet-based source detection and source selection based mainly on likelihood fitting of both source existence and extent. This resulted in 287 extended sources with fluxes above $1.4 \times 10^{-13}$ergs $s^{-1}$ cm$^{-2}$. We note here that DR3 has $> 1300$ cluster candidates with $> 300$ counts in 229deg$^2$.

To calculate the 400d selection function, the authors create a non-evolving reference population of $\beta$-model clusters using a core radius and beta distribution from the Einstein sample of Jones and Forman (1999). The distribution is corrected for a trend in $r_c$ with $L_X$ (approximated as $r_c \propto L_X^{0.5}$ for $L_X < 10^{44} erg\ s^{-1}$). The profiles are made to be elliptical following the distribution of axis ratios from Mohr et al. (1995). The profiles are then distributed over an X-ray luminosity function (XLF) that is taken to be a Schechter (1976) fit to the REFLEX survey data (Böhringer et al., 2002). The resulting detection probability can be seen in Figure 5.1 as a function of $r_c$.

Burenin et al. (2007) also tested the effects of varying $r_c$ and $\beta$ to assess the impact of the assumed parameter distributions. In order to cover the range of morphologies seen in the observed population the authors create images of the HIFLUGCS catalogue (Reiprich and Böhringer, 2002) clusters and simulate them over a range of redshifts. They found this produced no real deviation from the detection efficiency as measured from their reference population. Burenin et al argue that the HIFLUGCS sample is unbiased with respect to structure and so conclude that deviations in cluster morphology from the $\beta$-model do not play a significant role in the 400d survey selection function.

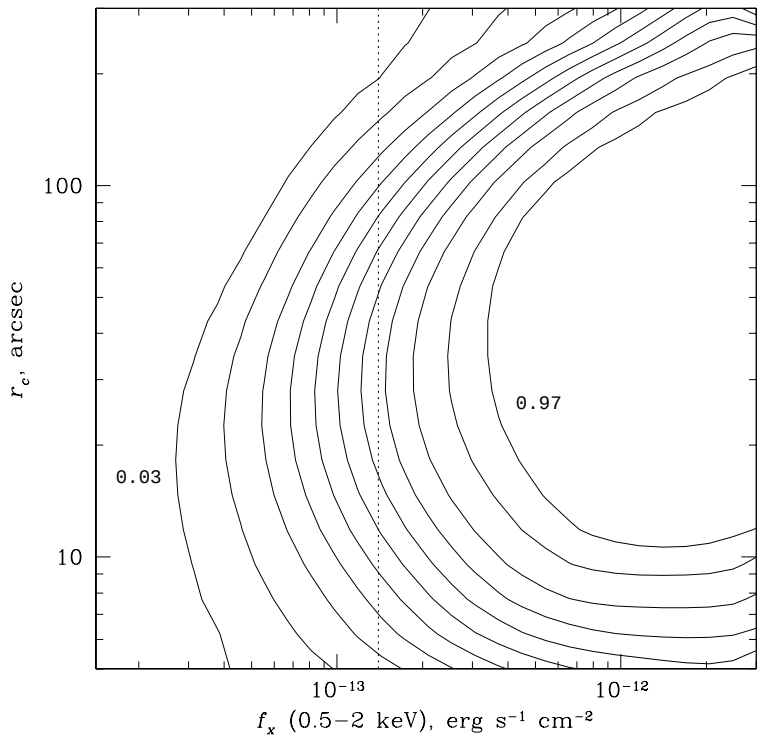


Figure 5.1: Figure 9 from Burenin et al (2007), Cluster detection probability as a function of input flux and angular core-radius. The contours represent probabilities of 0.03,0.1,0.2,0.3,0.4,...,0.9,and 0.97. Note that this figure does not include the effect of imposing the minimum flux requirement ($f_{min} = 1.4 \times 10^{-13}$erg s$^{-1}$ cm$^{-2}$,dotted line) for the clusters to enter the final catalogue.

### 5.1.2 The Bright Serendipitous High-redshift Archival ROSAT Cluster

The Bright Serendipitous High-redshift Archival ROSAT Cluster (Bright SHARC) survey (Romer et al., 2000) was comprised of 460 archival ROSAT pointings, each with an exposure time greater than 10ks, that lie at Galactic latitudes greater than $b = |20°|$. The survey selected extended objects in an annulus bounded by radii of $2.5'$ and $22.5'$ using a wavelet-based detection algorithm. Sources were selected that met three criteria; they were detected with signal-to-noise ratios of 8 or higher, they were more than $3\sigma$ extended, and had filling factors of less than $f = 1.3$. This resulted in 374 sources. The 94 brightest of which comprise the Bright SHARC sample. This sample was optically examined, resulting in 37 confirmed clusters with redshifts.

To quantify the Bright SHARC selection function Adami et al. (2000) ran a series of simulations comprising of artificial clusters placed in ROSAT pointings being run through the Bright SHARC pipeline processing. The first simulation run had the following properties: $\Omega_m = 1$, $\Omega_\Lambda = 0.0$, isothermal $\beta$ profile clusters with $\beta = 0.67$, $r_c = 250$kpc and $e = 0.15$. Each successive simulation run changed one of these properties and compared the results to the first run, which was used as a benchmark. Adami et al. (2000) present results of changing the assumed cosmology, ellipticity, $\beta$, $r_c$, and of changing the surface brightness model. The models they compare to their benchmark model are a pseudo-NFW profile and a pseudo-cooling flow profile. The authors demonstrate that the SHARC selection function is very sensitive to both $r_c$ and $\beta$, in some of the considered cases the detection efficency can vary by 100%.

Adami et al. (2000) also show how the variations in the selection function can influence the science results which depend apon it. The case they detail is that of the Cluster X-ray Luminosity Function (CXLF), and they extend the discussion to the impact on any attempt to measure $\Omega_m$. For the SHARC survey, if all clusters had larger core radii than assumed in their benchmark selection function, the CXLF would significantly underestimate the number density of clusters at high redshift, lending support to a higher $\Omega_m$ universe.

## 5.2 Method

In order to properly model the selection function of a survey like XCS, it is important to account for all of the observational variations presented in real data. We can achieve this by placing a sample of fake surface brightness profiles into real Obsids. This ensures that our simulated images re-create features and issues present in real images, such as clusters lying on or near chip edges and point source contamination.

### 5.2.1 Placing fake clusters in XCS images

We create a sample of surface brightness profiles from an Isothermal $\beta$ model (see Equation 1.17) with $\beta = 2/3$ and core radius, $r_c = 160$kpc (close to the mean values of $\beta = 0.64$, and $r_c = 163$kpc, obtained from a uniform ROSAT analysis of clusters from $0.1 < z < 1.0$ (Ota and Mitsuda, 2004)), and plasma metallicity $Z = 0.3Z_{\odot}$. For a given cosmology we simulate 700 sets of cluster parameters, see Table 5.1.

| *Parameter* | *Range* |
|---|---|
| Redshift | 10 values linearly spaced 0.1 : 1.0 |
| Luminosity | 10 values logarithmically spaced (0.178 : 31.623) $\times 10^{44}$erg s$^{-1}$ |
| Temperature | 7 values linearly spaced 2.0 : 8.0 keV |

Table 5.1: Parameter ranges used in XCS selection function

We limit our selection of Obsids to those that we would consider 'statistical' in a serendipitous survey, see Section 3.6 for all filters applied. This left 1847 suitable observations at the time this study began (i.e only DR1 StatSam Obsids are included). Before each selection function run, a smaller list of 100 Obsids is selected at random from the full set of 1847. These 100 Obsids are then copied from the main XCS archive to local processing nodes for temporary storage, to speed up the analysis. Tests have shown (see Davidson (2005)) that with 100 Obsids it is still possible to reproduce the variance in exposure time, target type, point source density, etc., inherent to the XCS. In the following we define a 'selection function run' as the analysis over the 700 sets of cluster parameters and 100 Obsids, a total of 70000 combinations.

For each of the 70000 simulations that comprise the selection function run the process is as follows:

1. The angular size of the cluster profile being generated is determined from the angular diameter distance (which is cosmology dependent, see Section 1.1.2) at the input redshift. The profile is then randomly positioned into a blank XMM style Obsid, with a uniform probability across the field of view, and convolved with the appropriate PSF model. For this purpose we use the two dimensional Medium accuracy model [1] (see Section 2.2). This is a natural choice of PSF model for two reasons; it accounts for the azimuthal variation in the PSF, also the Extended model (Ghizzardi, 2001) is implemented for source classification, so, to keep the simulations fair, we cannot use the same model for blurring as we do for classification. The convolution with the PSF creates a probability density function (PDF) for the cluster profile.

[1] http://xmm.vilspa.esa.es/external/xmm_sw_cal/calib/index.shtml

2. The profile is assigned an absorbed count rate taken from a series of arrays calculated using XSPEC [2](generated by K. Sabirli). The arrays tabulate conversions between combinations of temperature, redshift, hydrogen column density (nH), unabsorbed bolometric luminosity, and also the various cameras and filters aboard XMM.

3. The PDF is normalised to the absorbed count rate, thus creating a rate image.

4. The total number of counts to be placed in the PDF is determined by summation of a 'count image'. This is created by multiplying the rate image by the exposure map of the chosen Obsid to account for vignetting, masking and chip gaps.

5. The rate image is then renormalised to 1, and the counts are added randomly to this PDF.

6. The individual fake cluster images are co-added to the original Obsid, and can now be processed by our custom detection pipeline in the same way as any real data. The detection and classification algorithms used by XCS are described in Davidson (2005) are reviewed in section(3.3.2).

The above process of 70000 simulations per run is incredibly time consuming as it covers the whole $L-T$ plane within $T = 2-8$keV and $L = 0.178 - 31.623 \times 10^{44}$erg $s^{-1}$. We did this, rather than assuming an $L-T$ relation, to allow a more complete analysis with regard to XCS's ability to contrain cosmology. If we limited our simulations to those that fit a measured $L-T$ relation, it would not be possible to include the effects of scaling relation errors and/or evolution in the final analysis (see Sahlén et al. (2009)). In this way, our selection function method is more complete than Burenin et al. (2007).

### 5.2.2 Cluster Recovery

For a cluster be considered as RECOVERED there are 3 criteria that must be met:

1. The detection software must identify a new extended source in the input image, i.e. not point-like or PSF-sized extent (PSF-SIZED FLAG)

2. The extended source must not contain a significant amount of point source contamination (RUN1 CONTAMINATED FLAG or POINTSOURCE CONTAMINATED FLAG)

3. The extended source must not be mis-associated with a known cluster near/at the input position.

[2]http://heasarc.gsfc.nasa.gov/docs/xanadu/xspec/

**Test of the XAPA determinations of extended source count values**

Of interest to XCS is the number of detected source counts determined by the algorithms, since a count limit (see Section 3.6.1) is used to determine which cluster candidates will receive follow-up and ultimately be used for cosmological studies. Is this number of detected counts drawn from XAPA for RECOVERED clusters a reliable measure? We have been able to test this using the $\beta$ model selection function method described above. Plotted in Figure 5.2 is the count measurements from a set of RECOVERED simulated 3keV $\beta$ clusters vs the input counts. This shows that while XAPA usually underestimates the number of counts from extended sources, the behaviour for $> 300$ count objects is reasonably consistent within a range of $50\% - 100\%$ of the input counts. This may indicate that the flux aperture used for extended objects is too small, though since the fluxes are re-measured independently of XAPA this is not a major issue (See Appendix I). So although not perfect, XAPA can be used as an indicator of the total source counts. XCS currently uses count cuts of $> 300$ and $> 500$. At both of these levels, the underestimated value for the source counts means that a count limited sample will be $\sim 20\%$ smaller than expected. There are two main reasons for the loss of counts: loss due to chip-gaps, and aperture effects. These reasons are discussed and quantified in Davidson (2005). The key point is that very few low-count clusters will be erroneously included in a count-limited XCS cluster candidate sample, e.g. XCS300 or XCS500. Although some high-count clusters will be erroneously excluded from such samples, this is not a major concern, since their absence can be compensated for using the selection function. In other words, selection functions can correct for incompleteness, but cannot correct for contamination.

## 5.3 XCS selection function: testing the dependence on cosmology, $L$, $T$, and $z$, and location in the field of view

In order to fully assess the cosmological constraining power of XCS we need to understand how the selection function changes as a function of cosmological parameters, namely $\Omega_m$ and $\Omega_\Lambda$. $\Omega_m$ and $\Omega_\Lambda$ play a role in the selection function via the luminosity distance ($d_L$). Variations in $d_L$ affect both the angular size of an object on the sky and the flux received from the object (see Equations 1.9 and 1.10). To measure these effects the above process has been repeated using the parameters in Table 5.2.

An example set of results from run 4 can be seen in Figures 5.3 and 5.4 (the full set of plots can be seen in Appendix F), the error bars on which represent the $1\sigma$ statistical errors on the detection averages. To reduce the statistical uncertainty further would be incredibly time consuming since due to the binomial nature of the detection data, as the uncertainty in the mean detectability scales as $1/\sqrt{n}$.

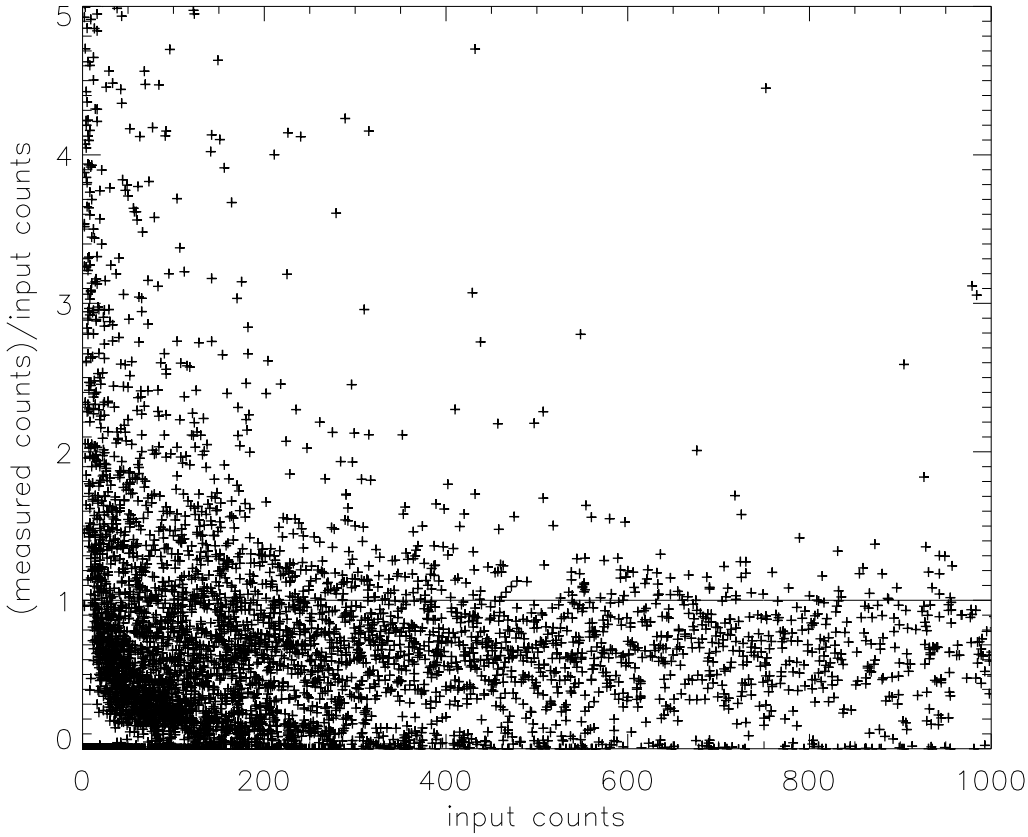


Figure 5.2: A ratio of measured counts/input counts as a function of input counts. The plotted results are for 3keV $r_c = 160$kpc, and $\beta = 2/3$ clusters. The horizontal solid black line marks the 1/1 ratio, i.e measured counts = input counts

| Run number | 1 | 2 | 3 | 4 | 5 | 6 | 7 |
|---|---|---|---|---|---|---|---|
| $\Omega_m$ | 0.22 | 0.26 | 0.28 | 0.30 | 0.32 | 0.34 | 0.38 |
| $\Omega_\Lambda$ | 0.78 | 0.74 | 0.72 | 0.70 | 0.68 | 0.66 | 0.62 |

| Run number | 8 | 9 | 10 | 11 | 12 | 13 | 14 | 15 | 16 |
|---|---|---|---|---|---|---|---|---|---|
| $\Omega_m$ | 0.26 | 0.26 | 0.26 | 0.30 | 0.30 | 0.30 | 0.34 | 0.34 | 0.34 |
| $\Omega_\Lambda$ | 0.60 | 0.70 | 0.80 | 0.60 | 0.70 | 0.80 | 0.60 | 0.70 | 0.80 |

Table 5.2: Cosmological parameter combinations used in selection function runs. Runs 1-7 are for flat ($k = 0$) cosmologies and were implemented in Sahlén et al. (2009). Runs 8-16 are for non-flat ($k \neq 0$) cases.

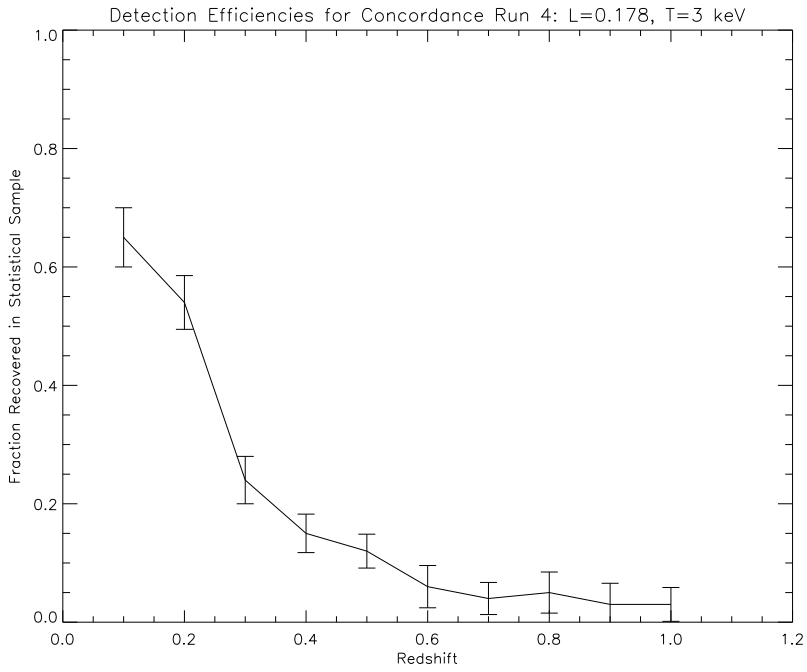


Figure 5.3: XCS StatSam detection and classification efficiency for 3keV clusters, with a Luminosity of $0.178 \times 10^{44}$ erg $s^{-1}$. All clusters are spherical and have $r_c = 160$kpc, and $\beta = 2/3$.

### 5.3.1 Testing the impact of a count cut on the selection function

The results as seen in Figure 5.4 and Appendix F refer to all clusters RECOVERED. However, when doing cosmology we will only be using those clusters detected with enough counts to allow a temperature estimate. As discussed in Chapter 3, a lower count limit for the XCS cosmological analysis has been set at 500 counts (see Sahlén et al. (2009)). The impact of the addition of this count cut to the selection function is shown in Figure 5.5. Note that in Figure 5.5, and all contour plots shown hereafter, the data have been interpolated and then smoothed.

### 5.3.2 Testing the impact of $L$, $T$, $z$ on the selection function

As Figure 5.5 shows, the XCS's ability to detect and classify clusters is a strong function of both $L$ and $z$, but only weakly dependent on $T$. For example, at $z = 0.2$: for a 3keV cluster, a change in $L$ from 0.178 to 31.6 ($\times 10^{44}$erg/s) causes an increase in detection from $\sim 25\%$ to $\sim 85\%$, but for a $1.0 \times 10^{44}$erg/s cluster, a change in $T$ from 2 to 8 (keV) only causes a decrease in detection from $\sim 73\%$ to $\sim 68\%$. In fact the variation seen with temperature ($\sim 5\%$) is of comparable size to the $1\sigma$ statistical uncertainty in the selection function.

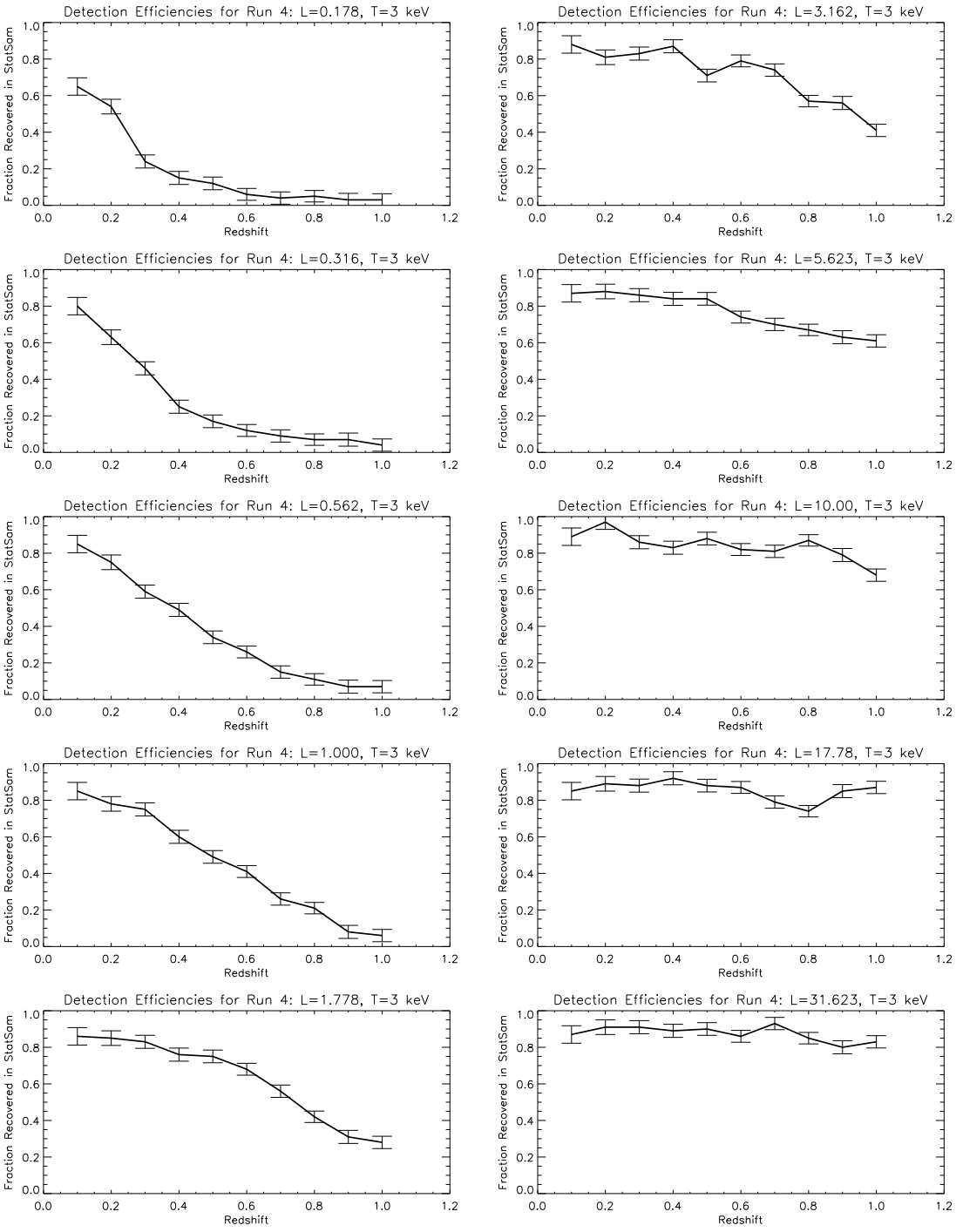


Figure 5.4: XCS StatSam detection and classification efficiency for 3keV clusters. All clusters are spherical and have $r_c = 160$kpc, and $\beta = 2/3$. Luminosities (L) are given in units of $10^{44}$erg $s^{-1}$.

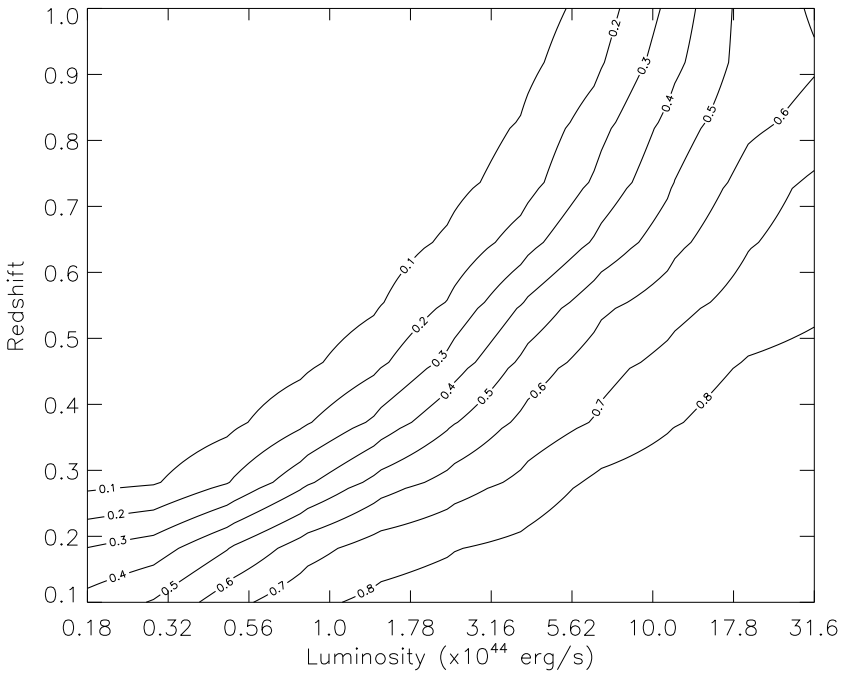


(a)

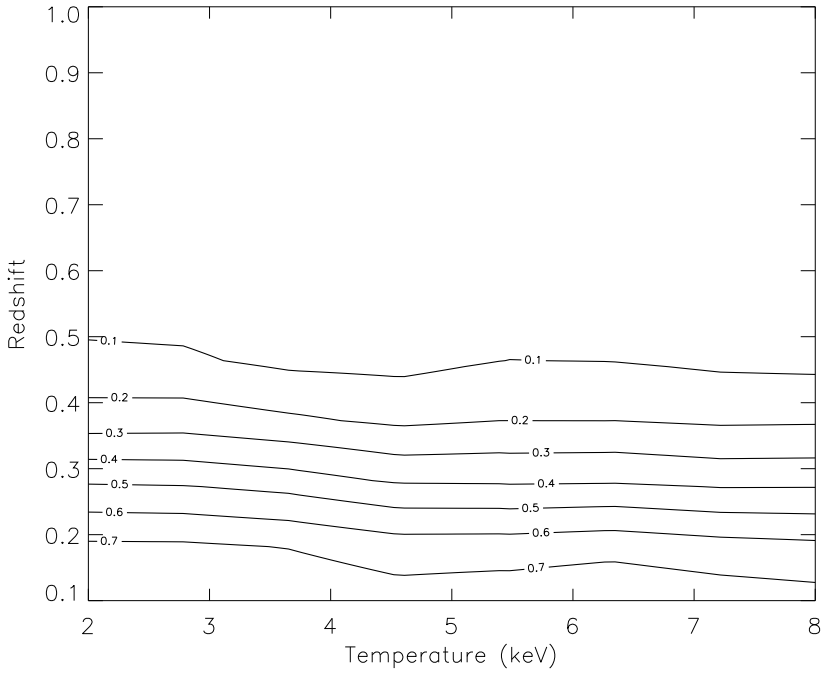


(b)

Figure 5.5: XCS StatSam detection and classification efficiency for clusters detected with $\geq$ 500 counts, and with structural properties as in Figure 5.4 (i.e $r_c$ = 160kpc, $\beta$ = 2/3). Figure 5.5(a): Detection efficiency is shown for 3keV clusters as a function of bolometric luminosity and redshift. Figure 5.5(b): Detection efficiency shown as a function of temperature and redshift for clusters with a luminosity of $1.0 \times 10^{44}$erg/s.

### 5.3.3 Testing the impact of scaling relations on the selection function

Figure 5.6 demonstrates how the selection function changes with differing evolution in the $L-T$ relation (Figure 5.6 was created by M. Sahlen using data provided by the author). Figure 5.7 shows the effect that different $L-T$ evolution is expected to have on the number of clusters in the final XCS500 sample (Figure 5.7 was created by M. Sahlen). A comparison of the pink and green histograms (or blue and orange), in Figure 5.7(b) show that at $z > 0.7$, different $L-T$ evolution can change the number of expected cluster detections by a factor of $\sim 2$.

### 5.3.4 Testing the impact of cosmological model on the selection function

Figure 5.8 shows how $\Omega_m$ and $\Omega_\Lambda$ influence detection for clusters with $T = 3$keV, $L = 1.358 \times 10^{44} erg\, s^{-1}$, $r_c = 160$kpc, and $\beta = 2/3$ at $z = 0.5$. Figure 5.8 demonstrates how detection within a cluster survey such as XCS is not insensitive to cosmology (via $d_L$), which shows that a single selection function is not adequate when making constraints. For example, the recovery efficiency for the clusters in Figure 5.8 for $\Omega_\Lambda = 0.7, \Omega_m = 0.3$ is 37% greater (relative difference) than $\Omega_\Lambda = 0.7, \Omega_m = 0.2$. However in order to make accurate measurements it is clear that the statistical uncertainty in the selection function must be minimized.

### 5.3.5 Testing the impact of detection location on the selection function

In Figure 5.9 we demonstrate that XAPA's detection and classification efficiency has some dependence on offaxis angle. Objects in the centre of the field of view are RECOVERED $\sim 40\%$ less than those in the outer regions of the image. This difference in RECOVERY is a result of the input objects being detected and classified as point-sources. This is independent of the flagging process, and so is due to the shape of the PSF-EEF's at low offaxis angle being similar to the EEF's of the input clusters. This is not entirely suprising since the Extended PSF model is based on a King profile, which is also the basis of the $\beta$ profile. The use of a better PSF model would likely improve the situation. An important point to note is that although this variation exists it has very little impact since 84% of the field of view lies outside $6'$ of the centre, and beyond this radius the XCS500 is $> 90\%$ complete.

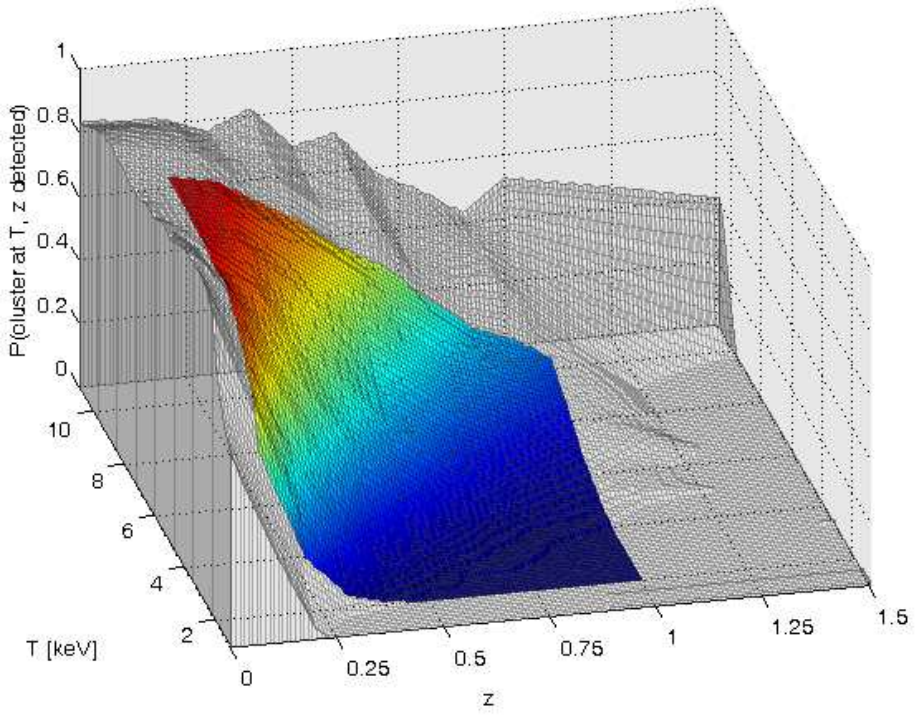


(a) Constant $L - T$ relation

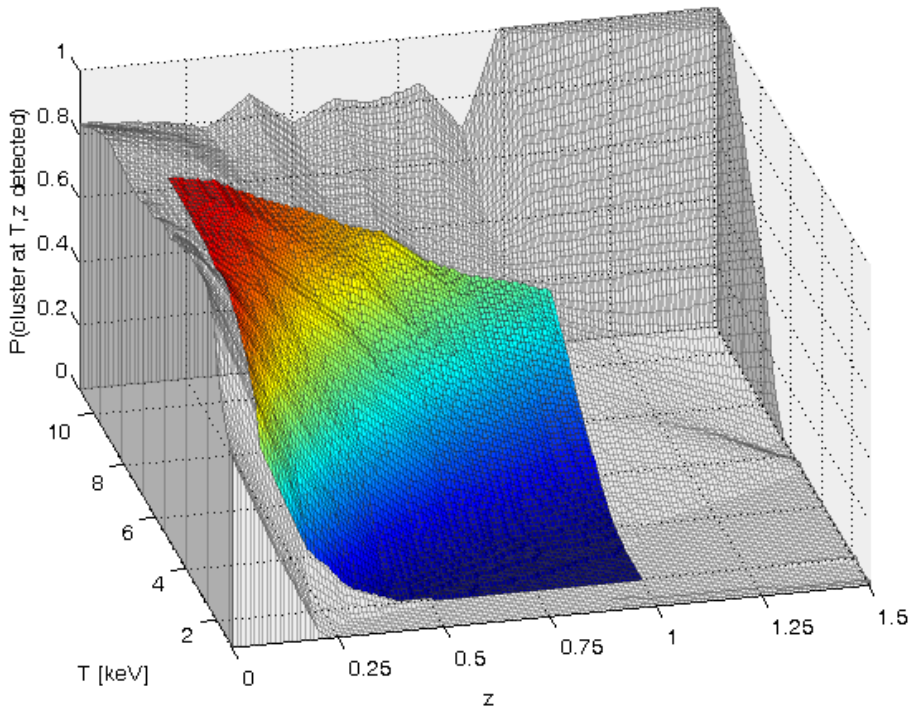


(b) Self-Similar $L - T$ relation

Figure 5.6: Figure 1 from Sahlén et al. (2009). Selection Function for our fiducial cosmology and different $L - T$ evolution.

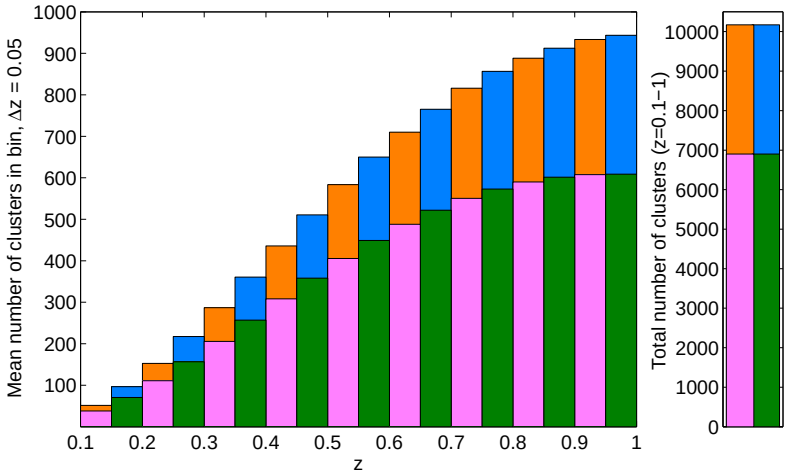


(a) Underlying cluster distribution

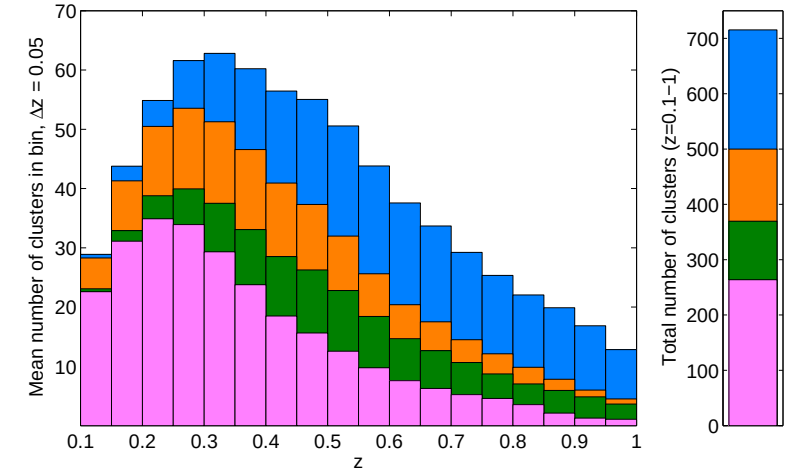


(b) Expected detections using selection function

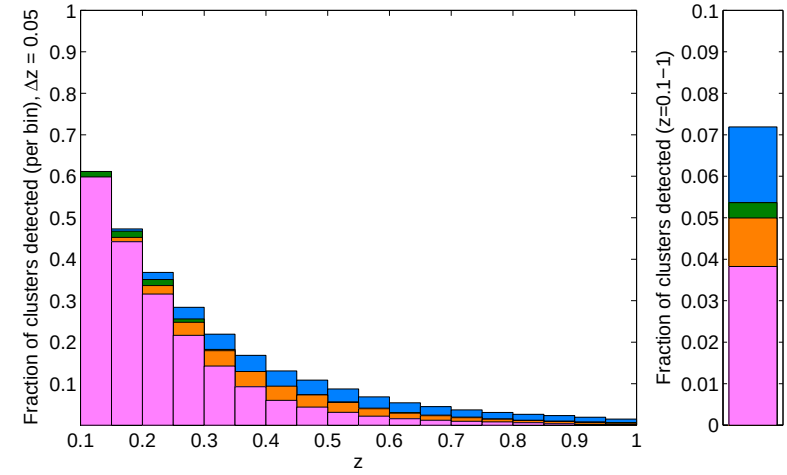


(c) Detected fraction of clusters per bin.

Figure 5.7: Figure 8 from Sahlén et al. (2009). Expected cluster number count distributions for the XCS500, for no $L-T$ nor $M-T$ scatter and no $L-T$ evolution (pink), no $L-T$ nor $M-T$ scatter and self-similar $L-T$ evolution (green), $L-T$ and $M-T$ scatter and no $L-T$ evolution (orange), and $L-T$ and $M-T$ scatter and self-similar $L-T$ evolution (blue). Bin sizes are $\Delta z = 0.05$ and $\Delta T = 0.5$ keV.

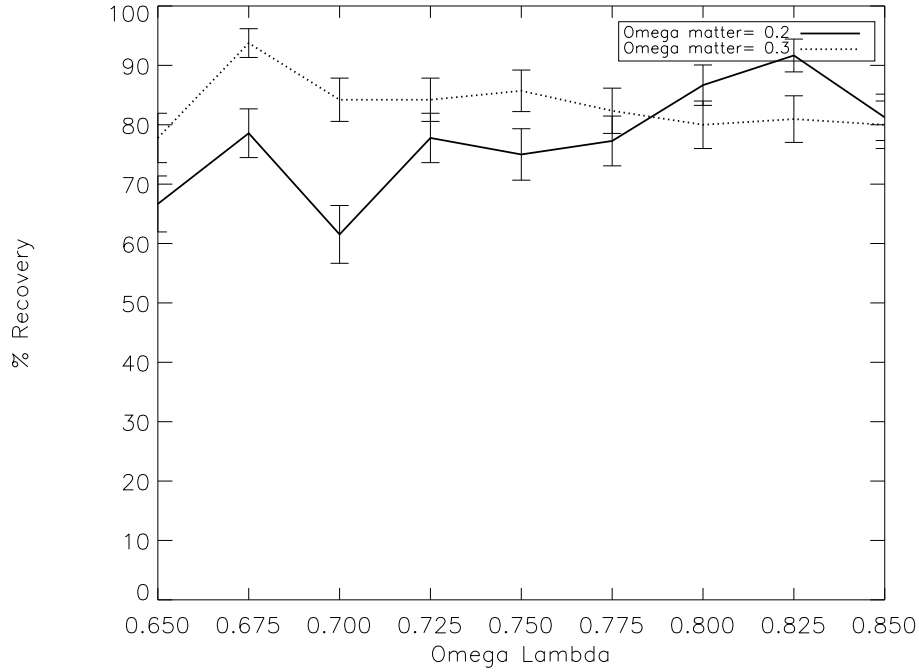


Figure 5.8: Variation of detection as a function of $\Omega_\Lambda$, and $\Omega_m$. All clusters have the following properties: $T = 3$keV, $L = 1.358 \times 10^{44}$erg s$^{-1}$, $r_c = 160$kpc, $\beta = 2/3$ and $z = 0.5$. Results plotted for those objects with $> 500$ input counts.

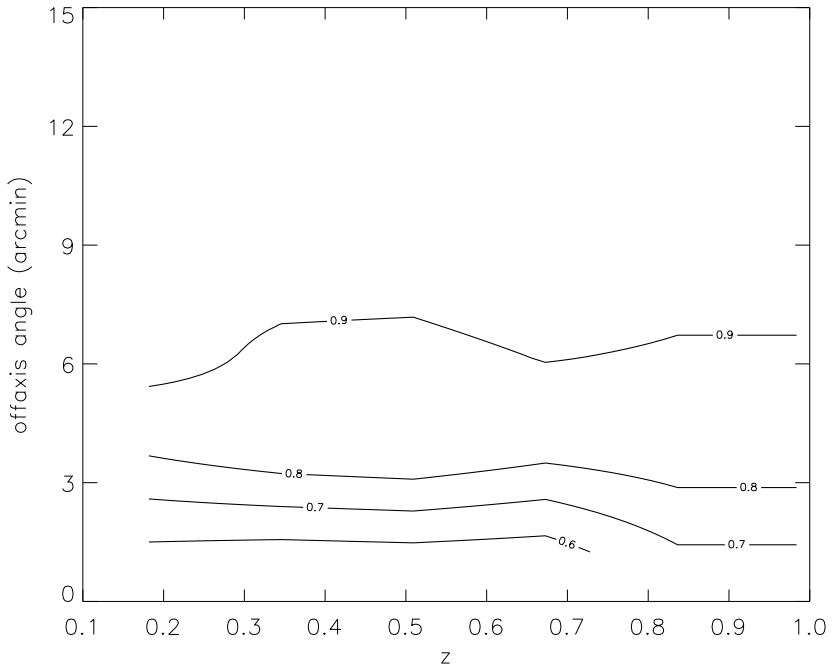


Figure 5.9: Variation of detection as a function of offaxis angle. Clusters have the following properties: $T = 3$keV, $L = 1.358 \times 10^{44}$erg s$^{-1}$, $r_c = 160$kpc, $\beta = 2/3$, in a $\Omega_\Lambda = 0.7, \Omega_m = 0.3$ cosmology. Results plotted for those objects with $> 500$ input counts.

## 5.4 XCS selection function: testing the dependence on assumed profile properties

Note that in this section we have now fixed the cosmology to $\Omega_\Lambda = 0.7$, $\Omega_m = 0.3$.
The XCS selection function as discussed in Section 5.2, is an oversimplification, i.e $\beta$ is not always 2/3, $r_c$ is not always 160 kpc, and clusters are not spherically symmetric. The underlying cluster population is not one with uniform properties. It is well known that clusters of galaxies have a range of morphologies, with core radii varying from a few tens of kpc, to a few hundred kpc and $\beta$ values varying generally between 0.45 and 0.85 (eg. Reiprich and Böhringer (2002); Ota and Mitsuda (2004); Maughan et al. (2008)). As other authors have rightly shown (Adami et al., 2000; Burenin et al., 2007) (see Section 5.1), it is important that we are able to quantify the effect that these variations in the population have on the selection function of a survey. The potential for knock-on effects onto other aspects of survey science is significant, and this should not be ignored. This was correctly noted by the referee of Sahlén et al. (2009), and held up the publishing for 6 months while these effects were quantified.

In the following section we shall discuss the impact of our morphological assumptions on the selection function. We will begin by analysing each of the important morphological parameters in turn, and then discuss them in combination. For the purposes of this section we have assumed an $L - T$ relation of the form given by Arnaud and Evrard (1999). Doing this enables us to isolate the effect of varying single parameters without including unnecessarily unrealistic objects. We have only simulated 3keV clusters as these are expected to best represent the average cluster population at a given redshift (M. Sahlen, private communication).

### 5.4.1 Core radius

As noted above there is a wide range of core radii seen in the observed population, for example if we look at two nearby clusters, Coma has a core radius of about 400 kpc, and Perseus has a core radius of about 50 kpc, the majority of clusters have core radii values that fall within these two extremes (eg. Jones and Forman (1999)). To understand how these variations in core radius effect the ability of XAPA to detect such objects, we have simulated a set of clusters with $r_c$ changing from 50kpc to 400kpc in steps of 50, the results of which can be seen in Figure 5.10.

Figure 5.10 demonstrates that XCS is able to detect objects with a wide range of physical sizes. The peak sensitivity across the majority of the redshift range is 100kpc $< r_c <$ 150 kpc. The relative change in detectability with respect to our assumed value (160kpc) in a range $\pm$100kpc is $\sim 10\%$ at $z = 0.1 : 0.2$, at higher redshifts this value can go up to $30 - 40\%$. However this simple plot does not take into account two key factors that occur

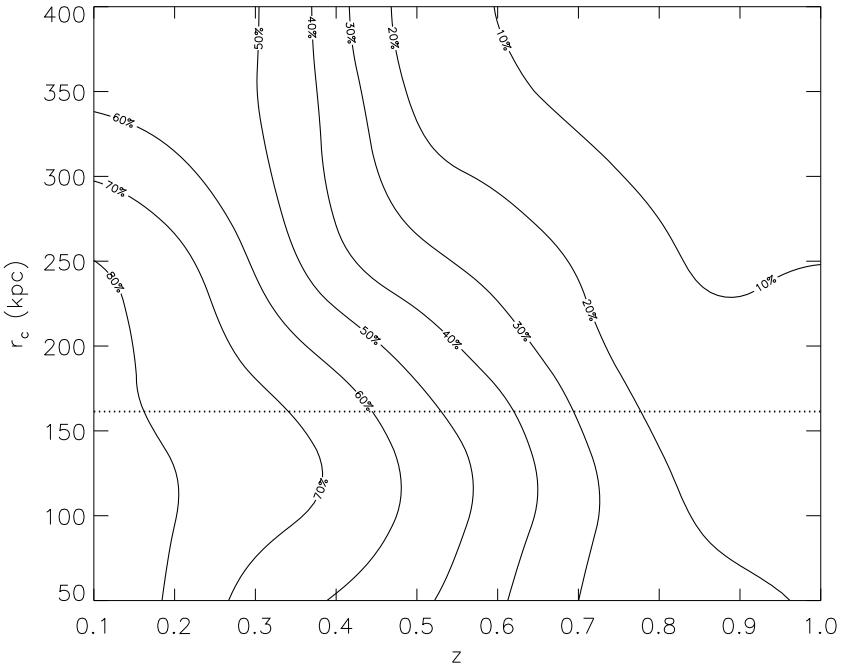


Figure 5.10: XCS StatSam detection and classification efficiency for 3keV clusters as a function of physical core radius and redshift. All clusters have $\beta = 2/3$. The dotted line represents the constant value assumed in the standard XCS selection function calculations.

as these objects are moved to higher redshifts. The angular core radius drops rapidly with redshift, meaning that a 400 kpc core at $z \sim 0.3$ has approximately the same angular size as a 160 kpc core at $z \sim 0.1$. Also the number of counts received from any object will decrease with increasing redshift. With this in mind it is perhaps better to compare detection of objects as a function of their angular core radius and number of counts (see Figure 5.12), as this is actually what the algorithms 'see'. To aid comparsion between Figures 5.10 and 5.12, Figure 5.11 shows the scaling of physical size with redshift in a $\Omega_m = 0.3, \Omega_\Lambda = 0.7$ cosmology. Figure 5.12 shows that, for objects with 500 counts or more, XCS detects $> 70\%$ of all objects in the range $10'' < r_c < 40''$. A comparison of Figure 5.12 with Figure 5.11 shows that this angular range encompasses the expected size of the majority of clusters over a significant redshift range. At small core radii a lower percentage of objects are correctly classified by XAPA, the objects are often detected but are not RECOVERED, i.e they are incorrectly classified as pointlike, or flagged as described in Section 3.3.3 (see Figure 5.13)

### 5.4.2 Profile slope

When a King profile is fit to observed surface brightness profiles, samples of clusters also show significant variation in values of $\beta$. In light of this we have simulated objects covering the range $0.4 < \beta < 0.8$. Figure 5.14 shows how this variation affects detection in the

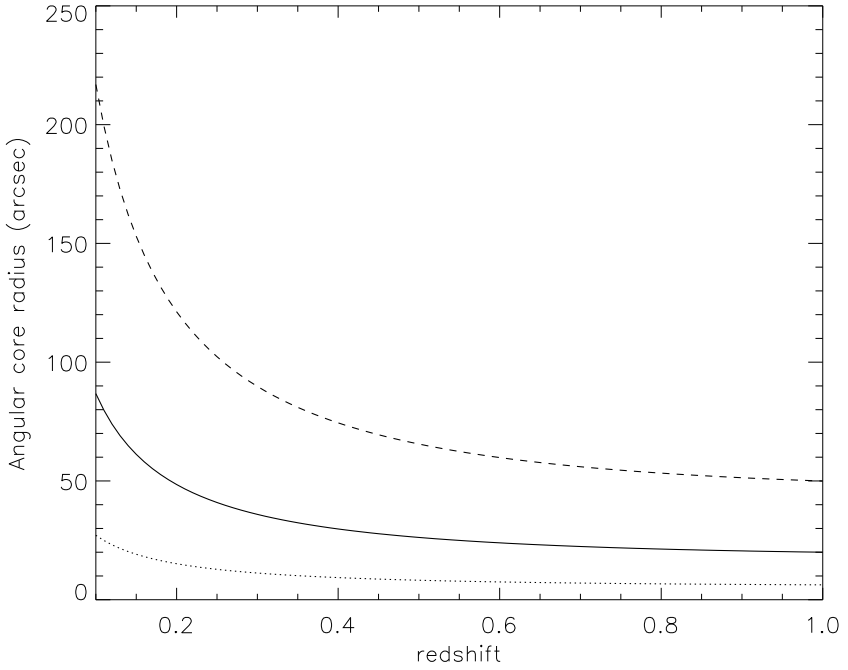


Figure 5.11: Angular core radius as a function of redshift shown for objects with a physical core radius of 50kpc (dotted line), 160kpc (Solid line), and 400kpc (Dashed line), in a $\Omega_m = 0.3, \Omega_\Lambda = 0.7$ cosmology.

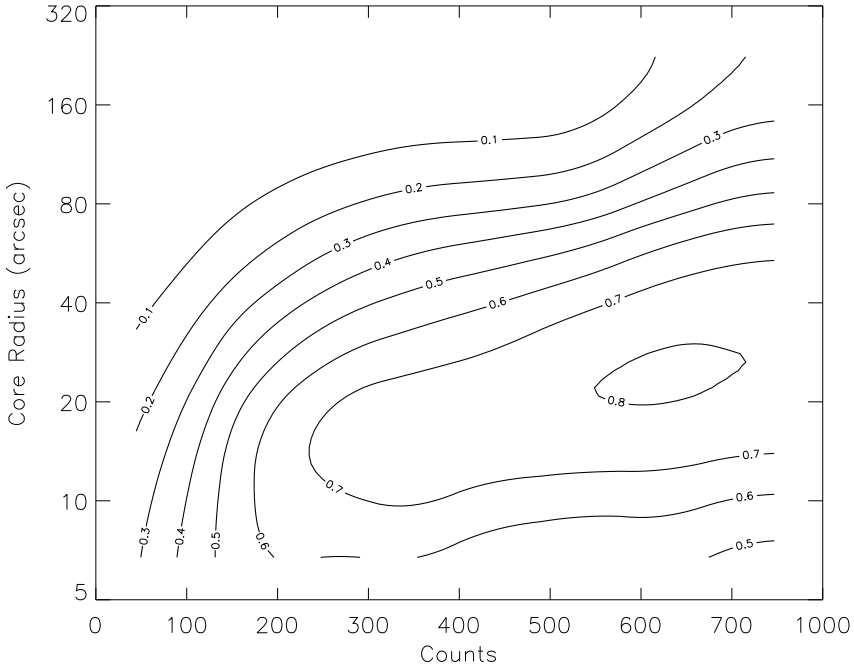


Figure 5.12: XCS StatSam RECOVERY efficiency for 3keV clusters as a function of angular core radius and input source counts.

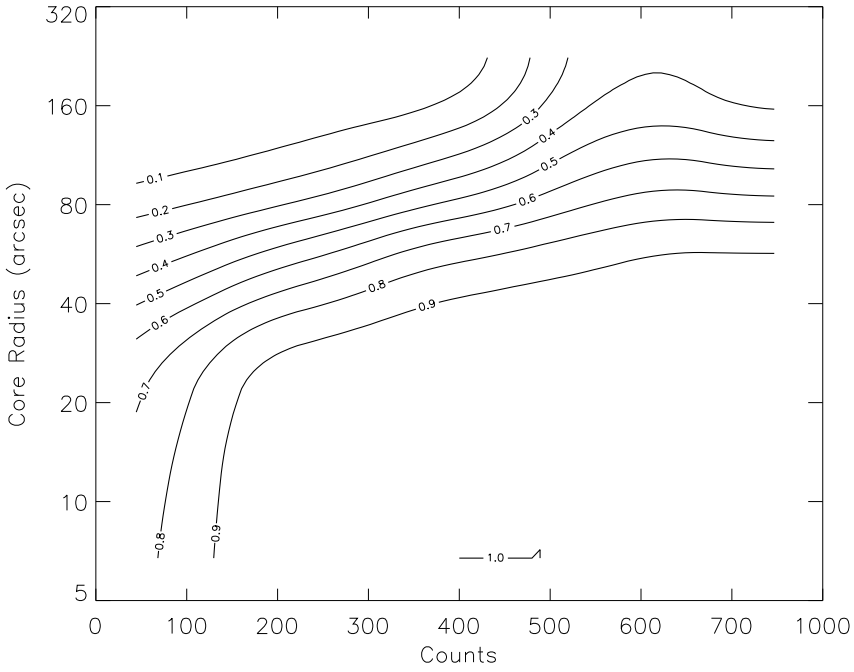


Figure 5.13: XCS StatSam detection efficiency for 3keV clusters as a function of angular core radius and input source counts. Same as Figure 5.12 but without the necessity for extent classification, i.e these sources have been detected but not RECOVERED.

XCS, for objects with $> 500$ counts. As seen in the figure, variations in $\beta$ in the range $0.55 < \beta < 0.75$ only alter the detection efficiency by $\sim 10\%$. There is a significant drop in XAPA's ability to detect and classify objects with a $\beta$ value below this range at redshifts of $z < 0.6$. Although it has been noted that objects that fall in this low $\beta$ range are rare/unrealistic, such low values are most likely artifacts of fitting a single $\beta$ model to clusters with strong cool cores and are in fact not found if the cores are properly excluded from the fit (Vikhlinin et al., 1999).

### 5.4.3 Core radius and profile slope

As is clear from the preceding sub-sections, XCS's cluster detection efficiency drops off with increasing core radius and also decreasing values of $\beta$. Both increasing $r_c$ and decreasing $\beta$ cause a spreading out of the cluster flux, as a result of which there will be some degeneracy in these two parameters as far as detection is concerned. The poor detectability of an object with a large core radius can be offset somewhat by a steeper slope in the brightness profile, and likewise the combination of a large core plus a small value of $\beta$ could make an object very hard to detect even at low redshift. For example a $\beta = 2/3$ cluster with a 400kpc core at $z = 0.1$ is detected in $\sim 55\%$ of the simulations, however if this object were to have a slope of $\beta = 0.8$ the detection would be $> 70\%$, and $\beta = 0.5$ would result in $< 35\%$ being recovered (see Figure 5.15). There are combinations of $r_c$ and $\beta$ that can

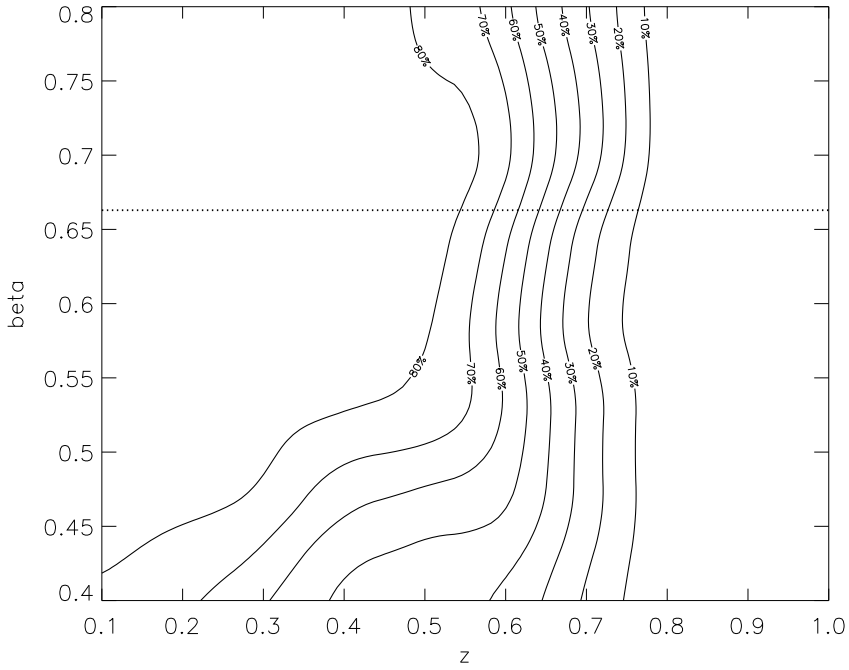


Figure 5.14: XCS StatSam detection and classification efficiency as a function of $\beta$ and redshift. All clusters have $r_c = 160$kpc. The dotted line represents the constant value assumed in the standard XCS selection function calculations.

cause a potential relative change in detection of 100% with respect to another combination, but these large changes are from extreme ends of the observed ranges and so are quite unlikely.

### 5.4.4 Ellipticity

In the preceding sections we have only considered surface brightness profiles that are spherically symmetric. However in reality this is often not the case. Here we define the ellipticity of an object such that a perfect circle has $e = 0.0$, see Equation 5.1

$$e = 1 - (\text{minor axis}/\text{major axis}) \tag{5.1}$$

Using this definition of ellipticity, clusters in the sample analyised by Mohr et al. (1995) fall in the range $0.0 < e < 0.6$. Figure 5.16 demonstrates that XAPA is relatively insensitive to variation in ellipticity within this range. There is an indication that highly elliptical objects may be easier to detect at $z \sim 1.0$ than spherically symmetrical ones, but the change in detection efficency is not significant enough to enable any conclusion to be drawn. Figure 5.16 highlights the need for the ellipticity cut on the DR3 StatSam (see Section 4.6).

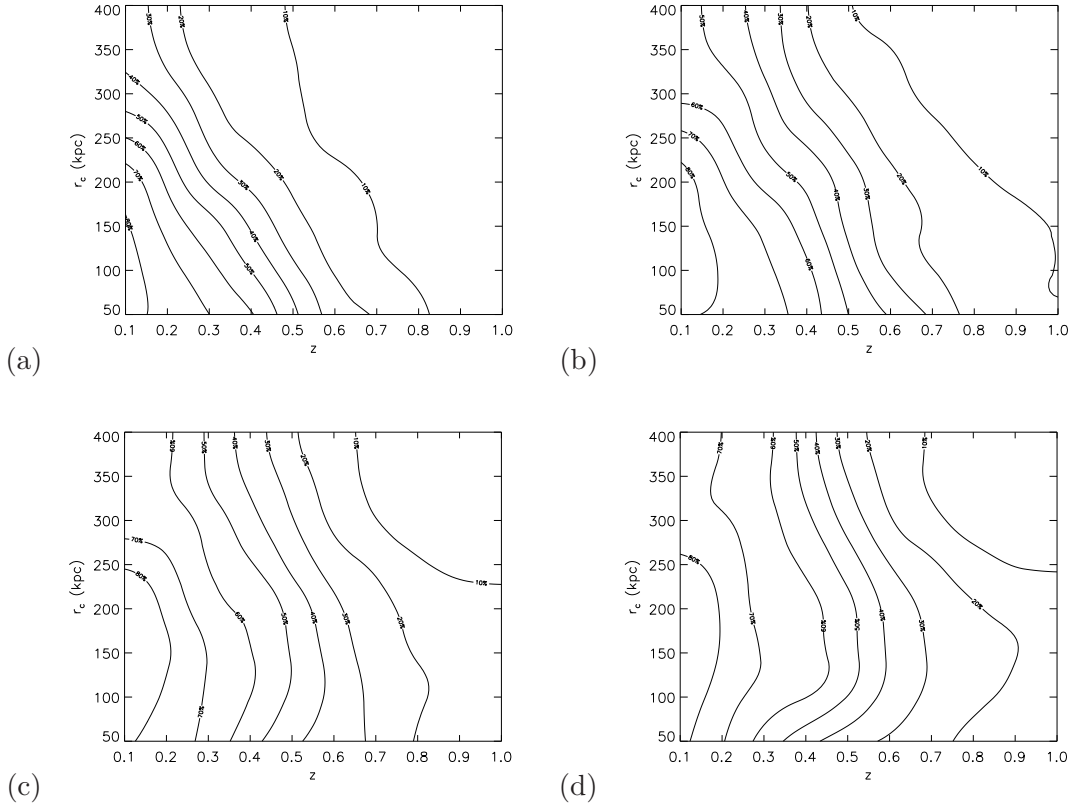


Figure 5.15: XCS StatSam detection and classification efficiency for $e = 0.0$, 3keV clusters as a function of $r_c$ and redshift, for different values of $\beta$. Fig(5.15(a)): $\beta = 0.5$. Fig(5.15(b)): $\beta = 0.6$. Fig(5.15(c)): $\beta = 0.7$. Fig(5.15(d)): $\beta = 0.8$.

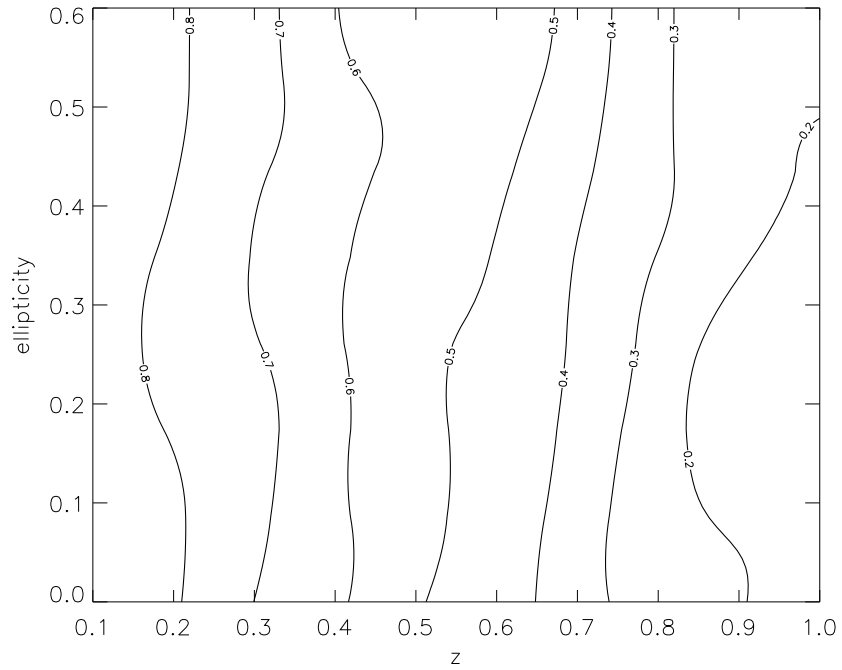


Figure 5.16: XCS StatSam detection and classification efficiency as a function of Ellipticity and redshift. All clusters have $r_c = 160kpc$ and $\beta = 2/3$.

## 5.5 Using the selection function to correct for selection effects

When using the cluster abundance to measure cosmological parameters, the selection function is a vital factor that must be understood. Cosmology enters into the prediction of cluster numbers as a function of temperature and redshift through the selection function, the cluster scaling relations, and the mass dispersion. The cluster scaling relations and the mass dispersion can be used to predict the propeties of the underlying cluster sample, however relating this to the observed sample produced by any given survey requires knowledge of the selection function. Once the dependance of the cluster abundance on these factors is understood, it is possible to determine the likelihood of any observed catalogue of clusters given an assumed cosmology (see Sahlén et al. (2009) for further discussion).

We expect the XCS $L-T$ relation to be self-calibrated at the same time as the cosmological analysis, a full description of this will be given in future XCS publications. When attempting to just measure cluster scaling relations the selection function must be used in much the same way as for cosmology. Pacaud et al. (2007) demonstrate how this can be done. Studies of cluster scaling relations generally consider redshift evolution of the form $F(z) = (1+z)^{\alpha}$. Pacaud et al. (2007) create a probability distribution function (PDF), which models the distribution of clusters around the mean scaling relation. This PDF is then multiplied by the selection function (the probability of detection, given $L$, $T$ and $z$) and is used to estimate the likelihood of their data given a $F(z)$ model. This is the first demonstration of how large an impact the selection function has on scaling relation studies. The results of Pacaud et al. (2007) are discussed more in Section 6.3.7.

## 5.6 XCS selection function: a tool for future survey design

Using the methods applied in this chapter we are able investigate source detection in way that enables us to optimise future observations/surveys. Due to the nature of the XMM archive, there is an enormous amount of variation in the properties of the images. Of particular relevance is the variation of exposure time between observations (see Figure 5.17). A question one might ask is what is the optimum exposure time for cluster finding? This is not something that there is an intuitive answer to; a deeper exposure means more source counts, but too many photons can increase source confusion, and background effects must also be taken into account.

To address this another set of selection functions have been computed. This time the cosmology and profiles have been fixed. The Obsids are selected not at random but on the basis of their exposure times. This work is very relevant at the present time. XMM is approaching the end of its life cycle, and a lot of thought has gone into determining the best use of the remaining time. There are 3 main options being considered, deep narrow-angle

surveys, shallow wide-angle surveys (slew), or deep follow-up of known clusters (e.g from XCS). The effectiveness of the different time usage for serendipitous detection is assessed in this section. Some of this work has already been used in an XMM survey proposal by D. Alexander.

Figure 5.18 demonstrates the effect of exposure time on XCS's ability to detect and correctly classify input clusters (All clusters have $r_c = 160$kpc, $\beta = 2/3$, $e = 0.0$, and cover the full range of $L$ and $T$ as in Table 5.1). It can be seen in the figure that the increase in RECOVERY with exposure time is not significant beyond $\sim 30$ks. A comparison with Figure 5.19 shows that there is no increase in detection beyond $\sim 20$ks, and that any further increases are due to an increased ability to classify the objects as extended. Note that due to the creation of profiles covering a wide range in both $L$ and $T$, Figures 5.18 and 5.19 contain a large number of unrealistic objects and so do not represent the expected trend for the real XCS survey. They do however, demonstrate the effect of exposure time on detection and RECOVERY.

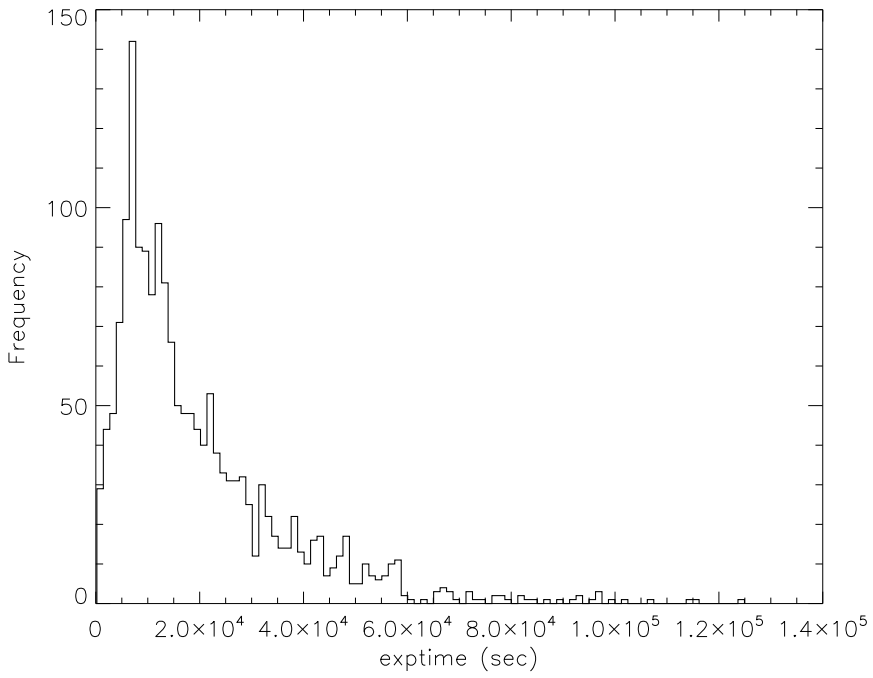


Figure 5.17: Distribution of XCS StatSam exposure times from the DR1 StatSam, see Section 3.6)

An important consideration point in cluster survey design is the question of area vs. depth, with a limited amount of XMM telescope time would it be better to take a few very deep observations or many more shorter exposure ones?

To address this we have combined the above selection functions featured in Figure 5.18 with the model $T > 2$ keV cluster catalogues presented in Sahlén et al. (2009), since he uses a mass function and observed scaling relations to predict actual (rather than observed)

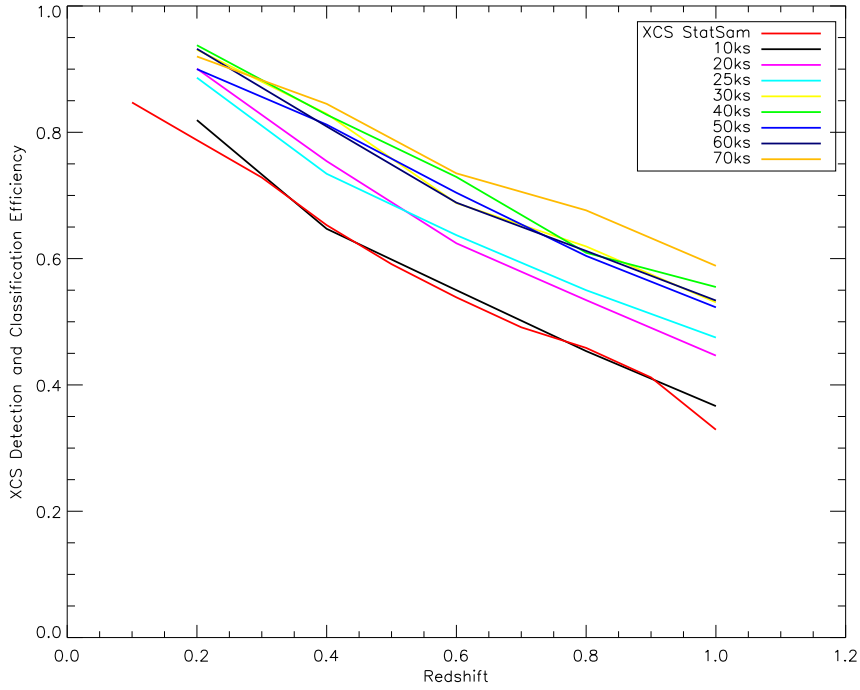


Figure 5.18: XCS detection and classification efficiency as a function of exposure time and redshift. All clusters have $r_c = 160kpc$, $\beta = 2/3$ and $e = 0.0$.

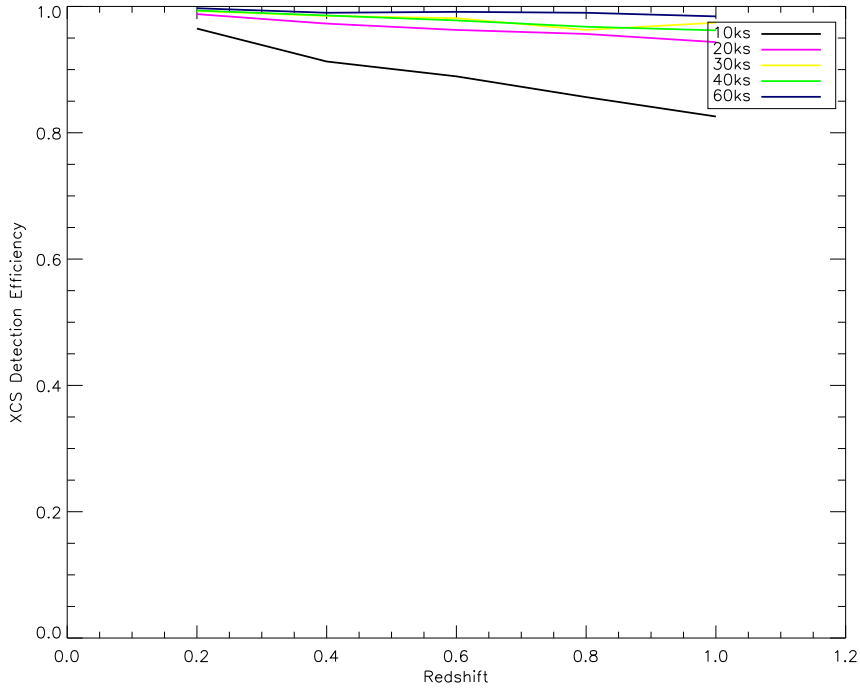


Figure 5.19: XCS detection efficiency as a function of exposure time and redshift. All clusters have $r_c = 160kpc$, $\beta = 2/3$ and $e = 0.0$. Same as fig 5.18 but without the necessity for extent classification.

number densities as a function of redshift. Figure 5.20 clearly shows the benefits of longer exposure times. At all redshifts a deeper survey (50ks), would detect many more clusters than an XCS type survey of the same area, at $z \sim 1.0$ the difference is as much as a factor of 3. However, how would a 10 deg$^2$ 50ks, i.e that proposed by D. Alexander, survey compare to XCS, when XCS makes use of all the data in the archive? Figure 5.21 shows that even with 100 deg$^2$ (already surpassed with DR1) of archival data, the detected number of clusters is significantly higher than the small, but much deeper, survey.

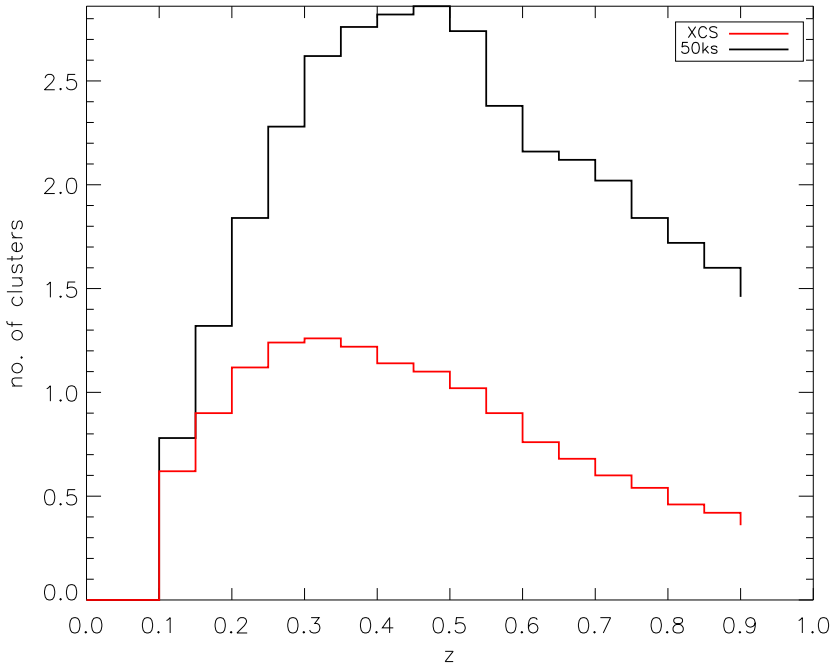


Figure 5.20: Expected cluster detections in 10 deg$^2$, the red line shows the expected number for a distribution of exposure times matching that in XCS, the black line is for a 50ks survey.

Despite not supplying a greater abundance of $T > 2$ keV clusters there are still reasons for proposing a small deep survey as a complement to the archive. Figures 5.22 and 5.23 show the difference in temperature distribution one would expect at low and high redshifts respectively. The most striking difference is that $\sim 4-5$ times more low temperature clusters would be found at higher redshifts in 50ks pointings, compared to the same area in XCS. For studies of scaling relation evolution this would be invaluable. One can expect the trend seen in Figures 5.22 and 5.23 to extend into the group regime ($T < 2$keV), meaning that a new narrow-deep XMM survey may beat XCS when it comes to group studies. At the time of writing we are unable to explore this potential, because Sahlen's mock catalogues are limited to $T > 2$keV. We are, therefore, looking into an alternative strategy that bootstraps from the measured XCS temperature relation.

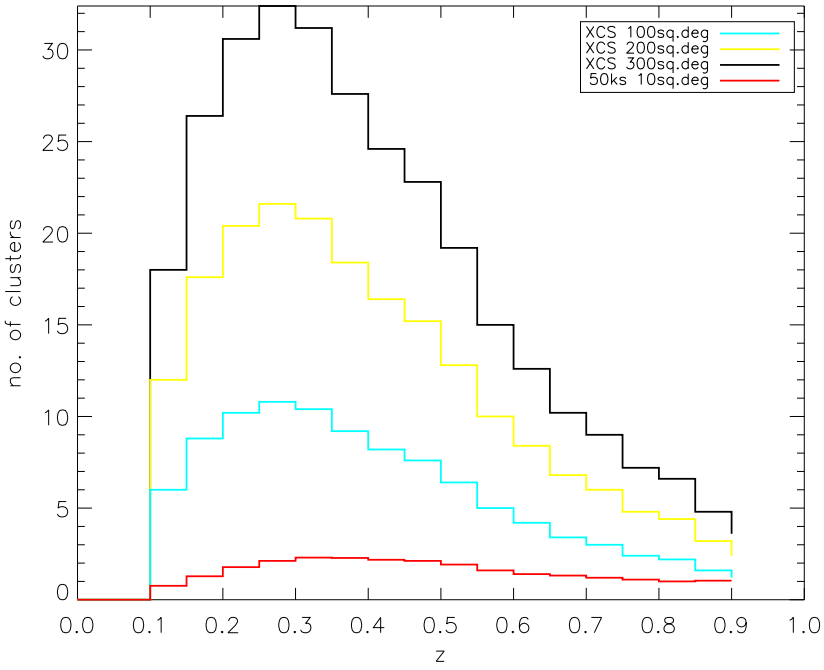


Figure 5.21: A comparision of expected cluster detections in a 10 deg$^2$ 50ks survey, to XCS with varying area coverage.

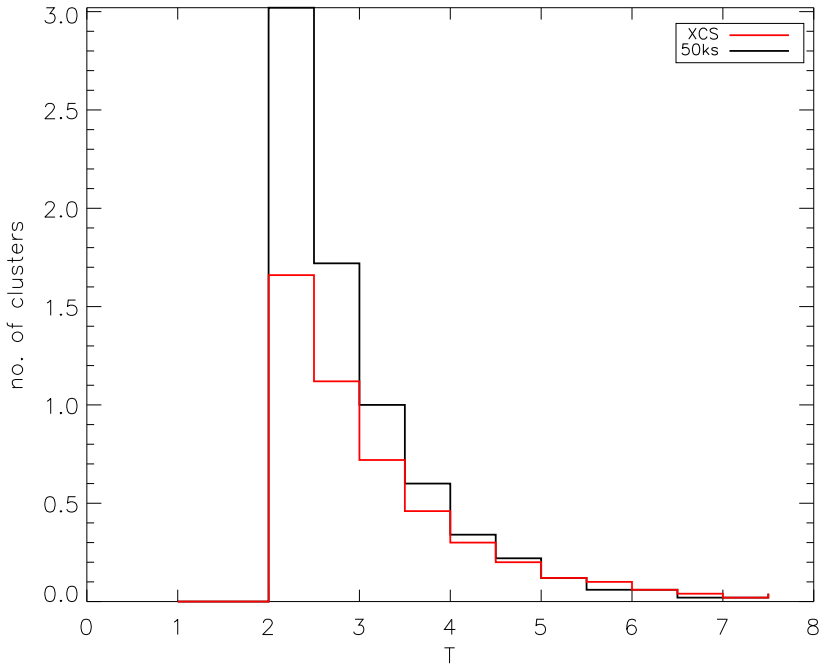


Figure 5.22: Expected cluster detections as a function of Temperature in 10 deg$^2$ at $z < 0.3$, the red line shows the expected number for a distribution of exposure times matching that in XCS, the black line is for a 50ks survey.

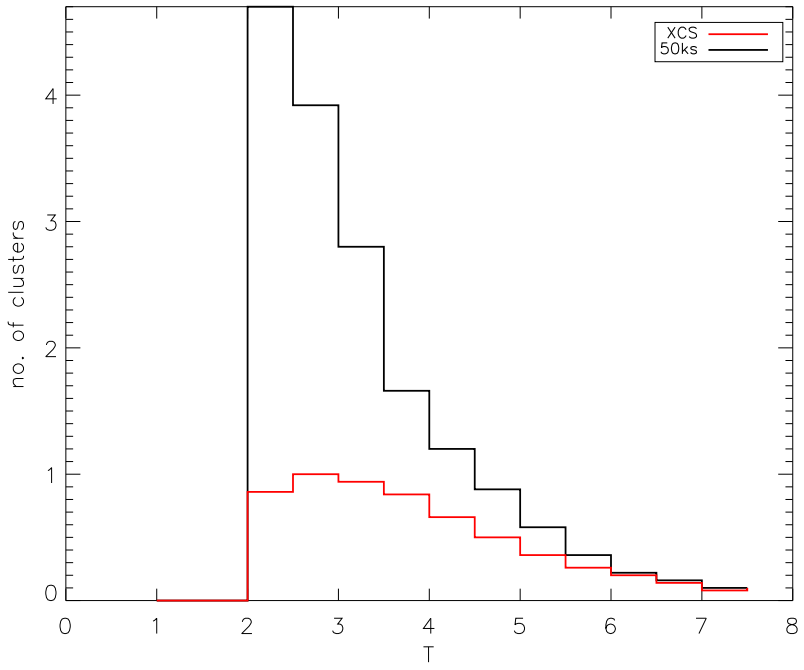


Figure 5.23: Same as Fig 5.22 but for $z < 0.7$.

## 5.7 Future work

### 5.7.1 Cosmology application

As seen in Sahlén et al. (2009), the final XCS sample will place competitive constraints on cosmological parameters. We expect to measure $\Omega_m$ to $\pm 0.03$ (and $\Omega_\Lambda$ to the same accuracy assuming flatness), and $\sigma_8$ to $\pm 0.05$.

The $k \neq 0$ selection function runs in this chapter are yet to be utilised, but could be used to further generalise the XCS cosmology constraints.

The current XCS cosmological analysis has been focused on $\Lambda$CDM cosmology, however it is preferable to generalise $\Lambda$ to include more dark energy models ($w < -1/3$). The ideal way of doing this is to sample the parameter space in terms of $d_L$, rather than ($\Omega_m$, $\Omega_\Lambda$ and $z$). While there is some overlap with the selection functions presented in this Chapter, a significant number of simulations still need to be run.

The parameters we plan to assess are as follows:

10 points in cluster temperature (2 to 10 keV in steps of 1 keV, plus 1.5 keV to quantify the level of contamination of the $T > 2$ keV range by lower mass systems);

10 points in cluster bolometric luminosity (0.05 to 10 logarithmically spaced) in units of

$h^{-2}10^{44}$ erg/s;

12 points in redshift (0.1 to 1.2 in steps of 0.1) for a fiducial ($\Omega_m = 0.3$, $\Omega_\Lambda = 0.7$) cosmology.

we will then sample either side of the fiducal $d_L$ by sampling 5 points in luminosity distance for each redshift point, as follows:

$\Delta d_L$ =-0.030 to 0.030 for $z$=0.1
$\Delta d_L$ =-0.055 to 0.055 for $z$=0.2
$\Delta d_L$ =-0.075 to 0.075 for $z$=0.3
$\Delta d_L$ =-0.090 to 0.090 for $z$=0.4
$\Delta d_L$ =-0.100 to 0.100 for $z$=0.5
$\Delta d_L$ = -0.110 to 0.110 for $z$=0.6
$\Delta d_L$ =-0.120 to 0.120 for $z$=0.7
$\Delta d_L$ =-0.130 to 0.130 for $z$=0.8
$\Delta d_L$ =-0.135 to 0.135 for $z$=0.9
$\Delta d_L$ =-0.140 to 0.140 for $z$=1.0
$\Delta d_L$ =-0.145 to 0.145 for $z$=1.1
$\Delta d_L$ =-0.150 to 0.150 for $z$=1.2

At present these selection functions are $\sim 20\%$ complete, and will take many months more to finish. Once complete we can assess XCS's ability to place constraints on dark energy models in a way similar to that which Sahlén et al. (2009) used to forecast the ΛCDM contraints.

### 5.7.2 Determining a statistical description of cluster profiles

E. Lloyd-Davies is currently measuring $r_c$'s and $\beta$'s for the XCS clusters. In combination with the work presented in this chapter, it will be possible to construct a statistical description of the likely morphology of the underlying sample. This will be a valuable resource for many areas of cluster science; some examples include optimising source detection algorithms, studying the departures from self-similarity and understanding the selection function of other surveys.

### 5.7.3 $L - T$ correction

It has been shown that when measuring evolution in the $L - T$ relation, selection effects must be corrected for (Pacaud et al., 2007). The work in this chapter will enable XCS to do this (See Section 6.4).

### 5.7.4 Group proposal?

In Section 5.6 we showed that a deep survey would detect more low-mass clusters at high redshift than the current archive. We plan to extend this to the group regeme. If the trend seen in Figure 5.23 continues down below 2keV, then a narrow survey of $>$ 50ks would be of tremendous value. Below 2keV systems do not scale in the same way as those considered in this chapter. To assess this properly we need a new set of ECF's for groups and we must consider the best type of profile to use in such a selection function.

## 5.8 Summary

The work presented in this chapter has demonstrated the way in which many variables can influence cluster detection.

The dependence of the selection function on cosmology enables cluster surveys to constrain cosmological parameters. The results presented and discussed in Section 5.3 enable the XCS to do just that, and were crucial for the production of Sahlén et al. (2009). The selection function used in Sahlén et al. (2009) assumed a fixed cluster profile, the impact of this assumption has been tested in Section 5.4. We see that $r_c$ in particular can strongly influence the detection of clusters; however the more counts a source has, the more this effect is reduced, and the impact on the XCS500 sample is small.

As discussed above, it is widely recognised that an understanding of a survey's selection function must be obtained before any strong conclusions can be drawn, either for cosmology or scaling relation studies. The simulations presented so far in this chapter further highlight this; in particular it is clear that the morphology of the population must be better understood before any naive selection function is applied.

In Section 5.6 we investigated the impact of exposure time on cluster detection. It was shown that in terms of cluster numbers, a shallower wide field survey would be preferable, and exposures greater than 30ks would not give substantial increases. However a 10deg$^2$, 50 ks survey would yield significantly greater numbers of low $T$ (and hence low mass) systems at high redshift.

# Chapter 6

# XCS Selection Function with Two-Dimensional Cluster Profiles from Hydrodynamic Simulations.

It is vital that the selection function of a cluster survey been known accurately before science studies (cosmology, scaling relations etc) be attempted. For the XCS we are forced to use simple, isothermal $\beta$ models (with fixed core radii and profile slopes) to explore how our selection function depends on the underlying cosmology. This is because the simplicity of the model allows the required number (hundreds of thousands) of detection tests to be made. However, as shown in the previous chapter, the inputs to the beta model can influence the derived selection function dramatically: reasonable adjustments to $r_c$ and $\beta$ can change the detection efficiency by a factor of 2. The application of a count cut to the XCS cluster catalogue (of 500 counts) mitigates this problem for cosmology studies in the short term. However applying such a cut means that the majority of XCS clusters could not be used for science applications (even after re-observation with XMM or IXO). So, in order to fully exploit XCS in future, it is important that the selection function be better understood at the low-count end. For this, we have explored a new approach to selection function calculations: the use of synthetic clusters produced by N-body SPH simulations. These synthetic clusters have many advantages over isothermal $\beta$ models because they encode the full structural properties of the clusters (cooling cores, sub structure, projected filaments, temperature gradients etc.). Only recently have simulation boxes been large enough to produce synthetic samples that fully explore the range of temperatures and redshifts seen in a real cluster survey. In this chapter, we present the first attempt to use the CLEF (Kay et al., 2007) synthetic cluster sample to determine the selection function of XCS (albeit under one assumed cosmological model).

In Section 6.3.1 we compare a sample CLEF selection function with an equivalent $\beta$ profile selection function. We do this to assess the overall reliability of the Chapter 5 selection

functions in comparison with a more realisic alternative. In Section 6.3.3 we assess XAPA's ability to detect clusters with cool cores. In Section 6.3.4 we assess XAPA's ability to detect clusters with centrally peaked surface brightness profiles. In Section 6.3.5 we assess XAPA's ability to detect clusters with various dynamical states. In Section 6.3.6 we determine the impact of the above on the XCS500.

## 6.1 Motivation

### 6.1.1 Selection function studies to date

In Chapter 5, all clusters were represented by smooth, isothermal $\beta$ profiles. Although this simplification allows a full coverage of the relevant parameters ($\Omega_m$, $\Omega_\Lambda$, $L$, $T$, $z$, $r_c$, $\beta$, $e$) it does lack realism. After all, real clusters are neither smooth in their surface brightness profile, nor are they isothermal; some clusters have cool cores, while others have a large amount of substructure. In efforts to include more realistic types of objects some authors have begun to use profiles of real clusters in their selection function studies, by scaling them to various redshifts. For example Burenin et al. (2007) use this method to give a comparision to their standard ($\beta$-model) selection function. This comparison gave them an indication of how large an effect departures from the $\beta$ model had on their calculated selection function. They concluded that using "re-observation" of known clusters should allow an understanding of the effects of substructure and cool cores on detection. There are however a few potential pitfalls that must be avoided before using this method alone to determine the final selection function of a survey: if drawn from an inhomogenous sample, or one without a known selection function, the use of real clusters may lead to using clusters that are inherently biased toward one property or another. In worst cases this could result in not having a selection function for some real but undetected objects, leading to an over estimation of completeness. Another complication lies with the re-scaling necessary to create a large enough test sample across a relevant redshift range. The scaling is non-trivial since many of the relationships between parameters used in the modelling of clusters are not clearly understood. $r_c$ for example should be expected to scale with cluster mass, as it is related to the size of the cluster, thus due to the M-L relation, more luminous clusters should have different sized cores to less luminous clusters. Many authors have attempted to measure the $r_c - T$, relation with little agreement being seen between the various studies (Ota and Mitsuda (2004), Sanderson and Ponman (2003)). The $\beta - T$ relation is also not well understood although $\beta$ is seen to drop with temperature. Until these relations are well constrained it is very difficult to properly construct a realistic sample with which to test the selection function of a survey using re-observations of a limited set of input clusters.

### 6.1.2 Alternative approach

With recent developments in the area of numerical simulations we are presented with an alternative to the above approaches. Many simulations now exist that are able to both reproduce the observed scaling relations, and also produce samples of clusters with a wide range of morphologies similar to that seen in the observed population (e.g. Kay et al. (2007), Gazzola and Pearce (2007)). Some authors have also created 'observational' data for their simulated clusters in order to compare them to real cluster data, including both images and spectra. This work 'observing' simulated clusters is akin to pointed, follow-up analysis of the clusters (e.g. Cheng et al. (2005), Henning et al. (2009), Ameglio et al. (2009)). However the samples now being generated in these simulations are in fact large enough that we can also utilize them for a statistical study of detection biases.

Some members and affiliates of XCS are actively involved in cosmological simulations and so have provided us with emission measure profiles from the CLEF (Kay et al., 2007) simulation for use in this work.

## 6.2 The CLEF Cosmological Simulation

This section will give a description of the sample of clusters drawn from CLEF. The text in this section has been edited from Kay et al. (2007) (hereafter KAY07), with minor textual alterations and some additional infomation to suit the context. Before we do this it is necessary to define a few terms used in the description.

### 6.2.1 Definition of terms

- **Spectroscopic-like temperature.** Theoretical models of X-ray clusters commonly use an emission-weighted temperature to estimate the temperature of a cluster. This involves weighting the temperature contribution from each particle in favour or hotter, denser particles. Mazzotta et al. (2004) applied the same methods used by observers to measure the spectroscopic temperature of simulated clusters, and found that it was always lower than this emission-weighted estimator. They propose a Spectroscopic-like temperature ($T_{sl}$) estimator that weights the particle contributions in favour of cooler, denser particles. This estimator more accurately matches the temperatures measured observationally.

- **R500.** The virial radius of a gravitationally bound object, such as a cluster of galaxies, is the radius of the sphere within which the virial theorem holds. This radius is observationally difficult to determine, and so a more easily defined value is commonly used. This alternative refers to objects in terms of their overdensity with respect to the critical value ($\rho_c(z)$). The radius at which the overdensity has a value

of $\rho(z)/\rho_c(z) = 500$ is commonly used in cluster studies as it roughly corresponds to the smallest density contrast accessible to the deepest X-ray observations. This radius is called R500 and the mass enclosed within is called M500.

### 6.2.2 An overview of CLEF

The CLEF simulation (Kay et al., 2005) is a large N-body SPH (Smoothed Particle Hydrodynamic) simulation of the ΛCDM cosmology with radiative cooling, star formation, and feedback. The simulation contains $2 \times 428^3$ particales within a $200h^{-1}$Mpc comoving box, half of which are dark matter ($m_{dark} = 7.1 \times 10^9\ h^{-1}M_\odot$), and half baryonic gas ($m_{gas} = 1.4 \times 10^9\, h^{-1}M_\odot$). The intitial conditions were evolved to $z = 0$ using a version of GADGET2 (Springel, 2005), allowing any gas with $T > 10^4$K to cool radiatively assuming a plasma of $Z = 0.3Z_\odot$. The authors mimic feedback from galactic outflows in such a way that reproduces the observed excess entropy (see Section 1.3.4) in groups/clusters. Cooled gas with an overdensity $\delta > 100$, $n_H > 10^{-3}\text{cm}^{-3}$,and $T < 12,000$K is identified as starforming, $\sim 10\%$ of the cooled gas particles are reheated and given an entropy of $S = 1000\text{keV cm}^2$ , the rest is converted to collisionless star particles. The reheated gas has a much higher thermal energy than the viral temperature of typical haloes, causing the gas to be redistributed through viscous interactions and shocks.

### 6.2.3 The CLEF cluster sample

The sample of clusters drawn from CLEF (KAY07) is one of the largest to come from a single simulation, with nearly one hundred clusters ($KT > 2$keV) at z=0 and sixty at z=1. Figure 6.1 illustrates spectroscopic temperature maps with surface brightness contours of the 5 most massive clusters at $z = 0.0$ and $z = 1.0$. There is a large amount of temperature stucture within the CLEF clusters, particularly cold spots due to cool, low-entropy gas trapped within infalling sub-clusters. The intensity scale in Figure 6.1 is defined by the minimum and maximum temperature; the dynamic range is typically an order of magnitude ($T_{max}/T_{min}$), with maximum temperatures being around twice that of the mean. This temperature structure is also reflected in the surface brightness maps (see Section 6.2.4), as seen in real clusters (e.g. The famous 'Bullet Cluster', Figure 6.2).

In the rest of this section we will look at some of the key parameters used by KAY07 to describe the features of the CLEF sample, and in Section 6.3.1 we will discuss why this is relevant and useful to XCS.

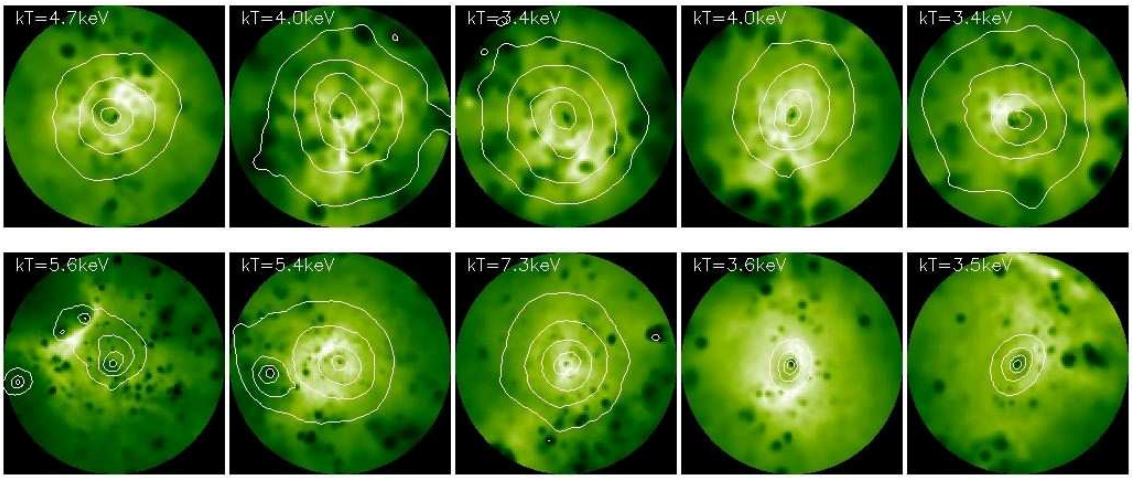


Figure 6.1: Figure 2 and caption from Kay et al. (2007). *"Spectroscopic-like temperature maps of the 5 most massive clusters (in order of decreasing mass, left to right) at z = 1 (top panels) and z = 0 (bottom panels). The spectroscopic-like temperature is given in each panel. Surface-brightness contours (normalised to the maximum value) are overlaid; adjacent contours correspond to a difference in surface brightness of a factor of 4. Images are centred on the maximum surface-brightness pixel and are shown out to R500."*

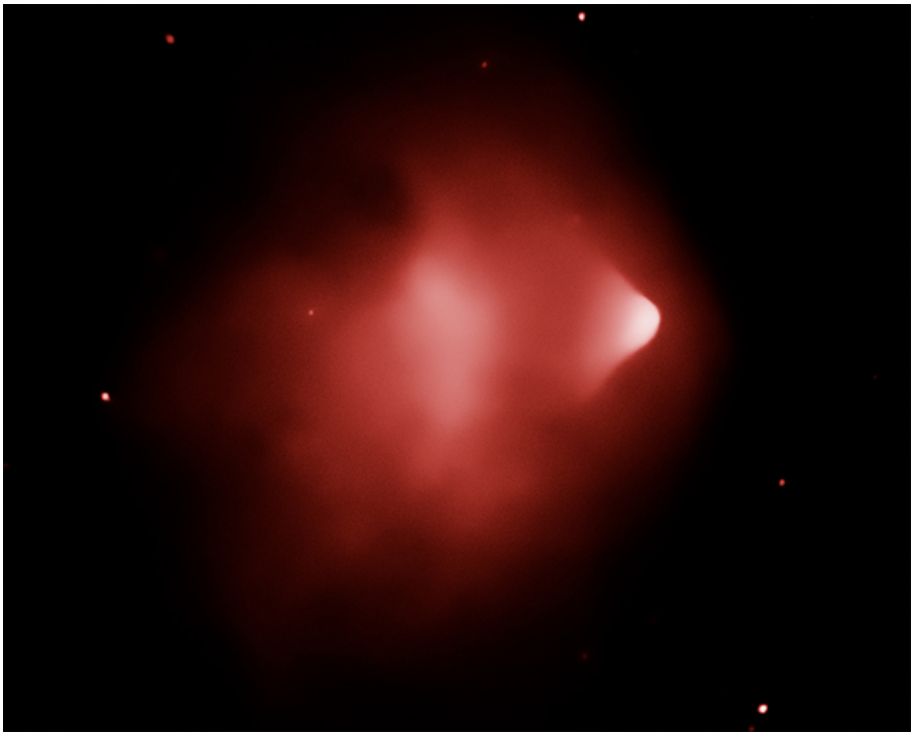

Figure 6.2: A Chandra X-ray image of the 'Bullet Cluster' 1E 0657-56. Image credit: NASA/CXC/CfA/M.Markevitch et al.

### 6.2.4 Substructure

As seen in Figure 6.3 there is a varied amount of substructure in the CLEF clusters. KAY07 quantify this using a centroid shift method to measure substructure in their clusters surface brightness maps.

$$S_X = \frac{R_{\Sigma,max} - R_{\Sigma,cen}}{R_{500}} \tag{6.1}$$

where $R_{\Sigma,max}$ is the position of the pixel with maximum surface brightness (taken to be the centre of the cluster) and $R_{\Sigma,cen}$ is the surface-brightness centroid. The authors have split the sample into regular ($S_X \leq 0.1$) and irregular ($S_X > 0.1$) clusters. This division is somewhat arbitrary but does allow an easy way of comparing the most disturbed clusters with the rest of the sample. Figure 6.4 shows the distribution of $S_X$ within the cluster sample as a function of temperature. Figure 6.3 shows surface brightness maps of clusters with both high and low $S_X$ values.

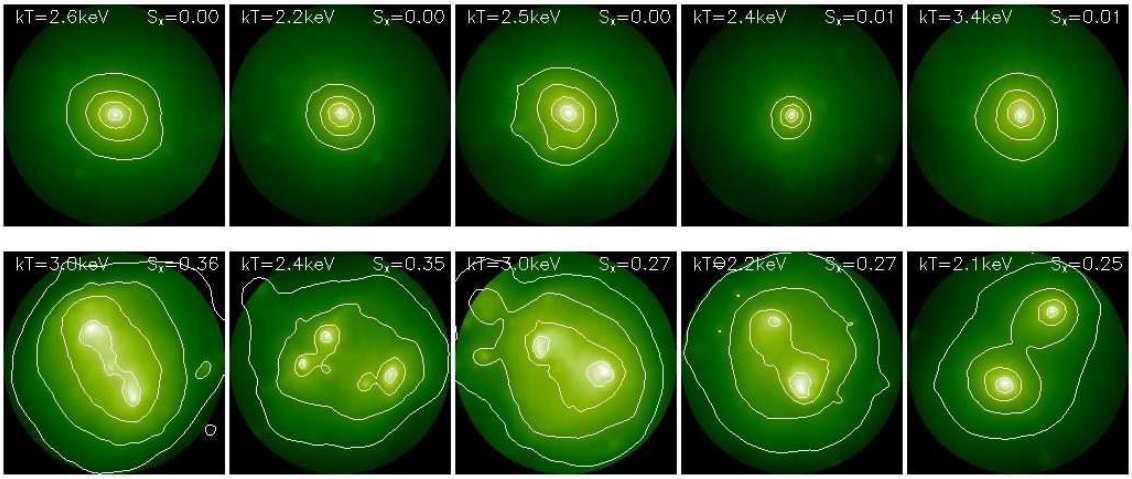


Figure 6.3: Figure 6 and caption from Kay et al. (2007). *" Bolometric surface-brightness maps of the 5 clusters with the lowest (top panels) and 5 with the highest (bottom panels) substructure statistic ($S_X$) at $z = 0$. In this case, clusters are centred on the surface-brightness centroid."*

### 6.2.5 Core structure parameters

As seen from the temperature profiles shown in Figure 6.5, the majority of clusters from CLEF have cool cores. Cool cores result in centrally peaked surface brightness profiles (see Figure 6.6). In order to quantify the strength of the cores KAY07 have defined two parameters, $f_T$ and $f_L$.

$$f_T = \frac{T_{sl}(< R_1)}{T_{sl}(R_1 \leq R \leq R_2)} \tag{6.2}$$

$$f_L = \frac{L_{bol}(< R_1)}{L_{bol}(R_3)} \tag{6.3}$$

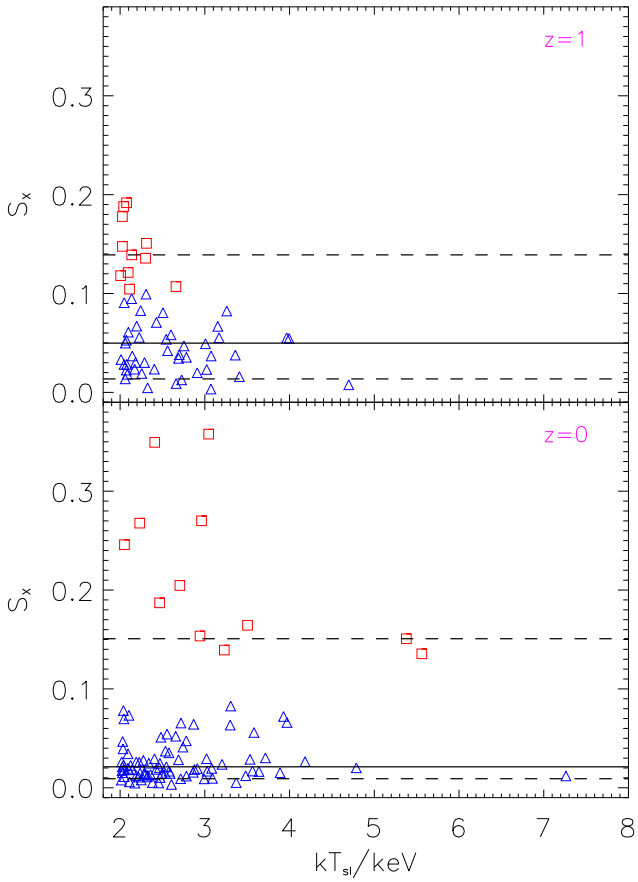


Figure 6.4: Figure 5 and caption from Kay et al. (2007). *"Substructure statistic, $S_X$, versus spectroscopic-like temperature for clusters at $z = 1$ and $z = 0$. Triangles illustrate regular clusters with $S_X \leq 0.1$ and squares irregular clusters with $S_X > 0.1$. The solid horizontal line is the median $S_X$ and the dashed lines the 10 and 90 percentiles."*

where $[R_1, R_2, R_3] = [0.1, 0.3, 1.0]R_{500}$. $R_1$ approximately defines the radius where the temperature profile stops rising, $R_1$ and $R_2$ approximately define the (maximum) temperature plateau, and $R_3$ is the outer radius of the cluster. Given these definitions $f_T$ measures the ratio of the core the maximum temperature of the cluster, i.e a lower $f_T$ value indicates a cooler core. $f_L$ measures the fraction of bolometric luminosity coming from the core, clusters with the highest core surface brightness having the highest $f_L$ values. The distribution in the two parameters can be seen in Figure 6.7, as the Figure shows the median $f_T$ increases with redshift, and $f_L$ decreases, i.e. the cluster cores are cooler and more X-ray concentrated at lower redshift.

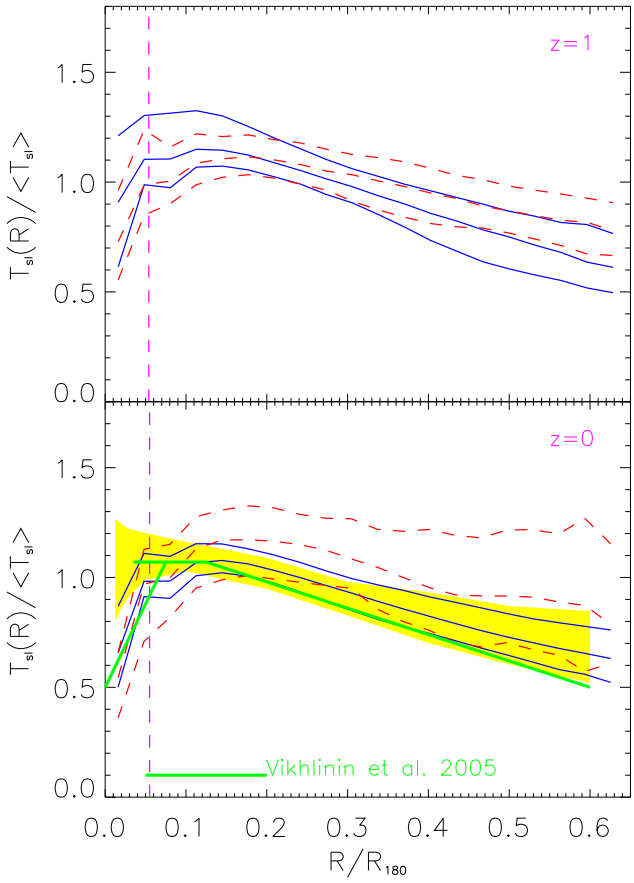


Figure 6.5: Figure 7 and caption from Kay et al. (2007). *"Scaled projected spectroscopic-like temperature profiles at $z = 1$ and $z = 0$. Solid curves are median and 10/90 percentiles for regular clusters, and dashed curves for irregular clusters. The vertical dashed line illustrates the median scaled softening radius (i.e. where the gravitational force becomes softer than Newtonian). The thick solid lines (with zero and negative gradient) are fits to the average observed temperature profile of cool core clusters, as measured by Vikhlinin et al. (2005); the inner line is a rough fit to their data to illustrate the cool core. The shaded region encloses the mean and $1\sigma$ standard deviation temperature profile for a representative sample of nearby clusters by Pratt et al. (2007)."*

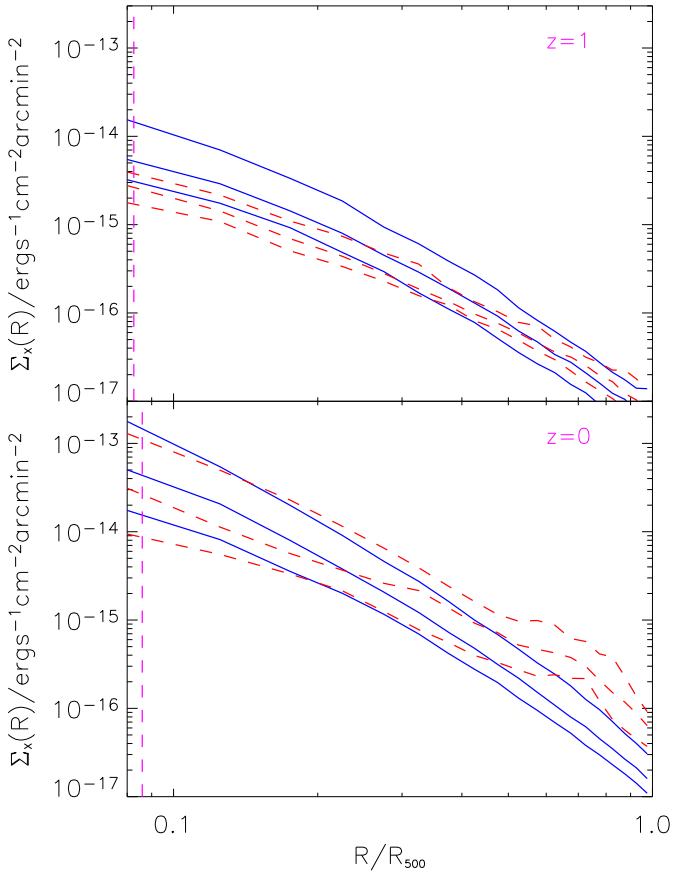


Figure 6.6: Figure 8 and caption from Kay et al. (2007). *"Bolometric surface-brightness profiles at $z = 1$ and $z = 0$. Again, solid curves are median and 10/90 percentile values for regular clusters, and dashed curves for irregular clusters. The vertical dashed line marks the median force resolution, $2.8\epsilon/R500$."*

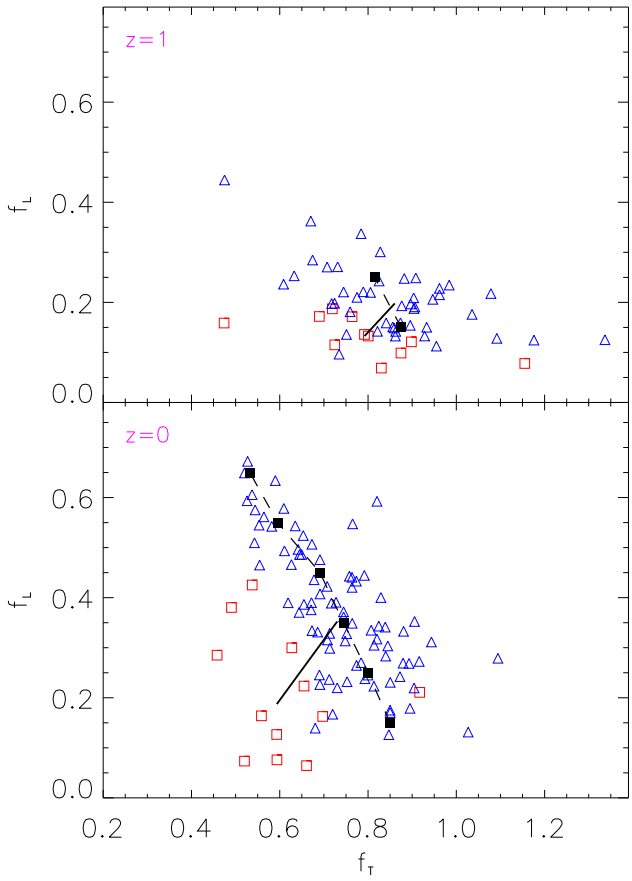


Figure 6.7: Figure 11 and caption from Kay et al. (2007). *"X-ray concentration parameter, $f_L$, versus core-to-maximum temperature ratio, $f_T$, for clusters at $z = 1$ and $z = 0$. Triangles are regular clusters and squares irregular clusters, with their median ($f_T$, $f_L$) co-ordinates connected by a solid line. Solid squares, joined by dashed lines, illustrate the median $f_T$ at fixed intervals of* 0.1 *in $f_L$, for regular clusters."*

## 6.3 XCS selection function: testing the dependence on the core properties and substructure

### 6.3.1 Method

#### Inputting CLEF clusters into XMM images

The process by which the CLEF profiles are input into the XMM images is basically the same as described in Section 5.2, aside from the creation of the fake cluster profile. Note that for calculating the total count rates we use the mean cluster temperature of the CLEF clusters, as opposed to using the varying temperature profile; these counts are then distributed using the emission measure profile (see Onuora et al. (2003) for details) as a probability map. The emission measure maps fully encode variations in temperature and density and so this approach will preserve any substructure in the surface brightness and also the presence of any central peak caused by a cool core. The rest of the process follows the steps outlined in Section 5.2. The initial set of selection function runs using the CLEF clusters proceeded as follows: Cluster profiles were randomly drawn from the CLEF sample and run through the detection pipelines, the process was repeated until each CLEF cluster ($T_{sl} > 2$keV) had been 'observed' a sufficient number of times to determine reliable mean detection efficencies. The number of clusters in the selection function run is the dominant factor in the size of the errors. To reduce the size of the error bars seen previously (See e.g. Figure 5.3), we ran this until at least 150 input clusters were present in each redshift bin; this number was increased to 200 for the two most distant bins. This should more clearly distinguish any potential differences in detection between the CLEF sample and the $\beta$ clusters.

#### Direct comparison with standard $\beta$ profiles

Using the data from the CLEF selection function run, we ran a duplicate set of simulations replacing each CLEF cluster with a $\beta$ profile of the type used in the standard XCS selection function (i.e $\beta = 2/3$, $r_c = 160$kpc). The second run exactly copied the first in terms of cluster placement, luminosities and temperatures, thus enabling an understanding of the impact of the differing morphology between the two samples.

### 6.3.2 Comparison of the two selection function methods

Figure 6.8 shows the results of this initial test with $1\sigma$ error bars. At low redshift the difference in RECOVERY efficiency is relatively small (at $z = 0.1$, the change when using the CLEF clusters is 91% to 85%, a relative drop of $\sim 7\%$), however at high redshift the

differences become more important, at $z = 1.0$ XCS would detect $\sim 60\%$ more clusters (11% vs 17.5%) if the underlying sample was more CLEF-like than the isothermal $\beta$ assumption made previously. The reasons for this difference in RECOVERY will be addressed in the following subsections. Within Figure 6.8 there appears to either be a slight drop in RECOVERY of the $\beta$ profile clusters at $z = 0.6$, or a slight increase in RECOVERY at $z = 0.7$, this is most likely statistical noise in the data. Overall, the two methods are very similar, and are within the statistical errors. This similarity justifies the use of the $\beta$ profiles in Sahlén et al. (2009).

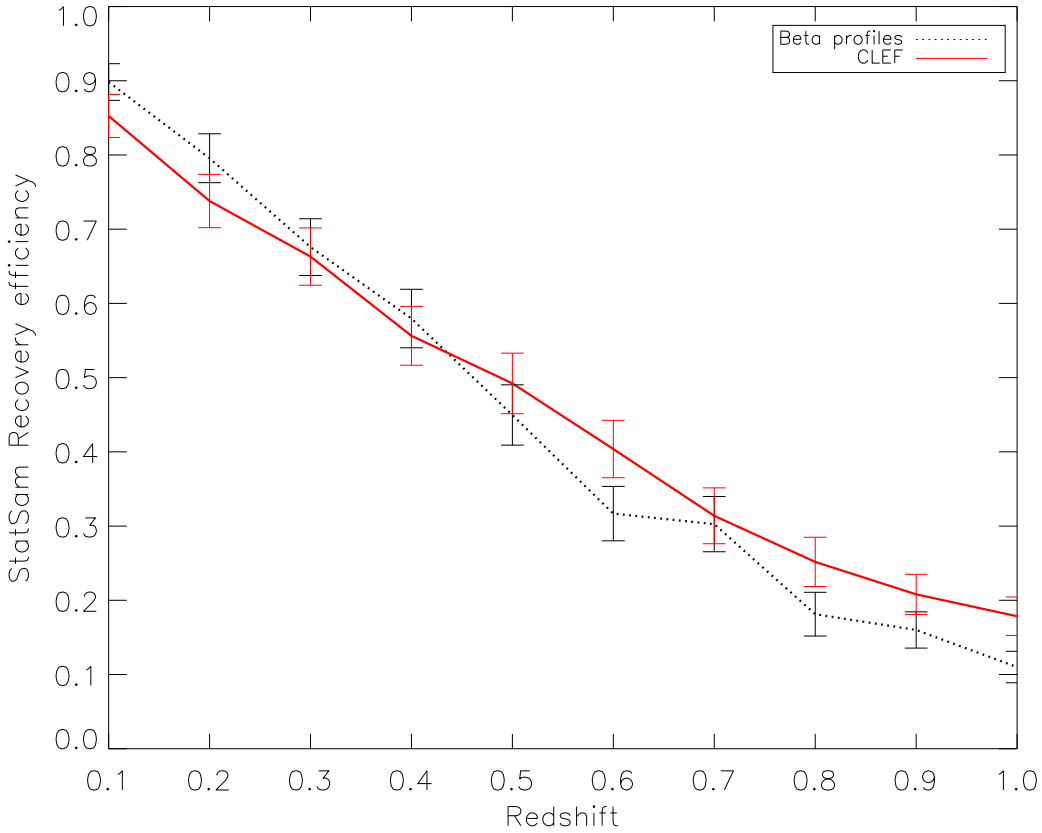


Figure 6.8: A comparison of the detectability of CLEF clusters vs. the $\beta$ profiles used in the standard XCS selection function ($\beta = 2/3$, $r_c = 160$kpc).

### 6.3.3 RECOVERY efficiency of cool-core clusters

As discussed in Section 6.2, the majority of clusters in the CLEF sample contain cool cores. This property of CLEF enables us to test how effective XAPA is at RECOVERING cool-core clusters over a range of redshifts. Figure 6.9 demonstrates the trend in RECOVERY for two sub-samples of CLEF clusters, those with $f_T < 1.0$ (mild cool core), and those with $f_T <$ median $f_T$ (strong cool core). There is little difference seen between these two sub-samples. This is not very suprising, the strength of the cool core is defined by $f_T$, but it is the X-ray concentration ($f_L$) that will influence detection (i.e $T$ is not particularly important, see

Section 5.3 and Figure 5.5). Figure 6.7 showed that while there is a clear anti-correlation between $f_T$ and $f_L$, there is also a significant amount of scatter. Understanding the detection trend with $f_L$ will give us the best indication of how well XAPA is able to detect clusters that are most likely to contain a cool-core.

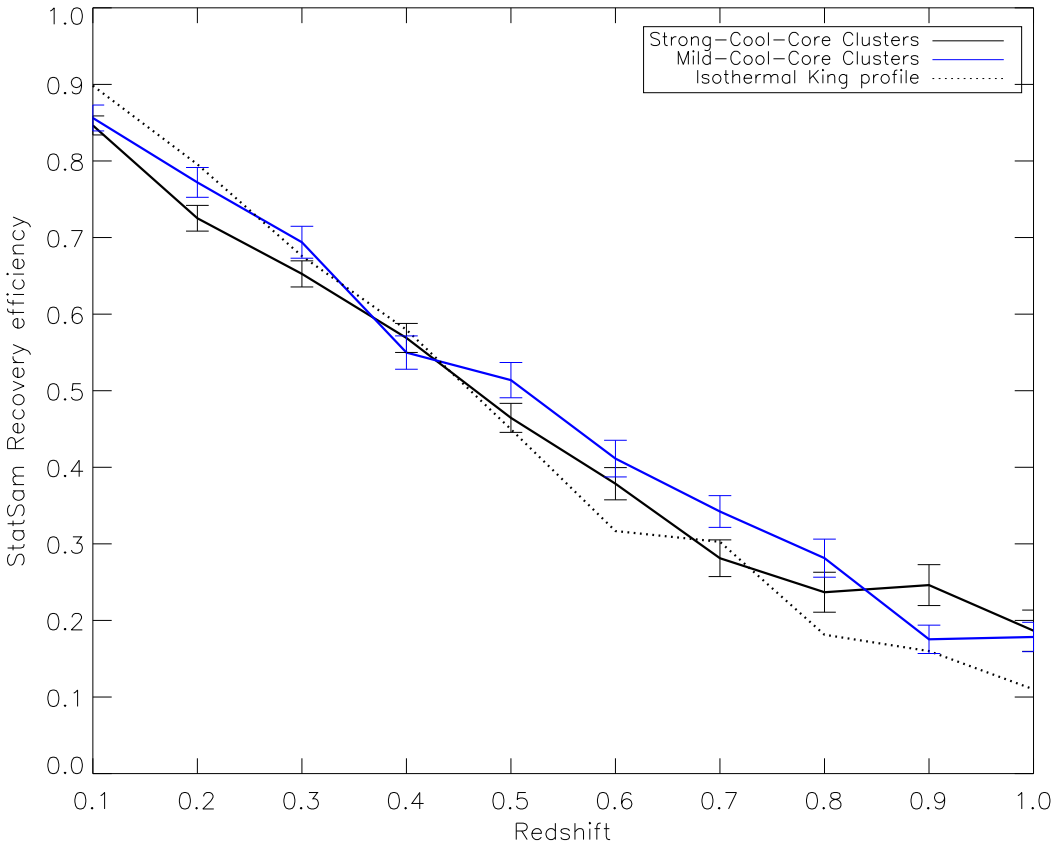


Figure 6.9: Detection and classification efficiency shown for 2 CLEF cluster sub-samples based on cool core strength: mild: $f_T < 1.0$, and strong: $f_T <$ median $f_T$

### 6.3.4 Recovery efficiency of clusters with centrally peaked profiles

Figure 6.10 shows that when separating the sub-samples by $f_L$, a clearer difference in recovery appears. The sub-samples are defined in Table 6.1. It can be seen in the figure that those clusters with the strongest core emission are recovered 50% less than those that are less concentrated across much of the considered redshift range (e.g at $z = 0.5$: 60% of the Non-Cool-Core clusters are recovered, however only 30% of the Strong-Cool-Core sample is recovered).

Figures 6.11 demonstrates that the drop in recovery is not due to a drop in detection. Figure 6.11 shows the fraction of input objects that are detected, regardless of extent classification or flagging (see Section 3.3.3 for details of the warning flags). The samples show similar behaviour at $z \leq 0.5$; beyond this redshift the detectability of the samples

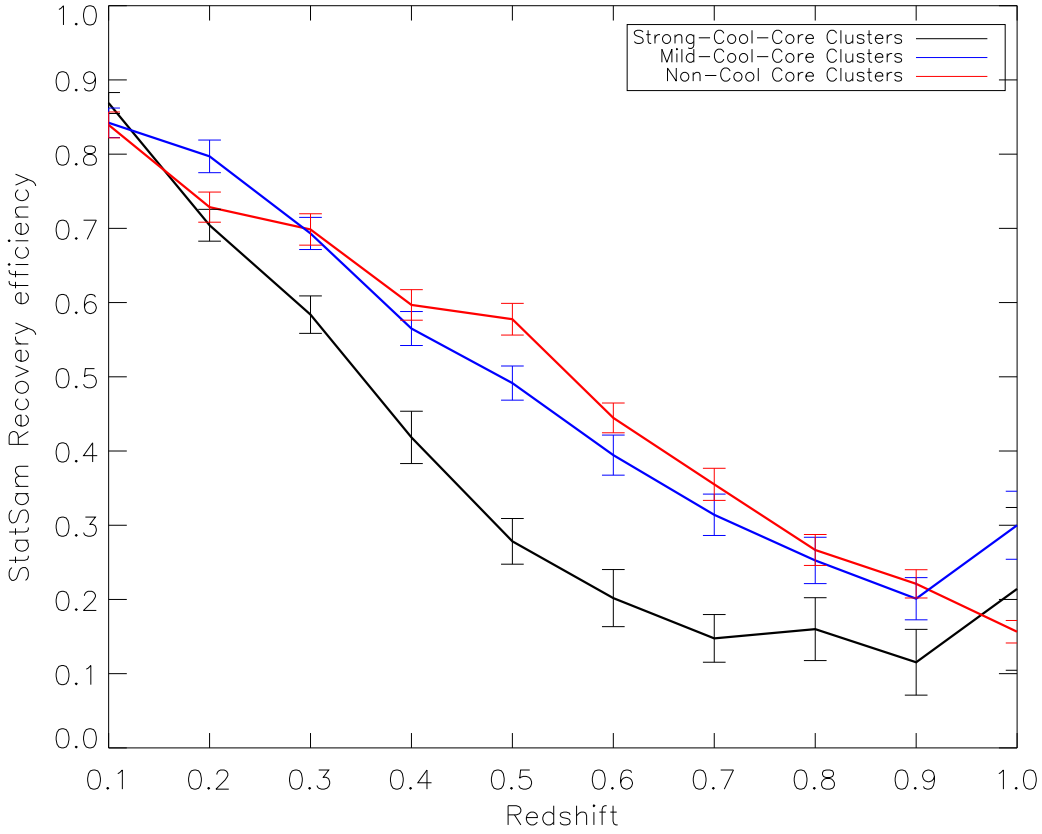


Figure 6.10: RECOVERY efficiency shown for 3 CLEF cluster sub-samples based on X-ray concentration: non-cool-core: $f_L <$ median $f_L$, mild-cool-core: $f_L >$ median $f_L$, strong-cool-core: $f_L > 1.5\times$ median $f_L$

begins to diverge. The data shows that the stronger the core the more likely it is that the cluster will be detected at high $z$. We see from Figure 6.12 that the RECOVERY bias is due to XAPA's mis-classification of the Strong-Cool-Core sample as point sources, or due to the sources being flagged as suspicious. The clusters that are more concentrated are easier to detect, however they are also more likely to be classified as pointlike, having PSF-sized extent, or to be detected with significant internal point sources (See Figure 6.12) and so rejected from the final XCS Statistical Sample (see Section 3.6). This effect shows an increasing trend with redshift, and by $z = 0.8$, 5 times more clusters are rejected from the Strong-Cool-Core sample than the Non-Cool-Core sample for this reason. Figure 6.12(b) enables us to distinguish between the reasons for clusters not being RECOVERED; it shows that cool-core clusters are often correctly classified as extended, but XAPA also tends to detect the core as a contaminating point source within the region of extent. It may be that an adjustment of the flagging criteria would remove this trend. The flagging proceedures are in place to lessen the chance of mis-classification caused by inadequacies in the PSF model. A better model might not require the flags at all, although further investigation will need to be done when a new PSF model is implemented.

| Sample name | $f_L$ range |
|---|---|
| non-cool-core | $f_L <$ median $f_L$ |
| mild-cool-core | $f_L >$ median $f_L$ |
| strong-cool-core | $f_L > 1.5\times$ median $f_L$ |

Table 6.1: Definitions of the CLEF subsamples based on their X-ray concentration, $f_L$.

Splitting the CLEF sample into subsamples defined by $f_T$ and $f_L$ provides a useful way of examining the detection of clusters with largely differing core properties, however the divisions that create these samples are artificial. $f_T$ and $f_L$ are both parameters with continuous variation. Figure 6.13 demonstrates XAPA's sensitivity to $f_T$ and $f_L$ as a function of redshift. The median values are shown with solid black lines, and the 10 and 90 percentiles of the data are shown with dotted lines, beyond which the data is too sparse to draw strong conclusions. The peak in detection lies in the range $0.25 > f_L > 0.2$ across the whole of $0.1 < z < 1.0$. The behaviour seen in Figure 6.10 is also apparent in Figure 6.13(b), where the clusters with higher $f_L$ values are recovered less frequently. Figure 6.13(a) further supports the conclusions drawn from Figure 6.9, in that the contours are approximately vertical, indicating that $f_T$ does not directly influence detection.

### 6.3.5 Detection of clusters containing substructure

CLEF also provides us with the opportunity to assess how the presence of internal cluster substucture influences detection. This is a very important question to investigate. Favoured models of structure formation predict increased merger rates at higher redshifts, therefore any attempt to detect clusters at high-$z$ must take substructure into account.

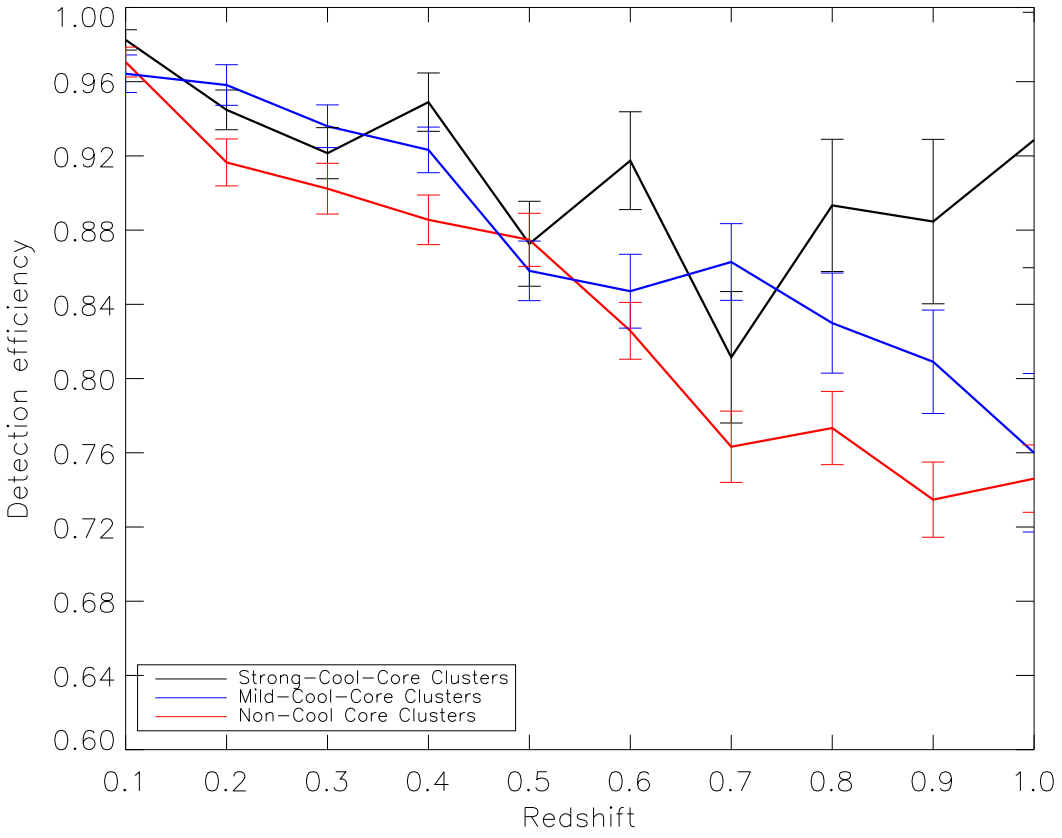


Figure 6.11: Figure 6.10 without the constraint on classification. All detected objects are plotted regardless of extent.

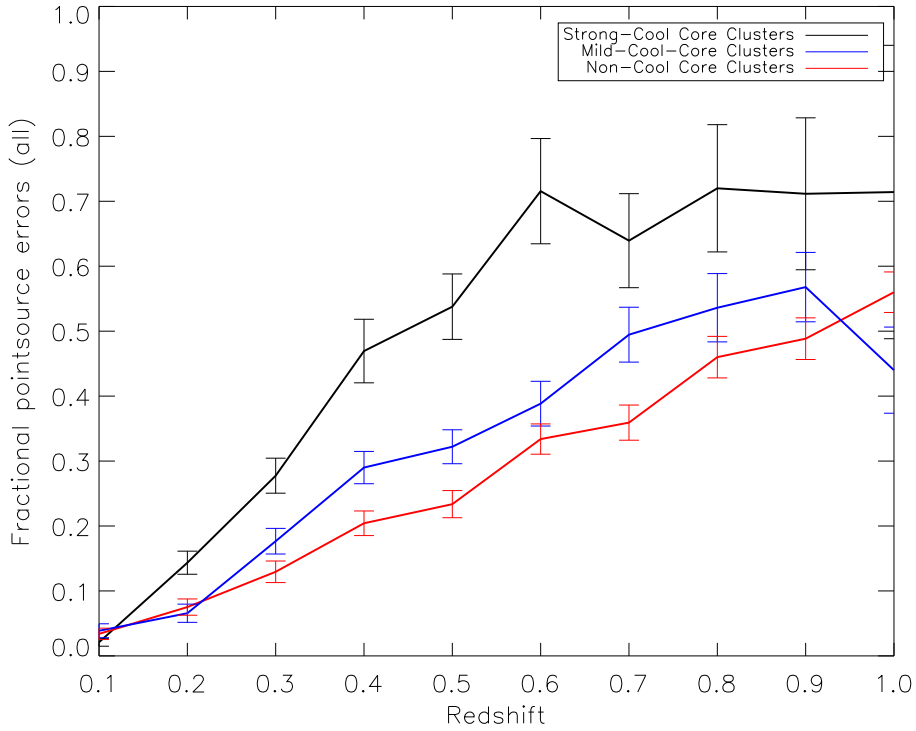


(a)

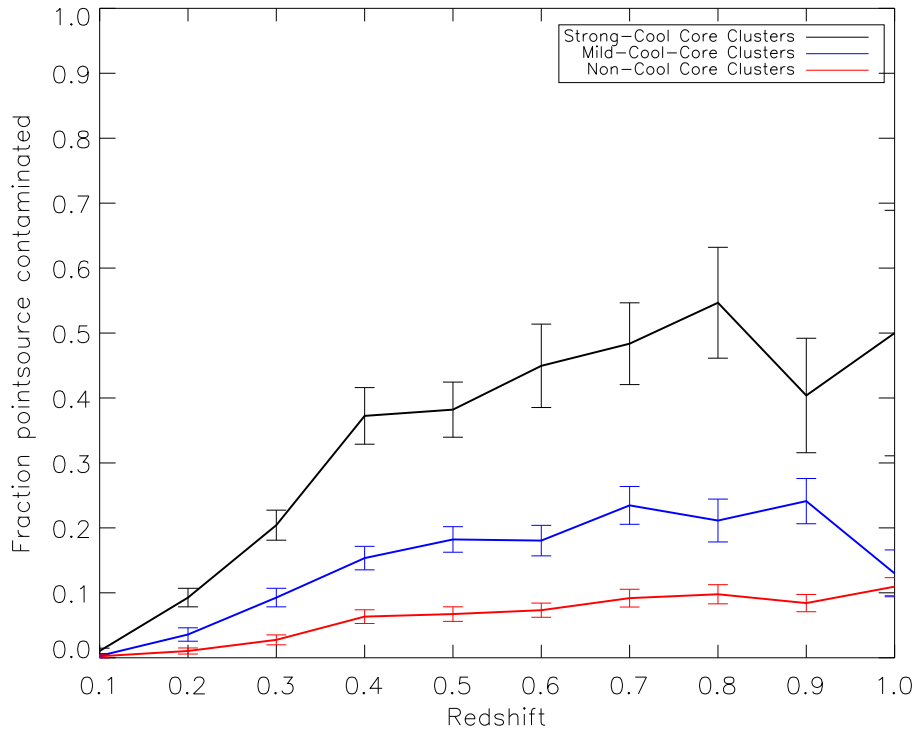


(b)

Figure 6.12: Fig 6.12(a): The percentage of input clusters that are detected, but classified as pointlike, or have one or more of PSF-sized flag, Pointsource contaminated flag or Run1 contaminated flag, for the CLEF sub-samples defined by $f_L$. Fig 6.12(b) shows only those detected as extended but having the Pointsource contaminated flag or Run1 contaminated flag.

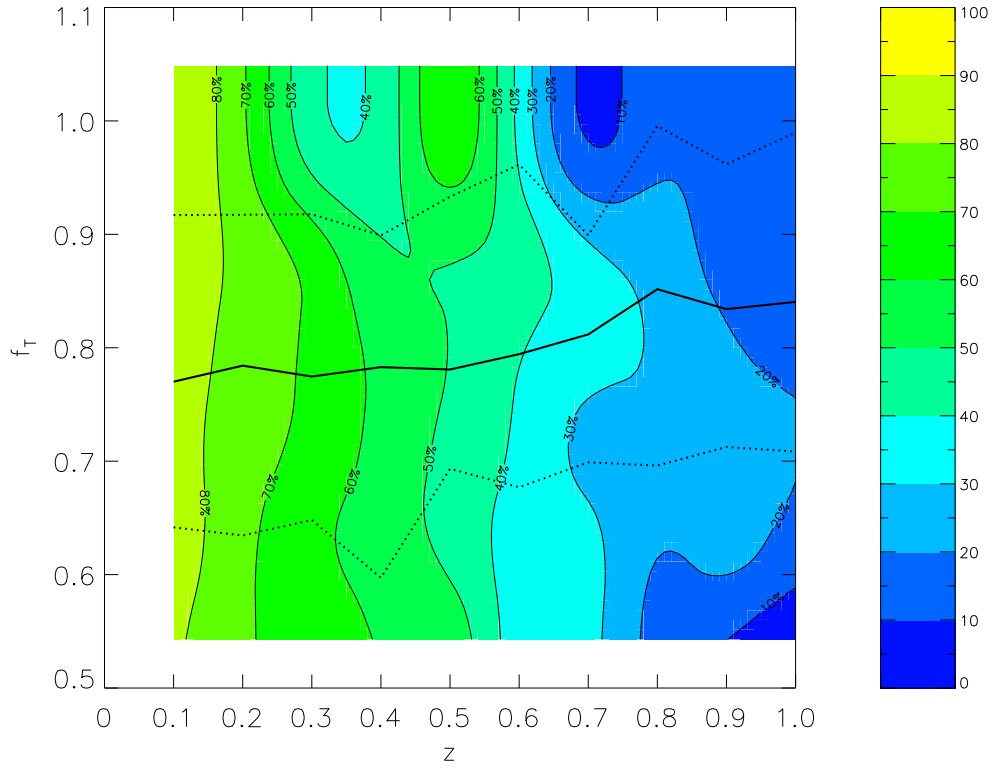


(a)

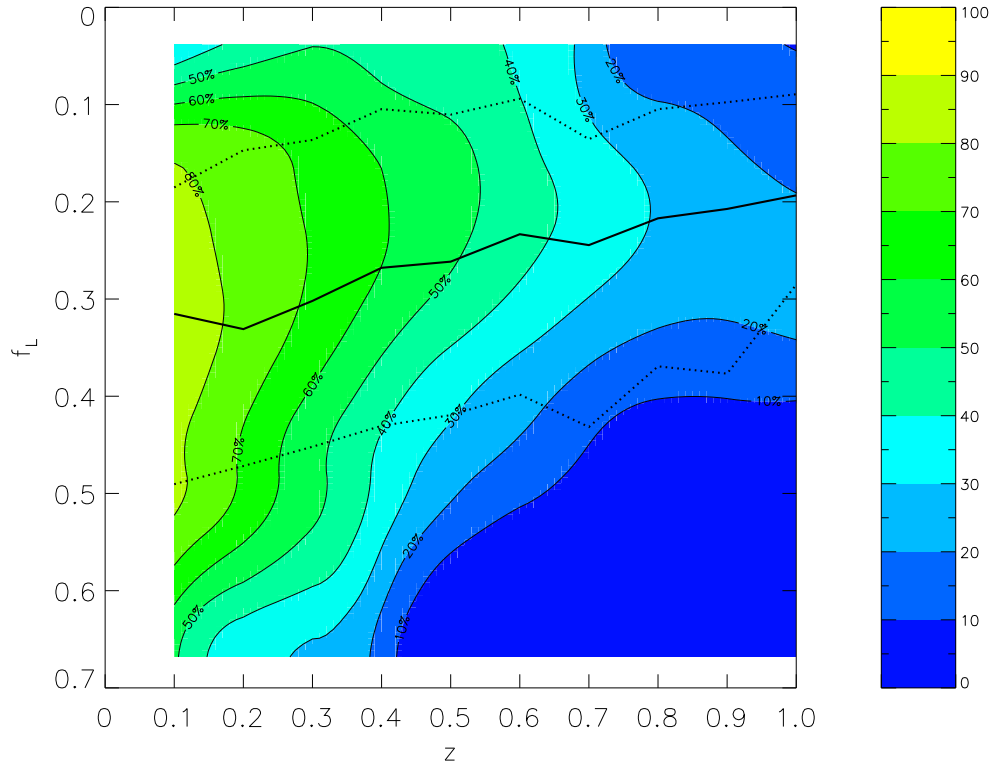


(b)

Figure 6.13: XCS StatSam recovery efficiency for CLEF clusters as a function of redshift and $f_T$ (Fig6.13(a)), and redshift and $f_L$ (Fig6.13(b)). The solid black line represents the median value at each redshift, the dotted lines mark the 10 and 90 percentiles of the data.

Figure 6.14(a) shows the XCS StatSam recovery efficiency for the regular ($S_X \leq 0.1$) and irregular ($S_X > 0.1$) CLEF clusters (See Section 6.2.4 for definitions). The irregular sample is seen to be systematically easier to detect and correctly classify than the regular sample in the range $0.3 < z < 0.8$. Figure 6.14(b) shows that this is due to regular clusters being more likely to be mis-classified as point sources or containing point source contamination. This result may however be an artifact of the nature of CLEF. Clusters in the simulation that have not undergone a recent merger event tend to have the coolest cores, and likewise irregular clusters tend to have low $f_L$ values as the presence of a sub-cluster boosts the overall luminosity without affecting the core luminosity. The variation in recovery with $S_X$ seen in figure 6.15 may be just as much a result of the absence of strongly peaked cool cores as it is the presence of substructure. It should be noted here that the apparent drop in RECOVERY at larger $S_X$ is due to a lack of objects in this region of the plot, and not because of any real trend (the 90 percentile line shows that very few objects have $S_X > 0.15$). To investigate the effect of $S_X$ on RECOVERY in more detail we would require a larger set of non-cool-core clusters that have a wide variation in amount of substructure. Larger simulations do now exist, containing more objects than CLEF, The Millenium Gas project (Gazzola and Pearce (2007), Hartley et al. (2008)) for example may contain such objects, however this will have to be investigated at a future date.

### 6.3.6 Applying a count cut to the sample

As discussed in Section 3.6.1, the addition of a minimum 500 count detection limit has been set on the cluster sample being used by XCS for cosmology. In Section 5.4.1 it was shown that the addition of this count cut removes some of the detection biases caused by profile variations. It is important at this point to see if the trends seen thus far in this chapter would be present in the XCS500, or whether a large enough number of counts enables XAPA to properly recover the CLEF clusters regardless of core strength or dynamical state. Figure 6.16 shows how the effect of $f_L$ on recovery changes as a count limit is applied and increased through 100, 200 and 500 counts. It is clear that increasing the count cut reduces the large variation in recovery as a function of $f_L$. Based on this evidence the XCS500 should contain clusters with a range X-ray concentrations, and so should be unbiased with repected to Cool-Core clusters. If a 500 count criteria is applied to Figure 6.8 we should expect therefore that the CLEF sample and $\beta$ profile clusters should have overlapping recovery trends (See Figure 6.17). Figure 6.17 shows that the two samples have similar behaviour with respect to redshift, and all the bins, except at $z = 0.4$, have overlapping $1\sigma$ uncertainties.

### 6.3.7 The impact of the selection function upon the $L - T$ relation

The XCS cluster sample will be used to make an accurate measurement of the $L - T$ relation; we expect to measure the normalization and slope to $\pm 6\%$ and $\pm 13\%$ respectively

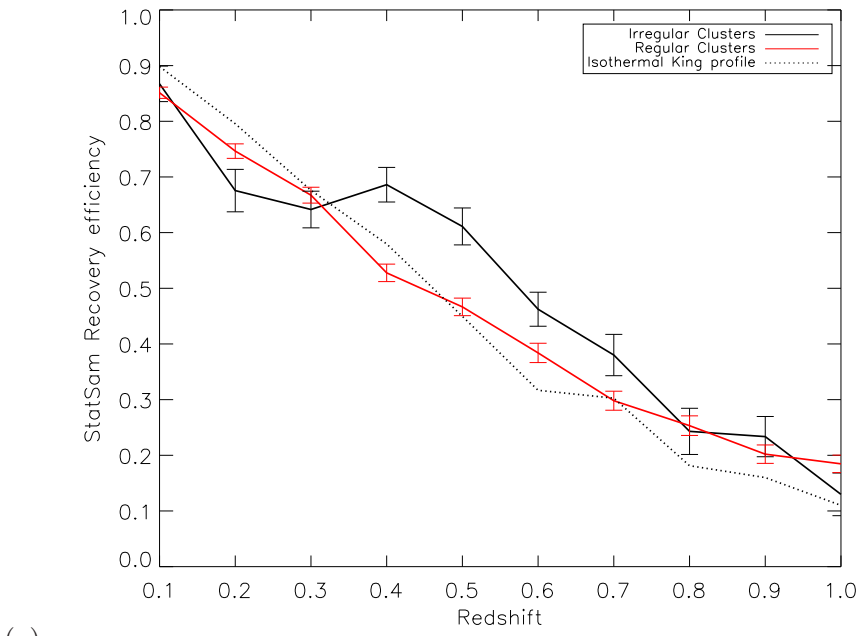


(a)

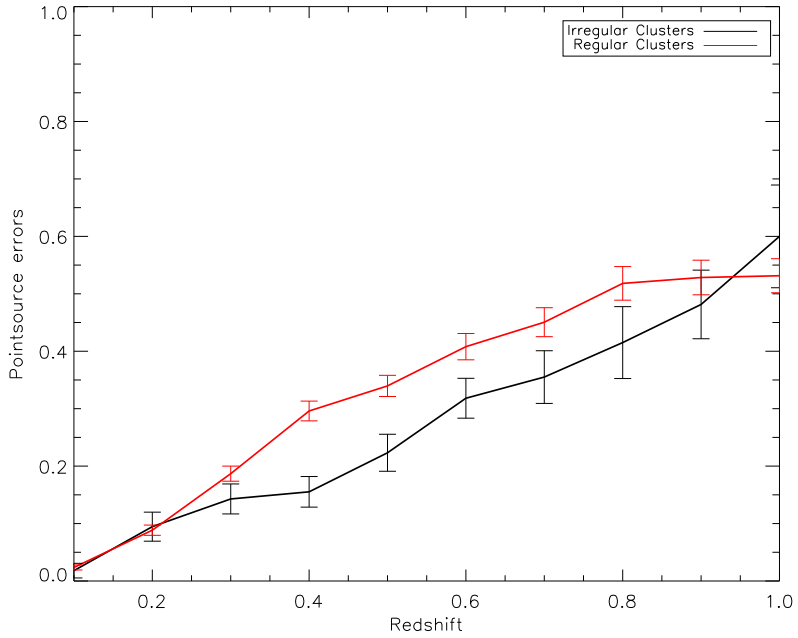


(b)

Figure 6.14: Fig 6.14: Detection and classification efficiency for both the regular ($S_X \leq 0.1$) and irregular ($S_X > 0.1$) CLEF clusters. The XCS $\beta$ profile data is overplotted for comparison (Dotted line). Fig 6.14(b) shows the percentage of input clusters that are detected, but classified as pointlike, PSF sized, or as having significant point source contamination.

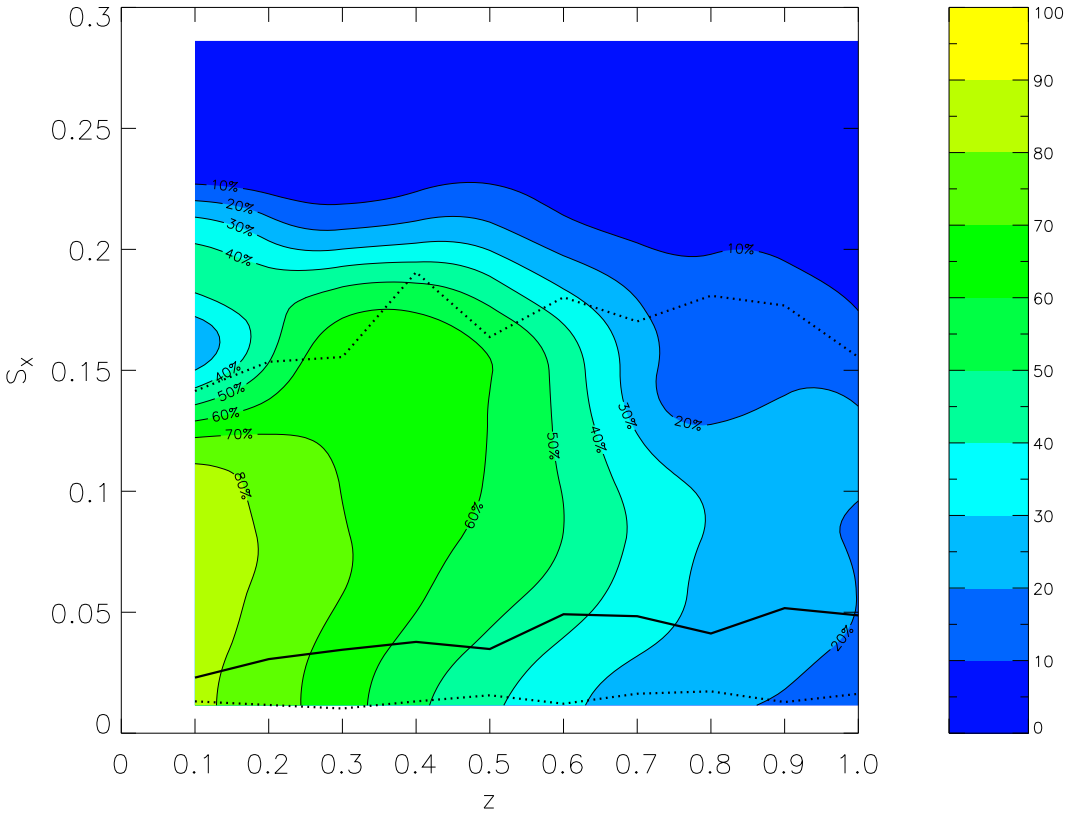


Figure 6.15: XCS StatSam recovery efficiency for CLEF clusters as a function of redshift and the amount of substructure, $S_X$. The solid black line represents the median value at each redshift, the dotted lines mark the 10 and 90 percentiles of the data.

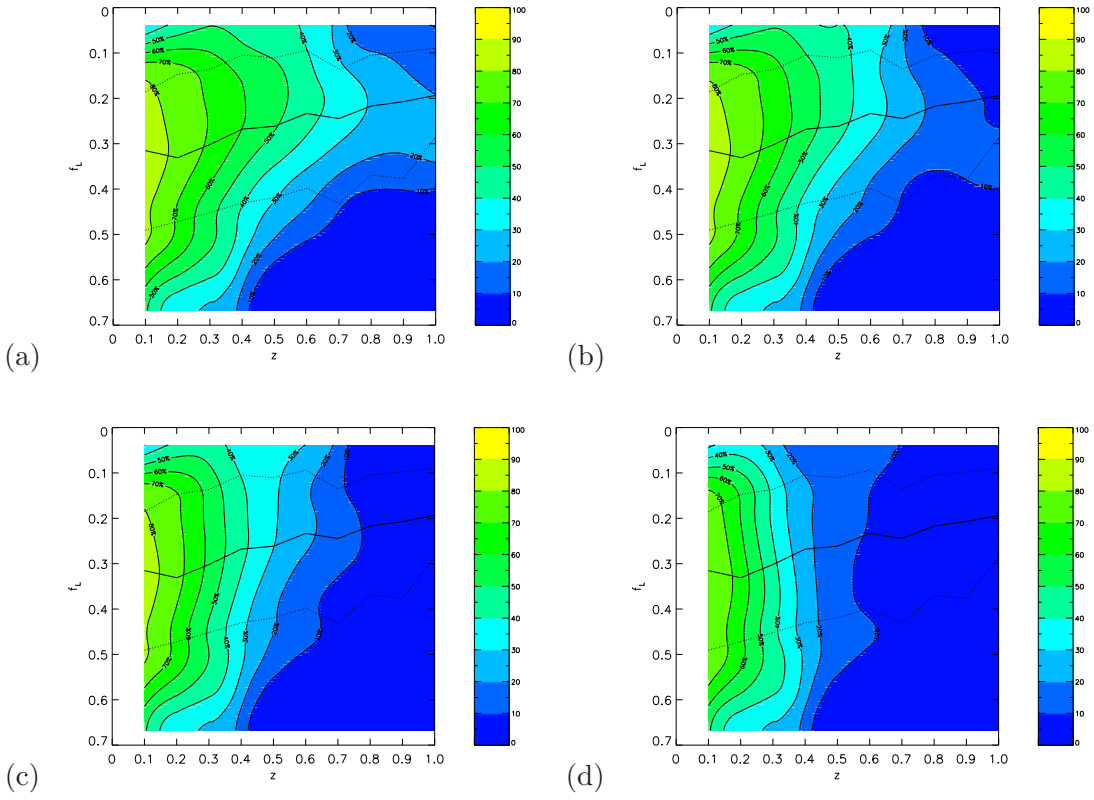


Figure 6.16: Same as Figure 6.13(b), but with additional requirements on the detected number of counts; Figure 6.16(a): $\geq 0$ counts (same as Figure 6.10), Figure 6.16(b): $\geq 100$ counts, Figure 6.16(c): $\geq 200$ counts, Figure 6.16(d): $\geq 500$ counts, .

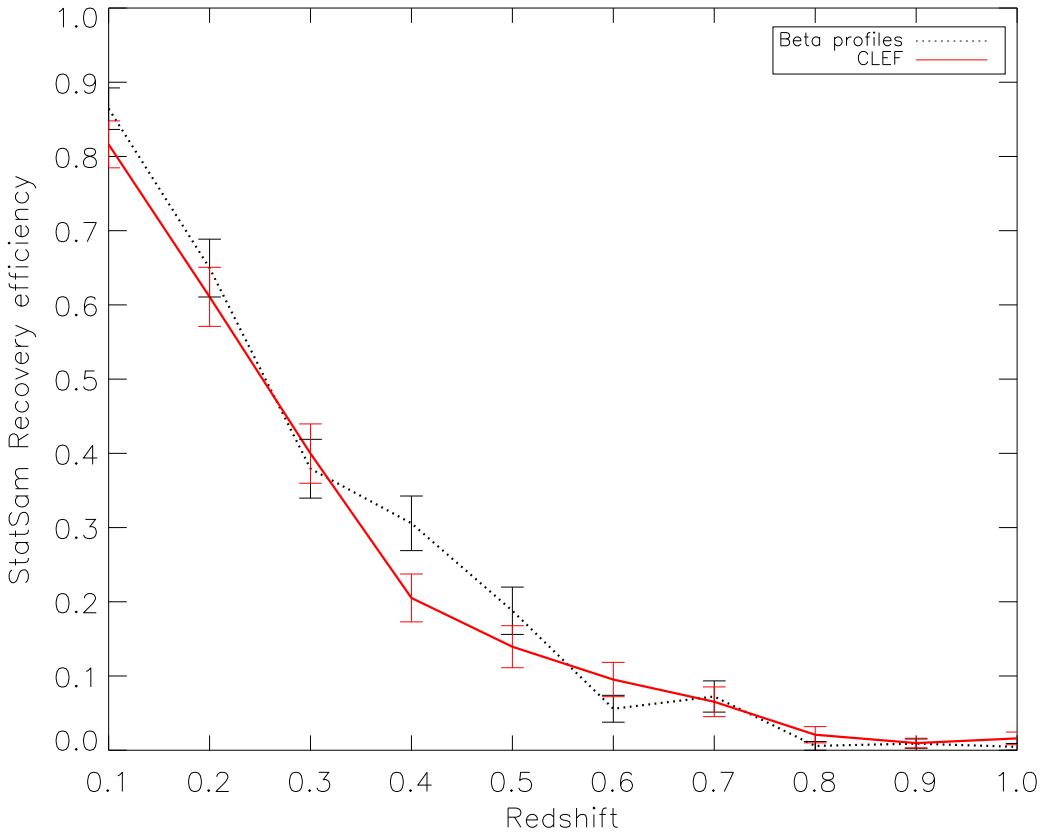


Figure 6.17: Same as Figure 6.8, but with the additional requirement that clusters be detected with at least 500 counts.

(at $1\sigma$) (Sahlén et al., 2009). Pacaud et al. (2007) demonstrated that the inclusion of selection effects is essential for the correct determination of the evolution of the $L-T$ relation (See Figure 6.18). Pacaud et al. (2007) have shown that having an understanding of the selection function can significantly alter the measured evolution in the $L-T$ relation, though they were not able to show if this is actually an improvement. As a precursor to the analysis of the real XCS $L-T$ relation, we have used the selection functions from Chapter 5 to correct the "XCS - CLEF" $L-T$ relation. The CLEF cluster sample can be treated as a complete, if not realistic, population. The sample can be run through the detection software in the same way as Section 6.3.1, producing a sub-sample of detected clusters. The scaling relations of the whole population can be compared that of the detected clusters. As expected XAPA preferentially detects clusters above the mean relation (See the red line in Figure 6.19). Using our standard selection function from Chapter 5 we have corrected the measured relation by weighting the data depending on how efficiently we expect to detect clusters with the same $L, T, z$ combination (Yellow line), clusters detected less frequently are given a higher weighting than those detected more often.

## 6.4 Future Work

In Figure 6.19 the $L, T, z$ data for the detected clusters are drawn straight from the simulation data. We do not take into account measurement errors, as a result of the limited size of the CLEF simulation. As a minimum, it would be desirable to make a count cut on the detected cluster sample, and then scatter the temperature values based on a real temperature error distribution. However the majority of CLEF clusters are in the $2-3$keV range, and so are not very luminous; a 300 or 500 count cut leaves so few clusters that this exercise becomes meaningless. So, instead, we plan to undertake this task with artificial catalogues of $\beta$ profile clusters, it will be interesting to see if it is possible to distinguish between different types of $L-T$ evolution using this method, and how many clusters we need at high redshifts in order to achieve this goal.

In future we will repeat our selection function analysis using the Millenium Gas simulation, since this is larger, and contains more high-redshift and high-temperature clusters.

## 6.5 Summary

We have shown in this chapter that the selection function of the CLEF sample does not differ substantially from that of the $\beta$ profile clusters used in Sahlén et al. (2009). We have then focussed on specific cluster properties (i.e $f_T$, $f_L$, $S_X$), to test the selection function in a way we were not able to do in Chapter 5. This has shown that XAPA has no inherent biases with regard to cool-core clusters, though the often associated centrally peaked surface brightness profiles do affect RECOVERY. These centrally peaked surface brightness

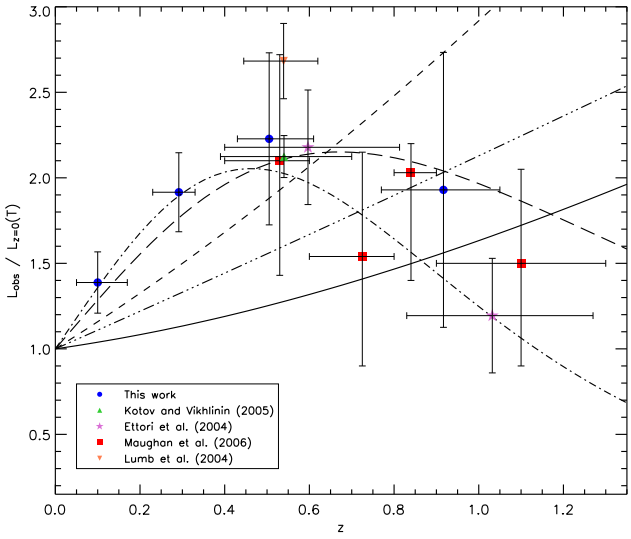


(a)

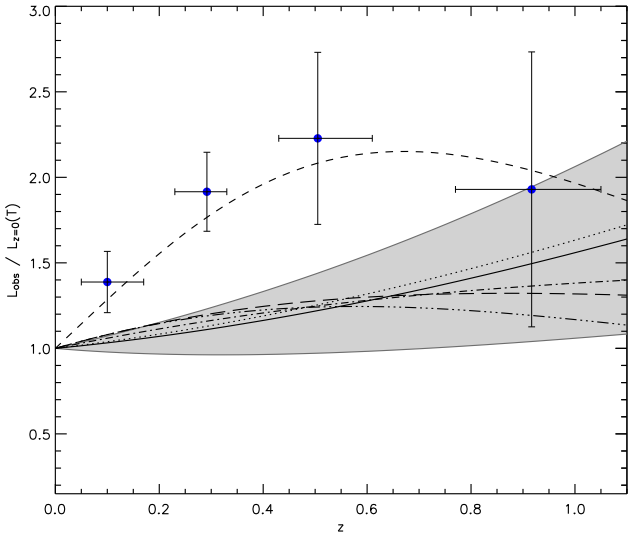


(b)

Figure 6.18: Figure 7 and caption from Pacaud et al. (2007). "Evolution of the LX-T relation. (a): **Raw analysis.** The data points from several studies are plotted (stacked into redshift bins for clarity). Whenever possible, we converted luminosity estimates from the other samples to $L_{500}$ using the information provided by the authors." "Overlaid are several enhancement factor fits from our baseline analysis: the $(1+z)$ power law and ad-hoc 2 parameter fits to our data alone (resp. short and long dashed lines), and the $(1+z)$ power law and ad-hoc 2 parameter fits (resp. dot-dashed and 3dot-dashed lines) fitted to the C1 clusters combined with the samples of Kotov & Vikhlinin (2005) and Ettori et al. (2004). For comparison, the self-similar prediction is indicated by the solid line. (b): **Taking into account selection effects.** The filled circles and short dashed line recalls the location of our raw data points, and best fit model from the preliminary analysis. The corrected enhancement factor fit for the 2 parameter model is shown as the long dashed line. The final 1 parameter fit and its $1\sigma$ confidence interval is displayed by the solid line and the shaded region. Expectations from several intra-cluster gas models are plotted for comparison: the self-similar predictions (dotted line) and two models by Voit (2005) including non gravitational physics (dot-dashed and 3dot-dashed lines)."

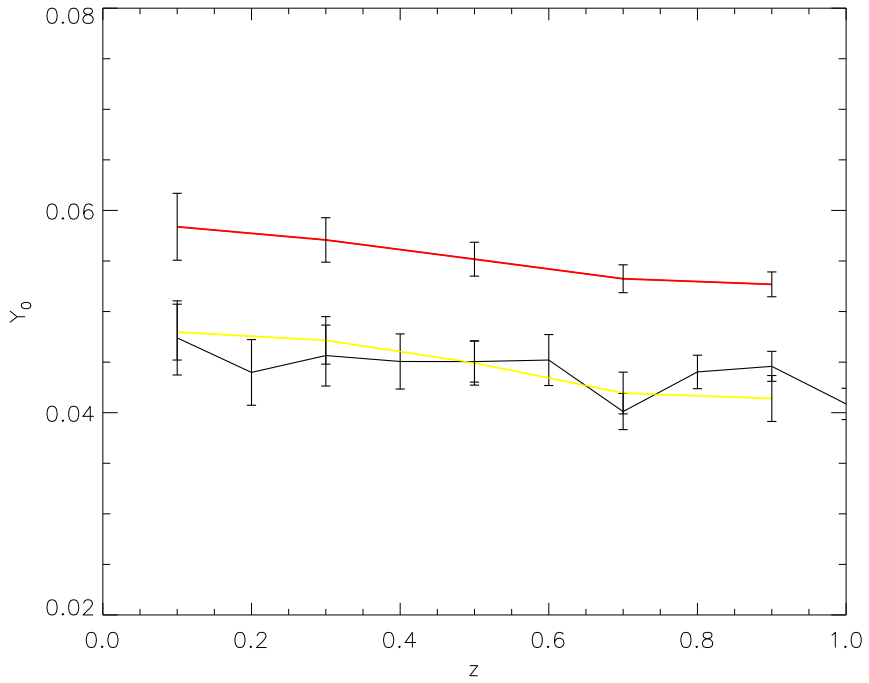


Figure 6.19: The redshift evolution of the $L-T$ normalisation, $Y_0$. Shown in black is the data from the underlying CLEF population, the red line is the detected sub-sample, the yellow line is the detected sub-sample after correction for the selection function.

profiles are easily detected, but XAPA often associates the profile with heavy point source contamination, and so these objects are flagged and removed from the candidate list. This is likely another symptom of the inadequate PSF model; with a better model this bias may be substantially reduced. The results of the substructure investigation may indicate that morphologically disturbed clusters are more effectively RECOVERED, but the trend of $S_X$ with $f_L$ make this difficult to substantiate, and it is possible that this is the same $f_L$ bias, diluted by the scatter in the $S_X$, $f_L$ relation. Finally we see that a 500 count cut leaves the CLEF-selection function and the $\beta$-selection function with overlapping $1\sigma$ uncertainties, and so the XCS500 should not be significantly biased with respect to the considered parameters.

The selection function presented in Chapter 5 and in this chapter, with its dependencies on morphology, will allow the XCS to produce a statistical description of the cluster population. This will be a valuable tool for studies of cluster physics and structure formation, for example Santos et al. (2008) use the ratio of cool-core to non-cool-core clusters as a function of redshift to study cluster evolution (with possible links to merger rates). The use of cluster profiles drawn from N-body simulations has enabled this work to assess XCS's completeness with respect to cool-cores and dynamical state. As far as the author is aware this direct use of simulated clusters has not been done before, and highlights the ever increasing complementarity of observational surveys and theorectical studies.

We have also carried out preliminary work to investigate the practicalities of using XCS selection functions to correct XCS $L - T$ relations.

# Chapter 7

# Conclusions

In this thesis we have presented the XCS DR3, a major update of the source data produced by the XCS collaboration. The resultant cluster candidate list, after follow-up and confirmation, is expected to produce the largest homogenous sample of clusters ever compiled. XCS will grow with the XMM archive, thus we do not expect the XCS sample to be superceeded, in terms of size, with the current generation of satellites. A cluster catalogue is only of limited use for cosmology without a selection function; this is also presented in detail. The following discussion is a compilation of the summary sections at the end of Chapters 3, 4, 5 and 6, and contains no new work.

## 7.1 XCS and XCS DR1 & DR2

The DR1+DR2 StatSam will produce the first XCS catalogue of clusters (E. Lloyd-Davies, (in prep)). The DR2 clusters which comprise $\sim 25\%$ of this catalogue are a result of the work done by the author.

Using images, exposure maps and ECF's produced by K. Sabirli, and the XAPA pipeline designed by M. Davidson, we have been able to produce a source list of 81528 entries, and a StatSam cluster candidate list of 1874. Of these 1874, 250 already have redshifts. The author had responsibility for the DR2 extension of XCS, representing a 25% increase in the number of sources, cluster candidates, and confirmed clusters. The confirmed clusters from the XCS300 sample have now been subjected to X-ray spectroscopy and morphological analysis by E. Lloyd-Davies, see Appendix I.

## 7.2 The XCS DR3

The total, non-overlapping area of DR3 is 522.29 deg$^2$, and the available StatSam area amounts to 229.73 deg$^2$. DR3 has extended the total area covered by XCS (from the DR1+DR2 area) by $\sim 70\%$, and increased the number of StatSam cluster candidates by a factor of 2. Using a $1'$ radius to search the literature: there are 1365 StatSam cluster candidates with $> 300$ counts, 159 of which are already listed in NED as being known clusters/groups. This corresponds to $\sim 6$ serendipitous $> 300$ count candidates per deg$^2$. This is greater than the source density in DR1+DR2 due to the improvements made in the source list creation (see Section 4.1). For comparison the 400d survey find $\sim 0.75$ candidates per deg$^2$ with fluxes $> 1.4 \times 10^{-13}$ergs s$^{-1}$ cm$^{-2}$. The XMM-LSS find 5.4 'C1' clusters per deg$^2$ and estimate $\sim 12$ 'C2' per deg$^2$ (the C2 clusters have not yet been published).

We can potentially measure temperatures for these all DR3 XCS300 candidates, once redshifts are known. 709 redshifts have already been obtained from NXS and SDSS and other literature data. The temperature fitting is currently underway (E. Lloyd-Davies); at present there are 227 DR3 clusters with both temperature and redshift measurements (See Table H.3 in Appendix H), although most of these have come from DR1+DR2. This is already a significant improvement over the samples in the literature, see Table 7.1. A preliminary XCS $L - T$ relation is shown in Figure 7.1.

| Survey | Data | Clusters | z range |
|---|---|---|---|
| HIFLUGS | Rosat | 63 | 0.005 - 0.2 |
| Maughan et al. | Chandra | 115 | 0.1 - 0.3 |
| O'Hara et al. | Chandra | 70 | 0.18 -1.24 |
| 400SD | Chandra | 36 | 0.35 - 0.9 |
| XMM-LSS | XMM | 29 | 0.05 - 1.05 |
| XCS300 | XMM | 227 | 0.003 - 1.457 |

Table 7.1: Literature cluster samples with measured temperature and redshifts. Also added is the current size of the XCS300 sample with temperatures and redshifts.

In addition to the large cluster sample that will come from DR3, Campbell et al. (in prep) have used the DR3 point source catalogue to find 11 high quality isolated neuton star candidates. These candidates are mostly new to DR3.

With the construction of DR3 the XCS expects to have a sample of $\sim 1000$ clusters with redshifts, and the potential to measure temperatures for the majority of these. This will be significantly larger than any other homogenous sample of clusters.

The current distribution of the DR3 cluster redshifts is displayed in Figure 7.2.

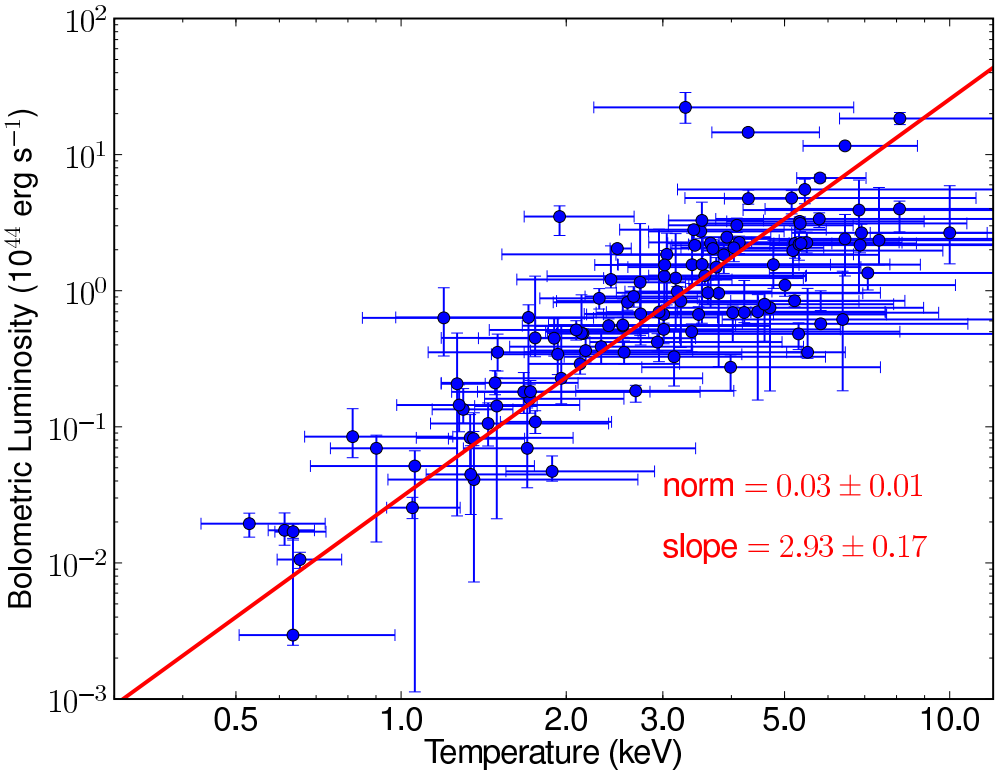


Figure 7.1: A preliminary XCS $L - T$ relation. Figure courtesy of E. Lloyd-Davies.

## 7.3 XCS Selection Function with Two-Dimensional $\beta$ profiles.

The work presented in this chapter has demonstrated the way in which many variables can influence cluster detection.

The dependance of the selection function on cosmology enables cluster surveys to constrain cosmological parameters. The results presented and discussed in Section 5.3 enable the XCS to do just that, and were crucial for the production of Sahlén et al. (2009). The selection function used in Sahlén et al. (2009) assumed a fixed cluster profile, the impact of this assumption has been tested in Section 5.4. We see that $r_c$ in particular can strongly influence the detection of clusters, however the more counts a source has, the more this effect is reduced, and the impact on the XCS500 sample is small.

As discussed above, it is widely recognised that an understanding of a surveys selection function must be had before any strong conclusions can be drawn, either for cosmology or scaling relation studies. The simulations presented so far in this chapter further highlight this, in particular it is clear that the morphology of the population must be better understood before any naive selection function is applied.

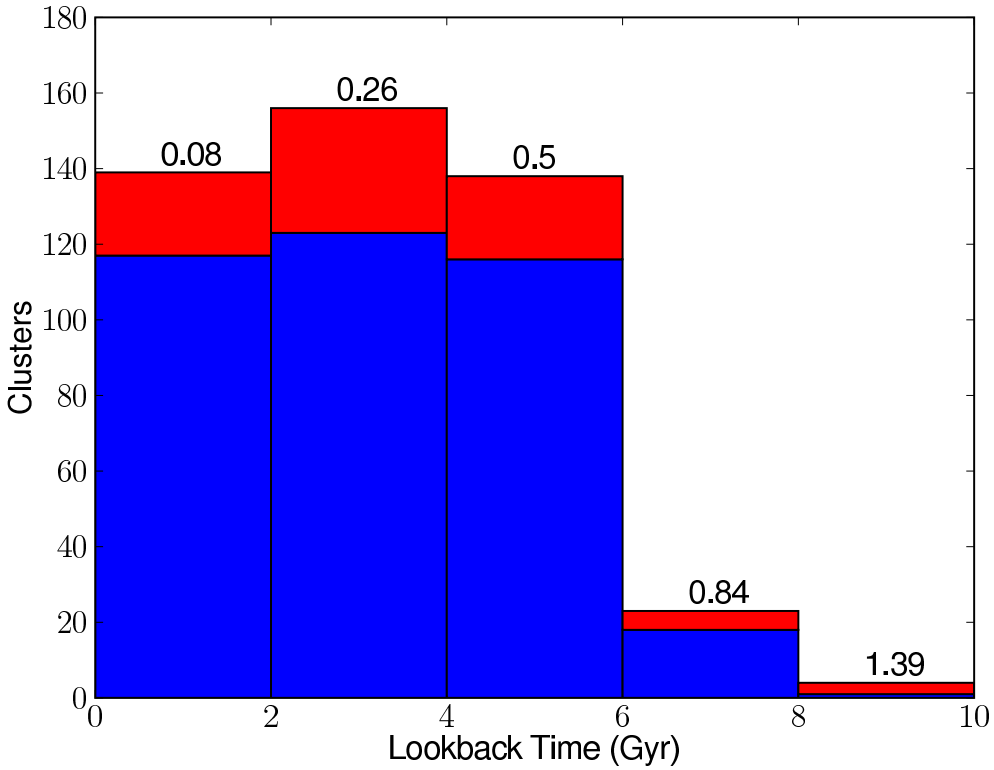


Figure 7.2: A histogram of the lookback time of DR3 clusters with measured redshifts. The red histogram is for spectroscopic redshifts, the blue histogram is for photometric redshifts. The numbers above the bins are the centre of the bin in redshift space. Figure courtesy of E. Lloyd-Davies.

In Section 5.6 we investigated the impact of exposure time on cluster detection. It was shown that in terms of cluster numbers, a shallower wide field survey would be preferable, and exposures greater than 30ks would not give substantial increases. However a 10deg$^2$, 50 ks survey would yield significantly greater numbers of low $T$ (and hence low mass) systems at high redshift.

## 7.4 XCS Selection Function with Two-Dimensional Cluster Profiles from Hydrodynamic Simulations.

We have shown in this chapter that the selection function of the CLEF sample does not differ substantially from that of the $\beta$ profile clusters used in Sahlén et al. (2009). We have then focussed on specific cluster properties (i.e $f_T$, $f_L$, $S_X$), to test the selection function in a way we were not able to do in Chapter 5. This has shown that XAPA has no inherent biases with regard to cool core clusters, though the often associated centrally peaked surface brightness profiles do affect RECOVERY. These centrally peaked surface brightness profiles are easily detected, but XAPA often associates the profile with heavy point source contamination, and so these objects are flagged and removed from the candidate list. This is likely another symptom of the inadequate PSF model, with a better model this bias may be substantially reduced. The results of the substructure investigation may indicate that morphologically disturbed clusters are more effectively RECOVERED, however the trend of $S_X$ with $f_L$ make this difficult to substantiate, and it is possible that this is the same $f_L$ bias, diluted by the scatter in the $S_X$, $f_L$ relation. Finally we see that a 500 count cut leaves the CLEF-selection function and the $\beta$-selection function with overlapping $1\sigma$ uncertainties, and so the XCS500 should not be significantly biased with respect to the considered parameters.

The selection function presented in Chapter 5 and in this chapter, with its dependencies on morphology, will allow the XCS to produce a statistical description of the cluster population. This will be a valuable tool for studies of cluster physics and structure formation, for example Santos et al. (2008) use the ratio of cool-core to non-cool-core clusters as a function of redshift to study cluster evolution (with possible links to merger rates). The use of cluster profiles drawn from N-body simulations has enabled this work to assess XCS's completeness with respect to cool-cores and dynamical state. As far as the author is aware this direct use of simulated clusters has not been done before, and highlights the ever increasing complementarity of observational surveys and theorectical studies.

We have also carried out preliminary work to investigate the practicalities of using XCS selection functions to correct XCS $L-T$ relations.

# Bibliography

Abazajian, K. N., Adelman-McCarthy, J. K., Agüeros, M. A., Allam, S. S., Allende Prieto, C., An, D., Anderson, K. S. J., Anderson, S. F., Annis, J., Bahcall, N. A., Bailer-Jones, C. A. L., Barentine, J. C., Bassett, B. A., Becker, A. C., Beers, T. C., Bell, E. F., Belokurov, V., Berlind, A. A., Berman, E. F., Bernardi, M., Bickerton, S. J., Bizyaev, D., Blakeslee, J. P., Blanton, M. R., Bochanski, J. J., Boroski, W. N., Brewington, H. J., Brinchmann, J., Brinkmann, J., Brunner, R. J., Budavári, T., Carey, L. N., Carliles, S., Carr, M. A., Castander, F. J., Cinabro, D., Connolly, A. J., Csabai, I., Cunha, C. E., Czarapata, P. C., Davenport, J. R. A., de Haas, E., Dilday, B., Doi, M., Eisenstein, D. J., Evans, M. L., Evans, N. W., Fan, X., Friedman, S. D., Frieman, J. A., Fukugita, M., Gänsicke, B. T., Gates, E., Gillespie, B., Gilmore, G., Gonzalez, B., Gonzalez, C. F., Grebel, E. K., Gunn, J. E., Györy, Z., Hall, P. B., Harding, P., Harris, F. H., Harvanek, M., Hawley, S. L., Hayes, J. J. E., Heckman, T. M., Hendry, J. S., Hennessy, G. S., Hindsley, R. B., Hoblitt, J., Hogan, C. J., Hogg, D. W., Holtzman, J. A., Hyde, J. B., Ichikawa, S.-i., Ichikawa, T., Im, M., Ivezić, Ž., Jester, S., Jiang, L., Johnson, J. A., Jorgensen, A. M., Jurić, M., Kent, S. M., Kessler, R., Kleinman, S. J., Knapp, G. R., Konishi, K., Kron, R. G., Krzesinski, J., Kuropatkin, N., Lampeitl, H., Lebedeva, S., Lee, M. G., Lee, Y. S., Leger, R. F., Lépine, S., Li, N., Lima, M., Lin, H., Long, D. C., Loomis, C. P., Loveday, J., Lupton, R. H., Magnier, E., Malanushenko, O., Malanushenko, V., Mandelbaum, R., Margon, B., Marriner, J. P., Martínez-Delgado, D., Matsubara, T., McGehee, P. M., McKay, T. A., Meiksin, A., Morrison, H. L., Mullally, F., Munn, J. A., Murphy, T., Nash, T., Nebot, A., Neilsen, E. H., Newberg, H. J., Newman, P. R., Nichol, R. C., Nicinski, T., Nieto-Santisteban, M., Nitta, A., Okamura, S., Oravetz, D. J., Ostriker, J. P., Owen, R., Padmanabhan, N., Pan, K., Park, C., Pauls, G., Peoples, J., Percival, W. J., Pier, J. R., Pope, A. C., Pourbaix, D., Price, P. A., Purger, N., Quinn, T., Raddick, M. J., Fiorentin, P. R., Richards, G. T., Richmond, M. W., Riess, A. G., Rix, H.-W., Rockosi, C. M., Sako, M., Schlegel, D. J., Schneider, D. P., Scholz, R.-D., Schreiber, M. R., Schwope, A. D., Seljak, U., Sesar, B., Sheldon, E., Shimasaku, K., Sibley, V. C., Simmons, A. E., Sivarani, T., Smith, J. A., Smith, M. C., Smolčić, V., Snedden, S. A., Stebbins, A., Steinmetz, M., Stoughton, C., Strauss, M. A., Subba Rao, M., Suto, Y., Szalay, A. S., Szapudi, I., Szkody, P., Tanaka, M., Tegmark, M., Teodoro, L. F. A., Thakar, A. R., Tremonti, C. A., Tucker, D. L., Uomoto, A., Vanden Berk, D. E., Vandenberg, J., Vidrih, S., Vogeley, M. S., Voges, W., Vogt, N. P., Wadadekar, Y., Watters, S., Weinberg, D. H., West, A. A., White,

S. D. M., Wilhite, B. C., Wonders, A. C., Yanny, B., Yocum, D. R., York, D. G., Zehavi, I., Zibetti, S., and Zucker, D. B. (2009). The Seventh Data Release of the Sloan Digital Sky Survey. *ApJS*, 182:543–558.

Abell, G. O. (1958). The Distribution of Rich Clusters of Galaxies. *ApJS*, 3:211–+.

Abell, G. O., Corwin, Jr., H. G., and Olowin, R. P. (1989). A catalog of rich clusters of galaxies. *ApJS*, 70:1–138.

Adami, C., Ulmer, M. P., Romer, A. K., Nichol, R. C., Holden, B. P., and Pildis, R. A. (2000). The Bright SHARC Survey: The Selection Function and Its Impact on the Cluster X-Ray Luminosity Function. *ApJS*, 131:391–412.

Alexander, D. M., Bauer, F. E., Brandt, W. N., Schneider, D. P., Hornschemeier, A. E., Vignali, C., Barger, A. J., Broos, P. S., Cowie, L. L., Garmire, G. P., Townsley, L. K., Bautz, M. W., Chartas, G., and Sargent, W. L. W. (2003). The Chandra Deep Field North Survey. XIII. 2 Ms Point-Source Catalogs. *AJ*, 126:539–574.

Allen, S. W., Schmidt, R. W., and Fabian, A. C. (2002). Cosmological constraints from the X-ray gas mass fraction in relaxed lensing clusters observed with Chandra. *MNRAS*, 334:L11–L15.

Ameglio, S., Borgani, S., Pierpaoli, E., Dolag, K., Ettori, S., and Morandi, A. (2009). Reconstructing mass profiles of simulated galaxy clusters by combining Sunyaev-Zeldovich and X-ray images. *MNRAS*, 394:479–490.

Arnaud, M., Aghanim, N., and Neumann, D. M. (2002). The X-ray surface brightness profiles of hot galaxy clusters up to vec z $\sim$ 0.8: Evidence for self-similarity and constraints on $\Omega_0$. *A&A*, 389:1–18.

Arnaud, M. and Evrard, A. E. (1999). The L_X-T relation and intracluster gas fractions of X-ray clusters. *MNRAS*, 305:631–640.

Arnaud, M., Pointecouteau, E., and Pratt, G. W. (2007). Calibration of the galaxy cluster $M_{500} - Y_X$ relation with XMM-Newton. *A&A*, 474:L37–L40.

Bahcall, N. A. and Lubin, L. M. (1994). Resolving the beta-discrepancy for clusters of galaxies. *ApJ*, 426:513–515.

Balogh, M. L., Pearce, F. R., Bower, R. G., and Kay, S. T. (2001). Revisiting the cosmic cooling crisis. *MNRAS*, 326:1228–1234.

Bartelmann, M. and Schneider, P. (2001). Weak gravitational lensing. *Physics Reports*, 340:291–472.

Bertin, E. and Arnouts, S. (1996). SExtractor: Software for source extraction. *A&AS*, 117:393–404.

Böhringer, H., Collins, C. A., Guzzo, L., Schuecker, P., Voges, W., Neumann, D. M., Schindler, S., Chincarini, G., De Grandi, S., Cruddace, R. G., Edge, A. C., Reiprich, T. H., and Shaver, P. (2002). The ROSAT-ESO Flux-limited X-Ray (REFLEX) Galaxy Cluster Survey. IV. The X-Ray Luminosity Function. *ApJ*, 566:93–102.

Böhringer, H., Schuecker, P., Guzzo, L., Collins, C. A., Voges, W., Schindler, S., Neumann, D. M., Cruddace, R. G., De Grandi, S., Chincarini, G., Edge, A. C., MacGillivray, H. T., and Shaver, P. (2001). The ROSAT-ESO flux limited X-ray (REFLEX) galaxy cluster survey. I. The construction of the cluster sample. *A&A*, 369:826–850.

Böhringer, H., Schuecker, P., Pratt, G. W., Arnaud, M., Ponman, T. J., Croston, J. H., Borgani, S., Bower, R. G., Briel, U. G., Collins, C. A., Donahue, M., Forman, W. R., Finoguenov, A., Geller, M. J., Guzzo, L., Henry, J. P., Kneissl, R., Mohr, J. J., Matsushita, K., Mullis, C. R., Ohashi, T., Pedersen, K., Pierini, D., Quintana, H., Raychaudhury, S., Reiprich, T. H., Romer, A. K., Rosati, P., Sabirli, K., Temple, R. F., Viana, P. T. P., Vikhlinin, A., Voit, G. M., and Zhang, Y.-Y. (2007). The representative XMM-Newton cluster structure survey (REXCESS) of an X-ray luminosity selected galaxy cluster sample. *A&A*, 469:363–377.

Burenin, R. A., Vikhlinin, A., Hornstrup, A., Ebeling, H., Quintana, H., and Mescheryakov, A. (2007). The 400 Square Degree ROSAT PSPC Galaxy Cluster Survey: Catalog and Statistical Calibration. *ApJS*, 172:561–582.

Cavaliere, A. and Fusco-Femiano, R. (1976). X-rays from hot plasma in clusters of galaxies. *A&A*, 49:137–144.

Cheng, L.-M., Borgani, S., Tozzi, P., Tornatore, L., Diaferio, A., Dolag, K., He, X.-T., Moscardini, L., Murante, G., and Tormen, G. (2005). Simulating the soft X-ray excess in clusters of galaxies. *A&A*, 431:405–413.

Colless, M., Dalton, G., Maddox, S., Sutherland, W., Norberg, P., Cole, S., Bland-Hawthorn, J., Bridges, T., Cannon, R., Collins, C., Couch, W., Cross, N., Deeley, K., De Propris, R., Driver, S. P., Efstathiou, G., Ellis, R. S., Frenk, C. S., Glazebrook, K., Jackson, C., Lahav, O., Lewis, I., Lumsden, S., Madgwick, D., Peacock, J. A., Peterson, B. A., Price, I., Seaborne, M., and Taylor, K. (2001). The 2dF Galaxy Redshift Survey: spectra and redshifts. *MNRAS*, 328:1039–1063.

Collins, C. A., Stott, J. P., Hilton, M., Kay, S. T., Stanford, S. A., Davidson, M., Hosmer, M., Hoyle, B., Liddle, A., Lloyd-Davies, E., Mann, R. G., Mehrtens, N., Miller, C. J., Nichol, R. C., Romer, A. K., Sahlén, M., Viana, P. T. P., and West, M. J. (2009). Early assembly of the most massive galaxies. *Nat*, 458:603–606.

Croston, J. H., Pratt, G. W., Böhringer, H., Arnaud, M., Pointecouteau, E., Ponman, T. J., Sanderson, A. J. R., Temple, R. F., Bower, R. G., and Donahue, M. (2008). Galaxy-cluster gas-density distributions of the representative XMM-Newton cluster structure survey (REXCESS). *A&A*, 487:431–443.

Davé, R., Katz, N., and Weinberg, D. H. (2002). X-Ray Scaling Relations of Galaxy Groups in a Hydrodynamic Cosmological Simulation. *ApJ*, 579:23–41.

Davidson, M. (2005). *A Serendipitous Survey of Galaxy Clusters with XMM-Newton*. PhD thesis, Institute for Astronomy, University of Edinburgh.

Ebeling, H., Edge, A. C., Bohringer, H., Allen, S. W., Crawford, C. S., Fabian, A. C., Voges, W., and Huchra, J. P. (1998). The ROSAT Brightest Cluster Sample - I. The compilation of the sample and the cluster log N-log S distribution. *MNRAS*, 301:881–914.

Eke, V. R., Navarro, J. F., and Frenk, C. S. (1998). The Evolution of X-Ray Clusters in a Low-Density Universe. *ApJ*, 503:569–+.

Felten, J. E., Gould, R. J., Stein, W. A., and Woolf, N. J. (1966). X-Rays from the Coma Cluster of Galaxies. *ApJ*, 146:955–958.

Finoguenov, A., Reiprich, T. H., and Böhringer, H. (2001). Details of the mass-temperature relation for clusters of galaxies. *A&A*, 368:749–759.

Forman, W., Kellogg, E., Gursky, H., Tananbaum, H., and Giacconi, R. (1972). Observations of the Extended X-Ray Sources in the Perseus and Coma Clusters from UHURU. *ApJ*, 178:309–316.

Gazzola, L. and Pearce, F. R. (2007). A Heating Model for the Millennium Gas Run. In Böhringer, H., Pratt, G. W., Finoguenov, A., and Schuecker, P., editors, *Heating versus Cooling in Galaxies and Clusters of Galaxies*, pages 412–+.

Ghizzardi, S. (2001). In flight Calibration of the PSF for the MOS1 and MOS2 Cameras. Technical report, Milano Calibration Team, Istituto di Fisica Cosmica.

Giacconi, R., Zirm, A., Wang, J., Rosati, P., Nonino, M., Tozzi, P., Gilli, R., Mainieri, V., Hasinger, G., Kewley, L., Bergeron, J., Borgani, S., Gilmozzi, R., Grogin, N., Koekemoer, A., Schreier, E., Zheng, W., and Norman, C. (2002). Chandra Deep Field South. 1 Ms catalog (Giacconi+, 2002). *VizieR Online Data Catalog*, 213:90369–+.

Gioia, I. M., Maccacaro, T., Schild, R. E., Wolter, A., Stocke, J. T., Morris, S. L., and Henry, J. P. (1990). The Einstein Observatory Extended Medium-Sensitivity Survey. I - X-ray data and analysis. *ApJS*, 72:567–619.

Gladders, M. D. and Yee, H. K. C. (2000). A new method for galaxy cluster detection i: The algorithm. *Astronomical Journal*, 120:2148.

Gladders, M. D. and Yee, H. K. C. (2005). The Red-Sequence Cluster Survey. I. The Survey and Cluster Catalogs for Patches RCS 0926+37 and RCS 1327+29. *ApJS*, 157:1–29.

Gorenstein, P., Fabricant, D., Topka, K., Harnden, Jr., F. R., and Tucker, W. H. (1978). Soft X-ray structure of the Perseus cluster of galaxies. *ApJ*, 224:718–723.

Gursky, H., Kellogg, E., Murray, S., Leong, C., Tananbaum, H., and Giacconi, R. (1971). A Strong X-Ray Source in the Coma Cluster Observed by UHURU. *ApJ*, 167:L81+.

Hartley, W. G., Gazzola, L., Pearce, F. R., Kay, S. T., and Thomas, P. A. (2008). Nature versus nurture: the curved spine of the galaxy cluster X-ray luminosity-temperature relation. *MNRAS*, 386:2015–2021.

Helsdon, S. F. and Ponman, T. J. (2000). The intragroup medium in loose groups of galaxies. *MNRAS*, 315:356–370.

Henning, J. W., Gantner, B., Burns, J. O., and Hallman, E. J. (2009). On the Origin of Cool Core Galaxy Clusters: Comparing X-ray Observations with Numerical Simulations. *ApJ*, 697:1597–1620.

Hilton, M., Collins, C. A., Stanford, S. A., Lidman, C., Dawson, K. S., Davidson, M., Kay, S. T., Liddle, A. R., Mann, R. G., Miller, C. J., Nichol, R. C., Romer, A. K., Sabirli, K., Viana, P. T. P., and West, M. J. (2007). The XMM Cluster Survey: The Dynamical State of XMMXCS J2215.9-1738 at z = 1.457. *ApJ*, 670:1000–1009.

Hilton, M., Stanford, S. A., Stott, J. P., Collins, C. A., Hoyle, B., Davidson, M., Hosmer, M., Kay, S. T., Liddle, A. R., Lloyd-Davies, E., Mann, R. G., Mehrtens, N., Miller, C. J., Nichol, R. C., Romer, A. K., Sabirli, K., Sahlén, M., Viana, P. T. P., West, M. J., Barbary, K., Dawson, K. S., Meyers, J., Perlmutter, S., Rubin, D., and Suzuki, N. (2009). The XMM Cluster Survey: Galaxy Morphologies and the Color-Magnitude Relation in XMMXCS J2215.9 − 1738$atz = 1.46$. *ApJ*, 697:436–451.

Jones, C. and Forman, W. (1999). Einstein Observatory Images of Clusters of Galaxies. *ApJ*, 511:65–83.

Kaiser, N. (1986). Evolution and clustering of rich clusters. *MNRAS*, 222:323–345.

Kaiser, N. (1991). Evolution of clusters of galaxies. *ApJ*, 383:104–111.

Katz, N. (1992). Dissipational galaxy formation. II - Effects of star formation. *ApJ*, 391:502–517.

Katz, N. and White, S. D. M. (1993). Hierarchical galaxy formation - Overmerging and the formation of an X-ray cluster. *ApJ*, 412:455–478.

Kay, S. T., da Silva, A. C., Aghanim, N., Blanchard, A., Liddle, A. R., Puget, J.-L., Sadat, R., and Thomas, P. A. (2005). Clusters of galaxies: new results from the CLEF hydrodynamics simulation. *Advances in Space Research*, 36:694–697.

Kay, S. T., da Silva, A. C., Aghanim, N., Blanchard, A., Liddle, A. R., Puget, J.-L., Sadat, R., and Thomas, P. A. (2007). The evolution of clusters in the CLEF cosmological simulation: X-ray structural and scaling properties. *MNRAS*, 377:317–334.

Kay, S. T., Thomas, P. A., Jenkins, A., and Pearce, F. R. (2004). Cosmological simulations of the intracluster medium. *MNRAS*, 355:1091–1104.

Kellogg, E., Gursky, H., Tananbaum, H., Giacconi, R., and Pounds, K. (1972). The Extended X-Ray Source at M87. *ApJ*, 174:L65+.

Knop, R. A., Aldering, G., Amanullah, R., Astier, P., Blanc, G., Burns, M. S., Conley, A., Deustua, S. E., Doi, M., Ellis, R., Fabbro, S., Folatelli, G., Fruchter, A. S., Garavini, G., Garmond, S., Garton, K., Gibbons, R., Goldhaber, G., Goobar, A., Groom, D. E., Hardin, D., Hook, I., Howell, D. A., Kim, A. G., Lee, B. C., Lidman, C., Mendez, J., Nobili, S., Nugent, P. E., Pain, R., Panagia, N., Pennypacker, C. R., Perlmutter, S., Quimby, R., Raux, J., Regnault, N., Ruiz-Lapuente, P., Sainton, G., Schaefer, B., Schahmaneche, K., Smith, E., Spadafora, A. L., Stanishev, V., Sullivan, M., Walton, N. A., Wang, L., Wood-Vasey, W. M., and Yasuda, N. (2003). New Constraints on $\Omega_M$, $\Omega_\Lambda$, and w from an Independent Set of 11 High-Redshift Supernovae Observed with the Hubble Space Telescope. *ApJ*, 598:102–137.

Koester, B. P., McKay, T. A., Annis, J., Wechsler, R. H., Evrard, A. E., Rozo, E., Bleem, L., Sheldon, E. S., and Johnston, D. (2007). MaxBCG: A Red-Sequence Galaxy Cluster Finder. *ApJ*, 660:221–238.

Komatsu, E., Dunkley, J., Nolta, M. R., Bennett, C. L., Gold, B., Hinshaw, G., Jarosik, N., Larson, D., Limon, M., Page, L., Spergel, D. N., Halpern, M., Hill, R. S., Kogut, A., Meyer, S. S., Tucker, G. S., Weiland, J. L., Wollack, E., and Wright, E. L. (2009). Five-Year Wilkinson Microwave Anisotropy Probe Observations: Cosmological Interpretation. *ApJS*, 180:330–376.

Kravtsov, A. V. and Yepes, G. (2000). On the supernova heating of the intergalactic medium. *MNRAS*, 318:227–238.

Lamer, G., Schwope, A., Böhringer, H., Faßbender, R., Schuecker, P., Mullis, C., and Rosati, P. (2006). The XMM-Newton Distant Cluster Project. In A. Wilson, editor, *The X-ray Universe 2005*, volume 604 of *ESA Special Publication*, pages 729–+.

Lewis, G. F., Babul, A., Katz, N., Quinn, T., Hernquist, L., and Weinberg, D. H. (2000). The Effects of Gasdynamics, Cooling, Star Formation, and Numerical Resolution in Simulations of Cluster Formation. *ApJ*, 536:623–644.

Liddle, A. R., Viana, P. T. P., Romer, A. K., and Mann, R. G. (2001). Apparent and actual galaxy cluster temperatures. *MNRAS*, 325:875–880.

Linder, E. V. and Jenkins, A. (2003). Cosmic structure growth and dark energy. *MNRAS*, 346:573–583.

Markevitch, M. (1998). The L X-T Relation and Temperature Function for Nearby Clusters Revisited. *ApJ*, 504:27–+.

Maughan, B. J., Jones, C., Forman, W., and Van Speybroeck, L. (2008). Images, Structural Properties, and Metal Abundances of Galaxy Clusters Observed with Chandra ACIS-I at $0.1 < z < 1.3$. *ApJS*, 174:117–135.

Mazzotta, P., Rasia, E., Moscardini, L., and Tormen, G. (2004). Comparing the temperatures of galaxy clusters from hydrodynamical N-body simulations to Chandra and XMM-Newton observations. *MNRAS*, 354:10–24.

Miller, C. J., Nichol, R. C., Reichart, D., Wechsler, R. H., Evrard, A. E., Annis, J., McKay, T. A., Bahcall, N. A., Bernardi, M., Boehringer, H., Connolly, A. J., Goto, T., Kniazev, A., Lamb, D., Postman, M., Schneider, D. P., Sheth, R. K., and Voges, W. (2005). The C4 Clustering Algorithm: Clusters of Galaxies in the Sloan Digital Sky Survey. *AJ*, 130:968–1001.

Mohr, J. J., Evrard, A. E., Fabricant, D. G., and Geller, M. J. (1995). Cosmological Constraints from Observed Cluster X-Ray Morphologies. *ApJ*, 447:8–+.

Muanwong, O., Kay, S. T., and Thomas, P. A. (2006). Evolution of X-Ray Cluster Scaling Relations in Simulations with Radiative Cooling and Nongravitational Heating. *ApJ*, 649:640–648.

Muanwong, O., Thomas, P. A., Kay, S. T., and Pearce, F. R. (2002). The effect of cooling and preheating on the X-ray properties of clusters of galaxies. *MNRAS*, 336:527–540.

Mullis, C. R., Rosati, P., Lamer, G., Böhringer, H., Schwope, A., Schuecker, P., and Fassbender, R. (2005). Discovery of an X-Ray-luminous Galaxy Cluster at z=1.4. *ApJ*, 623:L85–L88.

Navarro, J. F., Frenk, C. S., and White, S. D. M. (1995). Simulations of X-ray clusters. *MNRAS*, 275:720–740.

Navarro, J. F. and White, S. D. M. (1994). Simulations of dissipative galaxy formation in hierarchically clustering universes-2. Dynamics of the baryonic component in galactic haloes. *MNRAS*, 267:401–412.

Onuora, L. I., Kay, S. T., and Thomas, P. A. (2003). Simulated X-ray cluster temperature maps. *MNRAS*, 341:1246–1252.

Ota, N. and Mitsuda, K. (2004). A uniform X-ray analysis of 79 distant galaxy clusters with ROSAT and ASCA. *A&A*, 428:757–779.

Pacaud, F., Pierre, M., Adami, C., Altieri, B., Andreon, S., Chiappetti, L., Detal, A., Duc, P.-A., Galaz, G., Gueguen, A., Le Fèvre, J.-P., Hertling, G., Libbrecht, C., Melin, J.-B., Ponman, T. J., Quintana, H., Refregier, A., Sprimont, P.-G., Surdej, J., Valtchanov, I., Willis, J. P., Alloin, D., Birkinshaw, M., Bremer, M. N., Garcet, O., Jean, C., Jones, L. R., Le Fèvre, O., Maccagni, D., Mazure, A., Proust, D., Röttgering, H. J. A., and Trinchieri, G. (2007). The XMM-LSS survey: the Class 1 cluster sample over the initial $5deg^2$ and its cosmological modelling. *MNRAS*, 382:1289–1308.

Pearce, F. R., Thomas, P. A., Couchman, H. M. P., and Edge, A. C. (2000). The effect of radiative cooling on the X-ray properties of galaxy clusters. *MNRAS*, 317:1029–1040.

Percival, W. J., Cole, S., Eisenstein, D. J., Nichol, R. C., Peacock, J. A., Pope, A. C., and Szalay, A. S. (2007). Measuring the Baryon Acoustic Oscillation scale using the Sloan Digital Sky Survey and 2dF Galaxy Redshift Survey. *MNRAS*, 381:1053–1066.

Perlmutter, S. and Schmidt, B. P. (2003). Measuring Cosmology with Supernovae. In K. Weiler, editor, *Supernovae and Gamma-Ray Bursters*, volume 598 of *Lecture Notes in Physics, Berlin Springer Verlag*, pages 195–217.

Pierre, M., Chiappetti, L., Pacaud, F., Gueguen, A., Libbrecht, C., Altieri, B., Aussel, H., Gandhi, P., Garcet, O., Gosset, E., Paioro, L., Ponman, T. J., Read, A. M., Refregier, A., Starck, J.-L., Surdej, J., Valtchanov, I., Adami, C., Alloin, D., Alshino, A., Andreon, S., Birkinshaw, M., Bremer, M., Detal, A., Duc, P.-A., Galaz, G., Jones, L., Le Fèvre, J.-P., Le Fèvre, O., Maccagni, D., Mazure, A., Quintana, H., Röttgering, H. J. A., Sprimont, P.-G., Tasse, C., Trinchieri, G., and Willis, J. P. (2007). The XMM-Large Scale Structure catalogue: X-ray sources and associated optical data. Version I. *MNRAS*, 382:279–290.

Ponman, T. J., Cannon, D. B., and Navarro, J. F. (1999). The thermal imprint of galaxy formation on X-ray clusters. *Nat*, 397:135–137.

Pratt, G. W., Böhringer, H., Croston, J. H., Arnaud, M., Borgani, S., Finoguenov, A., and Temple, R. F. (2007). Temperature profiles of a representative sample of nearby X-ray galaxy clusters. *A&A*, 461:71–80.

Pratt, G. W., Croston, J. H., Arnaud, M., and Boehringer, H. (2008). Galaxy cluster X-ray luminosity scaling relations from a representative local sample (REXCESS). *ArXiv e-prints*.

Press, W. H. and Schechter, P. (1974). Formation of Galaxies and Clusters of Galaxies by Self-Similar Gravitational Condensation. *ApJ*, 187:425–438.

Puchwein, E., Sijacki, D., and Springel, V. (2008). Simulations of AGN feedback in galaxy clusters and groups: impact on gas fractions and the Lx-T scaling relation. *ArXiv e-prints*.

Reiprich, T. H. and Böhringer, H. (2002). The Mass Function of an X-Ray Flux-limited Sample of Galaxy Clusters. *ApJ*, 567:716–740.

Romer, A. K., Nichol, R. C., Holden, B. P., Ulmer, M. P., Pildis, R. A., Merrelli, A. J., Adami, C., Burke, D. J., Collins, C. A., Metevier, A. J., Kron, R. G., and Commons, K. (2000). The Bright SHARC Survey: The Cluster Catalog. *ApJS*, 126:209–269.

Romer, A. K., Viana, P. T. P., Liddle, A. R., and Mann, R. G. (2001). A Serendipitous Galaxy Cluster Survey with XMM: Expected Catalog Properties and Scientific Applications. *ApJ*, 547:594–608.

Rosati, P. (1998). Results from the ROSAT Deep Cluster Survey. *Astronomische Nachrichten*, 319:79–+.

Rosati, P., Borgani, S., and Norman, C. (2002). The Evolution of X-ray Clusters of Galaxies. *ARA&A*, 40:539–577.

Rozo, E., Wechsler, R. H., Rykoff, E. S., Annis, J. T., Becker, M. R., Evrard, A. E., Frieman, J. A., Hansen, S. M., Hao, J., Johnston, D. E., Koester, B. P., McKay, T. A., Sheldon, E. S., and Weinberg, D. H. (2009). Cosmological Constraints from the SDSS maxBCG Cluster Catalog. *ArXiv e-prints*.

Sahlén, M., Viana, P. T. P., Liddle, A. R., Romer, A. K., Davidson, M., Hosmer, M., Lloyd-Davies, E., Sabirli, K., Collins, C. A., Freeman, P. E., Hilton, M., Hoyle, B., Kay, S. T., Mann, R. G., Mehrtens, N., Miller, C. J., Nichol, R. C., Stanford, S. A., and West, M. J. (2009). The XMM Cluster Survey: forecasting cosmological and cluster scaling-relation parameter constraints. *MNRAS*, 397:577–607.

Sanderson, A. J. R. and Ponman, T. J. (2003). The Birmingham-CfA cluster scaling project - II. Mass composition and distribution. *MNRAS*, 345:1241–1254.

Sanderson, A. J. R., Ponman, T. J., Finoguenov, A., Lloyd-Davies, E. J., and Markevitch, M. (2003). The Birmingham-CfA cluster scaling project - I. Gas fraction and the$M-T_X$ relation. *MNRAS*, 340:989–1010.

Santos, J. S., Rosati, P., Tozzi, P., Böhringer, H., Ettori, S., and Bignamini, A. (2008). Searching for cool core clusters at high redshift. *A&A*, 483:35–47.

Sarazin, C. L. and Bahcall, J. N. (1977). X-ray line emission for clusters of galaxies. II - Numerical models. *ApJS*, 34:451–467.

Schlegel, D. J., Finkbeiner, D. P., and Davis, M. (1998). Maps of Dust Infrared Emission for Use in Estimation of Reddening and Cosmic Microwave Background Radiation Foregrounds. *ApJ*, 500:525–+.

Schneider, D. P., Hall, P. B., Richards, G. T., Strauss, M. A., Vanden Berk, D. E., Anderson, S. F., Brandt, W. N., Fan, X., Jester, S., Gray, J., Gunn, J. E., SubbaRao, M. U., Thakar, A. R., Stoughton, C., Szalay, A. S., Yanny, B., York, D. G., Bahcall, N. A., Barentine, J., Blanton, M. R., Brewington, H., Brinkmann, J., Brunner, R. J., Castander, F. J., Csabai, I., Frieman, J. A., Fukugita, M., Harvanek, M., Hogg, D. W., Ivezić, Ž., Kent, S. M., Kleinman, S. J., Knapp, G. R., Kron, R. G., Krzesiński, J., Long, D. C., Lupton, R. H., Nitta, A., Pier, J. R., Saxe, D. H., Shen, Y., Snedden, S. A., Weinberg, D. H., and Wu, J. (2007). The Sloan Digital Sky Survey Quasar Catalog. IV. Fifth Data Release. *AJ*, 134:102–117.

Schuecker, P., Böhringer, H., Collins, C. A., and Guzzo, L. (2003). The REFLEX galaxy cluster survey. VII. $\Omega_m and \sigma_8$ from cluster abundance and large-scale clustering. *A&A*, 398:867–877.

Short, C. J. and Thomas, P. A. (2009). Combining Semianalytic Models with Simulations of Galaxy Clusters: The Need for Heating from Active Galactic Nuclei. *ApJ*, 704:915–929.

Smith, J. A., Tucker, D. L., Kent, S., Richmond, M. W., Fukugita, M., Ichikawa, T., Ichikawa, S.-i., Jorgensen, A. M., Uomoto, A., Gunn, J. E., Hamabe, M., Watanabe, M., Tolea, A., Henden, A., Annis, J., Pier, J. R., McKay, T. A., Brinkmann, J., Chen, B., Holtzman, J., Shimasaku, K., and York, D. G. (2002). The u'g'r'i'z' Standard-Star System. *AJ*, 123:2121–2144.

Smith, S. (1936). The Mass of the Virgo Cluster. *ApJ*, 83:23–+.

Springel, V. (2005). The cosmological simulation code GADGET-2. *MNRAS*, 364:1105–1134.

Stanford, S. A., Romer, A. K., Sabirli, K., Davidson, M., Hilton, M., Viana, P. T. P., Collins, C. A., Kay, S. T., Liddle, A. R., Mann, R. G., Miller, C. J., Nichol, R. C., West, M. J., Conselice, C. J., Spinrad, H., Stern, D., and Bundy, K. (2006). The XMM Cluster Survey: A Massive Galaxy Cluster at z = 1.45. *ApJ*, 646:L13–L16.

Suginohara, T. and Ostriker, J. P. (1998). The Effect of Cooling on the Density Profile of Hot Gas in Clusters of Galaxies: Is Additional Physics Needed? *ApJ*, 507:16–23.

Thomas, P. A. and Couchman, H. M. P. (1992). Simulating the formation of a cluster of galaxies. *MNRAS*, 257:11–31.

Valdes, F. G. (1998). The IRAF Mosaic Data Reduction Package. In R. Albrecht, R. N. Hook, & H. A. Bushouse, editor, *Astronomical Data Analysis Software and Systems VII*, volume 145 of *Astronomical Society of the Pacific Conference Series*, pages 53–+.

Véron-Cetty, M.-P. and Véron, P. (2006). A catalogue of quasars and active nuclei: 12th edition. *A&A*, 455:773–777.

Viana, P. T. P. and Liddle, A. R. (1996). The cluster abundance in flat and open cosmologies. *MNRAS*, 281:323–+.

Vikhlinin, A., Forman, W., and Jones, C. (1999). Outer Regions of the Cluster Gaseous Atmospheres. *ApJ*, 525:47–57.

Vikhlinin, A., Kravtsov, A., Forman, W., Jones, C., Markevitch, M., Murray, S. S., and Van Speybroeck, L. (2006). Chandra Sample of Nearby Relaxed Galaxy Clusters: Mass, Gas Fraction, and Mass-Temperature Relation. *ApJ*, 640:691–709.

Vikhlinin, A., Kravtsov, A. V., Burenin, R. A., Ebeling, H., Forman, W. R., Hornstrup, A., Jones, C., Murray, S. S., Nagai, D., Quintana, H., and Voevodkin, A. (2009). Chandra Cluster Cosmology Project III: Cosmological Parameter Constraints. *ApJ*, 692:1060–1074.

Vikhlinin, A., Markevitch, M., Murray, S. S., Jones, C., Forman, W., and Van Speybroeck, L. (2005). Chandra Temperature Profiles for a Sample of Nearby Relaxed Galaxy Clusters. *ApJ*, 628:655–672.

Vikhlinin, A., McNamara, B. R., Forman, W., Jones, C., Quintana, H., and Hornstrup, A. (1998). Evolution of Cluster X-Ray Luminosities and Radii: Results from the 160 Square Degree ROSAT Survey. *ApJ*, 498:L21+.

Watson, M. G., Schröder, A. C., Fyfe, D., Page, C. G., Lamer, G., Mateos, S., Pye, J., Sakano, M., Rosen, S., Ballet, J., Barcons, X., Barret, D., Boller, T., Brunner, H., Brusa, M., Caccianiga, A., Carrera, F. J., Ceballos, M., Della Ceca, R., Denby, M., Denkinson, G., Dupuy, S., Farrell, S., Fraschetti, F., Freyberg, M. J., Guillout, P., Hambaryan, V., Maccacaro, T., Mathiesen, B., McMahon, R., Michel, L., Motch, C., Osborne, J. P., Page, M., Pakull, M. W., Pietsch, W., Saxton, R., Schwope, A., Severgnini, P., Simpson, M., Sironi, G., Stewart, G., Stewart, I. M., Stobbart, A.-M., Tedds, J., Warwick, R., Webb, N., West, R., Worrall, D., and Yuan, W. (2009). The XMM-Newton serendipitous survey. V. The Second XMM-Newton serendipitous source catalogue. *A&A*, 493:339–373.

White, S. D. M. and Rees, M. J. (1978). Core condensation in heavy halos - A two-stage theory for galaxy formation and clustering. *MNRAS*, 183:341–358.

Wu, K. K. S., Fabian, A. C., and Nulsen, P. E. J. (2000). Non-gravitational heating in the hierarchical formation of X-ray clusters. *MNRAS*, 318:889–912.

Young, M., Elvis, M., and Risaliti, G. (2009). The Fifth Data Release Sloan Digital Sky Survey/XMM-Newton Quasar Survey. *ApJS*, 183:17–32.

Zwicky, F. (1933). Die Rotverschiebung von extragalaktischen Nebeln. *Helvetica Physica Acta*, 6:110–127.

Zwicky, F. (1937). On the Masses of Nebulae and of Clusters of Nebulae. *ApJ*, 86:217–+.

# Appendix A

# Lumdist: The IDL routine used to calculate $d_L$

This is the code source for Lumdist. Written by W. Landsman , this code is used, unchanged, to calculate cosmological distances for use in the Selection function.

;+
; NAME:
; LUMDIST
;
; PURPOSE:
; Calculate luminosity distance (in Mpc) of an object given its redshift
; EXPLANATION:
; The luminosity distance in the Friedmann-Robertson-Walker model is
; taken from Caroll, Press, and Turner (1992, ARAA, 30, 499), p. 511
; Uses a closed form (Mattig equation) to compute the distance when the
; cosmological constant is zero. Otherwise integrates the function using
; QSIMP.
; CALLING SEQUENCE:
; result = lumdist($z, [H0 =, k =, Omega_M =, Lambda0 =, q0 =, /SILENT]$)
;
; INPUTS:
; z = redshift, positive scalar or vector
;
; OPTIONAL KEYWORD INPUTS:
; /SILENT - If set, the program will not display adopted cosmological
; parameters at the terminal.
; H0: Hubble parameter in km/s/Mpc, default is 70
;

; No more than two of the following four parameters should be
; specified. None of them need be specified – the adopted defaults
; are given.
; k - curvature constant, normalized to the closure density. Default is
; 0, indicating a flat universe
; $Omega_m$ - Matter density, normalized to the closure density, default
; is 0.3. Must be non-negative
; Lambda0 - Cosmological constant, normalized to the closure density,
; default is 0.7
; q0 - Deceleration parameter, numeric scalar= $-R*(R'')/(R')^2$, default
; is -0.5
;
; OUTPUTS:
; The result of the function is the luminosity distance (in Mpc) for each
; input value of z.
;
; EXAMPLE:
; (1) Plot the distance of a galaxy in Mpc as a function of redshift out
; to z = 5.0, assuming the default cosmology ($Omega_m = 0.3, Lambda = 0.7$,
; H0 = 70 km/s/Mpc)
;
; IDL¿ z = findgen(50)/10.
; IDL¿ plot,z,lumdist(z),xtit='z',ytit='Distance (Mpc)'
; ; Now overplot the relation for zero cosmological constant and
; $Omega_m = 0.3$
; IDL¿ oplot,z,lumdist(z,lambda=0,omega=0.3),linestyle=1
; COMMENTS:
; (1) Integrates using the IDL Astronomy Version procedure QSIMP. (The
; intrinsic IDL QSIMP function is not called because of its ridiculous
; restriction that only scalar arguments can be passed to the integrating
; function.)
; (2) Can fail to converge at high redshift for closed universes with
; non-zero lambda. This can presumably be fixed by replacing QSIMP with
; an integrator that can handle a singularity
; PROCEDURES CALLED:
; $COSMO\_PARAM, QSIMP$
; REVISION HISTORY:
; Written W. Landsman Raytheon ITSS April 2000
; Avoid integer overflow for more than 32767 redshifts July 2001
;-
function ldist, z, q0 = q0, lambda0 = lambda0
term1 = $(1. + z)^2$
term2 = 1.+2.*(q0+lambda0)*z

```
term3 = z*(2.+z)*lambda0
denom = (term1*term2 - term3)
out = z*0.
good = where(denom GT 0.0, Ngood)
if Ngood GT 0 then out[good] = 1./sqrt(denom[good])
return, out
end


FUNCTION lumdist, z, h0=h0, k = k, Lambda0 = lambda0, Omega_m = Omega_m, $
q0 = q0, Silent = silent


if N_params() eq 0 then begin
print,'Syntax: result = lumdist(z, H0 = ,k=, Lambda0 = ])'
print,'Returns luminosity distance in Mpc'
return, 0.
endif

n = N_elements(z)
cosmo_param, Omega_m, Lambda0, k, q0

; Check keywords

c = 2.9979e5 ;; speed of light in km/s
if N_elements(H0) EQ 0 then H0 = 70
if not keyword_set(silent) then $
print,'LUMDIST : H0 :', h0,' Omega_m :', omega_m,' Lambda0', lambda0, $
' q0: ',q0, ' k: ', k, f='(A,I3,A,f5.2,A,f5.2,A,f5.2,A,F5.2)'


; For the case of Lambda = 0, we use the closed form from equation 5.238 of
; Astrophysical Formulae (Lang 1998). This avoids terms that almost cancel
; at small q0*z better than the more familiar Mattig formula.
;
if lambda0 EQ 0 then begin
denom = sqrt(1+2*q0*z) + 1 + q0*z
dlum = (c*z/h0)*(1 + z*(1-q0)/denom)
return,dlum

; For non-zero lambda
endif else begin
dlum = z*0.0
```

```
for i=0L,N-1 do begin
if z[i] LE 0.0 then dlum[i] = 0.0 else begin
qsimp,'LDIST',0,z[i], lz,q0 = q0, Lambda0 = lambda0
dlum[i] = lz
endelse
endfor

if k GT 0 then $
dlum = sinh(sqrt(k)*dlum)/sqrt(k) $
else if k LT 0 then $
dlum = sin(sqrt(-k)*dlum)/sqrt(-k) ¿ 0
return, c*(1+z)*dlum/h0
endelse

end
```

# Appendix B

# XAPA flow charts

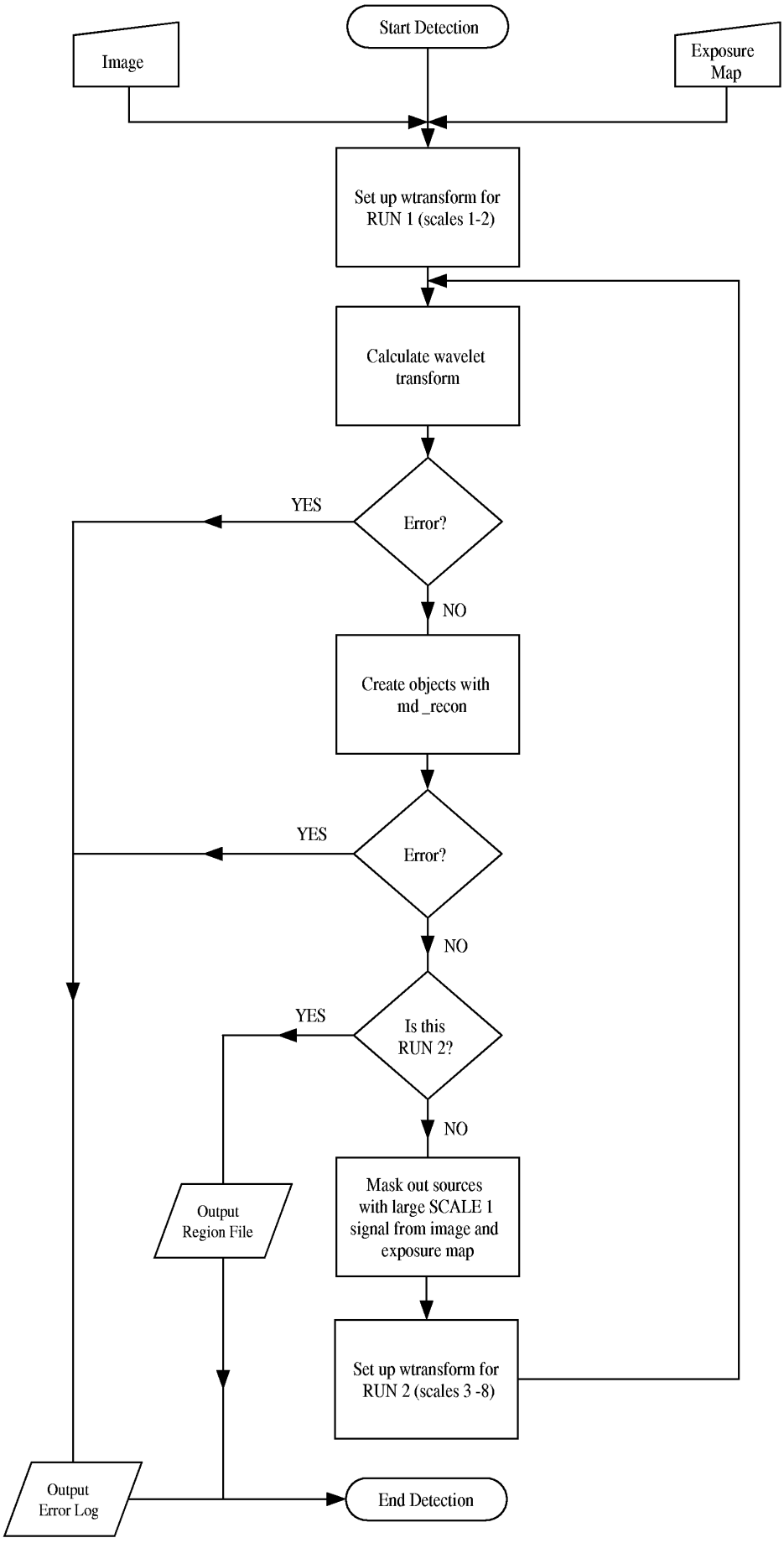


Figure B.1: Detection Flow chart. Image credit: Davidson (2005)

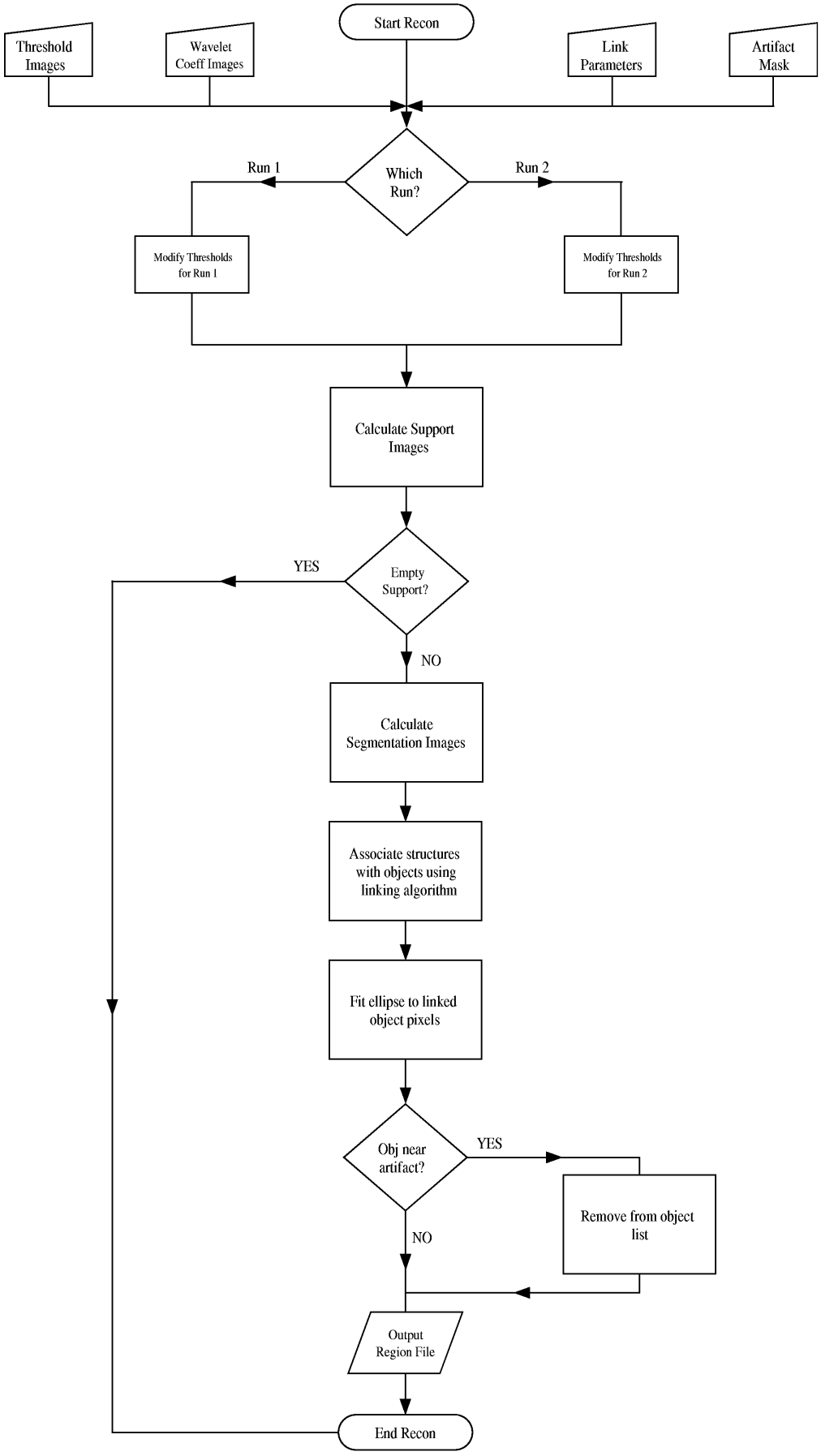


Figure B.2: Reconstruction Flow chart. Image credit: Davidson (2005)

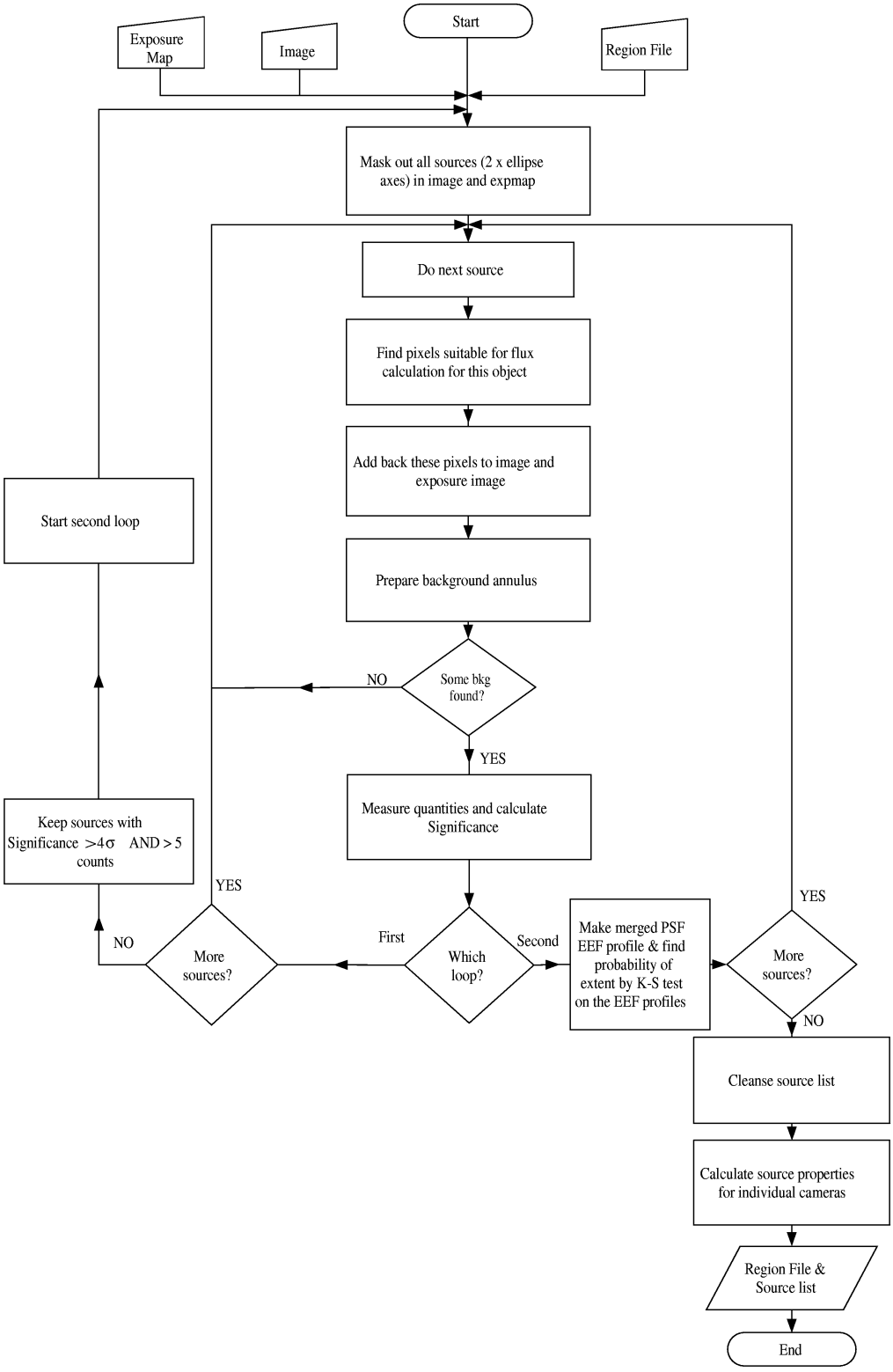


Figure B.3: Find Source Properties Flow chart. Image credit: Davidson (2005)

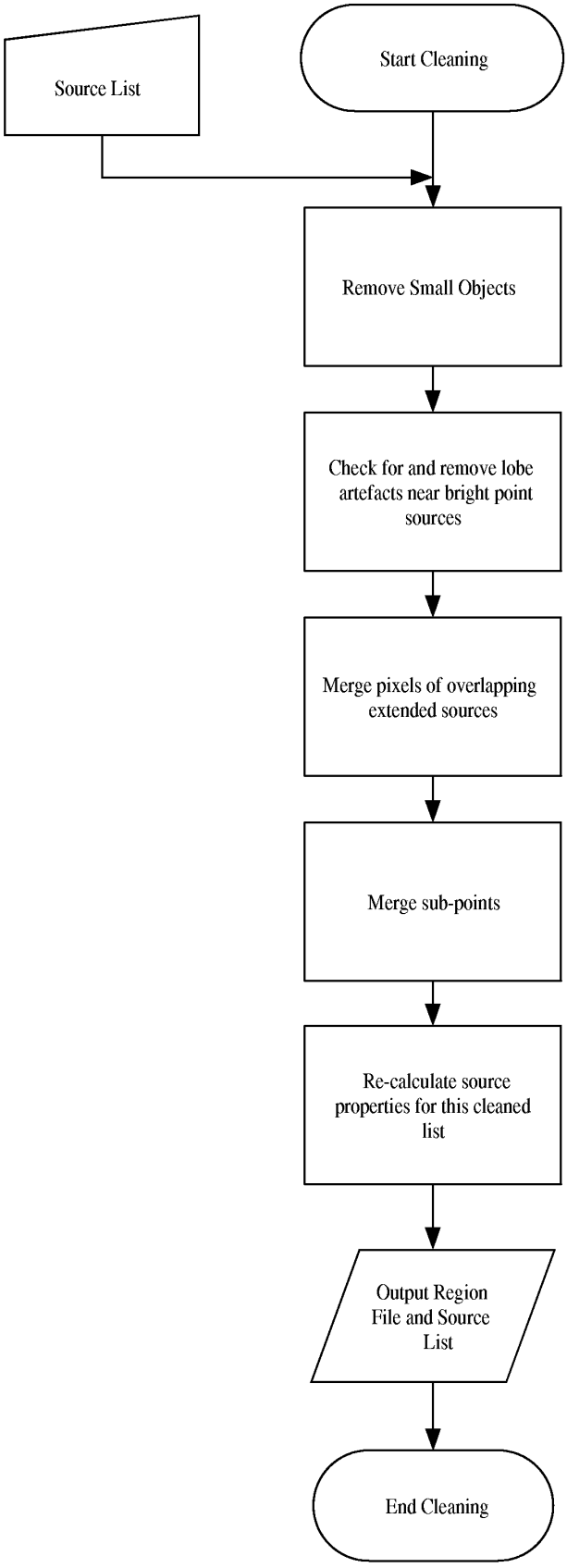


Figure B.4: Source List Cleaning Flow chart. Image credit: Davidson (2005)

# Appendix C

# The NXS

The following text has been edited from that provided by N. Merhtens, who undertook the data reduction and redshift fitting described in this Appendix.

Thirty-eight nights of wide-field mosaic CCD imaging were awarded at the NOAO 4m telescopes at KPNO, Arizona; and CTIO, Chile between November 2005 and April 2008 in 6 observing campaigns. An additional 10 nights were subsequently awarded and carried out in April 2009. Each mosaic field is $36'$ by $36'$ wide and thus encompasses an entire XCS ObsID usually containing multiple cluster candidates. This method therefore enables a relatively cheap and efficient method of cluster detection. During each observing campaign, Sloan $r'$- and $z'$- band imaging were taken in a sequence of exposures totaling 1200s and 1500s respectively. Using these exposure times the NXS survey reached a typical $r'$-band depth of 25.00 and $z'$-band depth of 23.79, allowing the detection of galaxy clusters out to a redshift of $z$=1.

Upon completion of the NXS survey, 174 XCS fields had been observed with full exposure times (160 from XCS DR1, 14 from XCS DR2), containing 473 cluster candidates (435 from XCS DR1, 38 from XCS DR2). Unfortunately ∼50% of the awarded 48 nights were lost to bad weather and instrumentation failure.

Data reduction was largely carried out following version 7.02 of Buell Jannuzi's reduction notes [1] using the IRAF MSCRED Valdes (1998) package which treats a mosaic field as a single CCD. Photometric calibration was conducted using a combination of SDSS photometric standard stars Smith et al. (2002), fields with SDSS coverage,and NXS fields used as standard frames achieving a zeropoint accuracy of ∼2%. Galaxy catalogs were extracted from each NXS image using Source Extractor Bertin and Arnouts (1996) and magnitudes corrected for atmospheric extinction and galactic extinction using the Schlegel et al dust maps Schlegel et al. (1998).

[1] http://www.noao.edu/noao/noaodeep/ReductionOpt/frames.html

The NXS survey uses a redshift algorithm which seeks out overdensities of galaxies with similar colours above that of the background field distribution (similar to the MAXBCG cluster finder Koester et al. (2007) ). The NXS redshift algorithm derives photometric redshifts for the cluster candidates within each NXS image by comparing an observed cluster red sequence to an empirical red sequence model. The theoretical model is created from a fiducial low red-sequence colour magnitude relation at $z$=0.1 that has been evolved with redshift using a galaxy population synthesis code. Potential cluster galaxies are extracted from within twice the X-ray extent of each cluster candidate and a background field is derived from the remainder of the NXS image. An unbinned likelihood function is then used to identify overdensities in colour space of these potential cluster galaxies above that of the background field distribution. The colour of the overdensity peak corresponds to a redshift estimate for the cluster. The algorithm assumes a simple Gaussian distribution in colour as its cluster model (similar to MAXBCG) and a histogram in colour of the field galaxies within each NXS image as its background model. This model is then maximized to produce simultaneous redshift and richness estimates. Finally, a Kolmogorov-Smirnov test (KS-test) is used to assess the significance of the cluster detection and a high-z flag assigned by counting the number galaxies solely detected in the $z'$-band.

# Appendix D

# XCS DR3 StatSam Tables

| XCS Name | Obsid | RA | Dec | Counts | Flux | Literature Name | Match Distance | Literature Redshift | Sig |
|---|---|---|---|---|---|---|---|---|---|
| XMMXCS J033911.9 − 352621.8 | 0012830101 | 54.799616 | −35.439397 | 2063.4316 | 1.5341144e−13 | CXOU J033912.0-352609 | 12.8853 | - | 123.95 |
| XMMXCS J105341.9 + 573521.9 | 0022740301 | 163.42487 | 57.589439 | 571.04563 | 4.7314597e−14 | RX J1053.7+5735 | 17.8693 | 1.140000 | 222.00 |
| XMMXCS J012435.2 + 040051.7 | 0025541601 | 21.147054 | 4.0143851 | 90.921156 | 3.4976529e−14 | XDCS mf J012435.6+040107 | 4.01732 | 0.422000 | 43.07 |
| XMMXCS J230251.8 + 084135.3 | 0032140201 | 345.71622 | 8.6931421 | 88.770209 | 2.6913258e−14 | CXOMP J230252.0+084137 | 2.34371 | 0.041500 | 74.68 |
| XMMXCS J230227.1 + 083906.4 | 0032140201 | 345.61297 | 8.6517960 | 49.229621 | 7.7738997e−15 | CXOMP J230227.7+083859 | 10.0271 | 0.425600 | 14.63 |
| XMMXCS J022457.8 − 034851.1 | 0037980301 | 36.241172 | −3.8142060 | 585.82884 | 8.1788013e−14 | XLSSC 001 | 11.8229 | 0.612800 | 466.41 |
| XMMXCS J022643.7 − 034107.7 | 0037980401 | 36.682290 | −3.6854855 | 186.41260 | 4.1341701e−14 | XLSSC 009 | 15.3508 | 0.327000 | 28.75 |
| XMMXCS J022400.2 − 032517.8 | 0037980801 | 36.001190 | −3.4216135 | 50.508664 | 1.9648002e−14 | XLSSC 032 | 8.79816 | 0.810000 | 34.16 |
| XMMXCS J022721.8 − 032151.0 | 0037981001 | 36.841036 | −3.3641888 | 495.92062 | 8.5185648e−14 | XLSSC 010 | 12.1339 | 0.329000 | 255.96 |
| XMMXCS J022738.4 − 031801.1 | 0037981501 | 36.910238 | −3.3003186 | 212.31872 | 5.2785782e−14 | XLSSC 003 | 5.64544 | 0.837800 | 99.76 |
| XMMXCS J022145.4 − 034618.0 | 0037982501 | 35.439232 | −3.7716749 | 1667.9955 | 3.4508902e−13 | SL J0221.7-0345 | 11.5537 | 0.429000 | - |
| XMMXCS J030317.3 + 001235.6 | 0041170101 | 45.822455 | 0.20991029 | 152.04488 | 1.1630191e−14 | BLOX J0303.3+0012.8 | 17.0677 | - | 51.17 |
| XMMXCS J030211.2 − 000132.6 | 0041170101 | 45.546819 | −0.025739038 | 213.52219 | 1.0640209e−14 | BLOX J0302.2-0001.5 | 11.4765 | - | 136.34 |
| XMMXCS J030205.5 − 000001.8 | 0041170101 | 45.523223 | −0.00051526286 | 393.51373 | 2.3111142e−14 | BLOX J0302.0-0000.0 | 3.17265 | - | 235.23 |
| XMMXCS J163340.9 + 571422.0 | 0049540301 | 248.42046 | 57.239450 | 136.18277 | 1.1602591e−14 | RIXOS F223 572 | 12.7068 | 0.239000 | 32.60 |
| XMMXCS J033831.2 − 352653.2 | 0055140101 | 54.630354 | −35.448113 | 42221.219 | 3.6646123e−12 | NGC 1399 GROUP | 23.3727 | 0.004600 | - |
| XMMXCS J031833.0 − 030258.7 | 0056022201 | 49.637507 | −3.0496424 | 5514.9682 | 3.7252625e−13 | 400d J0318-0302 | 12.7990 | 0.370000 | - |
| XMMXCS J133129.5 + 110755.9 | 0061940101 | 202.87332 | 11.132208 | 141.93434 | 6.7383514e−14 | RX J1331.5+1108 | 1.45478 | .081 | 95.07 |
| XMMXCS J052215.3 − 362514.2 | 0065760201 | 80.563976 | −36.420612 | 1703.4121 | 1.3847965e−13 | 400d J0522-3624 | 17.2415 | 0.472000 | - |
| XMMXCS J023759.7 − 522403.9 | 0067190101 | 39.498768 | −52.401092 | 2338.2078 | 4.3529081e−13 | ABELL 3038 | 18.1076 | 0.135000 | - |
| XMMXCS J095341.4 + 014157.7 | 0070940401 | 148.42286 | 1.6993759 | 6028.2509 | 6.5754715e−13 | SDSS-C4-DR3 1212 | 4.89132 | 0.098000 | - |
| XMMXCS J135047.9 + 600702.8 | 0071340501 | 207.69961 | 60.117458 | 785.61486 | 1.0867162e−13 | RDCS J1350+6007 | 6.15660 | 0.804000 | 144.56 |
| XMMXCS J121334.8 + 025349.4 | 0081340801 | 183.39536 | 2.8970609 | 2071.8156 | 1.5801999e−13 | BLOX J1213.5+0253.7 | 4.94957 | 0.409000 | - |
| XMMXCS J111834.4 + 074430.6 | 0082340101 | 169.64362 | 7.7418598 | 206.91977 | 5.5889600e−15 | BLOX J1118.5+0744.5 | 5.95584 | - | 69.53 |
| XMMXCS J111726.1 + 074327.5 | 0082340101 | 169.35893 | 7.7243106 | 1247.5803 | 8.5386703e−14 | XDCS mf J111726.2+074316 | 7.51158 | 0.232000 | 547.21 |
| XMMXCS J125313.8 + 155544.6 | 0082990101 | 193.30753 | 15.929061 | 1027.5642 | 1.2561390e−13 | NSCS J125309+155549 | 14.2621 | 0.275000 | 395.86 |
| XMMXCS J135452.3 + 691727.2 | 0083960101 | 208.71793 | 69.290890 | 451.72417 | 3.7392553e−14 | RX J1354.8+6917 | 18.4760 | 0.207000 | 63.31 |
| XMMXCS J084834.9 + 445339.7 | 0085150101 | 132.14568 | 44.894380 | 96.561593 | 4.0247268e−15 | Lynx W | 9.38778 | 1.270000 | 23.05 |
| XMMXCS J084848.2 + 445606.1 | 0085150101 | 132.20084 | 44.935042 | 921.03782 | 4.4473035e−14 | RX J0848.7+4456 | 15.2344 | 0.574000 | 338.80 |
| XMMXCS J052111.0 − 253106.2 | 0085640101 | 80.295973 | −25.518411 | 174.12312 | 4.3218595e−14 | 400d J0521-2530 | 22.7458 | 0.581000 | 73.09 |
| XMMXCS J093709.6 + 611611.9 | 0085640201 | 144.29016 | 61.269984 | 464.32714 | 3.6124770e−14 | MaxBCG J144.28663+61.27052 | 6.38664 | 0.229550 | 75.26 |
| XMMXCS J141832.1 + 251112.8 | 0089960301 | 214.63394 | 25.186895 | 5467.8892 | 1.0868799e−11 | WARP J1418.5+2511 | 26.8740 | 0.296000 | - |
| XMMXCS J115811.6 + 552126.0 | 0090020101 | 179.54852 | 55.357236 | 63.744409 | 1.3228002e−14 | RX J1158.1+5521 | 18.9599 | 0.135000 | 21.87 |
| XMMXCS J004231.6 + 005118.8 | 0090070201 | 10.632023 | 0.85523324 | 238.44844 | 4.3860238e−14 | MaxBCG J010.63093+00.85021 | 18.5064 | 0.153950 | 61.43 |
| XMMXCS J004333.8 + 010108.9 | 0090070201 | 10.891174 | 1.0191638 | 573.97963 | 9.5037796e−14 | SDSS CE J010.888028+01.015296 | 18.2383 | 0.185942 | 204.08 |
| XMMXCS J235117.1 + 201351.1 | 0093190301 | 357.82155 | 20.230863 | 168.29494 | 9.7921500e−15 | USGC U857 | 11.0332 | 0.014413 | 86.62 |
| XMMXCS J101933.0 + 080353.4 | 0093640301 | 154.88759 | 8.0648583 | 1086.6229 | 1.4367639e−13 | MaxBCG J154.88074+08.06467 | 24.4322 | 0.178250 | 160.22 |
| XMMXCS J014908.5 + 135740.4 | 0094383401 | 27.285609 | 13.961241 | 64.311101 | 9.1844736e−14 | SDSS-C4 2000 | 7.48944 | 0.069900 | 29.71 |
| XMMXCS J023605.2 − 522508.0 | 0098810101 | 39.021978 | −52.418893 | 708.28873 | 4.2614564e−14 | WARP J0236.0-5224 | 5.05512 | - | 505.00 |
| XMMXCS J111729.8 + 174450.9 | 0099030101 | 169.37440 | 17.747478 | 470.38089 | 8.6510012e−14 | 400d J1117+1744 | 8.44266 | 0.548000 | 195.46 |
| XMMXCS J111654.6 + 180352.9 | 0099030101 | 169.22786 | 18.064714 | 172.37392 | 2.1542795e−14 | NGC 3607 GROUP | 24.6281 | 0.002990 | 46.11 |
| XMMXCS J222759.3 − 052859.9 | 0100440101 | 336.99751 | −5.4833139 | 219.85798 | 2.5398469e−14 | BLOX J2227.9-0528.9 | 6.62340 | - | 51.68 |
| XMMXCS J222833.5 − 052827.8 | 0100440101 | 337.13989 | −5.4744131 | 310.41458 | 2.4811876e−14 | BLOX J2228.5-0528.3 | 7.12950 | - | 52.60 |
| XMMXCS J222818.8 − 050753.4 | 0100440101 | 337.07849 | −5.1315176 | 248.04311 | 1.9479327e−14 | BLOX J2228.3-0507.8 | 6.09480 | - | 39.17 |
| XMMXCS J004615.6 + 853117.1 | 0100640201 | 11.565363 | 85.521435 | 1643.5328 | 7.2216682e−14 | Cl J0046.3+8530 | 8.06370 | 0.615000 | - |
| XMMXCS J003604.9 + 851324.8 | 0100640201 | 9.0204654 | 85.223563 | 728.92203 | 6.1558449e−14 | RDCS J0035+8513 | 13.0615 | 0.810000 | 199.25 |
| XMMXCS J004753.0 + 852717.1 | 0100640201 | 11.971199 | 85.454773 | 717.66655 | 2.6583772e−14 | XMMU J004751.7+852722 | 5.08785 | 0.250000 | 217.36 |
| XMMXCS J020019.3 + 001932.3 | 0101640201 | 30.080471 | 0.32564536 | 175.70533 | 4.2175398e−14 | SEXCLAS 03 | 3.61589 | 0.510000 | 64.14 |
| XMMXCS J103059.9 + 305138.8 | 0102040301 | 157.74995 | 30.860793 | 895.45945 | 9.7710450e−14 | MaxBCG J157.75753+30.86197 | 23.7731 | 0.143150 | 257.98 |
| XMMXCS J221556.7 − 175140.8 | 0106660101 | 333.98652 | −17.861337 | 93.043787 | 3.8202192e−15 | BLOX J2215.9-1751.6 | 2.97920 | - | 25.65 |
| XMMXCS J221559.5 − 173814.6 | 0106660101 | 333.99798 | −17.637397 | 362.43867 | 1.4841887e−14 | BLOX J2215.9-1738.1 | 18.9971 | 1.450000 | 104.40 |
| XMMXCS J221557.3 − 174034.7 | 0106660601 | 333.98878 | −17.676305 | 219.26844 | 5.5262949e−15 | BLOX J2215.9-1740.4 | 7.04118 | - | 57.57 |
| XMMXCS J221621.1 − 173222.0 | 0106660601 | 334.08807 | −17.539461 | 23.806567 | 1.5337418e−17 | CFHTLS CL J221620-173224 | 16.5481 | 0.700000 | 15.46 |
| XMMXCS J131302.5 + 351946.5 | 0109080201 | 198.26069 | 35.329606 | 322.85863 | 8.8220271e−14 | MaxBCG J198.26268+35.32836 | 7.36194 | 0.288950 | 196.18 |
| XMMXCS J015415.1 − 593756.6 | 0109460201 | 28.563226 | −59.632397 | 178.16024 | 7.7149755e−14 | 400d J0154-5937 | 9.08082 | 0.360000 | 76.64 |
| XMMXCS J131339.5 − 325037.4 | 0109462301 | 198.41487 | −32.843740 | 155.28376 | 1.3572797e−13 | 400d J1313-3250 | 9.05490 | 0.052000 | 36.85 |
| XMMXCS J022610.3 − 045804.9 | 0109520301 | 36.543201 | −4.9680355 | 475.74949 | 4.4530185e−14 | XLSSC 011 | 10.0212 | 0.050000 | 179.70 |
| XMMXCS J022303.1 − 043621.5 | 0109520601 | 35.763167 | −4.6059941 | 89.539829 | 7.7526560e−15 | XLSSC 046 | 2.43570 | 1.220000 | 24.31 |
| XMMXCS J133407.3 + 380633.0 | 0109660801 | 203.53063 | 38.109174 | 36.229759 | 2.5851510e−15 | [MJM98] 074 | 6.61722 | 0.382000 | 13.04 |
| XMMXCS J133434.8 + 375700.2 | 0109661001 | 203.64540 | 37.950074 | 863.66345 | 1.6671176e−14 | NSC J133433+375708 | 4.07073 | 0.308000 | 347.60 |
| XMMXCS J133457.3 + 375021.6 | 0109661001 | 203.73892 | 37.839343 | 696.32390 | 1.7645390e−14 | NSCS J133503+374945 | 9.30432 | 0.382000 | 139.21 |
| XMMXCS J133531.0 + 374524.4 | 0109661001 | 203.87946 | 37.756778 | 159.01394 | 1.0497480e−14 | [MJM98] 077 | 15.4563 | 0.307000 | 22.26 |
| XMMXCS J133514.4 + 374908.8 | 0109661001 | 203.81006 | 37.819134 | 349.44749 | 1.1532805e−14 | [MJM98] 034 | 14.6573 | 0.595000 | 124.04 |
| XMMXCS J141731.9 + 251135.2 | 0109960101 | 214.38323 | 25.193130 | 123.46935 | 5.4776528e−14 | MaxBCG J214.37758+25.19479 | 19.3632 | 0.191750 | 26.40 |
| XMMXCS J005655.3 − 221407.4 | 0110890401 | 14.230831 | −22.235413 | 625.80805 | 3.2785699e−13 | 400d J0056-2213 | 15.5129 | 0.116000 | 208.12 |
| XMMXCS J124454.0 − 003331.1 | 0110980201 | 191.22541 | −0.55865638 | 1347.8584 | 4.1330734e−14 | SDSS CE J191.220871-00.560489 | 17.8469 | 0.231327 | 367.61 |

Continued on Next Page...

Table D.1 – Continued

| XCS Name | Obsid | RA | Dec | Counts | Flux | Literature Name | Match Distance | Literature Redshift | Sig |
|---|---|---|---|---|---|---|---|---|---|
| XMMXCS J124453.1 − 002628.1 | 0110980201 | 191.22128 | −0.44114727 | 418.82595 | 1.0227501e−14 | SDSS CE J191.220749-00.444507 | 11.9678 | 0.219981 | 119.68 |
| XMMXCS J124448.5 − 001951.8 | 0110980201 | 191.20216 | −0.33108290 | 228.62142 | 8.4844150e−15 | BLOX J1244.8-0019.8 | 4.75895 | - | 62.82 |
| XMMXCS J125233.8 − 292507.3 | 0111020101 | 193.14095 | −29.418708 | 211.42549 | 2.9394916e−12 | CXOU J1252.6-2925 | 29.2852 | - | 60.25 |
| XMMXCS J125204.1 − 292038.8 | 0111020201 | 193.01716 | −29.344113 | 888.24503 | 6.3667399e−13 | 400d J1252-2920 | 18.2231 | 0.188000 | 516.50 |
| XMMXCS J022401.8 − 050528.7 | 0111110401 | 36.007904 | −5.0913221 | 341.32988 | 2.1693370e−14 | XLSSC 018 | 19.7491 | 0.322000 | 112.95 |
| XMMXCS J005624.5 − 281831.9 | 0111280801 | 14.102132 | −28.308874 | 90.726757 | 4.0017245e−14 | XMM2DF J005623.2-281818 | 22.2284 | - | 24.12 |
| XMMXCS J134139.1 + 001736.6 | 0111281001 | 205.41329 | 0.29351054 | 263.25338 | 6.6658567e−14 | [BPG2004] J205.417+00.287 | 2.95708 | 0.400000 | 135.59 |
| XMMXCS J005656.5 − 274031.7 | 0111282001 | 14.235806 | −27.675485 | 343.04627 | 9.4965273e−14 | J1888.16CL | 4.01256 | 0.560000 | 204.59 |
| XMMXCS J134446.4 − 003020.4 | 0111282501 | 206.19364 | −0.50567028 | 40.895646 | 1.0037685e−14 | [GPB2005] 5 | 1.81118 | - | 26.07 |
| XMMXCS J142758.2 + 263019.5 | 0111290601 | 216.99275 | 26.505436 | 2843.6834 | 1.5351829e−13 | 400d J1427+2630 | 3.53336 | 0.032400 | - |
| XMMXCS J113804.0 + 031535.5 | 0111970701 | 174.51680 | 3.2598773 | 265.69856 | 5.3311423e−14 | BLOX J1138.0+0315.3 | 15.5559 | - | 120.81 |
| XMMXCS J113844.2 + 031536.2 | 0111970701 | 174.68450 | 3.2600651 | 876.87747 | 1.6641653e−13 | BLOX J1138.7+0315.6 | 5.92967 | 0.127000 | 554.11 |
| XMMXCS J230247.7 + 084353.3 | 0112170301 | 345.69898 | 8.7314743 | 335.88831 | 7.4504348e−14 | WARP J2302.8+0843 | 9.40578 | 0.722000 | 188.46 |
| XMMXCS J123144.3 + 413731.1 | 0112280201 | 187.93491 | 41.625314 | 564.23047 | 1.6301376e−13 | 400d J1231+4137 | 6.03816 | 0.176000 | 237.34 |
| XMMXCS J021832.4 − 050052.7 | 0112370101 | 34.635072 | −5.0146475 | 266.73413 | 1.2885818e−14 | [VCB2006] 06 | 12.0406 | 0.870000 | 106.45 |
| XMMXCS J021734.7 − 051326.7 | 0112370701 | 34.394646 | −5.2241013 | 460.68948 | 2.2673008e−14 | [VCB2006] 01A | 13.8629 | 0.650000 | 138.21 |
| XMMXCS J110024.6 + 285844.3 | 0112550101 | 165.10260 | 28.978983 | 356.75777 | 6.2329394e−14 | NGC 3486:[HK83] 067 | 4.63385 | - | 106.57 |
| XMMXCS J123615.7 + 255438.2 | 0112550301 | 189.06558 | 25.910626 | 268.19411 | 3.0365640e−14 | RX J1236.2+2554 | 21.7452 | - | 127.29 |
| XMMXCS J120801.2 + 433927.3 | 0112551201 | 182.00510 | 43.657594 | 310.49142 | 1.8338923e−13 | MaxBCG J182.00318+43.65537 | 9.40128 | 0.264650 | 344.98 |
| XMMXCS J013352.2 − 401538.2 | 0112630201 | 23.467686 | −40.260617 | 104.88210 | 1.5605955e−14 | BLOX J0133.8-4015.8 | 16.5133 | - | 22.00 |
| XMMXCS J022709.4 − 041806.5 | 0112680101 | 36.789380 | −4.3018110 | 93.397975 | 7.3699402e−15 | XLSSC 005 | 4.03197 | 1.050000 | 60.28 |
| XMMXCS J022634.6 − 040408.7 | 0112680101 | 36.644569 | −4.0691111 | 278.35496 | 3.5319475e−14 | CFHTLS CL J022635-040411 | 12.2719 | 0.400000 | 90.76 |
| XMMXCS J022509.6 − 040141.3 | 0112680301 | 36.290094 | −4.0281516 | 160.15033 | 2.4629350e−14 | CFHTLS CL J022508-040118 | 28.5029 | 0.400000 | 48.30 |
| XMMXCS J022726.4 − 043207.4 | 0112680401 | 36.860012 | −4.5353957 | 268.35659 | 2.4870263e−14 | CFHTLS CL J022725-043232 | 10.6570 | 0.307000 | 111.85 |
| XMMXCS J022827.3 − 042543.9 | 0112680401 | 37.114047 | −4.4288680 | 504.32073 | 5.2154970e−14 | SL J0228.4-0425 | 4.09916 | 0.433000 | 139.62 |
| XMMXCS J022812.5 − 100537.9 | 0112860101 | 37.052222 | −10.093885 | 250.12329 | 1.4819385e−13 | WARP J0228.1-1005 | 10.0366 | 0.149000 | 131.68 |
| XMMXCS J113232.3 − 344349.4 | 0112880101 | 173.13465 | −34.730409 | 864.97301 | 7.7516266e−14 | BLOX J1132.5-3443.7 | 3.75332 | - | 501.87 |
| XMMXCS J233227.5 + 195822.1 | 0112880301 | 353.11483 | 19.972828 | 410.14654 | 6.8399812e−14 | SEXCLAS 19 | 17.5225 | 0.270000 | 141.03 |
| XMMXCS J033756.7 + 002859.8 | 0117890901 | 54.486401 | 0.48328385 | 377.15011 | 3.0591357e−14 | SDSS CE J054.487713+00.485329 | 9.02424 | 0.322096 | 52.34 |
| XMMXCS J105245.1 + 574043.9 | 0123701001 | 163.18798 | 57.678865 | 170.80640 | 1.8147183e−14 | RX J105244.4+574045 | 14.4735 | 0.074000 | 49.46 |
| XMMXCS J122019.2 + 752203.9 | 0124110101 | 185.08034 | 75.367754 | 17730.285 | 5.7373422e−13 | 400d J1220+7522 | 7.11234 | 0.005900 | - |
| XMMXCS J104407.5 − 012725.4 | 0125300101 | 161.03161 | −1.4570575 | 100.29361 | 4.5127898e−15 | BLOX J1044.1-0127.3 | 3.41713 | - | 27.68 |
| XMMXCS J141652.4 + 522052.5 | 0127921001 | 214.21841 | 52.347941 | 736.31771 | 1.7943891e−14 | HST J141653+52210 | 13.3378 | - | - |
| XMMXCS J005053.5 − 521312.5 | 0133120401 | 12.722953 | −52.220141 | 66.078830 | 1.2405779e−14 | BLOX J0050.9-5213.0 | 8.75148 | - | 19.25 |
| XMMXCS J033556.1 + 003214.3 | 0134540601 | 53.984146 | 0.53730963 | 750.47982 | 7.5103445e−14 | SDSS CE J053.980568+00.534098 | 17.5416 | 0.401519 | 207.67 |
| XMMXCS J154932.2 + 213302.2 | 0136040101 | 237.38440 | 21.550619 | 485.33887 | 5.8193990e−14 | [B2002a] 30 | 3.86651 | 0.800000 | 239.84 |
| XMMXCS J140615.8 + 283047.8 | 0140960101 | 211.56598 | 28.513296 | 372.56062 | 7.6151026e−14 | NSCS J140614+282911 | 7.36728 | 0.546000 | 167.34 |
| XMMXCS J030617.7 − 000829.8 | 0142610101 | 46.573831 | −0.14161382 | 2902.1468 | 1.8228705e−13 | SDSS-C4 2007 | 7.17096 | 0.109000 | 661.25 |
| XMMXCS J125047.4 + 263352.9 | 0143150201 | 192.69754 | 26.564714 | 406.84955 | 4.8128124e−14 | FSVS CL J125048+263418 | 26.2634 | 0.300000 | 103.32 |
| XMMXCS J135358.8 + 335003.1 | 0143650801 | 208.49539 | 33.834209 | 566.63541 | 8.6297395e−14 | NSCS J135400+335023 | 24.1509 | 0.230000 | 339.05 |
| XMMXCS J161720.3 + 345413.2 | 0143651101 | 244.33480 | 34.903683 | 1204.4903 | 7.2463496e−13 | SDSS-C4-DR3 3091 | 7.74408 | 0.031000 | 151.15 |
| XMMXCS J083724.3 + 553251.0 | 0143653901 | 129.35132 | 55.547523 | 290.29123 | 1.1010117e−13 | MaxBCG J129.35330+55.54785 | 4.19899 | 0.278150 | 142.84 |
| XMMXCS J083454.9 + 553420.7 | 0143653901 | 128.72883 | 55.572419 | 5846.5767 | 2.1742733e−12 | ClG J0834+5534 | 0.358096 | .240 | - |
| XMMXCS J160434.1 + 174345.6 | 0147210101 | 241.14235 | 17.729345 | 54707.449 | 5.1513773e−12 | NSC J160433+174311 | 28.1155 | 0.037000 | - |
| XMMXCS J105255.8 + 573210.2 | 0147511001 | 163.23261 | 57.536182 | 135.51925 | 4.9922303e−15 | SEXCLAS 13 | 13.0915 | 0.580000 | 32.50 |
| XMMXCS J105345.9 + 573514.8 | 0147511601 | 163.44167 | 57.587455 | 1691.7534 | 4.1452755e−14 | RX J105346.6+573517 | 5.27265 | 1.263000 | 517.87 |
| XMMXCS J105318.7 + 572048.4 | 0147511701 | 163.32815 | 57.346798 | 2124.1601 | 3.6705680e−13 | SL J1053.4+5720 | 3.24154 | 0.340000 | 497.00 |
| XMMXCS J094632.6 − 140954.0 | 0147920301 | 146.63595 | −14.165006 | 95.370468 | 2.7404545e−14 | RX J0946.5-1410 | 5.28185 | 0.230000 | 37.60 |
| XMMXCS J141558.3 + 230718.6 | 0148250201 | 213.99328 | 23.121839 | 298.59398 | 1.3783651e−13 | [DSM2002] OC03 J1415+2307 | 25.2692 | - | 226.08 |
| XMMXCS J092018.6 + 370621.1 | 0149010201 | 140.07781 | 37.105880 | 29168.788 | 8.3372082e−13 | MaxBCG J140.07821+37.10510 | 3.05261 | 0.248450 | - |
| XMMXCS J232018.1 + 082220.0 | 0149240101 | 350.07580 | 8.3722487 | 46.231165 | 4.0095044e−15 | WBL 708 | 28.1941 | 0.013640 | 24.41 |
| XMMXCS J223924.4 − 054718.3 | 0149410401 | 339.85182 | −5.7884370 | 2429.1388 | 2.3481101e−13 | WARP J2239.4-0547 | 14.9064 | 0.242000 | - |
| XMMXCS J223939.4 − 054327.0 | 0149410401 | 339.91422 | −5.7241804 | 2630.2471 | 2.6879468e−13 | WARP J2239.6-0543 | 11.8635 | 0.243000 | - |
| XMMXCS J223934.0 − 060018.1 | 0149410401 | 339.89180 | −6.0050550 | 577.86307 | 7.4884863e−14 | WARP J2239.5-0600 | 6.86010 | 0.173000 | 200.81 |
| XMMXCS J023345.5 − 085027.2 | 0150470601 | 38.439667 | −8.8408931 | 339.75083 | 7.7964599e−14 | MaxBCG J038.43299-08.84562 | 29.1979 | 0.256550 | 36.30 |
| XMMXCS J072052.9 + 710907.3 | 0150495601 | 110.22048 | 71.152055 | 934.59980 | 1.3763511e−13 | 400d J0720+7108 | 10.9360 | 0.230900 | 371.60 |
| XMMXCS J103554.5 − 033155.2 | 0150870401 | 158.97745 | −3.5320133 | 299.32627 | 3.9887178e−14 | BLOX J1035.9-0331.9 | 6.43056 | - | 80.43 |
| XMMXCS J103636.4 − 033302.3 | 0150870401 | 159.15196 | −3.5506489 | 176.07320 | 1.6190640e−14 | BLOX J1036.6-0333.0 | 5.70782 | - | 41.56 |
| XMMXCS J104136.8 + 061536.8 | 0151390101 | 160.40364 | 6.2602440 | 57.161949 | 3.3724621e−15 | [W78] 13 | 26.5524 | .02271 | 11.51 |
| XMMXCS J011922.9 − 011017.8 | 0153170101 | 19.845632 | −1.1716231 | 139.25164 | 2.9880426e−14 | SDSS CE J019.844770-01.170951 | 4.74575 | 0.197288 | 24.85 |
| XMMXCS J154610.8 + 484851.4 | 0153220401 | 236.54521 | 48.814289 | 115.64894 | 1.9962146e−14 | MaxBCG J236.54322+48.81638 | 8.89938 | 0.118850 | 23.52 |
| XMMXCS J041704.8 + 011325.8 | 0161160101 | 64.270103 | 1.2238562 | 676.62549 | 8.0326381e−14 | ZwCl 0414.3+0103 | 21.6631 | 0.320000 | 317.94 |
| XMMXCS J142907.8 + 424106.0 | 0165770201 | 217.28258 | 42.685006 | 1080.1519 | 7.6507108e−14 | Cl J1429.0+4241 | 16.1324 | 0.920000 | 724.87 |
| XMMXCS J014430.2 + 021231.6 | 0200430701 | 26.125883 | 2.2087784 | 304.64204 | 7.0403822e−14 | WARP J0144.5+0212 | 12.6635 | 0.166000 | 111.98 |
| XMMXCS J081919.6 + 705457.7 | 0200470101 | 124.83198 | 70.916041 | 1589.3533 | 1.1276664e−13 | RX J0819.3+7054 | 17.3465 | 0.226000 | 372.25 |

Continued on Next Page...

Table D.1 – Continued

| XCS Name | Obsid | RA | Dec | Counts | Flux | Literature Name | Match Distance | Literature Redshift | Sig |
|---|---|---|---|---|---|---|---|---|---|
| XMMXCS J123558.5 + 131239.7 | 0200650101 | 188.99411 | 13.211037 | 266.27563 | 1.6564751e−14 | MaxBCG J188.99457+13.20756 | 12.6185 | 0.170150 | 22.75 |
| XMMXCS J102552.5 + 470842.1 | 0201040101 | 156.46909 | 47.145042 | 203.46528 | 2.5807201e−13 | RX J1025.8+4709 | 25.7545 | - | 43.73 |
| XMMXCS J111926.2 + 210640.2 | 0201940201 | 169.85918 | 21.111169 | 93.902975 | 1.0615335e−13 | OC04 J1119+2107 | 15.5548 | 0.176000 | 63.34 |
| XMMXCS J111942.8 + 212646.6 | 0201940201 | 169.92859 | 21.446284 | 41.876330 | 3.3452781e−14 | RIXOS F123 005 | 12.2865 | 0.061000 | 33.07 |
| XMMXCS J100051.4 + 683347.7 | 0201980101 | 150.21427 | 68.563264 | 179.23767 | 1.2941637e−14 | MaxBCG J150.21758+68.56865 | 19.8788 | 0.256550 | 37.82 |
| XMMXCS J124202.6 + 332203.5 | 0202180201 | 190.51104 | 33.367657 | 312.41560 | 1.0617652e−14 | MaxBCG J190.51188+33.37343 | 20.9739 | 0.137750 | 95.85 |
| XMMXCS J134305.1 − 000056.6 | 0202460101 | 205.77140 | −0.015727482 | 1360.4507 | 1.2828690e−13 | [BPG2004] J134304.8-000056.3 | 5.00527 | 0.670000 | - |
| XMMXCS J134800.2 + 075219.1 | 0202890201 | 207.00107 | 7.8719855 | 83.630668 | 3.0471893e−14 | RX J1347.9+0752 | 13.1186 | 0.464900 | 42.10 |
| XMMXCS J093205.6 + 473311.8 | 0203050701 | 143.02344 | 47.553295 | 263.05462 | 7.9942055e−14 | MaxBCG J143.01990+47.55526 | 11.1732 | 0.234950 | 139.21 |
| XMMXCS J121156.6 + 502917.6 | 0203170101 | 182.98614 | 50.488237 | 532.67445 | 4.0517493e−14 | PCG J1211+5029 | 10.1134 | - | 110.32 |
| XMMXCS J124928.8 − 060010.7 | 0203270301 | 192.37002 | −6.0029972 | 352.01359 | 1.4167810e−14 | BLOX J1249.4-0600.0 | 8.18196 | - | 122.46 |
| XMMXCS J100201.6 + 021333.0 | 0203360301 | 150.50685 | 2.2258393 | 826.65981 | 4.9792870e−14 | [FGH2007] 032 | 7.06212 | 0.900000 | 371.09 |
| XMMXCS J100141.6 + 022538.6 | 0203360701 | 150.42368 | 2.4273895 | 2437.5963 | 1.0428107e−13 | CFHTLS CL J100142+022510 | 29.6402 | 0.132350 | - |
| XMMXCS J100219.0 + 015548.0 | 0203360901 | 150.57926 | 1.9300158 | 133.72484 | 3.5335799e−14 | [FGH2007] 025 | 27.6995 | 0.300000 | 34.49 |
| XMMXCS J100042.7 + 014551.4 | 0203361001 | 150.17813 | 1.7642919 | 201.17288 | 3.0608887e−14 | [SAB2007] LSS 28 | 15.9011 | 0.300000 | 25.69 |
| XMMXCS J100023.0 + 022358.5 | 0203361201 | 150.09620 | 2.3996096 | 53.659732 | 5.8206053e−15 | [FGH2007] 085 | 24.8693 | 0.220000 | 37.81 |
| XMMXCS J100027.0 + 022133.3 | 0203361301 | 150.11286 | 2.3592614 | 100.96848 | 8.1507819e−15 | [FGH2007] 078 | 22.1492 | 0.220000 | 27.66 |
| XMMXCS J095950.7 + 021246.4 | 0203361301 | 149.96146 | 2.2128906 | 79.402358 | 6.8192231e−15 | [FGH2007] 101 | 12.9681 | 0.430000 | 25.35 |
| XMMXCS J100013.8 + 022234.8 | 0203361301 | 150.05786 | 2.3763404 | 71.989098 | 6.6101088e−15 | [FGH2007] 087 | 13.1846 | 0.400000 | 25.30 |
| XMMXCS J100021.5 + 022332.3 | 0203361301 | 150.08988 | 2.3923091 | 113.20699 | 1.0053055e−14 | [FGH2007] 085 | 10.5659 | 0.220000 | 51.89 |
| XMMXCS J095940.8 + 023112.4 | 0203361701 | 149.92005 | 2.5201357 | 1001.3396 | 4.7040269e−14 | SL J0959.6+0231 | 21.7661 | 0.730000 | 643.95 |
| XMMXCS J095901.3 + 024740.3 | 0203362101 | 149.75558 | 2.7945407 | 257.69402 | 1.1145482e−14 | [FGH2007] 120 | 3.95850 | 0.490000 | 43.89 |
| XMMXCS J095737.1 + 023424.8 | 0203362101 | 149.40496 | 2.5735600 | 3132.7229 | 2.7575386e−13 | [SAB2007] LSS 26 | 17.6540 | 0.390000 | - |
| XMMXCS J095823.4 + 024853.1 | 0203362101 | 149.59776 | 2.8147560 | 1321.2800 | 4.6951374e−14 | [FGH2007] 132 | 23.4989 | 0.340000 | 481.81 |
| XMMXCS J111730.6 + 074630.7 | 0203560401 | 169.37751 | 7.7752137 | 959.29157 | 2.6918491e−14 | BLOX J1117.5+0746.3 | 13.4914 | 0.160000 | 218.65 |
| XMMXCS J231806.0 − 423536.1 | 0204610101 | 349.52520 | −42.593367 | 1666.6277 | 1.0257638e−13 | 400d J2318-4235 | 15.0941 | 0.209000 | 506.07 |
| XMMXCS J000141.3 − 154030.5 | 0204790101 | 0.42236334 | −15.675149 | 1605.1326 | 9.3688878e−13 | BMW-HRI J000141.3-154042 | 11.4938 | - | - |
| XMMXCS J122025.4 + 290534.2 | 0205010101 | 185.10600 | 29.092840 | 136.78945 | 1.6933036e−14 | NSC J122026+290511 | 25.7424 | 0.144400 | 16.19 |
| XMMXCS J041646.5 − 552501.8 | 0205090201 | 64.193769 | −55.417180 | 710.01685 | 2.0447368e−13 | RX J0416.7-5525 | 16.0144 | 0.365000 | 144.81 |
| XMMXCS J010743.3 − 465448.8 | 0205470301 | 16.930784 | −46.913574 | 1334.2872 | 4.8909151e−13 | ABELL 2870 | 10.8422 | 0.023700 | - |
| XMMXCS J130749.6 + 292549.3 | 0205910101 | 196.95674 | 29.430371 | 7303.2244 | 3.5136078e−13 | ZwCl 1305.4+2941 | 7.37226 | 0.241000 | - |
| XMMXCS J095343.5 + 694734.0 | 0206080101 | 148.43166 | 69.792778 | 2323.6088 | 1.9913353e−13 | 400d J0953+6947 | 7.20762 | 0.214000 | - |
| XMMXCS J080712.8 + 152701.5 | 0206100101 | 121.80341 | 15.450433 | 1631.7052 | 1.4156211e−13 | MaxBCG J121.81094+15.45007 | 26.1419 | 0.108050 | 386.90 |
| XMMXCS J133934.0 − 001658.5 | 0211080701 | 204.89190 | −0.28292073 | 258.42016 | 7.8705704e−14 | [BMA2003] BH 601 | 5.85403 | - | 51.91 |
| XMMXCS J083811.1 + 250549.1 | 0302260201 | 129.54636 | 25.096996 | 411.95900 | 3.8653804e−13 | 400d J0838+2506 | 16.1969 | 0.028600 | 131.39 |
| XMMXCS J163015.6 + 243423.8 | 0302260701 | 247.56512 | 24.573281 | 1075.3695 | 4.2417043e−13 | MCG +04-39-010 | 25.2430 | - | 351.75 |
| XMMXCS J100109.4 + 013331.8 | 0302351001 | 150.28931 | 1.5588524 | 340.29942 | 2.2405591e−14 | [FGH2007] 057 | 17.9482 | 0.360000 | 55.30 |
| XMMXCS J100047.4 + 013927.7 | 0302351001 | 150.19753 | 1.6577194 | 2969.7894 | 1.9535959e−13 | NSC J100047+013912 | 5.74633 | 0.220000 | - |
| XMMXCS J100009.0 + 023258.1 | 0302351101 | 150.03783 | 2.5494802 | 906.23013 | 5.1448383e−15 | [FGH2007] 093 | 24.6371 | 1.250000 | 53.50 |
| XMMXCS J095946.9 + 025519.7 | 0302351601 | 149.94573 | 2.9221445 | 59.456645 | 2.1234463e−14 | [FGH2007] 104 | 16.8781 | 0.130000 | 50.07 |
| XMMXCS J095944.4 + 023615.1 | 0302351601 | 149.93511 | 2.6042077 | 237.89383 | 1.5510422e−14 | CFHTLS CL J095945+023627 | 15.7923 | 0.260000 | 23.78 |
| XMMXCS J095959.3 + 021534.3 | 0302351701 | 149.99731 | 2.2595438 | 31.137077 | 9.5156012e−15 | CFHTLS CL J095959+021512 | 22.6600 | 0.400000 | 10.15 |
| XMMXCS J095952.1 + 014048.7 | 0302352001 | 149.96717 | 1.6802212 | 523.17202 | 6.4509576e−14 | [FGH2007] 099 | 8.32374 | 0.370000 | 98.26 |
| XMMXCS J103513.2 + 575025.7 | 0303260201 | 158.80508 | 57.840477 | 268.37577 | 1.1370028e−13 | [B2002a] 17 | 8.23296 | - | 51.98 |
| XMMXCS J141534.9 + 282334.7 | 0304071701 | 213.89544 | 28.392989 | 737.30533 | 1.0430970e−13 | NSCS J141531+282421 | 22.9462 | 0.220000 | 259.28 |
| XMMXCS J141553.8 + 281717.9 | 0304071701 | 213.97438 | 28.288319 | 126.31866 | 4.2659430e−14 | MaxBCG J213.97657+28.28441 | 15.6887 | 0.137750 | 31.50 |
| XMMXCS J144811.2 − 002509.7 | 0304200901 | 222.04692 | −0.41936930 | 72.480700 | 4.3373226e−14 | SDSS CE J222.053848-00.414730 | 29.7670 | 0.151904 | 24.90 |
| XMMXCS J010659.1 + 320934.9 | 0305290101 | 16.746267 | 32.159708 | 896.90197 | 2.5412090e−15 | 400d J0106+3209 | 5.12937 | 0.112000 | 163.08 |
| XMMXCS J023759.8 − 522434.2 | 0305370101 | 39.499496 | −52.409504 | 3679.4186 | 4.3223530e−13 | 400d J0237-5224 | 13.0568 | 0.136000 | - |
| XMMXCS J150824.8 − 001533.7 | 0305750201 | 227.10350 | −0.25936155 | 468.31521 | 2.1093884e−13 | SDSS-C4 1011 | 28.5312 | 0.090000 | 97.01 |
| XMMXCS J171521.3 + 572451.9 | 0305750401 | 258.83911 | 57.414433 | 6542.5490 | 3.4952146e−12 | SDSS-C4-DR3 3152 | 17.4160 | - | - |
| XMMXCS J134124.7 − 010207.4 | 0305750901 | 205.35299 | −1.0353977 | 199.11060 | 5.6323767e−14 | MaxBCG J205.35590-01.04186 | 25.5047 | 0.288950 | 41.09 |
| XMMXCS J005603.0 − 373248.1 | 0305860301 | 14.012611 | −37.546719 | 13727.734 | 1.1731820e−12 | 400d J0056-3732 | 24.3069 | 0.162500 | - |
| XMMXCS J005544.2 − 372503.8 | 0305860301 | 13.934375 | −37.417738 | 1440.3843 | 2.1897599e−13 | ABELL S0102 | 24.5585 | 0.055825 | 422.22 |
| XMMXCS J010720.5 + 141615.9 | 0305920101 | 16.835579 | 14.271108 | 7000.2976 | 3.6185377e−13 | SDSS-C4 2049 | 20.6765 | 0.074410 | - |
| XMMXCS J033810.8 − 225623.7 | 0305930101 | 54.545401 | −22.939919 | 2714.6738 | 1.2974012e−13 | 400d J0338-2256 | 12.5001 | 0.173000 | - |
| XMMXCS J122227.7 + 142810.7 | 0306060101 | 185.61567 | 14.469664 | 373.41683 | 4.8066711e−14 | MaxBCG J185.62052+14.47192 | 18.7096 | 0.234950 | 81.01 |
| XMMXCS J030433.9 − 005406.8 | 0307000701 | 46.141581 | −0.90190258 | 982.05844 | 4.2369309e−13 | [SBV2004] RS 63 | 20.5600 | 0.158600 | - |
| XMMXCS J074100.8 + 650349.3 | 0307001501 | 115.25358 | 65.063722 | 93.367900 | 5.6947176e−15 | OC01 J0740+6504 | 25.5602 | 0.300000 | 20.99 |
| XMMXCS J074234.2 + 651712.3 | 0307001501 | 115.64258 | 65.286775 | 223.09136 | 5.1700010e−14 | RIXOS F234 505 | 8.19330 | 0.167000 | 37.13 |
| XMMXCS J090100.9 + 600607.8 | 0312191001 | 135.25415 | 60.102168 | 2202.9989 | 4.0418408e−13 | MaxBCG J135.25325+60.10133 | 3.39452 | 0.291650 | 466.32 |
| XMMXCS J092325.4 + 225648.0 | 0312191401 | 140.85595 | 22.946669 | 821.81453 | 1.1903365e−13 | MaxBCG J140.85564+22.94378 | 10.4513 | 0.183650 | 347.03 |
| XMMXCS J033445.3 + 001705.7 | 0402320201 | 53.689032 | 0.28493253 | 119.22562 | 5.8398678e−14 | SDSS CE J053.695625+00.289605 | 29.9338 | 0.299404 | 41.53 |
| XMMXCS J092540.1 + 362709.3 | 0402370101 | 141.41725 | 36.452610 | 3262.2503 | 3.0862664e−13 | RCS J092540+3626.8 | 20.7289 | 0.233000 | - |
| XMMXCS J092659.0 + 361221.1 | 0402370101 | 141.74600 | 36.205869 | 246.81517 | 2.4442530e−14 | RCS J092658+3612.1 | 13.1902 | 0.489000 | 27.06 |

Continued on Next Page...

Table D.1 – Continued

| XCS Name | Obsid | RA | Dec | Counts | Flux | Literature Name | Match Distance | Literature Redshift | Sig |
|---|---|---|---|---|---|---|---|---|---|
| XMMXCS J092622.6 + 362132.2 | 0402370101 | 141.59456 | 36.358959 | 278.42167 | 1.7898745e−14 | RCS J092621+3621.8 | 17.5324 | 0.887000 | 73.01 |
| XMMXCS J004624.5 + 420429.6 | 0402561401 | 11.602322 | 42.074903 | 10961.142 | 6.2217720e−13 | RX J0046.4+4204 | 7.21836 | 0.300000 | - |
| XMMXCS J003101.5 + 262632.4 | 0402750601 | 7.7565767 | 26.442357 | 412.40261 | 5.0393743e−14 | [B2002a] 01 | 7.17306 | - | 136.90 |
| XMMXCS J001639.6 − 010205.2 | 0403760701 | 4.1651984 | −1.0348049 | 666.16877 | 6.6069339e−14 | MaxBCG J004.16184-01.03538 | 12.2284 | 0.162050 | 63.60 |
| XMMXCS J144720.1 + 631626.4 | 0404050301 | 221.83376 | 63.274004 | 106.71207 | 1.2335837e−13 | MaxBCG J221.83176+63.27200 | 7.87344 | 0.194450 | 65.03 |
| XMMXCS J103931.9 + 394737.1 | 0406610101 | 159.88300 | 39.793655 | 431.79124 | 7.8855494e−14 | 400d J1039+3947 | 24.8884 | 0.092600 | 132.81 |
| XMMXCS J002314.1 + 001202.1 | 0407030101 | 5.8091391 | 0.20058627 | 405.04183 | 3.2320770e−14 | SDSS CE J005.801610+00.197059 | 29.9230 | 0.254019 | 52.27 |
| XMMXCS J220204.9 − 315909.2 | 0414580101 | 330.52079 | −31.985890 | 3705.6457 | 2.2803301e−13 | KTS 66 | 21.1534 | 0.009000 | - |
| XMMXCS J095924.8 + 014613.5 | 0501170101 | 149.85374 | 1.7704194 | 862.66066 | 4.2559490e−14 | [FGH2007] 113 | 29.6833 | 0.120000 | 320.95 |
| XMMXCS J040448.2 − 435055.4 | 0501210701 | 61.201159 | −43.848736 | 380.19895 | 5.7292331e−14 | ABELL S0416 | 12.9413 | 0.064800 | 97.31 |
| XMMXCS J084105.4 + 383157.7 | 0502060201 | 130.27263 | 38.532699 | 345.55096 | 3.4537263e−14 | MaxBCG J130.27341+38.53306 | 2.55156 | 0.240350 | 112.40 |
| XMMXCS J143120.8 − 005344.6 | 0502060301 | 217.83695 | −0.89573268 | 778.64836 | 3.3044736e−13 | SDSS CE J217.834290-00.898368 | 13.6828 | 0.378827 | 502.38 |
| XMMXCS J102044.5 + 383113.7 | 0503601301 | 155.18576 | 38.520475 | 174.01154 | 1.3369924e−13 | 400d J1020+3831 | 16.5775 | 0.053000 | 79.18 |
| XMMXCS J115641.1 + 524323.0 | 0504100901 | 179.17129 | 52.723067 | 112.37857 | 7.8134596e−15 | NSCS J115642+524329 | 10.0560 | 0.470000 | 35.49 |
| XMMXCS J232537.9 − 544408.9 | 0505383201 | 351.40810 | −54.735828 | 791.92111 | 2.0925726e−13 | 400d J2325-5443 | 14.1115 | 0.102000 | 224.40 |

Table D.1: DR3 StatSam Known Clusters. Column descriptions are given in Section 4.4

| XCS Name | Obsid | RA | Dec | Counts | Flux | Literature Name | Match Distance | Literature Redshift | Sig |
|---|---|---|---|---|---|---|---|---|---|
| XMMXCS J002606.6 + 102750.4 | 0001930101 | 6.5275011 | 10.464019 | 37.707573 | 2.0515345e−14 | - | - | - | 7.88 |
| XMMXCS J002635.8 + 103445.5 | 0001930101 | 6.6492228 | 10.579308 | 310.05012 | 4.6093743e−14 | - | - | - | 73.96 |
| XMMXCS J125329.9 + 100653.9 | 0001930301 | 193.37494 | 10.114986 | 225.29630 | 2.6094818e−14 | - | - | - | 28.25 |
| XMMXCS J035424.1 + 233430.4 | 0002740101 | 58.600697 | 23.575131 | 282.26216 | 2.3190440e−14 | - | - | - | 23.12 |
| XMMXCS J122748.6 − 153612.5 | 0002740301 | 186.95270 | −15.603497 | 84.693017 | 3.5875496e−14 | - | - | - | 12.18 |
| XMMXCS J130659.5 − 234926.3 | 0002940101 | 196.74795 | −23.823976 | 41.740368 | 1.4235332e−14 | - | - | - | 26.15 |
| XMMXCS J130650.0 − 233127.0 | 0002940101 | 196.70846 | −23.524179 | 355.08271 | 1.3599282e−13 | - | - | - | 169.81 |
| XMMXCS J011034.3 − 375637.9 | 0002942301 | 17.643264 | −37.943863 | 48.239468 | 2.6303669e−14 | - | - | - | 13.08 |
| XMMXCS J233732.9 + 270136.6 | 0002960101 | 354.38745 | 27.026840 | 107.17602 | 3.4804412e−14 | - | - | - | 19.96 |
| XMMXCS J233858.1 + 270608.0 | 0002960101 | 354.74237 | 27.102249 | 125.18113 | 1.9474518e−14 | - | - | - | 7.49 |
| XMMXCS J144238.4 + 353720.4 | 0005010101 | 220.66028 | 35.622358 | 69.087270 | 1.9067509e−14 | - | - | - | 15.61 |
| XMMXCS J074528.1 + 280011.3 | 0006010301 | 116.36717 | 28.003151 | 1815.8652 | 9.1195714e−14 | - | - | - | 672.84 |
| XMMXCS J002409.8 − 771840.8 | 0006010401 | 6.0410802 | −77.311344 | 74.055450 | 4.4135926e−15 | - | - | - | 22.18 |
| XMMXCS J002530.8 − 772852.3 | 0006010401 | 6.3785062 | −77.481204 | 266.43540 | 2.9748008e−14 | - | - | - | 54.63 |
| XMMXCS J002323.1 − 771109.3 | 0006010401 | 5.8463702 | −77.185926 | 63.934177 | 5.0792102e−15 | - | - | - | 2.64 |
| XMMXCS J002201.9 − 772042.7 | 0006010401 | 5.5082924 | −77.345198 | 424.44078 | 9.1604672e−14 | - | - | - | 122.06 |
| XMMXCS J002807.2 − 771105.6 | 0006010401 | 7.0302973 | −77.184891 | 480.49277 | 4.2308717e−14 | - | - | - | 144.06 |
| XMMXCS J123644.7 − 395637.4 | 0006220201 | 189.18638 | −39.943743 | 192.76509 | 3.4179447e−14 | - | - | - | 60.59 |
| XMMXCS J125102.9 + 272205.6 | 0008220201 | 192.76234 | 27.368229 | 79.346917 | 7.9220135e−15 | - | - | - | 28.28 |
| XMMXCS J125219.1 + 273228.5 | 0008220201 | 193.07997 | 27.541263 | 93.268734 | 5.7630087e−15 | - | - | - | 34.57 |
| XMMXCS J125122.7 + 272550.5 | 0008220201 | 192.84492 | 27.430697 | 12.325972 | 2.1278322e−15 | - | - | - | 35.68 |
| XMMXCS J125220.8 + 274306.1 | 0008220201 | 193.08682 | 27.718369 | 90.205817 | 2.3350686e−14 | - | - | - | 27.21 |
| XMMXCS J061324.8 + 710342.3 | 0009220301 | 93.353451 | 71.061760 | 198.01655 | 5.4738060e−14 | - | - | - | 33.06 |
| XMMXCS J061804.5 + 711039.2 | 0009220301 | 94.518769 | 71.177582 | 46.820027 | 1.3997620e−13 | - | - | - | 17.24 |
| XMMXCS J061659.0 + 711435.0 | 0009220301 | 94.245924 | 71.243070 | 39.120656 | 2.0759854e−14 | - | - | - | 10.48 |
| XMMXCS J061335.8 + 710636.9 | 0009220301 | 93.399364 | 71.110252 | 165.31610 | 8.9440217e−14 | - | - | - | 14.95 |
| XMMXCS J061745.2 + 711254.5 | 0009220301 | 94.438727 | 71.215152 | 440.45467 | 7.8706526e−13 | - | - | - | 84.18 |
| XMMXCS J061606.9 + 711527.8 | 0009220401 | 94.028769 | 71.257745 | 37.899687 | 3.5039099e−14 | - | - | - | 18.32 |
| XMMXCS J061714.8 + 711206.7 | 0009220901 | 94.312026 | 71.201863 | 133.47813 | 3.5156778e−14 | - | - | - | 25.18 |
| XMMXCS J061503.8 + 710739.8 | 0009220901 | 93.766155 | 71.127748 | 103.21245 | 2.5542899e−14 | - | - | - | 11.15 |
| XMMXCS J061754.5 + 710320.7 | 0009221601 | 94.477201 | 71.055756 | 192.90458 | −4.4379115e−15 | - | - | - | 20.10 |
| XMMXCS J061242.2 + 710720.4 | 0009221601 | 93.175964 | 71.122359 | 172.63235 | 1.7391183e−13 | - | - | - | 29.31 |
| XMMXCS J061456.2 + 711413.4 | 0009221601 | 93.734441 | 71.237058 | 179.06245 | 6.7635247e−15 | - | - | - | 19.84 |
| XMMXCS J061342.9 + 705048.9 | 0009221601 | 93.429004 | 70.846939 | 293.44183 | 1.9582875e−13 | - | - | - | 19.46 |
| XMMXCS J061238.9 + 710439.7 | 0009221601 | 93.162360 | 71.077710 | 147.54530 | 1.2691702e−13 | - | - | - | 11.94 |
| XMMXCS J225535.9 − 025746.0 | 0009650101 | 343.89974 | −2.9627896 | 71.313036 | 2.2031117e−14 | - | - | - | 13.51 |
| XMMXCS J221726.0 − 082542.2 | 0009650201 | 334.35836 | −8.4283945 | 99.848212 | 2.8527515e−14 | - | - | - | 59.68 |
| XMMXCS J221707.2 − 081936.1 | 0009650201 | 334.28031 | −8.3267130 | 27.835966 | 9.4354616e−15 | - | - | - | 16.23 |
| XMMXCS J051507.8 + 010530.5 | 0010620101 | 78.782787 | 1.0918063 | 65.737479 | 6.0594314e−15 | - | - | - | 47.46 |
| XMMXCS J051609.8 + 010954.1 | 0010620101 | 79.041169 | 1.1650405 | 88.426726 | 1.3999095e−14 | - | - | - | 23.49 |
| XMMXCS J152609.4 + 513436.6 | 0011830201 | 231.53934 | 51.576853 | 29.971102 | 2.1827251e−15 | - | - | - | 23.01 |
| XMMXCS J152525.7 + 513043.2 | 0011830201 | 231.35722 | 51.512025 | 117.46977 | 6.7917493e−15 | - | - | - | 33.89 |
| XMMXCS J152516.7 + 513459.4 | 0011830401 | 231.31998 | 51.583172 | 657.79835 | 8.5171512e−14 | - | - | - | 23.10 |
| XMMXCS J152611.7 + 515134.0 | 0011830401 | 231.54895 | 51.859450 | 1124.0912 | 6.0870259e−13 | - | - | - | 127.75 |
| XMMXCS J152418.0 + 513853.1 | 0011830401 | 231.07524 | 51.648099 | 469.61871 | −1.6586233e−13 | - | - | - | 26.03 |
| XMMXCS J152421.5 + 514058.6 | 0011830401 | 231.08971 | 51.682955 | 606.60978 | 3.5309859e−13 | - | - | - | 29.62 |
| XMMXCS J152450.6 + 514805.0 | 0011830401 | 231.21088 | 51.801395 | 344.14885 | 1.9700112e−13 | - | - | - | 70.46 |
| XMMXCS J152458.1 + 512606.8 | 0011830401 | 231.24212 | 51.435221 | 1693.6530 | 7.9058866e−13 | - | - | - | 139.40 |
| XMMXCS J152437.5 + 514548.0 | 0011830401 | 231.15656 | 51.763354 | 1730.8564 | 1.0488748e−12 | - | - | - | 135.78 |
| XMMXCS J152535.8 + 515122.1 | 0011830401 | 231.39942 | 51.856157 | 2876.4145 | 1.4998913e−12 | - | - | - | 412.06 |
| XMMXCS J005606.1 − 011215.0 | 0012440101 | 14.025767 | −1.2041696 | 1239.1977 | 7.9585006e−14 | - | - | - | 250.68 |
| XMMXCS J005623.2 − 010804.5 | 0012440101 | 14.096958 | −1.1345888 | 2216.8483 | 2.0891278e−13 | - | - | - | 124.67 |
| XMMXCS J005603.1 − 012038.6 | 0012440101 | 14.013030 | −1.3440747 | 1071.0870 | 5.2765096e−14 | - | - | - | 118.84 |
| XMMXCS J005625.7 − 011757.4 | 0012440101 | 14.107496 | −1.2992863 | 6113.6675 | 3.0745087e−13 | - | - | - | - |
| XMMXCS J005613.6 − 011508.5 | 0012440101 | 14.056752 | −1.2523825 | 33239.670 | 1.8985971e−12 | - | - | - | - |
| XMMXCS J005656.4 − 011221.4 | 0012440101 | 14.235101 | −1.2059640 | 362.43045 | 3.7651803e−14 | - | - | - | 57.68 |
| XMMXCS J220420.4 − 020546.3 | 0012440301 | 331.08502 | −2.0962135 | 36.031990 | 7.9286510e−15 | - | - | - | 33.16 |
| XMMXCS J220550.0 − 015931.7 | 0012440301 | 331.45864 | −1.9921540 | 131.61500 | 1.0732504e−14 | - | - | - | 54.78 |
| XMMXCS J220559.2 − 015814.6 | 0012440301 | 331.49686 | −1.9707268 | 97.568993 | 1.1500578e−14 | - | - | - | 32.60 |
| XMMXCS J033856.1 − 354035.1 | 0012830101 | 54.733901 | −35.676440 | 55.325429 | −8.5713031e−13 | - | - | - | 14.19 |
| XMMXCS J033901.8 − 353959.5 | 0012830101 | 54.757615 | −35.666552 | 80.300050 | −1.4933989e−11 | - | - | - | 19.68 |
| XMMXCS J223615.1 + 335639.1 | 0021140201 | 339.06325 | 33.944208 | 548.37276 | 1.6067912e−14 | - | - | - | 277.01 |
| XMMXCS J223526.5 + 334800.7 | 0021140201 | 338.86058 | 33.800200 | 39.683519 | 1.4727566e−14 | - | - | - | 5.41 |
| XMMXCS J223535.1 + 340356.0 | 0021140201 | 338.89664 | 34.065566 | 48.327448 | 2.7436079e−15 | - | - | - | 18.85 |
| XMMXCS J223546.8 + 335243.7 | 0021140201 | 338.94506 | 33.878821 | 307.39135 | 1.5357733e−14 | - | - | - | 37.84 |
| XMMXCS J124357.4 + 113614.9 | 0021540201 | 190.98919 | 11.604162 | 217.53991 | 8.5068669e−15 | - | - | - | 63.21 |

Continued on Next Page...

Table D.2 – Continued

| XCS Name | Obsid | RA | Dec | Counts | Flux | Literature Name | Match Distance | Literature Redshift | Sig |
|---|---|---|---|---|---|---|---|---|---|
| XMMXCS J124302.7 + 113351.4 | 0021540201 | 190.76144 | 11.564303 | 156.08189 | 7.4137164e−15 | - | - | - | 32.07 |
| XMMXCS J124300.3 + 113656.0 | 0021540201 | 190.75154 | 11.615572 | 275.51750 | 1.9590673e−14 | - | - | - | 62.16 |
| XMMXCS J124252.5 + 112838.1 | 0021540201 | 190.71877 | 11.477270 | 164.40386 | 1.0464831e−14 | - | - | - | 46.52 |
| XMMXCS J150653.2 + 014415.7 | 0021540501 | 226.72189 | 1.7376955 | 155.81034 | 2.7630881e−14 | - | - | - | 29.96 |
| XMMXCS J150707.0 + 013215.5 | 0021540501 | 226.77938 | 1.5376522 | 207.01893 | 3.8473172e−14 | - | - | - | 32.50 |
| XMMXCS J094034.9 + 355950.2 | 0021740101 | 145.14570 | 35.997280 | 520.74654 | 4.0762153e−14 | - | - | - | 51.30 |
| XMMXCS J131020.0 + 272319.3 | 0021740201 | 197.58361 | 27.388696 | 79.161355 | 5.7985200e−15 | - | - | - | 16.71 |
| XMMXCS J131049.2 + 274043.8 | 0021740201 | 197.70523 | 27.678839 | 207.63234 | 1.6566674e−14 | - | - | - | 59.52 |
| XMMXCS J173053.0 + 520851.3 | 0021750201 | 262.72091 | 52.147588 | 45.446667 | 1.7423953e−14 | - | - | - | 27.80 |
| XMMXCS J173015.8 + 520551.6 | 0021751001 | 262.56589 | 52.097691 | 147.49030 | 4.5771371e−14 | - | - | - | 22.71 |
| XMMXCS J105044.5 + 572926.0 | 0022740301 | 162.68559 | 57.490560 | 51.555503 | 1.0228134e−14 | - | - | - | 29.73 |
| XMMXCS J041859.2 + 153944.1 | 0024140101 | 64.747013 | 15.662262 | 84.050128 | 8.1321936e−15 | - | - | - | 10.70 |
| XMMXCS J041855.6 + 153243.6 | 0024140101 | 64.731957 | 15.545460 | 79.824628 | 1.3114479e−14 | - | - | - | 28.62 |
| XMMXCS J041939.1 + 153417.7 | 0024140101 | 64.913038 | 15.571594 | 165.60620 | 5.7211694e−15 | - | - | - | 24.30 |
| XMMXCS J041905.3 + 154439.9 | 0024140101 | 64.772230 | 15.744429 | 87.806324 | 5.2788535e−15 | - | - | - | 13.87 |
| XMMXCS J041924.7 + 153205.1 | 0024140101 | 64.853277 | 15.534764 | 38.066403 | 2.5164011e−15 | - | - | - | 12.57 |
| XMMXCS J042021.7 + 154738.8 | 0024140101 | 65.090739 | 15.794137 | 131.47387 | 8.5254719e−15 | - | - | - | 35.13 |
| XMMXCS J010730.5 − 171932.1 | 0025540101 | 16.877426 | −17.325608 | 43.355225 | 1.0897040e−14 | - | - | - | 20.84 |
| XMMXCS J010739.7 − 174504.2 | 0025540101 | 16.915606 | −17.751182 | 228.97219 | 4.0608651e−13 | - | - | - | 30.21 |
| XMMXCS J010725.2 − 172029.1 | 0025540101 | 16.855205 | −17.341444 | 89.642252 | 3.5359041e−14 | - | - | - | 12.75 |
| XMMXCS J010744.2 − 171807.1 | 0025540101 | 16.934577 | −17.301973 | 248.27725 | 5.6260335e−14 | - | - | - | 39.98 |
| XMMXCS J083856.0 + 253807.3 | 0025540301 | 129.73363 | 25.635362 | 108.91032 | 3.2499490e−14 | - | - | - | 40.95 |
| XMMXCS J083905.4 + 254447.6 | 0025540301 | 129.77264 | 25.746557 | 89.680495 | 3.1470008e−14 | - | - | - | 40.53 |
| XMMXCS J084837.8 + 741702.6 | 0025540401 | 132.15763 | 74.284068 | 43.558967 | 2.4687061e−14 | - | - | - | 11.32 |
| XMMXCS J012414.9 + 033705.0 | 0025541601 | 21.062281 | 3.6180716 | 38.335559 | 7.4377874e−15 | - | - | - | 11.12 |
| XMMXCS J012400.0 + 035110.8 | 0025541601 | 21.000162 | 3.8530210 | 61.002209 | 1.2616481e−14 | - | - | - | 21.74 |
| XMMXCS J012414.4 + 035642.6 | 0025541601 | 21.060150 | 3.9451898 | 79.275142 | 2.0626172e−14 | - | - | - | 40.82 |
| XMMXCS J084924.5 + 735441.2 | 0025541701 | 132.35239 | 73.911451 | 59.065560 | 2.4018955e−14 | - | - | - | 19.75 |
| XMMXCS J093958.5 + 711404.6 | 0026340101 | 144.99404 | 71.234612 | 37.266919 | 1.7499200e−15 | - | - | - | 10.71 |
| XMMXCS J093941.5 + 710715.1 | 0026340101 | 144.92298 | 71.120889 | 178.70444 | 1.2575072e−14 | - | - | - | 35.02 |
| XMMXCS J094130.3 + 711132.3 | 0026340101 | 145.37645 | 71.192313 | 274.76637 | 2.2830160e−14 | - | - | - | 41.10 |
| XMMXCS J101051.1 − 045340.1 | 0026340201 | 152.71293 | −4.8944952 | 223.76292 | 3.1824195e−14 | - | - | - | 15.97 |
| XMMXCS J101032.7 − 045201.0 | 0026340201 | 152.63646 | −4.8669718 | 232.08992 | −2.5356470e−14 | - | - | - | 21.55 |
| XMMXCS J101049.4 − 042722.0 | 0026340201 | 152.70594 | −4.4561294 | 311.19349 | 8.4524158e−14 | - | - | - | 133.36 |
| XMMXCS J101007.5 − 044552.3 | 0026340201 | 152.53136 | −4.7645417 | 111.09518 | 4.9557916e−14 | - | - | - | 38.10 |
| XMMXCS J101016.5 − 044940.3 | 0026340201 | 152.56906 | −4.8278731 | 2185.2489 | 7.1885387e−13 | - | - | - | 198.56 |
| XMMXCS J101018.6 − 043359.1 | 0026340201 | 152.57757 | −4.5664256 | 16689.930 | 5.5913016e−12 | - | - | - | - |
| XMMXCS J102744.3 + 681121.1 | 0026340301 | 156.93497 | 68.189201 | 222.45187 | 4.6457032e−14 | - | - | - | 114.90 |
| XMMXCS J102837.6 + 682102.5 | 0026340301 | 157.15687 | 68.350701 | 186.90044 | 1.5720937e−14 | - | - | - | 110.73 |
| XMMXCS J001436.6 − 390016.6 | 0028740101 | 3.6525911 | −39.004631 | 184.52686 | 1.8651399e−14 | - | - | - | 28.64 |
| XMMXCS J001636.3 − 392511.5 | 0028740201 | 4.1515426 | −39.419864 | 99.195958 | 4.5794767e−14 | - | - | - | 8.87 |
| XMMXCS J001610.8 − 391659.3 | 0028740201 | 4.0452627 | −39.283143 | 341.39513 | 1.6746034e−14 | - | - | - | 128.83 |
| XMMXCS J001528.7 − 392636.5 | 0028740201 | 3.8696708 | −39.443497 | 303.17812 | 2.5584192e−14 | - | - | - | 45.16 |
| XMMXCS J101738.3 + 413233.1 | 0028740301 | 154.40972 | 41.542554 | 124.80602 | 2.2318085e−14 | - | - | - | 27.21 |
| XMMXCS J063945.8 + 821850.3 | 0029340101 | 99.941079 | 82.313978 | 1178.1340 | 4.8774927e−14 | - | - | - | 394.47 |
| XMMXCS J064424.0 + 822628.6 | 0029340101 | 101.10034 | 82.441287 | 211.34071 | 3.8997640e−14 | - | - | - | 63.69 |
| XMMXCS J064016.8 + 822903.5 | 0029340101 | 100.07036 | 82.484323 | 127.92240 | 1.8254562e−14 | - | - | - | 33.84 |
| XMMXCS J064802.9 + 821000.0 | 0029340101 | 102.01219 | 82.166670 | 242.77372 | 2.4279953e−14 | - | - | - | 13.50 |
| XMMXCS J063551.6 + 821206.5 | 0029340101 | 98.965057 | 82.201819 | 203.43195 | 9.1948648e−15 | - | - | - | 7.23 |
| XMMXCS J064245.1 + 822832.7 | 0029340101 | 100.68826 | 82.475756 | 79.150404 | 1.4701133e−14 | - | - | - | 12.68 |
| XMMXCS J063819.2 + 821306.0 | 0029340101 | 99.580067 | 82.218350 | 362.73643 | 1.4145071e−14 | - | - | - | 39.39 |
| XMMXCS J133502.1 − 341136.3 | 0029740101 | 203.75915 | −34.193420 | 267.63880 | 1.7099814e−13 | - | - | - | 56.23 |
| XMMXCS J133640.6 − 341115.7 | 0029740701 | 204.16953 | −34.187705 | 115.26744 | 8.4949018e−15 | - | - | - | 14.24 |
| XMMXCS J133514.7 − 341624.3 | 0029740801 | 203.81151 | −34.273432 | 547.30148 | 1.7990754e−14 | - | - | - | 140.34 |
| XMMXCS J133639.1 − 341047.6 | 0029740801 | 204.16309 | −34.179900 | 175.37302 | 1.0379034e−14 | - | - | - | 11.67 |
| XMMXCS J133608.7 − 340506.0 | 0029740801 | 204.03643 | −34.085013 | 396.12655 | 2.5655907e−14 | - | - | - | 31.78 |
| XMMXCS J121927.4 + 473603.7 | 0032140101 | 184.86426 | 47.601028 | 252.72238 | −4.3360599e−13 | - | - | - | 101.34 |
| XMMXCS J121857.4 + 472823.9 | 0032140101 | 184.73930 | 47.473313 | 55839.036 | 1.0697450e−11 | - | - | - | - |
| XMMXCS J121749.6 + 472435.5 | 0032140101 | 184.45677 | 47.409881 | 4255.7086 | −3.7451711e−12 | - | - | - | - |
| XMMXCS J121930.2 + 473913.6 | 0032140101 | 184.87601 | 47.653783 | 952.63009 | 2.1160410e−13 | - | - | - | 127.07 |
| XMMXCS J121832.5 + 475131.3 | 0032140101 | 184.63548 | 47.858716 | 3347.8765 | 4.9932048e−13 | - | - | - | 220.49 |
| XMMXCS J230159.0 + 082242.9 | 0032140201 | 345.49620 | 8.3786073 | 37.124491 | 2.8897053e−14 | - | - | - | 41.14 |
| XMMXCS J230159.9 + 084633.0 | 0032140201 | 345.49970 | 8.7758569 | 34.178236 | 2.0700831e−14 | - | - | - | 21.84 |
| XMMXCS J230246.9 + 084816.2 | 0032140201 | 345.69554 | 8.8045240 | 37.597299 | 1.3160412e−14 | - | - | - | 18.21 |
| XMMXCS J230218.6 + 082408.9 | 0032140201 | 345.57760 | 8.4024925 | 63.482666 | 3.1777174e−14 | - | - | - | 19.03 |

Continued on Next Page...

Table D.2 – Continued

| XCS Name | Obsid | RA | Dec | Counts | Flux | Literature Name | Match Distance | Literature Redshift | Sig |
|---|---|---|---|---|---|---|---|---|---|
| XMMXCS J014153.0 − 675142.1 | 0032140401 | 25.470842 | −67.861712 | 51.916427 | 1.6637990e−14 | - | - | - | 11.05 |
| XMMXCS J233146.2 + 192413.4 | 0032140701 | 352.94271 | 19.403731 | 28.360306 | 2.6491984e−14 | - | - | - | 29.55 |
| XMMXCS J233145.3 + 194309.9 | 0032140701 | 352.93880 | 19.719431 | 52.838462 | 9.6588888e−15 | - | - | - | 18.52 |
| XMMXCS J130549.4 − 102716.0 | 0032141201 | 196.45608 | −10.454452 | 52.495484 | 6.7315378e−15 | - | - | - | 22.96 |
| XMMXCS J130456.6 − 101011.0 | 0032141201 | 196.23605 | −10.169741 | 64.064383 | 1.2484013e−14 | - | - | - | 25.49 |
| XMMXCS J130424.2 − 102927.9 | 0032141201 | 196.10109 | −10.491100 | 100.85986 | 4.6842723e−14 | - | - | - | 27.35 |
| XMMXCS J130514.5 − 102306.4 | 0032141201 | 196.31046 | −10.385118 | 391.66420 | 3.7408174e−14 | - | - | - | 135.93 |
| XMMXCS J130505.7 − 101643.6 | 0032141201 | 196.27407 | −10.278802 | 115.77475 | 1.3502817e−14 | - | - | - | 81.65 |
| XMMXCS J120850.9 + 452951.2 | 0033540601 | 182.21218 | 45.497580 | 712.47090 | 2.1788872e−13 | - | - | - | 248.09 |
| XMMXCS J120911.3 + 453012.1 | 0033540601 | 182.29714 | 45.503364 | 117.08965 | 3.2388204e−14 | - | - | - | 28.16 |
| XMMXCS J163248.1 + 373846.9 | 0033540901 | 248.20055 | 37.646364 | 113.22123 | 1.5432262e−14 | - | - | - | 35.46 |
| XMMXCS J163133.4 + 374905.6 | 0033540901 | 247.88932 | 37.818240 | 91.800607 | 1.8831066e−14 | - | - | - | 25.03 |
| XMMXCS J163056.9 + 374223.2 | 0033540901 | 247.73713 | 37.706460 | 69.044594 | 2.7985967e−14 | - | - | - | 45.06 |
| XMMXCS J163156.7 + 374651.2 | 0033540901 | 247.98657 | 37.780895 | 61.400816 | 8.3296601e−15 | - | - | - | 29.85 |
| XMMXCS J121508.6 + 362007.4 | 0035940201 | 183.78598 | 36.335393 | 164.79248 | 2.2937452e−14 | - | - | - | 37.60 |
| XMMXCS J133946.7 − 314218.6 | 0035940301 | 204.94482 | −31.705172 | 119.05165 | 4.7954930e−15 | - | - | - | 22.96 |
| XMMXCS J133943.6 − 314709.7 | 0035940301 | 204.93205 | −31.786030 | 155.83973 | 1.0470582e−14 | - | - | - | 24.14 |
| XMMXCS J033858.7 + 001530.3 | 0036540101 | 54.744615 | 0.25843751 | 71.366414 | 7.2658997e−15 | - | - | - | 31.80 |
| XMMXCS J022214.5 − 034616.9 | 0037980101 | 35.560674 | −3.7713786 | 76.283924 | 1.1470757e−14 | - | - | - | 9.63 |
| XMMXCS J022246.3 − 035155.8 | 0037980101 | 35.693243 | −3.8655209 | 125.00147 | 1.1565626e−14 | - | - | - | 40.60 |
| XMMXCS J022148.0 − 034609.2 | 0037980101 | 35.450353 | −3.7692432 | 358.74941 | 1.0901185e−13 | - | - | - | 133.03 |
| XMMXCS J022405.8 − 035503.4 | 0037980201 | 36.024398 | −3.9176325 | 169.08572 | 2.3048061e−14 | - | - | - | 32.45 |
| XMMXCS J022306.4 − 035029.5 | 0037980201 | 35.776775 | −3.8415409 | 60.682166 | 2.8855511e−14 | - | - | - | 12.03 |
| XMMXCS J022528.9 − 040032.2 | 0037980301 | 36.370728 | −4.0089458 | 200.71659 | 4.8020206e−14 | - | - | - | 52.60 |
| XMMXCS J022551.4 − 034524.9 | 0037980401 | 36.464499 | −3.7569292 | 60.668957 | 2.1898269e−14 | - | - | - | 14.17 |
| XMMXCS J022343.3 − 033051.2 | 0037980801 | 35.930812 | −3.5142476 | 38.050067 | 2.8424535e−14 | - | - | - | 21.55 |
| XMMXCS J022454.0 − 032844.1 | 0037980801 | 36.225406 | −3.4789352 | 80.309078 | 1.7027369e−14 | - | - | - | 32.14 |
| XMMXCS J022251.0 − 031144.4 | 0037981101 | 35.712809 | −3.1956828 | 86.107201 | 1.0114141e−14 | - | - | - | 37.78 |
| XMMXCS J022236.6 − 025708.5 | 0037981101 | 35.652753 | −2.9523687 | 67.522051 | 2.3957334e−14 | - | - | - | 16.89 |
| XMMXCS J022356.1 − 030558.0 | 0037981201 | 35.983939 | −3.0994473 | 129.83887 | 1.7980823e−14 | - | - | - | 39.89 |
| XMMXCS J022539.9 − 031127.6 | 0037981301 | 36.416543 | −3.1910223 | 4226.3493 | 6.0747489e−13 | - | - | - | 652.70 |
| XMMXCS J022544.1 − 031150.0 | 0037981401 | 36.433981 | −3.1972245 | 1135.7813 | 4.5454143e−13 | - | - | - | 366.65 |
| XMMXCS J022707.7 − 030114.8 | 0037981401 | 36.782442 | −3.0207855 | 107.98377 | 2.8405438e−14 | - | - | - | 40.95 |
| XMMXCS J022801.6 − 030257.6 | 0037981501 | 37.006911 | −3.0493477 | 46.539544 | 1.0341428e−14 | - | - | - | 20.41 |
| XMMXCS J022347.6 − 025127.8 | 0037981601 | 35.948428 | −2.8577273 | 232.67330 | 3.9539765e−14 | - | - | - | 62.25 |
| XMMXCS J022616.2 − 023954.0 | 0037981801 | 36.567810 | −2.6650095 | 682.35118 | 1.2234775e−13 | - | - | - | 569.05 |
| XMMXCS J022511.4 − 024432.6 | 0037981801 | 36.297637 | −2.7424117 | 6.2704901 | 1.2010762e−15 | - | - | - | 51.93 |
| XMMXCS J022744.4 − 025648.4 | 0037981901 | 36.935265 | −2.9468055 | 24.415879 | 4.2656185e−15 | - | - | - | 16.30 |
| XMMXCS J022103.1 − 042556.6 | 0037982101 | 35.263112 | −4.4324021 | 88.056009 | 1.0176667e−14 | - | - | - | 56.46 |
| XMMXCS J022157.8 − 043800.0 | 0037982101 | 35.491082 | −4.6333364 | 115.57224 | 2.5156870e−14 | - | - | - | 14.09 |
| XMMXCS J022142.3 − 042723.0 | 0037982101 | 35.426345 | −4.4564009 | 39.156323 | 4.8937429e−15 | - | - | - | 44.81 |
| XMMXCS J022130.4 − 040545.3 | 0037982201 | 35.376775 | −4.0959314 | 183.89859 | 2.6633716e−14 | - | - | - | 28.60 |
| XMMXCS J021929.6 − 043312.2 | 0037982301 | 34.873683 | −4.5533958 | 84.728663 | 1.4431453e−14 | - | - | - | 55.64 |
| XMMXCS J022003.1 − 041212.0 | 0037982401 | 35.013316 | −4.2033374 | 32.424068 | 4.8155441e−15 | - | - | - | 26.71 |
| XMMXCS J022023.9 − 040303.5 | 0037982401 | 35.099712 | −4.0509926 | 79.923779 | 1.1114892e−14 | - | - | - | 21.71 |
| XMMXCS J021951.1 − 033231.8 | 0037982601 | 34.962993 | −3.5421913 | 123.57391 | 3.3443316e−14 | - | - | - | 31.68 |
| XMMXCS J022045.0 − 032556.6 | 0037982601 | 35.187867 | −3.4324081 | 586.79511 | 6.6536157e−14 | - | - | - | 237.77 |
| XMMXCS J021939.2 − 032517.1 | 0037982601 | 34.913582 | −3.4214217 | 45.154822 | 3.2339793e−14 | - | - | - | 47.42 |
| XMMXCS J022038.8 − 030145.9 | 0037982701 | 35.162076 | −3.0294234 | 80.477074 | 1.6489568e−14 | - | - | - | 42.64 |
| XMMXCS J022118.7 − 032323.9 | 0037982701 | 35.328285 | −3.3899933 | 59.246544 | 1.1669731e−14 | - | - | - | 10.95 |
| XMMXCS J022045.3 − 030100.0 | 0037982701 | 35.188884 | −3.0166753 | 89.405989 | 2.5613865e−14 | - | - | - | 31.89 |
| XMMXCS J210406.9 − 121659.9 | 0038540301 | 316.02905 | −12.283306 | 67.392736 | 1.1616354e−14 | - | - | - | 83.79 |
| XMMXCS J104030.1 + 085653.3 | 0038540401 | 160.12549 | 8.9481531 | 1890.7845 | 4.9755196e−13 | - | - | - | 118.71 |
| XMMXCS J103937.2 + 090327.7 | 0038540401 | 159.90535 | 9.0577098 | 2840.8761 | 3.0751682e−13 | - | - | - | 469.38 |
| XMMXCS J103929.6 + 090706.7 | 0038540401 | 159.87361 | 9.1185315 | 904.53879 | 5.2578205e−13 | - | - | - | 250.31 |
| XMMXCS J103941.4 + 091851.1 | 0038540401 | 159.92256 | 9.3142078 | 18370.093 | −3.2553469e−11 | - | - | - | - |
| XMMXCS J015924.2 + 081141.9 | 0038541101 | 29.850960 | 8.1949764 | 219.95582 | 1.6393187e−13 | - | - | - | 15.28 |
| XMMXCS J153301.5 + 322840.5 | 0039140101 | 233.25666 | 32.477945 | 829.24744 | 9.4914467e−14 | - | - | - | 100.90 |
| XMMXCS J153352.9 + 324448.4 | 0039140101 | 233.47080 | 32.746792 | 459.85434 | 1.4064702e−13 | - | - | - | 19.35 |
| XMMXCS J153240.2 + 325632.2 | 0039140101 | 233.16765 | 32.942289 | 979.33267 | 2.4046910e−13 | - | - | - | 45.57 |
| XMMXCS J153323.3 + 323021.1 | 0039140101 | 233.34739 | 32.505863 | 2618.3018 | 6.5197030e−13 | - | - | - | 253.45 |
| XMMXCS J153345.9 + 323555.2 | 0039140101 | 233.44146 | 32.598685 | 1029.3016 | 8.5936575e−08 | - | - | - | 113.29 |
| XMMXCS J030159.2 − 000219.0 | 0041170101 | 45.496679 | −0.038619669 | 53.405362 | 1.4391110e−14 | - | - | - | 29.10 |
| XMMXCS J030145.6 + 000333.6 | 0041170101 | 45.440261 | 0.059341301 | 102.42464 | 1.5797800e−14 | - | - | - | 42.91 |
| XMMXCS J095957.4 + 251631.3 | 0041170201 | 149.98926 | 25.275364 | 1798.9276 | 1.1867326e−13 | - | - | - | - |

Continued on Next Page...

Table D.2 – Continued

| XCS Name | Obsid | RA | Dec | Counts | Flux | Literature Name | Match Distance | Literature Redshift | Sig |
|---|---|---|---|---|---|---|---|---|---|
| XMMXCS J100115.4 + 250612.7 | 0041170201 | 150.31452 | 25.103551 | 317.97156 | 2.5535198e−14 | - | - | - | 113.81 |
| XMMXCS J100056.0 + 250648.4 | 0041170201 | 150.23350 | 25.113453 | 57.195137 | 2.2304574e−15 | - | - | - | 12.21 |

Table D.2: DR3 StatSam New Candidtates. Column descriptions are given in Section 4.4. This table has been truncated to 200 candidates, the full version has 3825 candidates and is available online.

# Appendix E

# A description of the XCS database tables

| Column name | Description |
|---|---|
| obsid | XMM pointing identifier |
| dateObs | Date and time of begining of exposure |
| dateEnd | Date and time of end of exposure |
| revolut | XMM revolution number |
| target | Name of observed object |
| observer | Name of PI observer |
| raTarget | RA of target (Deg) |
| decTarget | Dec of target (Deg) |
| raNom | RA of nominal boresight (Deg) |
| decNom | Dec of nominal boresight (Deg) |
| equinox | Equinox of sky co-ordinates |
| raPnt | Mean RA of pointing (Deg) |
| decPnt | Mean Dec of pointing (Deg) |
| paPnt | Mean position angle (Deg) |
| cdelt2 | Pixel size (Deg) |
| nhval | Hydrogen column density |
| type | Pointing type |
| maskflag | Binary flag indicating existence of image mask |

Table E.1: Column descriptions of the XCS Observation table.

| Column name | Description |
|---|---|
| id | Index for table |
| name | IAU XCS name |
| obsid | XMM pointing identifier |
| ra | Right Ascension (Deg) |
| dec | Declination (Deg) |
| x | Image x position |
| y | Image y position |
| xerr | $1\sigma$ error on x |
| yerr | $1\sigma$ error on y |
| major | Object ellipse major axis |
| minor | Object ellipse minor axis |
| orient | Object ellipse orientation |
| theta | Offaxis angle (arcmin) |
| phi | Azimuthal angle (Deg) |
| scts | Soft band source counts |
| ctrate | Soft band count rate |
| ctrateerr | Soft band count rate error |
| flux | Soft band flux |
| sig | Source significance |
| ppoint | Probablity of source being point-like |
| class | Source classification |
| psfsizeflag | Potential mis-classification flag |
| pntconflag | Potential contamination flag |
| run1conflag | Potential Run1 contamination flag |
| rinnermaj | Background annulus inner edge major axis |
| rinnermin | Background annulus inner edge minor axis |
| routermaj | Background annulus outer edge major axis |
| routermin | Background annulus outer edge minor axis |
| srcpix | Number of pixels used for source aperture |
| bkgpix | Number of pixels used for background aperture |
| avsrcexp | Average exposure across source |
| avbkgexp | Average exposure across background |
| bkgcts | Counts in background annulus |
| bkgctssrc | Background counts in source aperture |
| totcts | Total counts in source aperture |
| masterid | ID for master detection |

Table E.2: Column descriptions of the XCS Detection table.

| Column name | Description |
|---|---|
| id | Index for table |
| xcsname | IAU XCS name |
| detectionid | ID from Detection table |
| masterid | Master ID from Detection table |
| obsid | XMM pointing identifier |
| camera | EPIC camera |
| ident | Exposure identifier |
| scts | Individual exposure soft band source counts |
| ctrate | Individual exposure count-rate |
| flux | Individual exposure source flux |
| sig | Source significance |
| rinnermaj | Background annulus inner edge major axis |
| rinnermin | Background annulus inner edge minor axis |
| routermaj | Background annulus outer edge major axis |
| routermin | Background annulus outer edge minor axis |
| srcpix | Number of pixels used for source aperture |
| bkgpix | Number of pixels used for background aperture |
| avsrcexp | Average exposure across source |
| avbkgexp | Average exposure across background |
| bkgcts | Counts in background annulus |
| bkgctssrc | Background counts in source aperture |
| totcts | Total counts in source aperture |

Table E.3: Column descriptions of the XCS IndivExpProp table.

| Column name | Description |
|---|---|
| xcsname | IAU XCS name |
| obsid | XMM pointing identifier |
| ra | Right Ascension |
| dec | Declination |
| softcts | Soft band source counts |
| tmax | Maximum source exposure in soft band |
| softflux | Soft band source flux |
| hardcts | Hard band source counts |
| tmaxhard | Maximum source exposure in hard band |
| hardnessratio | Hardness ratio for source |
| softsig | Soft band source significance |
| hardsig | Hard band source significance |
| softppoint | Probability of source being point-like (soft band) |
| class | Source classification |
| masterdetectionid | Master ID in Detection table |
| masterpsfsizeflag | Master Detection PSF size warning |
| masterpntconflag | Master Detection point contamination |
| masterrun1conflag | Master Detection Run1 contamination |
| targetflag | Warning that source may be pointing target |
| clobsflag | Warning that source is in a Cluster Pointing |
| snrobsflag | Warning that source is in a SNR Pointing |

Table E.4: Column descriptions of the XCS Source table.

# Appendix F

# XCS Selection function plots

Following are the full set of plots demonstrating the XCS selection function, all the data is for clusters with $r_c = 160kpc, \beta = 2/3$, and $e = 0.0$, in a $\Omega_\Lambda = 0.7$, $\Omega_m = 0.3$ cosmology.

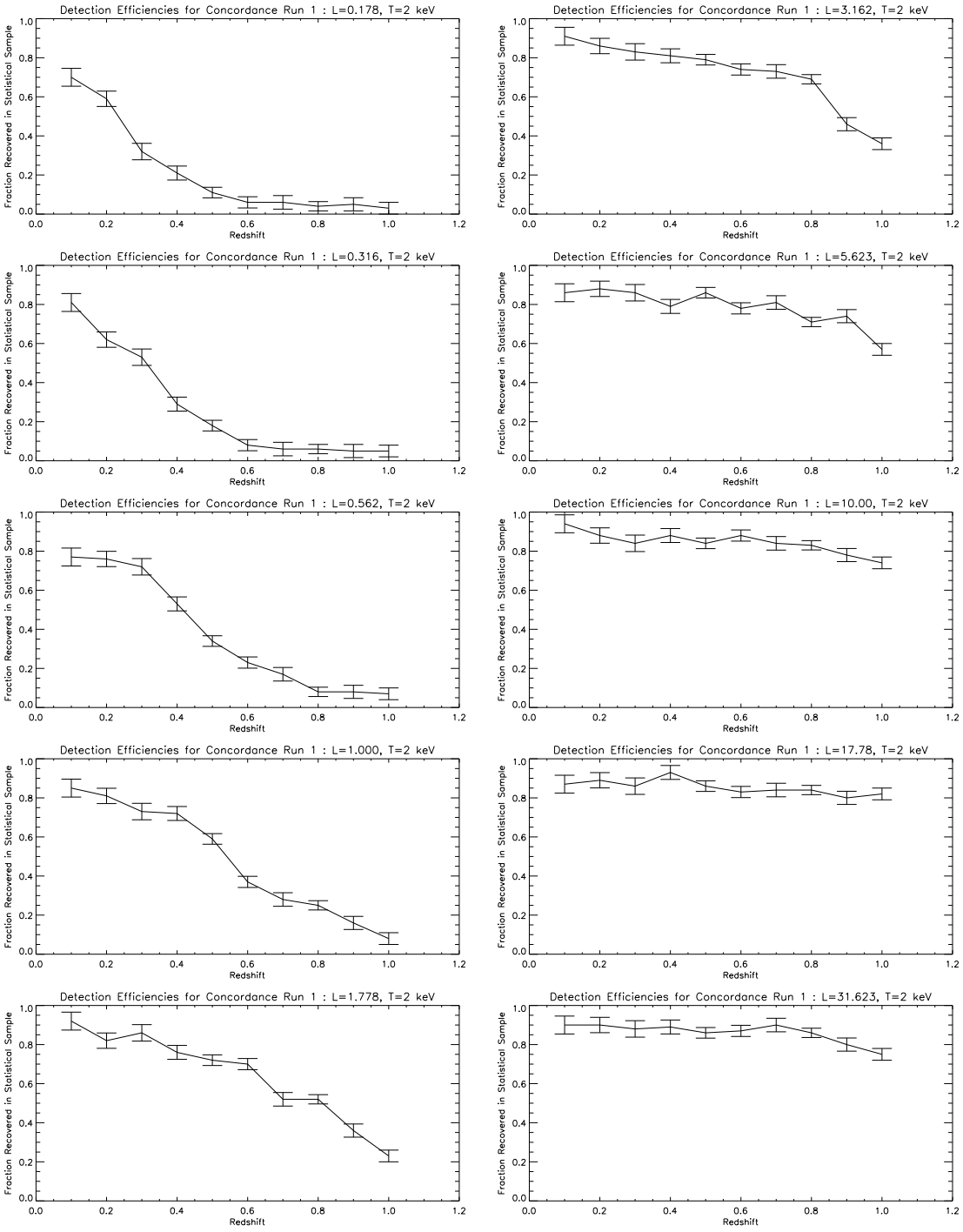


Figure F.1: XCS StatSam detection and classification efficiency for 2keV clusters.

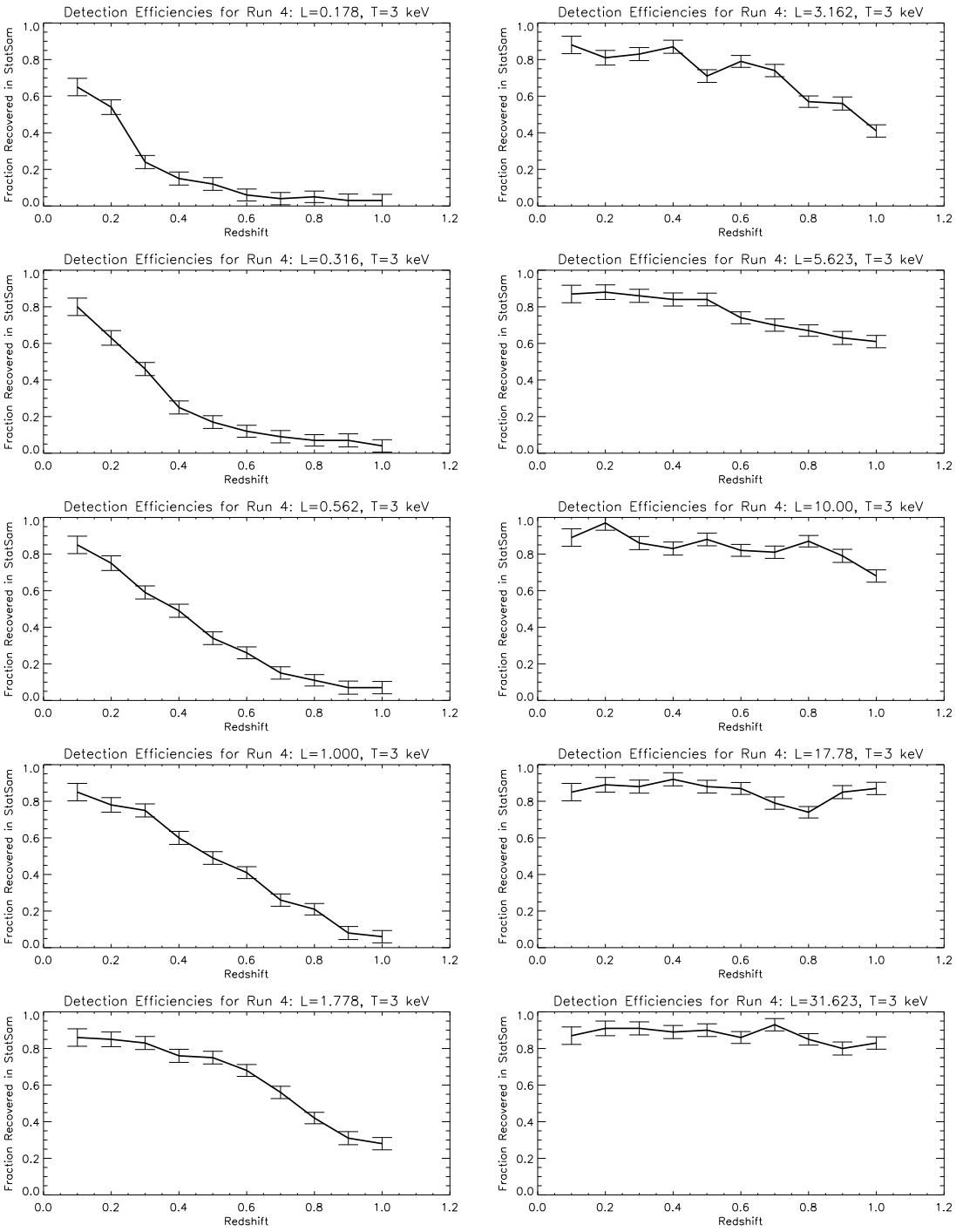


Figure F.2: XCS StatSam detection and classification efficiency for 3keV clusters.

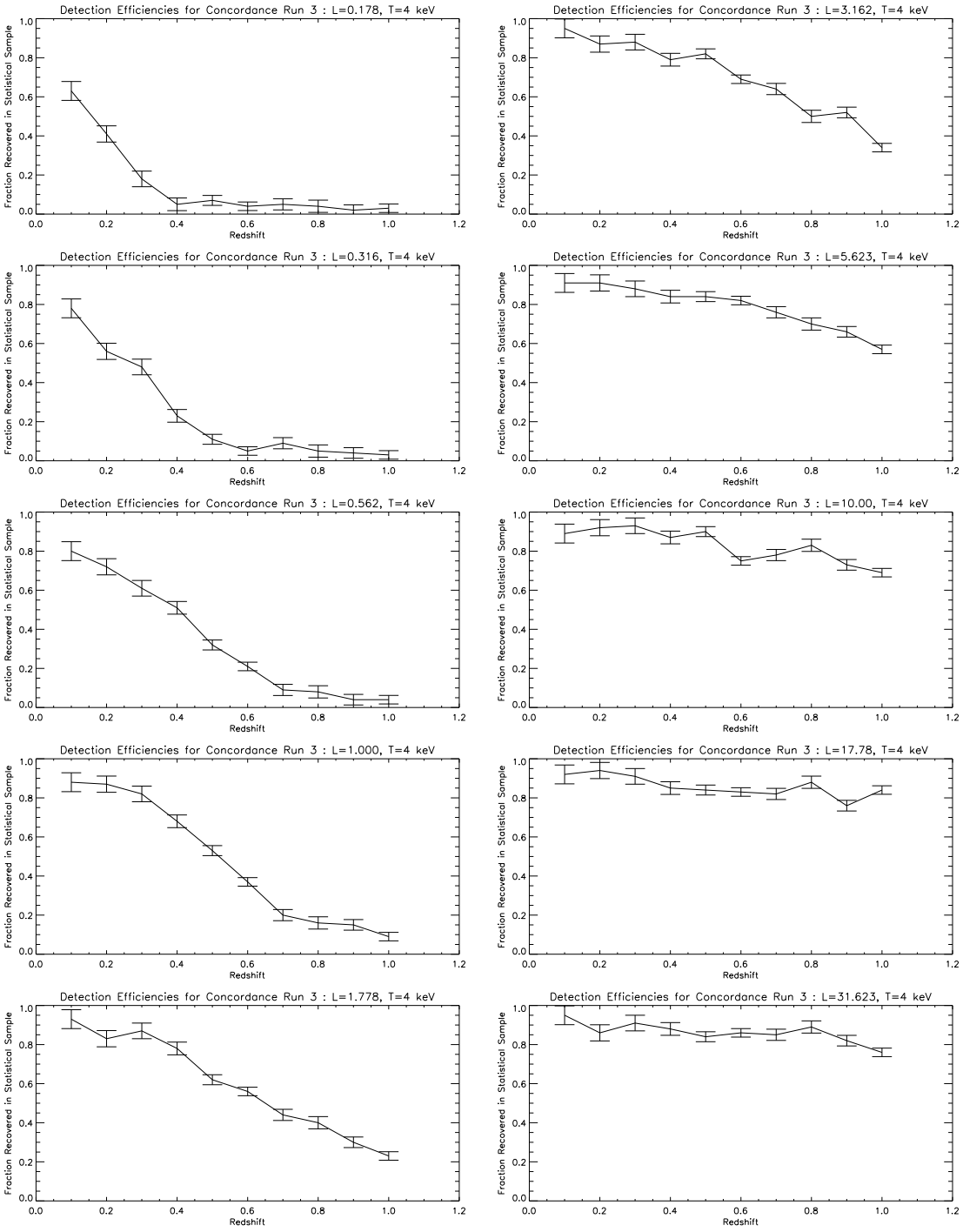


Figure F.3: XCS StatSam detection and classification efficiency for 4keV clusters.

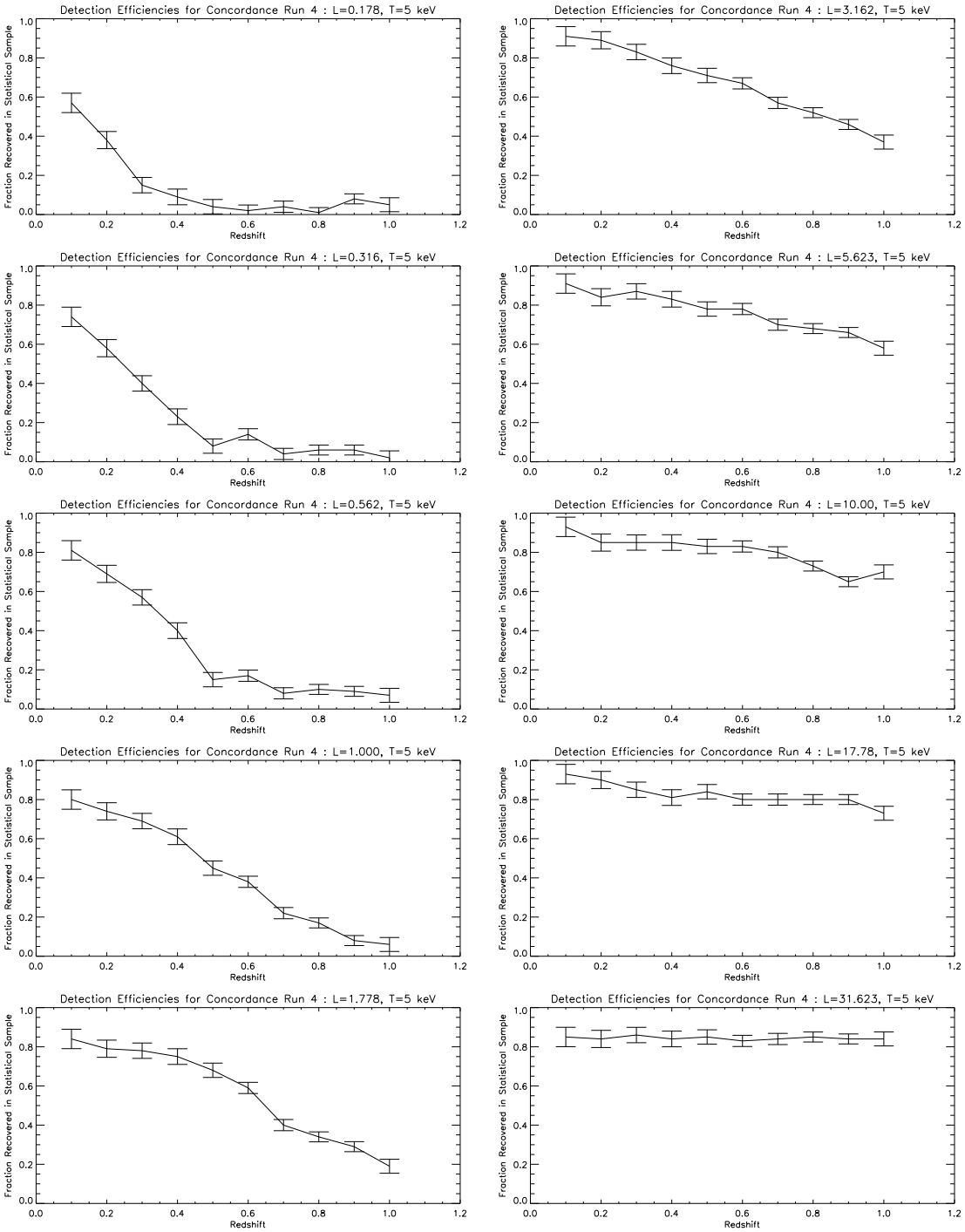


Figure F.4: XCS StatSam detection and classification efficiency for 5keV clusters.

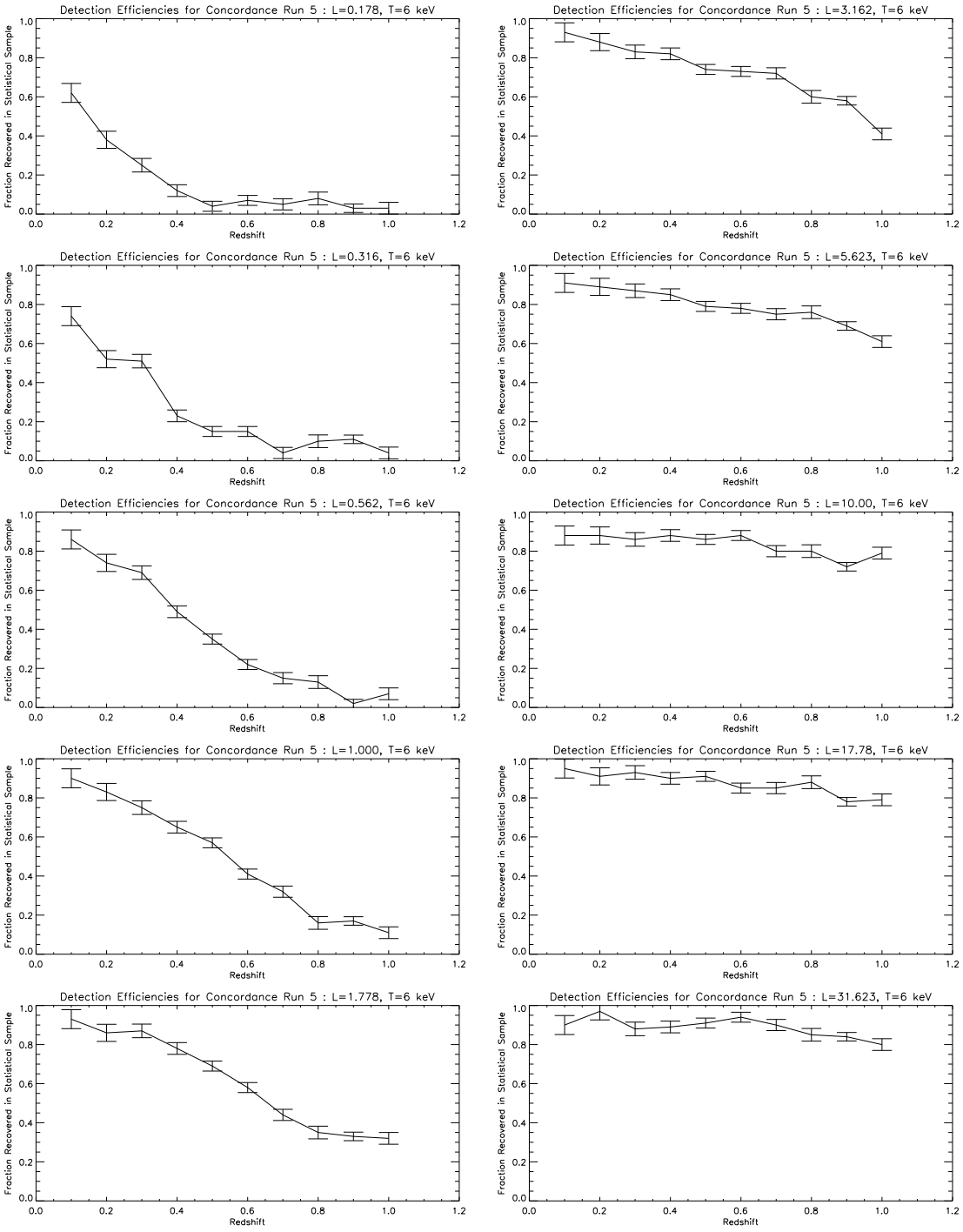


Figure F.5: XCS StatSam detection and classification efficiency for 6keV clusters.

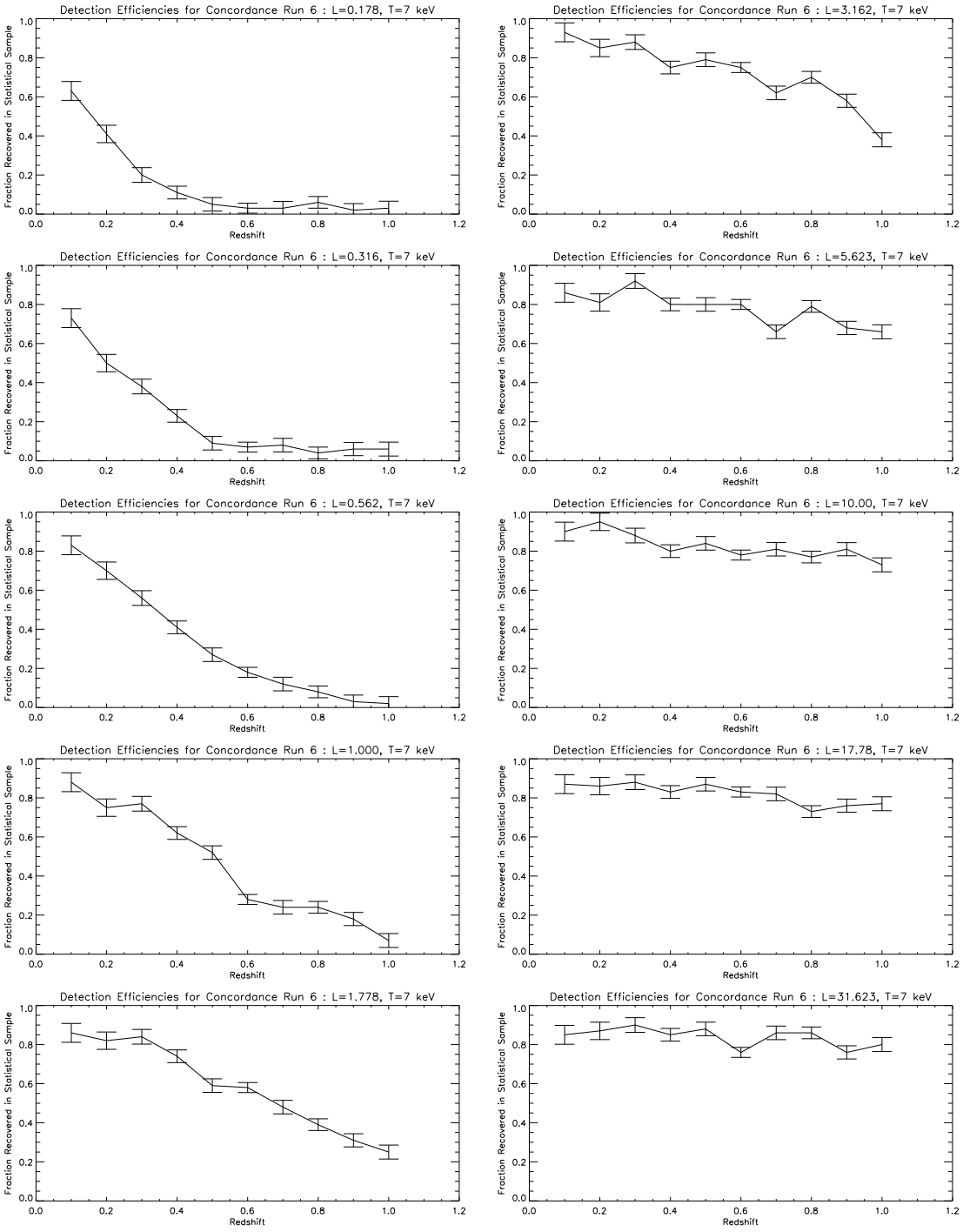


Figure F.6: XCS StatSam detection and classification efficiency for 7keV clusters.

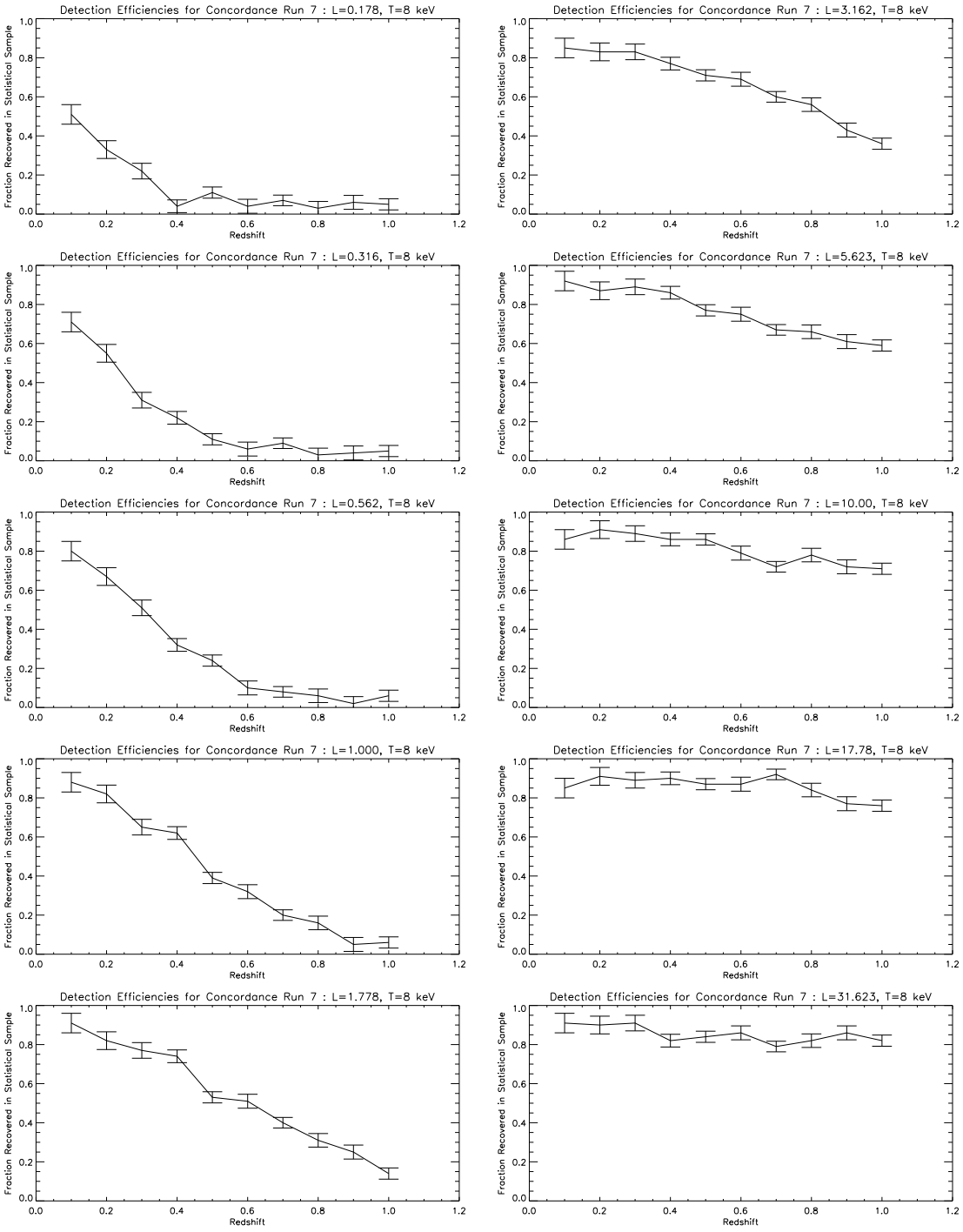


Figure F.7: XCS StatSam detection and classification efficiency for 8keV clusters.

# Appendix G

# A description of the XCS reduction of the XMM ODF's

The following text has been edited from that provided by E. Lloyd-Davies, who undertook the work described in this Appendix.

## G.1 Data reduction

Each observation in the XMM-Newton public archive that contains EPIC camera data was used. The data was download from the XMM-Newton Science Archive (XSA) using the Archive InterOperability System (AIO) to automate the process.

### G.1.1 Software versions

The data reduction pipeline was written using Python 2.5 but involved the use of several different software packages. Version 7.1.0 of the Science Analysis Software (SAS) was the main software package used in the data reduction but version 6.6.3 of HEASoft and version 4.0 of CIAO were also extensively used.

### G.1.2 Reduction procedure

The reduction of the XMM-Newton data was carried out in a standard way using the SAS software package. Only events with patterns 0-4 were used for the EPIC-pn and 0-12 for the EPIC-mos.

### G.1.3 Flare cleaning

To increase the signal-to-noise of the data, periods of high background (such as those resulting from enhanced solar activity) were removed. This was achieved by creating a lightcurve of the high energy (particle dominated) events (12-15 keV for the EPIC-pn and 10-12 keV for the EPIC-mos cameras). An iterative 3-sigma clipping procedure was then used to select the periods to remove. This involves calculating the mean and standard deviation of the lightcurve and then excluding bins more than 3-sigma from the mean. The mean and standard deviation are then recalculated and the choice of bins to exclude made using the new values. This procedure was repeated until a stable state was reached. On the initial pass the bins with values more than 25 percent greater than the mean are excluded. This is to handle cases where there is more bad (high background) data than there is good, as without this the algorithm would exclude the good data and keep the contaminated data. Starting from a position of excluding any data considerably greater than the mean makes this an unlikely outcome of the iteration procedure. Finally images and spectra can be produced using the good time intervals identified by this procedure.

### G.1.4 Energy conversion factors

In order to be able to convert source counts in the images into fluxes, energy conversion factors need to be calculated. These are necessarily model dependent and are affected not only by the source and instrument properties but also by the galactic column in the field. Since in general the source properties are not known (without much more detailed spectroscopic study) a generic model has to be assumed. Since the vast majority of the sources detected by XCS are point source that are likely to have powerlaw spectra, the model used to calculate the conversion is a powerlaw with an index of 1.7, with a photoelectric absorption set to the galactic HI radio column for the field. ECFs were calculated for each camera exposure in each observation. The XSpec spectral fitting package was used with the aforementioned model and the on-axis spectral responses for the observation to calculate the conversion factors.

### G.1.5 Image production

The images to be used for the source searching were produced for the cleaned event lists by binning spatial binning the events with a pixel size of 4.35 arcsec. Images were produced in two bands, soft (0.5-2.0 keV) and hard (2-10 keV). Exposure maps were also created for each image. EPIC-pn images were corrected for out of time events in the standard way (this correction was not used for the EPIC-mos images since their much lower readout rate results in the effect being negligible). The images and exposure maps for the individual cameras were merged to create single image and exposure map per observation. Due to the fact that the EPIC-mos cameras receive only about half the light that the EPIC-pn does in a second of exposure. In order to correct for this when merging the exposure maps, the maps for the EPIC-mos cameras were scaled using the ECFs to that of the EPIC-pn camera.

# Appendix H

# Tables of XCS cluster properties

| XCS name | R.A (J2000) | Dec (J2000) | Soft Counts | Redshift | Ngal |
|---|---|---|---|---|---|
| XMMXCS J000014.0-251057.3 | 0.058558 | -25.182606 | 1264.520 | 0.140 | 35 |
| XMMXCS J000018.8-245711.8 | 0.078654 | -24.953297 | 46.650 | 0.690 | 1 |
| XMMXCS J000047.1-251546.2 | 0.196368 | -25.262848 | 56.424 | 0.180 | 15 |
| XMMXCS J000103.5-250352.6 | 0.264907 | -25.064621 | 470.416 | 0.910 | 15 |
| XMMXCS J000626.3+195937.3 | 1.609940 | 19.993700 | 164.575 | 0.460 | 38 |
| XMMXCS J000634.9+201722.3 | 1.645555 | 20.289532 | 251.639 | 0.860 | 19 |
| XMMXCS J002935.4+345323.1 | 7.397867 | 34.889776 | 216.535 | 0.740 | 26 |
| XMMXCS J002953.8+350505.8 | 7.474367 | 35.084960 | 128.684 | 0.450 | 32 |
| XMMXCS J003407.3-432237.7 | 8.530773 | -43.377148 | 214.181 | 0.400 | 12 |
| XMMXCS J003412.4-433154.9 | 8.551851 | -43.531933 | 115.382 | 0.610 | 6 |
| XMMXCS J003414.9+852003.9 | 8.562299 | 85.334427 | 291.388 | 0.430 | 19 |
| XMMXCS J003427.6-431855.8 | 8.615233 | -43.315502 | 3550.930 | 0.410 | 50 |
| XMMXCS J003439.3-120716.0 | 8.663751 | -12.121112 | 487.336 | 0.440 | 50 |
| XMMXCS J003503.2-432839.4 | 8.763538 | -43.477636 | 40.823 | 0.110 | 1 |
| XMMXCS J003513.5-431016.2 | 8.806275 | -43.171169 | 160.382 | 0.150 | 6 |
| XMMXCS J003547.2-430530.0 | 8.947032 | -43.091675 | 66.306 | 0.370 | 3 |
| XMMXCS J003548.2-432230.6 | 8.951163 | -43.375168 | 884.349 | 0.550 | 46 |
| XMMXCS J003551.3-431217.8 | 8.964063 | -43.204964 | 479.606 | 0.390 | 19 |
| XMMXCS J003603.7+851321.4 | 9.015593 | 85.222633 | 590.678 | 0.700 | 10 |
| XMMXCS J003627.4-432835.6 | 9.114320 | -43.476566 | 1172.100 | 0.410 | 50 |
| XMMXCS J003646.4-432020.6 | 9.193531 | -43.339073 | 601.299 | 0.250 | 37 |
| XMMXCS J003832.0+853105.5 | 9.633369 | 85.518211 | 244.621 | 0.650 | 5 |
| XMMXCS J004047.2+850536.2 | 10.196878 | 85.093399 | 58.778 | 0.490 | 2 |
| XMMXCS J004128.7+852832.4 | 10.369600 | 85.475693 | 233.885 | 0.460 | 8 |
| XMMXCS J004616.1+853116.7 | 11.567438 | 85.521309 | 1688.790 | 0.660 | 24 |
| XMMXCS J004753.1+852716.9 | 11.971525 | 85.454704 | 584.735 | 0.310 | 11 |
| XMMXCS J005126.0+852456.3 | 12.858494 | 85.415665 | 120.815 | 0.590 | 4 |
| XMMXCS J011023.7+330543.4 | 17.598979 | 33.095399 | 372.837 | 0.600 | 38 |
| XMMXCS J011138.6-453858.9 | 17.911226 | -45.649704 | 846.144 | 0.390 | 50 |
| XMMXCS J011244.0-454237.5 | 18.183615 | -45.710442 | 69.387 | 0.680 | 4 |
| XMMXCS J011624.2+325718.5 | 19.101153 | 32.955143 | 175.020 | 0.450 | 50 |
| XMMXCS J011632.0+330324.6 | 19.133688 | 33.056855 | 408.671 | 0.630 | 50 |
| XMMXCS J011954.7+141655.1 | 19.977931 | 14.281974 | 93.330 | 0.550 | 16 |
| XMMXCS J014449.9-043231.5 | 26.208227 | -4.542109 | 1053.650 | 0.170 | 15 |
| XMMXCS J014506.3-043921.5 | 26.276590 | -4.655992 | 180.585 | 0.720 | 5 |
| XMMXCS J014523.2-042305.7 | 26.346951 | -4.384943 | 149.491 | 0.660 | 8 |
| XMMXCS J014525.9-044751.7 | 26.358292 | -4.797698 | 120.700 | 0.100 | 9 |
| XMMXCS J014547.5-042214.4 | 26.448021 | -4.370684 | 145.881 | 0.490 | 4 |
| XMMXCS J014557.3-043411.7 | 26.488785 | -4.569923 | 41.913 | 0.100 | 0 |
| XMMXCS J014603.4-044450.4 | 26.514175 | -4.747359 | 80.081 | 0.680 | 8 |
| XMMXCS J014801.3+055247.2 | 27.005644 | 5.879805 | 334.501 | 0.410 | 12 |
| XMMXCS J014920.6+055518.5 | 27.336079 | 5.921812 | 131.210 | 0.460 | 8 |
| XMMXCS J015653.6+284338.7 | 29.223354 | 28.727443 | 451.506 | 0.280 | 43 |
| XMMXCS J015656.0+375913.2 | 29.233646 | 37.987026 | 96.187 | 0.100 | 0 |
| XMMXCS J015719.5+375635.8 | 29.331545 | 37.943302 | 1343.200 | 0.240 | 50 |
| XMMXCS J015731.0+380207.1 | 29.379307 | 38.035309 | 113.878 | 0.700 | 17 |
| XMMXCS J015746.3+284918.1 | 29.442978 | 28.821697 | 62.756 | 0.400 | 20 |
| XMMXCS J015754.8+375239.1 | 29.478340 | 37.877537 | 250.217 | 0.630 | 1 |
| XMMXCS J015800.7+284256.6 | 29.503201 | 28.715744 | 91.267 | 0.840 | 2 |
| XMMXCS J021939.3-032514.8 | 34.913826 | -3.420789 | 45.817 | 0.500 | 12 |
| XMMXCS J021951.2-033234.3 | 34.963505 | -3.542864 | 101.813 | 0.170 | 5 |
| XMMXCS J022045.1-032555.8 | 35.187920 | -3.432190 | 557.249 | 0.300 | 35 |
| XMMXCS J022145.3-034617.7 | 35.439041 | -3.771597 | 1855.860 | 0.100 | 0 |
| XMMXCS J022205.0-043240.6 | 35.521023 | -4.544619 | 314.954 | 0.350 | 50 |
| XMMXCS J022206.5-030311.2 | 35.527328 | -3.053137 | 373.981 | 0.470 | 23 |
| XMMXCS J022222.3-024837.8 | 35.593155 | -2.810502 | 32.488 | 0.470 | 3 |
| XMMXCS J022225.4-043735.8 | 35.605961 | -4.626612 | 43.209 | 1.020 | 3 |
| XMMXCS J022247.0-035148.6 | 35.696087 | -3.863516 | 81.117 | 0.100 | 0 |
| XMMXCS J022251.2-041642.5 | 35.713482 | -4.278484 | 87.958 | 0.300 | 12 |
| XMMXCS J022258.6-040639.0 | 35.744167 | -4.110844 | 91.214 | 0.290 | 33 |
| XMMXCS J022258.8-041609.5 | 35.745140 | -4.269324 | 39.414 | 0.380 | 10 |
| XMMXCS J022303.0-043620.6 | 35.762665 | -4.605742 | 79.649 | 0.490 | 5 |
| XMMXCS J022307.3-041307.3 | 35.780560 | -4.218706 | 171.212 | 0.100 | 0 |
| XMMXCS J022317.0-030718.5 | 35.821033 | -3.121817 | 47.534 | 0.340 | 3 |
| XMMXCS J022328.1-042150.5 | 35.867149 | -4.364036 | 265.112 | 0.670 | 9 |
| XMMXCS J022341.7-043032.0 | 35.923981 | -4.508895 | 59.896 | 0.460 | 8 |
| XMMXCS J022341.8-025405.1 | 35.924229 | -2.901422 | 53.302 | 0.120 | 10 |
| XMMXCS J022346.7-042435.3 | 35.944989 | -4.409833 | 120.841 | 0.590 | 3 |
| XMMXCS J022347.5-025133.5 | 35.948063 | -2.859329 | 269.228 | 0.110 | 16 |
| XMMXCS J022351.0-044910.1 | 35.962662 | -4.819490 | 60.459 | 0.480 | 3 |
| XMMXCS J022351.4-041842.5 | 35.964333 | -4.311832 | 103.922 | 0.100 | 0 |
| XMMXCS J022356.2-030557.1 | 35.984318 | -3.099217 | 152.141 | 0.270 | 12 |
| XMMXCS J022404.2-041327.9 | 36.017582 | -4.224425 | 405.688 | 0.910 | 50 |
| XMMXCS J022406.1-035502.7 | 36.025448 | -3.917422 | 184.711 | 0.500 | 50 |
| XMMXCS J022433.8-041433.1 | 36.141029 | -4.242555 | 1989.460 | 0.260 | 50 |
| XMMXCS J022434.4-041427.1 | 36.143620 | -4.240875 | 340.109 | 0.250 | 50 |
| XMMXCS J022500.0-040021.8 | 36.250122 | -4.006071 | 72.375 | 0.100 | 15 |

Continued on Next Page...

Table H.1 – Continued

| XCS name | R.A (J2000) | Dec (J2000) | Soft Counts | Redshift | Ngal |
|---|---|---|---|---|---|
| XMMXCS J022508.9-040832.7 | 36.287441 | -4.142435 | 87.792 | 0.380 | 7 |
| XMMXCS J022509.6-041900.6 | 36.290016 | -4.316840 | 226.987 | 0.100 | 12 |
| XMMXCS J022510.2-040139.8 | 36.292763 | -4.027745 | 151.400 | 0.190 | 25 |
| XMMXCS J022529.1-040037.5 | 36.371342 | -4.010441 | 230.381 | 0.840 | 2 |
| XMMXCS J024249.6+372130.6 | 40.706852 | 37.358501 | 105.116 | 0.370 | 8 |
| XMMXCS J024311.6+372331.3 | 40.798641 | 37.392052 | 44.566 | 0.520 | 29 |
| XMMXCS J024403.9+372628.4 | 41.016441 | 37.441238 | 56.671 | 0.450 | 10 |
| XMMXCS J024409.8+373128.8 | 41.041058 | 37.524681 | 818.672 | 0.660 | 34 |
| XMMXCS J024426.3+371753.4 | 41.109715 | 37.298187 | 52.870 | 0.600 | 14 |
| XMMXCS J024902.2-312010.6 | 42.259411 | -31.336304 | 165.652 | 0.130 | 15 |
| XMMXCS J025006.5-310400.2 | 42.527138 | -31.066734 | 740.896 | 0.800 | 36 |
| XMMXCS J030159.0-000221.0 | 45.495949 | -0.039173 | 54.600 | 0.190 | 9 |
| XMMXCS J030205.5-000002.4 | 45.523251 | -0.000684 | 452.118 | 0.530 | 30 |
| XMMXCS J030211.3-000133.5 | 45.547230 | -0.025999 | 193.837 | 0.550 | 11 |
| XMMXCS J030212.0+000600.6 | 45.550259 | 0.100193 | 88.238 | 1.040 | 3 |
| XMMXCS J030212.0+001119.3 | 45.550388 | 0.188709 | 186.390 | 0.550 | 31 |
| XMMXCS J030237.0-000506.4 | 45.654472 | -0.085129 | 213.173 | 0.130 | 14 |
| XMMXCS J030248.6+002131.5 | 45.702866 | 0.358768 | 628.134 | 0.410 | 4 |
| XMMXCS J030253.9-000606.6 | 45.724693 | -0.101858 | 59.510 | 0.560 | 7 |
| XMMXCS J030317.4+001239.7 | 45.822582 | 0.211037 | 138.309 | 0.520 | 36 |
| XMMXCS J030534.3-000514.4 | 46.393321 | -0.087348 | 94.524 | 0.870 | 1 |
| XMMXCS J030542.3-001457.6 | 46.426316 | -0.249355 | 89.472 | 0.650 | 1 |
| XMMXCS J030614.6-000537.0 | 46.561031 | -0.093636 | 1297.670 | 0.440 | 15 |
| XMMXCS J030617.3-000837.7 | 46.572441 | -0.143828 | 2686.600 | 0.130 | 41 |
| XMMXCS J030625.3+001306.1 | 46.605831 | 0.218380 | 236.782 | 0.590 | 6 |
| XMMXCS J030707.1-001600.9 | 46.779909 | -0.266935 | 77.423 | 0.100 | 0 |
| XMMXCS J035317.9-000535.6 | 58.324852 | -0.093232 | 74.610 | 0.480 | 3 |
| XMMXCS J035415.8-001006.0 | 58.566212 | -0.168347 | 437.403 | 0.200 | 18 |
| XMMXCS J035726.1+011807.8 | 59.358776 | 1.302173 | 1244.480 | 0.130 | 50 |
| XMMXCS J035744.5+010137.0 | 59.435566 | 1.026969 | 897.978 | 0.280 | 50 |
| XMMXCS J041938.0+142116.4 | 64.908745 | 14.354565 | 53.912 | 0.590 | 3 |
| XMMXCS J041944.9+143905.9 | 64.937363 | 14.651662 | 300.172 | 0.350 | 14 |
| XMMXCS J041945.6+021319.0 | 64.940331 | 2.221969 | 281.903 | 0.100 | 1 |
| XMMXCS J042029.2+022645.3 | 65.121780 | 2.445937 | 87.364 | 0.330 | 5 |
| XMMXCS J045438.5-531907.9 | 73.660744 | -53.318878 | 65.115 | 0.460 | 4 |
| XMMXCS J045459.9-532945.4 | 73.749863 | -53.495964 | 50.740 | 0.600 | 4 |
| XMMXCS J045506.0-532342.5 | 73.775154 | -53.395149 | 803.746 | 0.390 | 45 |
| XMMXCS J051326.3+792919.5 | 78.359779 | 79.488777 | 43.284 | 0.820 | 5 |
| XMMXCS J051510.9+010609.6 | 78.795685 | 1.102675 | 53.101 | 0.110 | 3 |
| XMMXCS J051528.4+793425.4 | 78.868675 | 79.573746 | 312.687 | 0.410 | 26 |
| XMMXCS J051549.8+794000.9 | 78.957771 | 79.666924 | 302.882 | 0.610 | 13 |
| XMMXCS J051554.0+010413.9 | 78.975327 | 1.070535 | 53.568 | 0.120 | 7 |
| XMMXCS J051609.9+010946.3 | 79.041267 | 1.162873 | 156.729 | 0.240 | 16 |
| XMMXCS J063945.9+821849.6 | 99.941635 | 82.313782 | 1149.960 | 0.410 | 50 |
| XMMXCS J064023.4+822858.3 | 100.097542 | 82.482864 | 153.628 | 0.790 | 25 |
| XMMXCS J064246.4+822837.5 | 100.693398 | 82.477104 | 122.887 | 0.700 | 5 |
| XMMXCS J064424.1+822634.0 | 101.100609 | 82.442780 | 289.835 | 0.840 | 5 |
| XMMXCS J065046.2+742838.1 | 102.692551 | 74.477264 | 190.866 | 0.540 | 5 |
| XMMXCS J075427.9+220952.1 | 118.616287 | 22.164482 | 275.158 | 0.370 | 50 |
| XMMXCS J075433.7+214839.3 | 118.640450 | 21.810928 | 42.720 | 0.770 | 2 |
| XMMXCS J075457.7+221313.2 | 118.740593 | 22.220335 | 44.945 | 0.670 | 21 |
| XMMXCS J075534.3+220240.2 | 118.893143 | 22.044514 | 53.201 | 0.150 | 7 |
| XMMXCS J075602.0+215849.5 | 119.008553 | 21.980444 | 75.223 | 0.400 | 2 |
| XMMXCS J080532.0+152136.9 | 121.383568 | 15.360264 | 86.674 | 0.610 | 6 |
| XMMXCS J080613.2+152243.8 | 121.555397 | 15.378855 | 153.567 | 0.300 | 9 |
| XMMXCS J080633.4+153224.5 | 121.639389 | 15.540142 | 82.966 | 0.180 | 19 |
| XMMXCS J080713.6+152658.8 | 121.807022 | 15.449694 | 722.051 | 0.110 | 14 |
| XMMXCS J083025.8+524129.1 | 127.607658 | 52.691433 | 3886.600 | 0.780 | 45 |
| XMMXCS J083054.3+524538.9 | 127.726547 | 52.760807 | 63.108 | 0.660 | 3 |
| XMMXCS J083115.4+523453.8 | 127.814339 | 52.581615 | 263.184 | 0.520 | 38 |
| XMMXCS J083147.8+525036.1 | 127.949257 | 52.843365 | 668.885 | 0.460 | 50 |
| XMMXCS J083154.4+523217.7 | 127.976768 | 52.538277 | 179.977 | 0.370 | 8 |
| XMMXCS J083213.6+524830.2 | 128.056839 | 52.808395 | 360.823 | 0.490 | 9 |
| XMMXCS J083215.3+525808.9 | 128.063828 | 52.969158 | 104.674 | 0.730 | 3 |
| XMMXCS J083216.6+523201.8 | 128.069275 | 52.533855 | 110.117 | 0.360 | 16 |
| XMMXCS J083856.2+253806.7 | 129.734406 | 25.635206 | 57.246 | 0.900 | 16 |
| XMMXCS J083901.2+705003.7 | 129.755249 | 70.834366 | 110.209 | 0.450 | 18 |
| XMMXCS J083913.9+704803.1 | 129.808243 | 70.800880 | 129.715 | 0.470 | 10 |
| XMMXCS J091821.8+211447.5 | 139.590973 | 21.246546 | 345.749 | 0.690 | 14 |
| XMMXCS J092544.7+305430.7 | 141.436560 | 30.908543 | 112.484 | 0.400 | 11 |
| XMMXCS J092545.6+305857.2 | 141.440400 | 30.982583 | 1101.520 | 0.520 | 50 |
| XMMXCS J092555.3+304944.2 | 141.480440 | 30.828957 | 108.894 | 0.480 | 22 |
| XMMXCS J092641.3+310309.5 | 141.672450 | 31.052644 | 145.989 | 0.670 | 20 |
| XMMXCS J092650.5+310128.8 | 141.710800 | 31.024669 | 481.382 | 0.490 | 38 |
| XMMXCS J092655.0+305007.5 | 141.729380 | 30.835443 | 86.314 | 0.150 | 4 |
| XMMXCS J092703.2+310037.9 | 141.763520 | 31.010551 | 141.151 | 0.480 | 18 |
| XMMXCS J092726.0+310306.6 | 141.858520 | 31.051858 | 175.255 | 0.960 | 2 |
| XMMXCS J092735.8+305339.7 | 141.899220 | 30.894361 | 66.844 | 0.540 | 4 |
| XMMXCS J093259.4+551545.0 | 143.247894 | 55.262505 | 380.345 | 0.520 | 3 |
| XMMXCS J093350.2+552620.1 | 143.459259 | 55.438927 | 187.277 | 0.490 | 40 |
| XMMXCS J093358.2+550946.1 | 143.492538 | 55.162830 | 52.454 | 0.180 | 9 |
| XMMXCS J093423.1+551743.5 | 143.596283 | 55.295433 | 130.094 | 0.620 | 1 |
| XMMXCS J093438.5+551335.7 | 143.660675 | 55.226585 | 172.692 | 0.810 | 20 |
| XMMXCS J093532.8+552142.6 | 143.887054 | 55.361851 | 80.043 | 0.390 | 3 |
| XMMXCS J095105.8+391741.3 | 147.774429 | 39.294827 | 113.257 | 0.440 | 17 |
| XMMXCS J095127.7+392009.1 | 147.865601 | 39.335869 | 48.611 | 0.440 | 4 |
| XMMXCS J095957.8+251630.4 | 149.990982 | 25.275124 | 1740.810 | 1.070 | 2 |
| XMMXCS J100031.5+251714.3 | 150.131592 | 25.287312 | 119.786 | 0.650 | 11 |
| XMMXCS J100104.2+252625.0 | 150.267670 | 25.440285 | 156.436 | 0.530 | 14 |
| XMMXCS J100115.3+250612.4 | 150.314117 | 25.103470 | 353.618 | 0.670 | 35 |
| XMMXCS J100124.2+250653.9 | 150.351166 | 25.114977 | 50.458 | 0.490 | 9 |
| XMMXCS J104348.0-012408.2 | 160.950104 | -1.402283 | 82.808 | 0.410 | 3 |
| XMMXCS J104407.2-012722.2 | 161.030029 | -1.456194 | 86.810 | 0.180 | 4 |
| XMMXCS J104448.6-011155.7 | 161.202805 | -1.198813 | 113.625 | 0.510 | 4 |
| XMMXCS J104507.9-013617.7 | 161.283325 | -1.604921 | 93.622 | 0.100 | 4 |
| XMMXCS J113055.0+311332.7 | 172.729385 | 31.225756 | 195.889 | 0.810 | 13 |
| XMMXCS J122114.6+280234.2 | 185.311111 | 28.042847 | 243.077 | 0.270 | 1 |
| XMMXCS J122118.7+275732.3 | 185.327957 | 27.958979 | 402.026 | 0.740 | 19 |
| XMMXCS J122124.3+275410.3 | 185.351471 | 27.902882 | 170.297 | 0.540 | 31 |
| XMMXCS J130424.4-102932.0 | 196.102036 | -10.492246 | 109.054 | 1.000 | 6 |
| XMMXCS J130456.5-101012.4 | 196.235718 | -10.170132 | 86.367 | 0.640 | 17 |
| XMMXCS J130505.8-101645.5 | 196.274506 | -10.279314 | 136.651 | 0.330 | 20 |
| XMMXCS J130514.7-102311.5 | 196.311279 | -10.386551 | 385.894 | 0.130 | 2 |
| XMMXCS J130549.2-102717.5 | 196.455093 | -10.454864 | 47.346 | 0.280 | 9 |
| XMMXCS J130650.1-233129.4 | 196.708878 | -23.524857 | 306.803 | 0.210 | 50 |
| XMMXCS J131455.1-163838.3 | 198.729980 | -16.643982 | 489.975 | 0.610 | 14 |
| XMMXCS J131507.4-163206.9 | 198.780975 | -16.535254 | 707.865 | 0.110 | 4 |
| XMMXCS J131524.8-163227.9 | 198.853745 | -16.541088 | 533.012 | 0.490 | 10 |
| XMMXCS J131825.4-145030.3 | 199.605835 | -14.841766 | 165.457 | 0.800 | 2 |
| XMMXCS J131844.6-150133.9 | 199.686157 | -15.026097 | 208.355 | 0.300 | 9 |
| XMMXCS J131937.2-145444.5 | 199.905212 | -14.912371 | 250.930 | 0.190 | 15 |
| XMMXCS J131950.1-144957.5 | 199.958817 | -14.832642 | 234.516 | 0.340 | 17 |
| XMMXCS J133511.6-232919.0 | 203.798580 | -23.488623 | 704.471 | 0.100 | 20 |
| XMMXCS J140408.4-341135.3 | 211.035385 | -34.193146 | 77.918 | 0.900 | 1 |

Continued on Next Page...

Table H.1 – Continued

| XCS name | R.A (J2000) | Dec (J2000) | Soft Counts | Redshift | Ngal |
|---|---|---|---|---|---|
| XMMXCS J140436.9-334921.2 | 211.153778 | -33.822563 | 174.229 | 0.160 | 8 |
| XMMXCS J140439.3-341235.3 | 211.164139 | -34.209827 | 471.146 | 0.840 | 22 |
| XMMXCS J150543.3+013639.9 | 226.430832 | 1.611093 | 77.038 | 0.630 | 15 |
| XMMXCS J150654.7+014405.4 | 226.728302 | 1.734854 | 190.307 | 0.630 | 28 |
| XMMXCS J153133.9-083308.4 | 232.891647 | -8.552355 | 74.459 | 0.170 | 8 |
| XMMXCS J153226.0-084020.6 | 233.108414 | -8.672410 | 59.639 | 0.130 | 5 |
| XMMXCS J155624.5-234255.2 | 239.102386 | -23.715359 | 235.090 | 0.560 | 9 |
| XMMXCS J155628.5-235138.7 | 239.119034 | -23.860764 | 284.576 | 0.960 | 13 |
| XMMXCS J200758.9-110251.6 | 301.995514 | -11.047685 | 285.332 | 0.110 | 16 |
| XMMXCS J201338.0-415347.8 | 303.408722 | -41.896633 | 104.658 | 0.630 | 5 |
| XMMXCS J201354.3-243341.7 | 303.476470 | -24.561587 | 132.714 | 0.720 | 5 |
| XMMXCS J204130.5-351653.8 | 310.377360 | -35.281627 | 2062.290 | 0.510 | 33 |
| XMMXCS J204134.7-350900.7 | 310.394650 | -35.150218 | 3266.030 | 0.670 | 50 |
| XMMXCS J204252.7-350946.2 | 310.719670 | -35.162844 | 254.734 | 0.990 | 2 |
| XMMXCS J204301.4-351856.9 | 310.755930 | -35.315830 | 144.294 | 0.360 | 4 |
| XMMXCS J205405.6-154728.5 | 313.523682 | -15.791275 | 221.991 | 0.270 | 38 |
| XMMXCS J205505.0-155309.5 | 313.770935 | -15.885974 | 91.897 | 0.720 | 6 |
| XMMXCS J210054.8+104518.1 | 315.228560 | 10.755046 | 139.846 | 0.160 | 10 |
| XMMXCS J210101.6+104004.7 | 315.256970 | 10.667993 | 84.011 | 0.510 | 4 |
| XMMXCS J210109.1+103847.1 | 315.288130 | 10.646439 | 70.248 | 0.410 | 7 |
| XMMXCS J212802.0-444959.0 | 322.008728 | -44.833080 | 144.888 | 0.390 | 20 |
| XMMXCS J212807.2-445409.7 | 322.030243 | -44.902695 | 264.253 | 0.500 | 16 |
| XMMXCS J212858.6-153422.6 | 322.244507 | -15.572965 | 295.882 | 0.650 | 35 |
| XMMXCS J215121.8-272336.3 | 327.840973 | -27.393440 | 135.966 | 0.250 | 10 |
| XMMXCS J215211.2-274347.9 | 328.046906 | -27.729984 | 119.222 | 0.420 | 25 |
| XMMXCS J215220.9-272525.3 | 328.087433 | -27.423706 | 45.349 | 0.980 | 2 |
| XMMXCS J215221.0-273025.5 | 328.087585 | -27.507092 | 215.998 | 0.770 | 14 |
| XMMXCS J215734.2-695256.8 | 329.392731 | -69.882469 | 131.600 | 0.520 | 12 |
| XMMXCS J215906.9-694342.1 | 329.778931 | -69.728386 | 102.701 | 0.280 | 7 |
| XMMXCS J215933.4-693743.3 | 329.889374 | -69.628700 | 133.283 | 1.010 | 3 |
| XMMXCS J220550.0-015930.4 | 331.458588 | -1.991795 | 79.872 | 0.600 | 4 |
| XMMXCS J220559.3-015815.7 | 331.497131 | -1.971032 | 68.170 | 0.570 | 10 |
| XMMXCS J221447.3-175248.3 | 333.697266 | -17.880089 | 501.048 | 0.340 | 18 |
| XMMXCS J221459.6-175036.8 | 333.748535 | -17.843578 | 231.552 | 0.470 | 2 |
| XMMXCS J221537.3-172903.3 | 333.905487 | -17.484255 | 67.461 | 0.350 | 2 |
| XMMXCS J221548.4-173827.4 | 333.951813 | -17.640953 | 33.817 | 0.440 | 6 |
| XMMXCS J221555.9-175149.8 | 333.983185 | -17.863853 | 106.661 | 0.140 | 9 |
| XMMXCS J221559.4-173815.5 | 333.997589 | -17.637657 | 443.712 | 0.420 | 23 |
| XMMXCS J221605.1-175418.3 | 334.021332 | -17.905100 | 160.777 | 0.280 | 6 |
| XMMXCS J221613.6-173519.9 | 334.056824 | -17.588863 | 246.973 | 1.030 | 2 |
| XMMXCS J222736.8-052113.6 | 336.903656 | -5.353783 | 151.782 | 0.550 | 10 |
| XMMXCS J222759.3-052858.7 | 336.997467 | -5.482976 | 196.150 | 0.520 | 18 |
| XMMXCS J222818.4-053405.3 | 337.076721 | -5.568149 | 279.243 | 0.450 | 7 |
| XMMXCS J222818.8-050746.8 | 337.078400 | -5.129668 | 351.375 | 0.130 | 2 |
| XMMXCS J222820.6-051329.1 | 337.086121 | -5.224759 | 139.107 | 0.640 | 2 |
| XMMXCS J222833.2-052826.2 | 337.138733 | -5.473969 | 333.731 | 0.210 | 8 |
| XMMXCS J222856.9-053053.5 | 337.237305 | -5.514864 | 237.397 | 0.100 | 10 |
| XMMXCS J223447.3-260459.4 | 338.697144 | -26.083181 | 68.388 | 0.270 | 6 |
| XMMXCS J223520.3-255742.2 | 338.834808 | -25.961729 | 142.148 | 0.990 | 2 |
| XMMXCS J223555.0-255554.3 | 338.979462 | -25.931772 | 66.622 | 0.310 | 4 |
| XMMXCS J223557.3-254928.4 | 338.989075 | -25.824583 | 57.013 | 0.630 | 5 |
| XMMXCS J223814.7-204710.6 | 339.561584 | -20.786285 | 82.041 | 0.780 | 6 |
| XMMXCS J223852.1-202610.3 | 339.717224 | -20.436209 | 324.598 | 0.350 | 34 |
| XMMXCS J223925.9+032144.0 | 339.858032 | 3.362236 | 49.005 | 0.790 | 1 |
| XMMXCS J224113.3+032833.0 | 340.305634 | 3.475834 | 409.158 | 0.190 | 15 |
| XMMXCS J232124.6+194515.9 | 350.352844 | 19.754438 | 4335.900 | 0.400 | 50 |
| XMMXCS J232152.7+195333.2 | 350.469757 | 19.892576 | 456.425 | 0.300 | 30 |
| XMMXCS J232155.9+193802.4 | 350.482971 | 19.634026 | 144.953 | 0.420 | 10 |
| XMMXCS J232221.3+193855.8 | 350.589081 | 19.648857 | 660.383 | 0.230 | 33 |
| XMMXCS J232227.7+195948.2 | 350.615479 | 19.996746 | 35.848 | 0.100 | 0 |
| XMMXCS J233949.7-121307.1 | 354.957428 | -12.218653 | 330.287 | 0.490 | 8 |
| XMMXCS J233950.6-120641.8 | 354.961151 | -12.111625 | 55.422 | 0.520 | 4 |
| XMMXCS J235708.5-241453.7 | 359.285797 | -24.248260 | 370.905 | 0.510 | 50 |

Table H.1: XCS DR1 and DR2 redshifts produced using NXS

| XCS name | R.A (J2000) | Dec (J2000) | Soft Counts | Redshift | Ngal |
|---|---|---|---|---|---|
| XMMXCS J001639.6-010205.3 | 4.165087 | -1.034814 | 649.772 | 0.170 | 18 |
| XMMXCS J001737.3-005235.4 | 4.405744 | -0.876519 | 16715.614 | 0.200 | 50 |
| XMMXCS J002314.2+001202.0 | 5.809201 | 0.200577 | 350.682 | 0.320 | 8 |
| XMMXCS J004119.5+252617.7 | 10.331591 | 25.438252 | 1410.006 | 0.160 | 50 |
| XMMXCS J004156.2+253146.0 | 10.484416 | 25.529459 | 494.076 | 0.150 | 14 |
| XMMXCS J004252.7+004301.4 | 10.719820 | 0.717058 | 383.325 | 0.290 | 31 |
| XMMXCS J004333.8+010108.9 | 10.891174 | 1.019164 | 574.477 | 0.140 | 19 |
| XMMXCS J004350.0+004720.3 | 10.958621 | 0.788977 | 322.688 | 0.460 | 25 |
| XMMXCS J005614.3-011451.7 | 14.059875 | -1.247713 | 38673.365 | 0.100 | 35 |
| XMMXCS J005623.1-010806.0 | 14.096478 | -1.135001 | 1382.514 | 0.100 | 22 |
| XMMXCS J005656.4-011221.2 | 14.235170 | -1.205889 | 364.385 | 0.290 | 11 |
| XMMXCS J005656.5-274031.7 | 14.235769 | -27.675484 | 339.385 | 0.170 | 7 |
| XMMXCS J005730.5-272331.8 | 14.377097 | -27.392188 | 306.063 | 0.170 | 12 |
| XMMXCS J010531.1+004300.7 | 16.379761 | 0.716872 | 1496.276 | 0.210 | 9 |
| XMMXCS J010720.5+141615.9 | 16.835566 | 14.271108 | 7101.062 | 0.100 | 29 |
| XMMXCS J011632.1+330325.0 | 19.133912 | 33.056950 | 419.339 | 0.640 | 7 |
| XMMXCS J012059.3+141603.8 | 20.247299 | 14.267730 | 1732.432 | 0.210 | 46 |
| XMMXCS J012103.0+142428.5 | 20.262710 | 14.407918 | 1291.993 | 0.100 | 8 |
| XMMXCS J012459.7+320148.1 | 21.249024 | 32.030045 | 408.868 | 0.340 | 16 |
| XMMXCS J012526.2+321452.9 | 21.359398 | 32.248055 | 1404.063 | 0.280 | 40 |
| XMMXCS J013915.5+062542.9 | 24.814901 | 6.428591 | 2277.453 | 0.100 | 11 |
| XMMXCS J014007.6+062322.6 | 25.031825 | 6.389614 | 1338.597 | 0.260 | 8 |
| XMMXCS J014044.0+062154.9 | 25.183375 | 6.365274 | 559.513 | 0.370 | 10 |
| XMMXCS J015444.8+003109.3 | 28.686848 | 0.519268 | 493.833 | 0.120 | 11 |
| XMMXCS J015448.8+002232.6 | 28.703670 | 0.375734 | 1049.041 | 0.160 | 50 |
| XMMXCS J015451.6+003446.5 | 28.715166 | 0.579605 | 670.818 | 0.120 | 12 |
| XMMXCS J015522.9+003818.5 | 28.845623 | 0.638487 | 704.819 | 0.100 | 24 |
| XMMXCS J015617.4+003506.4 | 29.072891 | 0.585124 | 944.541 | 0.110 | 34 |
| XMMXCS J020056.5-092123.3 | 30.235776 | -9.356496 | 392.504 | 0.320 | 7 |
| XMMXCS J020341.8-074705.4 | 30.924181 | -7.784840 | 983.716 | 0.390 | 24 |
| XMMXCS J021012.9-001451.6 | 32.554122 | -0.247681 | 311.217 | 0.220 | 14 |
| XMMXCS J021339.5-004419.9 | 33.414619 | -0.738870 | 515.157 | 0.350 | 18 |
| XMMXCS J021402.3-005645.3 | 33.509666 | -0.945938 | 360.454 | 0.300 | 40 |
| XMMXCS J021505.1-003445.3 | 33.771645 | -0.579273 | 635.054 | 0.100 | 13 |
| XMMXCS J021527.4-004711.2 | 33.864194 | -0.786448 | 830.287 | 0.590 | 14 |
| XMMXCS J023152.1-072907.5 | 37.967342 | -7.485422 | 936.376 | 0.200 | 27 |
| XMMXCS J030433.9-005406.8 | 46.141581 | -0.901903 | 976.856 | 0.520 | 7 |
| XMMXCS J030617.6-000830.1 | 46.573584 | -0.141706 | 3083.093 | 0.110 | 40 |
| XMMXCS J030634.1-000422.2 | 46.642350 | -0.072844 | 507.993 | 0.100 | 13 |
| XMMXCS J030720.5-002352.9 | 46.835685 | -0.398028 | 301.245 | 0.340 | 5 |
| XMMXCS J033556.1+003214.3 | 53.984125 | 0.537317 | 752.218 | 0.310 | 33 |
| XMMXCS J033557.5+003259.5 | 53.989603 | 0.549884 | 580.535 | 0.190 | 50 |
| XMMXCS J033640.4+003159.0 | 54.168553 | 0.533070 | 1068.758 | 0.100 | 9 |

Continued on Next Page...

Table H.2 – Continued

| XCS name | R.A (J2000) | Dec (J2000) | Soft Counts | Redshift | Ngal |
|---|---|---|---|---|---|
| XMMXCS J033700.8+003421.6 | 54.253541 | 0.572687 | 372.359 | 0.360 | 7 |
| XMMXCS J033701.2+003521.9 | 54.255315 | 0.589444 | 895.404 | 0.100 | 6 |
| XMMXCS J033756.7+002900.1 | 54.486313 | 0.483371 | 370.740 | 0.270 | 16 |
| XMMXCS J035415.7-001005.5 | 58.565808 | -0.168195 | 499.164 | 0.170 | 36 |
| XMMXCS J035744.5+010136.2 | 59.435600 | 1.026735 | 759.732 | 0.290 | 24 |
| XMMXCS J044758.0-061537.1 | 71.991868 | -6.260306 | 439.567 | 0.470 | 8 |
| XMMXCS J044813.7-063444.7 | 72.057300 | -6.579086 | 1642.936 | 0.330 | 8 |
| XMMXCS J051544.8-001034.8 | 78.937081 | -0.176336 | 326.015 | 0.510 | 5 |
| XMMXCS J071853.2+661106.1 | 109.721740 | 66.185040 | 577.258 | 0.340 | 13 |
| XMMXCS J073605.8+433909.6 | 114.024500 | 43.652687 | 2009.414 | 0.430 | 25 |
| XMMXCS J074134.3+305922.2 | 115.392920 | 30.989513 | 7430.255 | 0.260 | 44 |
| XMMXCS J074207.4+312104.2 | 115.531060 | 31.351187 | 420.777 | 0.330 | 6 |
| XMMXCS J074213.0+310857.7 | 115.554180 | 31.149371 | 61300.175 | 0.220 | 50 |
| XMMXCS J075722.6+392011.8 | 119.344270 | 39.336636 | 1273.978 | 0.100 | 50 |
| XMMXCS J075839.1+351942.0 | 119.662940 | 35.328344 | 667.307 | 0.120 | 13 |
| XMMXCS J080713.7+152700.7 | 121.807140 | 15.450218 | 606.487 | 0.100 | 14 |
| XMMXCS J080953.8+280455.9 | 122.474360 | 28.082206 | 446.543 | 0.410 | 13 |
| XMMXCS J081020.6+482052.8 | 122.585860 | 48.348021 | 1691.434 | 0.480 | 19 |
| XMMXCS J081058.1+500530.1 | 122.742320 | 50.091713 | 454.958 | 0.370 | 24 |
| XMMXCS J082412.9+300438.0 | 126.054130 | 30.077241 | 564.401 | 0.320 | 25 |
| XMMXCS J082857.3+495545.4 | 127.239110 | 49.929300 | 2303.302 | 0.140 | 16 |
| XMMXCS J082927.4+495438.5 | 127.364510 | 49.910705 | 971.597 | 0.100 | 7 |
| XMMXCS J083021.2+524823.2 | 127.588400 | 52.806467 | 2815.910 | 0.130 | 19 |
| XMMXCS J083021.9+501646.0 | 127.591590 | 50.279444 | 3172.236 | 0.140 | 16 |
| XMMXCS J083025.5+524128.2 | 127.606350 | 52.691171 | 3593.663 | 0.490 | 6 |
| XMMXCS J083027.4+500015.5 | 127.614290 | 50.004316 | 40254.573 | 0.120 | 50 |
| XMMXCS J083029.8+523654.4 | 127.624320 | 52.615124 | 638.158 | 0.100 | 9 |
| XMMXCS J083127.8+523212.9 | 127.865950 | 52.536920 | 3057.691 | 0.100 | 18 |
| XMMXCS J083147.7+525043.8 | 127.948800 | 52.845523 | 929.058 | 0.500 | 9 |
| XMMXCS J083227.4+523430.3 | 128.114280 | 52.575091 | 587.597 | 0.130 | 5 |
| XMMXCS J083301.2+524344.5 | 128.255250 | 52.729044 | 1926.333 | 0.140 | 6 |
| XMMXCS J083454.9+553420.7 | 128.728830 | 55.572419 | 5851.001 | 0.280 | 38 |
| XMMXCS J083724.3+553251.0 | 129.351280 | 55.547510 | 308.969 | 0.280 | 29 |
| XMMXCS J083811.1+250549.1 | 129.546360 | 25.096996 | 411.959 | 0.360 | 9 |
| XMMXCS J084044.2+383049.3 | 130.184570 | 38.513718 | 449.049 | 0.150 | 16 |
| XMMXCS J084052.5+383845.4 | 130.219140 | 38.645969 | 340.185 | 0.110 | 8 |
| XMMXCS J084105.4+383157.8 | 130.272520 | 38.532724 | 331.877 | 0.170 | 25 |
| XMMXCS J084124.5+004638.6 | 130.352150 | 0.777400 | 602.754 | 0.410 | 8 |
| XMMXCS J084140.4+544319.5 | 130.418740 | 54.722101 | 609.497 | 0.380 | 6 |
| XMMXCS J084244.3+544342.1 | 130.684730 | 54.728364 | 1617.863 | 0.270 | 34 |
| XMMXCS J084311.3+544909.9 | 130.797320 | 54.819427 | 921.118 | 0.180 | 18 |
| XMMXCS J084346.9+495855.8 | 130.945500 | 49.982178 | 7011.876 | 0.420 | 50 |
| XMMXCS J084439.2+502207.4 | 131.163720 | 50.368737 | 1003.504 | 0.310 | 23 |
| XMMXCS J084452.0+500539.6 | 131.217060 | 50.094341 | 48842.069 | 0.100 | 50 |
| XMMXCS J084500.8+501911.9 | 131.253720 | 50.319979 | 3358.819 | 0.250 | 16 |
| XMMXCS J084637.5+185456.8 | 131.656500 | 18.915793 | 414.065 | 0.530 | 10 |
| XMMXCS J084640.9+184933.4 | 131.670640 | 18.825962 | 3322.780 | 0.230 | 17 |
| XMMXCS J084848.2+445606.1 | 132.200940 | 44.935043 | 903.376 | 0.490 | 19 |
| XMMXCS J084957.5+445932.7 | 132.489770 | 44.992421 | 410.864 | 0.520 | 10 |
| XMMXCS J085307.8+180340.1 | 133.282600 | 18.061149 | 824.077 | 0.330 | 20 |
| XMMXCS J085331.9+150135.8 | 133.383280 | 15.026617 | 633.336 | 0.380 | 22 |
| XMMXCS J085337.7+180128.8 | 133.407490 | 18.024680 | 1888.148 | 0.170 | 28 |
| XMMXCS J085604.5+585705.8 | 134.019080 | 58.951614 | 870.577 | 0.160 | 8 |
| XMMXCS J085758.0+170414.7 | 134.492000 | 17.070753 | 464.435 | 0.290 | 30 |
| XMMXCS J085822.5+165723.3 | 134.594030 | 16.956499 | 935.575 | 0.380 | 42 |
| XMMXCS J090100.9+600607.9 | 135.254040 | 60.102202 | 2198.493 | 0.240 | 37 |
| XMMXCS J090541.9+005846.1 | 136.424760 | 0.979497 | 2977.034 | 0.240 | 43 |
| XMMXCS J090635.8+010938.5 | 136.649560 | 1.160700 | 3093.314 | 0.720 | 5 |
| XMMXCS J090715.0+005030.0 | 136.812900 | 0.841687 | 6156.910 | 0.320 | 35 |
| XMMXCS J091146.2+525511.5 | 137.942820 | 52.919875 | 1976.521 | 0.190 | 9 |
| XMMXCS J091200.2+525128.6 | 138.001030 | 52.857972 | 945.194 | 0.260 | 8 |
| XMMXCS J091341.0+531024.0 | 138.421080 | 53.173346 | 1028.069 | 0.110 | 5 |
| XMMXCS J091413.3+530853.4 | 138.555780 | 53.148191 | 365.170 | 0.160 | 6 |
| XMMXCS J091421.8+525304.5 | 138.591190 | 52.884590 | 45584.045 | 0.150 | 50 |
| XMMXCS J091426.1+530707.3 | 138.609080 | 53.118717 | 2091.767 | 0.150 | 20 |
| XMMXCS J092018.6+370621.2 | 140.077830 | 37.105905 | 29281.233 | 0.210 | 45 |
| XMMXCS J092325.4+225648.0 | 140.856000 | 22.946674 | 903.386 | 0.170 | 23 |
| XMMXCS J092335.8+225303.8 | 140.899570 | 22.884415 | 577.012 | 0.180 | 19 |
| XMMXCS J092540.1+362709.3 | 141.417250 | 36.452610 | 3263.760 | 0.140 | 50 |
| XMMXCS J092545.7+305857.5 | 141.440740 | 30.982652 | 991.578 | 0.530 | 19 |
| XMMXCS J092650.6+310128.3 | 141.710980 | 31.024554 | 426.955 | 0.490 | 13 |
| XMMXCS J093709.5+611612.0 | 144.289980 | 61.270025 | 482.181 | 0.200 | 19 |
| XMMXCS J093846.5+414158.7 | 144.694100 | 41.699660 | 402.486 | 0.100 | 5 |
| XMMXCS J094034.9+355950.3 | 145.145700 | 35.997318 | 517.782 | 0.320 | 9 |
| XMMXCS J094055.4+032309.0 | 145.231170 | 3.385858 | 6493.403 | 0.450 | 24 |
| XMMXCS J095341.4+014157.7 | 148.422860 | 1.699376 | 6047.482 | 0.110 | 17 |
| XMMXCS J095343.6+694734.2 | 148.431740 | 69.792855 | 2324.977 | 0.200 | 33 |
| XMMXCS J095418.1+012257.4 | 148.575580 | 1.382633 | 1495.768 | 0.430 | 6 |
| XMMXCS J095437.0+013039.2 | 148.654170 | 1.510897 | 4841.748 | 0.400 | 50 |
| XMMXCS J095737.1+023424.8 | 149.404960 | 2.573560 | 3132.723 | 0.310 | 36 |
| XMMXCS J095823.4+024853.1 | 149.597760 | 2.814756 | 1321.280 | 0.310 | 26 |
| XMMXCS J095851.2+014100.0 | 149.713590 | 1.683334 | 3013.690 | 0.230 | 6 |
| XMMXCS J095905.7+130455.5 | 149.774030 | 13.082109 | 1434.966 | 0.360 | 36 |
| XMMXCS J095917.6+015617.4 | 149.823500 | 1.938189 | 1709.478 | 0.390 | 10 |
| XMMXCS J095917.7+013752.5 | 149.824060 | 1.631264 | 46063.698 | 0.130 | 50 |
| XMMXCS J095924.9+014613.6 | 149.853800 | 1.770469 | 996.500 | 0.150 | 6 |
| XMMXCS J095932.7+303112.8 | 149.886650 | 30.520230 | 8432.274 | 0.260 | 50 |
| XMMXCS J095940.8+023112.6 | 149.920030 | 2.520179 | 985.279 | 0.660 | 7 |
| XMMXCS J095953.2+130438.5 | 149.971850 | 13.077372 | 585.312 | 0.100 | 9 |
| XMMXCS J095957.4+251631.3 | 149.989260 | 25.275364 | 1820.274 | 0.100 | 10 |
| XMMXCS J100000.9+015310.3 | 150.003890 | 1.886206 | 1304.408 | 0.110 | 16 |
| XMMXCS J100009.2+023257.2 | 150.038670 | 2.549229 | 964.137 | 0.330 | 13 |
| XMMXCS J100011.9+305427.4 | 150.049730 | 30.907621 | 1365.454 | 0.240 | 7 |
| XMMXCS J100015.0+015056.8 | 150.062820 | 1.849115 | 1792.135 | 0.130 | 12 |
| XMMXCS J100017.9+013827.9 | 150.074590 | 1.641086 | 31450.010 | 0.140 | 50 |
| XMMXCS J100019.2+025721.8 | 150.080350 | 2.956070 | 501.041 | 0.290 | 5 |
| XMMXCS J100020.7+303730.4 | 150.086490 | 30.625114 | 46028.117 | 0.160 | 50 |
| XMMXCS J100029.6+305030.1 | 150.123750 | 30.841710 | 6036.462 | 0.150 | 31 |
| XMMXCS J100047.4+013927.8 | 150.197560 | 1.657748 | 3024.574 | 0.180 | 50 |
| XMMXCS J100050.3+023005.5 | 150.209990 | 2.501536 | 703.595 | 0.500 | 8 |
| XMMXCS J100059.8+683945.3 | 150.249500 | 68.662595 | 686.464 | 0.470 | 9 |
| XMMXCS J100109.4+013332.3 | 150.289200 | 1.558990 | 348.852 | 0.350 | 14 |
| XMMXCS J100114.7+023502.0 | 150.311360 | 2.583899 | 2505.852 | 0.250 | 50 |
| XMMXCS J100125.7+024147.3 | 150.357120 | 2.696487 | 838.869 | 0.170 | 15 |
| XMMXCS J100141.6+022538.2 | 150.423720 | 2.427300 | 2446.651 | 0.140 | 30 |
| XMMXCS J100201.6+021333.0 | 150.506850 | 2.225839 | 832.920 | 0.250 | 5 |
| XMMXCS J100309.4+022601.9 | 150.789190 | 2.433876 | 2034.334 | 0.140 | 34 |
| XMMXCS J100452.0+411626.2 | 151.216780 | 41.273958 | 2417.431 | 0.500 | 5 |
| XMMXCS J101058.3+293403.0 | 152.742980 | 29.567502 | 3240.208 | 0.140 | 50 |
| XMMXCS J101110.4+295115.2 | 152.793740 | 29.854239 | 42045.065 | 0.140 | 50 |
| XMMXCS J101128.3+293155.0 | 152.867950 | 29.531959 | 2823.636 | 0.150 | 26 |
| XMMXCS J101301.1+463441.8 | 153.254760 | 46.578302 | 616.074 | 0.110 | 7 |
| XMMXCS J101838.7+195041.0 | 154.661650 | 19.844746 | 323.413 | 0.400 | 9 |
| XMMXCS J101843.6+370839.9 | 154.681960 | 37.144434 | 930.449 | 0.440 | 16 |

Continued on Next Page...

Table H.2 – Continued

| XCS name | R.A (J2000) | Dec (J2000) | Soft Counts | Redshift | Ngal |
|---|---|---|---|---|---|
| XMMXCS J101901.7+371020.8 | 154.757150 | 37.172449 | 1230.960 | 0.160 | 40 |
| XMMXCS J101903.2+200322.8 | 154.763560 | 20.056348 | 326.159 | 0.100 | 9 |
| XMMXCS J101922.9+371522.6 | 154.845830 | 37.256290 | 2247.246 | 0.130 | 50 |
| XMMXCS J101933.0+080353.5 | 154.887690 | 8.064863 | 998.079 | 0.150 | 50 |
| XMMXCS J102013.4+194131.9 | 155.056130 | 19.692202 | 350.818 | 0.100 | 15 |
| XMMXCS J102017.7+075931.8 | 155.073870 | 7.992190 | 526.053 | 0.190 | 21 |
| XMMXCS J102033.9+195236.1 | 155.141270 | 19.876719 | 515.982 | 0.210 | 50 |
| XMMXCS J102133.7+213748.9 | 155.390440 | 21.630269 | 1164.135 | 0.210 | 20 |
| XMMXCS J102245.9+194741.5 | 155.691640 | 19.794887 | 542.659 | 0.120 | 10 |
| XMMXCS J103007.1-030642.1 | 157.529880 | -3.111717 | 918.610 | 0.400 | 19 |
| XMMXCS J103023.1+310142.1 | 157.596420 | 31.028362 | 348.340 | 0.240 | 37 |
| XMMXCS J103100.0+305138.7 | 157.750040 | 30.860774 | 925.623 | 0.130 | 50 |
| XMMXCS J103104.9+052626.8 | 157.770680 | 5.440791 | 1182.362 | 0.230 | 24 |
| XMMXCS J103131.6+311315.9 | 157.881840 | 31.221085 | 359.204 | 0.380 | 17 |
| XMMXCS J103212.7+581623.3 | 158.053320 | 58.273147 | 631.192 | 0.320 | 15 |
| XMMXCS J103421.8+395113.1 | 158.591220 | 39.853656 | 396.218 | 0.100 | 9 |
| XMMXCS J103454.4+585054.2 | 158.726850 | 58.848408 | 378.131 | 0.420 | 15 |
| XMMXCS J103501.2+580456.4 | 158.755400 | 58.082341 | 900.157 | 0.340 | 6 |
| XMMXCS J103506.8+585601.5 | 158.778670 | 58.933761 | 2538.327 | 0.440 | 37 |
| XMMXCS J103508.1+584000.8 | 158.783980 | 58.666890 | 13041.753 | 0.110 | 50 |
| XMMXCS J103516.3+580845.2 | 158.818090 | 58.145900 | 852.460 | 0.340 | 10 |
| XMMXCS J103931.8+394737.1 | 159.882880 | 39.793651 | 443.945 | 0.120 | 16 |
| XMMXCS J103937.1+090329.2 | 159.904940 | 9.058136 | 3096.085 | 0.160 | 13 |
| XMMXCS J103941.3+091849.2 | 159.922310 | 9.313687 | 17995.979 | 0.190 | 50 |
| XMMXCS J104030.1+085654.1 | 160.125780 | 8.948382 | 1849.905 | 0.100 | 5 |
| XMMXCS J104041.4+395704.9 | 160.172830 | 39.951386 | 8497.983 | 0.150 | 50 |
| XMMXCS J104422.3+213025.7 | 161.093050 | 21.507142 | 2002.498 | 0.450 | 25 |
| XMMXCS J104422.6+064514.9 | 161.094210 | 6.754140 | 929.160 | 0.270 | 23 |
| XMMXCS J104546.9+063421.4 | 161.445440 | 6.572623 | 710.341 | 0.180 | 11 |
| XMMXCS J104551.8+213345.9 | 161.466110 | 21.562776 | 305.548 | 0.440 | 14 |
| XMMXCS J104947.8+572353.2 | 162.449210 | 57.398120 | 541.377 | 0.410 | 5 |
| XMMXCS J105132.5+572107.0 | 162.885680 | 57.351967 | 944.430 | 0.520 | 12 |
| XMMXCS J105134.9+572720.0 | 162.895670 | 57.455571 | 3782.039 | 0.590 | 28 |
| XMMXCS J105245.7+574208.0 | 163.190590 | 57.702224 | 2059.013 | 0.100 | 34 |
| XMMXCS J105247.2+573612.2 | 163.196950 | 57.603395 | 779.330 | 0.120 | 6 |
| XMMXCS J105302.1+571529.4 | 163.259120 | 57.258169 | 2800.793 | 0.170 | 40 |
| XMMXCS J105318.7+572048.4 | 163.328150 | 57.346798 | 1655.742 | 0.320 | 20 |
| XMMXCS J105352.0+573458.3 | 163.466670 | 57.582877 | 1587.485 | 0.290 | 15 |
| XMMXCS J105419.1+572514.9 | 163.579630 | 57.420816 | 3256.334 | 0.160 | 15 |
| XMMXCS J105655.6+065841.1 | 164.231760 | 6.978101 | 307.566 | 0.310 | 23 |
| XMMXCS J110340.4+382113.1 | 165.918550 | 38.353660 | 581.367 | 0.490 | 30 |
| XMMXCS J110359.5+380509.4 | 165.998020 | 38.085972 | 16248.726 | 0.100 | 50 |
| XMMXCS J110400.1+381543.5 | 166.000830 | 38.262085 | 2977.804 | 0.490 | 34 |
| XMMXCS J110400.5+380759.9 | 166.002320 | 38.133328 | 1489.300 | 0.100 | 5 |
| XMMXCS J110414.6+380828.3 | 166.061220 | 38.141202 | 1755.059 | 0.100 | 20 |
| XMMXCS J110421.8+380551.4 | 166.090830 | 38.097639 | 1546.239 | 0.100 | 13 |
| XMMXCS J110442.1+381534.7 | 166.175460 | 38.259659 | 2347.918 | 0.100 | 5 |
| XMMXCS J110447.6+381747.8 | 166.198670 | 38.296628 | 2393.565 | 0.470 | 8 |
| XMMXCS J110451.1+381019.7 | 166.213110 | 38.172155 | 2142.707 | 0.130 | 12 |
| XMMXCS J110454.6+380940.1 | 166.227690 | 38.161159 | 3453.797 | 0.100 | 35 |
| XMMXCS J110724.4-182731.0 | 166.851730 | -18.458614 | 106266.410 | 0.470 | 50 |
| XMMXCS J110954.2+482704.8 | 167.476050 | 48.451346 | 1181.306 | 0.510 | 36 |
| XMMXCS J111153.7+022856.2 | 167.973950 | 2.482299 | 622.487 | 0.100 | 5 |
| XMMXCS J111307.7+401759.0 | 168.282350 | 40.299730 | 471.357 | 0.100 | 23 |
| XMMXCS J111357.7+061053.3 | 168.490650 | 6.181479 | 790.086 | 0.140 | 14 |
| XMMXCS J111515.4+531948.3 | 168.814420 | 53.330096 | 2307.456 | 0.440 | 50 |
| XMMXCS J111726.1+074327.8 | 169.358930 | 7.724394 | 1238.075 | 0.450 | 40 |
| XMMXCS J111729.8+174450.7 | 169.374380 | 17.747439 | 481.976 | 0.480 | 22 |
| XMMXCS J111730.6+074631.2 | 169.377600 | 7.775361 | 1095.449 | 0.110 | 20 |
| XMMXCS J111745.0+073813.5 | 169.437770 | 7.637092 | 808.799 | 0.490 | 10 |
| XMMXCS J112006.6+600127.9 | 170.027530 | 60.024440 | 1275.644 | 0.440 | 7 |
| XMMXCS J112259.2+465915.6 | 170.747010 | 46.987675 | 625.932 | 0.440 | 12 |
| XMMXCS J112349.5+052951.7 | 170.956440 | 5.497718 | 328.490 | 0.610 | 9 |
| XMMXCS J112419.7+470006.9 | 171.082420 | 47.001938 | 409.136 | 0.490 | 6 |
| XMMXCS J113657.5+570617.2 | 174.239600 | 57.104780 | 539.942 | 0.120 | 38 |
| XMMXCS J113844.3+031536.5 | 174.684970 | 3.260144 | 912.236 | 0.130 | 15 |
| XMMXCS J113909.8+170334.2 | 174.791170 | 17.059504 | 433.755 | 0.270 | 27 |
| XMMXCS J114041.4+314811.1 | 175.172740 | 31.803111 | 38085.101 | 0.120 | 50 |
| XMMXCS J114057.5+602303.5 | 175.239960 | 60.384311 | 1226.811 | 0.380 | 6 |
| XMMXCS J114213.2+602933.6 | 175.555130 | 60.492685 | 13840.521 | 0.100 | 50 |
| XMMXCS J114333.1+602902.8 | 175.888170 | 60.484114 | 1291.754 | 0.130 | 17 |
| XMMXCS J114725.5+530343.4 | 176.856650 | 53.062057 | 26524.362 | 0.100 | 50 |
| XMMXCS J115112.0+550654.5 | 177.800230 | 55.115150 | 5241.947 | 0.100 | 21 |
| XMMXCS J115123.7+545010.0 | 177.849120 | 54.836129 | 573.406 | 0.150 | 27 |
| XMMXCS J115131.8+014814.5 | 177.882670 | 1.804033 | 338.903 | 0.170 | 16 |
| XMMXCS J115204.1+545848.1 | 178.017430 | 54.980047 | 350.630 | 0.120 | 10 |
| XMMXCS J115222.8+364652.7 | 178.095070 | 36.781319 | 843.262 | 0.260 | 29 |
| XMMXCS J115331.2+365306.3 | 178.380170 | 36.885098 | 1240.386 | 0.150 | 50 |
| XMMXCS J115817.9+524131.2 | 179.574860 | 52.692026 | 1023.075 | 0.660 | 5 |
| XMMXCS J115824.9+440536.6 | 179.603910 | 44.093526 | 452.411 | 0.380 | 42 |
| XMMXCS J120550.8+351059.9 | 181.461830 | 35.183329 | 741.476 | 0.450 | 11 |
| XMMXCS J120801.2+433927.3 | 182.005100 | 43.657594 | 312.983 | 0.270 | 30 |
| XMMXCS J120850.9+452951.2 | 182.212180 | 45.497580 | 756.808 | 0.330 | 23 |
| XMMXCS J120916.9+652242.4 | 182.320450 | 65.378465 | 1617.728 | 0.100 | 10 |
| XMMXCS J120929.4+392804.7 | 182.372880 | 39.467997 | 539.312 | 0.210 | 22 |
| XMMXCS J120934.3+392233.6 | 182.393170 | 39.376014 | 664.226 | 0.500 | 19 |
| XMMXCS J121156.6+502917.7 | 182.986040 | 50.488254 | 521.970 | 0.110 | 9 |
| XMMXCS J121334.8+025349.4 | 183.395360 | 2.897081 | 2044.047 | 0.390 | 28 |
| XMMXCS J121722.4+033242.3 | 184.343700 | 3.545084 | 642.072 | 0.130 | 29 |
| XMMXCS J121729.3+373020.3 | 184.372370 | 37.505641 | 784.383 | 0.150 | 5 |
| XMMXCS J121749.5+472436.0 | 184.456570 | 47.410005 | 4864.739 | 0.260 | 50 |
| XMMXCS J121753.1+472902.1 | 184.471510 | 47.483916 | 918.408 | 0.260 | 50 |
| XMMXCS J121755.5+472834.6 | 184.481500 | 47.476295 | 448.557 | 0.280 | 20 |
| XMMXCS J121806.9+373833.8 | 184.528860 | 37.642736 | 733.164 | 0.440 | 5 |
| XMMXCS J121811.9+374302.9 | 184.549920 | 37.717489 | 362.599 | 0.170 | 5 |
| XMMXCS J121848.3+293601.0 | 184.701290 | 29.600297 | 403.054 | 0.250 | 5 |
| XMMXCS J121857.5+472826.5 | 184.739620 | 47.474033 | 76621.968 | 0.120 | 50 |
| XMMXCS J121916.1+474439.1 | 184.817130 | 47.744201 | 2975.801 | 0.100 | 9 |
| XMMXCS J121929.1+474034.7 | 184.871640 | 47.676331 | 3359.011 | 0.100 | 16 |
| XMMXCS J121936.3+141609.2 | 184.901560 | 14.269235 | 17203.620 | 0.230 | 50 |
| XMMXCS J121938.1+143339.3 | 184.908910 | 14.560933 | 2804.330 | 0.100 | 8 |
| XMMXCS J121952.3+472622.8 | 184.968030 | 47.439694 | 466.596 | 0.220 | 14 |
| XMMXCS J122021.1+300737.4 | 185.088070 | 30.127057 | 484.775 | 0.210 | 10 |
| XMMXCS J122040.0+302041.6 | 185.166830 | 30.344916 | 563.399 | 0.100 | 12 |
| XMMXCS J122122.7+143253.8 | 185.344760 | 14.548284 | 344.308 | 0.450 | 7 |
| XMMXCS J122227.8+142809.7 | 185.615950 | 14.469379 | 336.934 | 0.160 | 10 |
| XMMXCS J122235.7+143536.0 | 185.648880 | 14.593359 | 703.703 | 0.510 | 13 |
| XMMXCS J122522.1+311817.4 | 186.342200 | 31.304847 | 662.290 | 0.330 | 24 |
| XMMXCS J122528.0+004228.3 | 186.367030 | 0.707883 | 577.087 | 0.230 | 50 |
| XMMXCS J122544.9+312516.5 | 186.437220 | 31.421276 | 811.218 | 0.400 | 6 |
| XMMXCS J122553.1+334609.3 | 186.471580 | 33.769267 | 2098.096 | 0.470 | 27 |
| XMMXCS J122600.5+333348.3 | 186.502450 | 33.563433 | 8101.708 | 0.290 | 39 |
| XMMXCS J122845.5+015501.2 | 187.189990 | 1.917007 | 755.771 | 0.270 | 5 |
| XMMXCS J122900.7+015226.2 | 187.253050 | 1.873971 | 520.543 | 0.300 | 7 |

Continued on Next Page...

Table H.2 – Continued

| XCS name | R.A (J2000) | Dec (J2000) | Soft Counts | Redshift | Ngal |
|---|---|---|---|---|---|
| XMMXCS J122908.8+014723.6 | 187.286810 | 1.789912 | 616.464 | 0.300 | 6 |
| XMMXCS J122925.5+075522.2 | 187.356360 | 7.922838 | 14742.005 | 0.100 | 30 |
| XMMXCS J122929.3+015130.6 | 187.372290 | 1.858510 | 764.333 | 0.250 | 5 |
| XMMXCS J122932.5+015030.6 | 187.385580 | 1.841848 | 1565.835 | 0.100 | 15 |
| XMMXCS J122944.5+133450.8 | 187.435760 | 13.580786 | 413.823 | 0.400 | 14 |
| XMMXCS J123001.8+080841.5 | 187.507820 | 8.144880 | 4603.839 | 0.100 | 32 |
| XMMXCS J123002.6+021018.4 | 187.510850 | 2.171789 | 2707.465 | 0.140 | 16 |
| XMMXCS J123012.8+080124.6 | 187.553740 | 8.023521 | 5260.712 | 0.140 | 13 |
| XMMXCS J123014.6+080044.4 | 187.560860 | 8.012341 | 695.948 | 0.240 | 8 |
| XMMXCS J123017.0+133905.0 | 187.571150 | 13.651398 | 368.745 | 0.270 | 8 |
| XMMXCS J123019.1+110059.1 | 187.579950 | 11.016431 | 640.675 | 0.130 | 16 |
| XMMXCS J123144.3+413730.9 | 187.935000 | 41.625274 | 527.972 | 0.240 | 43 |
| XMMXCS J123313.0+001130.0 | 188.304570 | 0.191694 | 467.154 | 0.410 | 14 |
| XMMXCS J123525.3+480154.6 | 188.855530 | 48.031832 | 966.367 | 0.100 | 10 |
| XMMXCS J123652.1+615817.6 | 189.217140 | 61.971580 | 706.131 | 0.250 | 11 |
| XMMXCS J123653.3+131428.7 | 189.222150 | 13.241315 | 350.623 | 0.120 | 6 |
| XMMXCS J124024.7-114806.2 | 190.103160 | -11.801748 | 814.544 | 0.190 | 18 |
| XMMXCS J124127.2-015824.2 | 190.363710 | -1.973391 | 352.297 | 0.150 | 14 |
| XMMXCS J124138.9+322822.5 | 190.412150 | 32.472943 | 408.067 | 0.390 | 8 |
| XMMXCS J124146.8+141923.6 | 190.445170 | 14.323230 | 530.612 | 0.220 | 18 |
| XMMXCS J124158.7+331716.7 | 190.494860 | 33.287978 | 866.357 | 0.240 | 50 |
| XMMXCS J124202.5+332203.9 | 190.510810 | 33.367753 | 322.324 | 0.100 | 19 |
| XMMXCS J124208.1+331320.2 | 190.534070 | 33.222284 | 727.078 | 0.230 | 27 |
| XMMXCS J124212.3+331949.5 | 190.551520 | 33.330436 | 330.506 | 0.130 | 18 |
| XMMXCS J124229.0+143100.0 | 190.620940 | 14.516680 | 391.889 | 0.460 | 5 |
| XMMXCS J124230.8+024049.7 | 190.628740 | 2.680474 | 2779.297 | 0.100 | 5 |
| XMMXCS J124235.4-112412.1 | 190.647830 | -11.403386 | 1013.554 | 0.100 | 8 |
| XMMXCS J124240.4+024651.2 | 190.668590 | 2.780904 | 621.262 | 0.110 | 10 |
| XMMXCS J124241.8-112844.5 | 190.674180 | -11.479044 | 1344.966 | 0.110 | 5 |
| XMMXCS J124248.7+112637.8 | 190.703120 | 11.443852 | 687.657 | 0.190 | 9 |
| XMMXCS J124259.2+332353.7 | 190.746710 | 33.398253 | 906.400 | 0.430 | 9 |
| XMMXCS J124300.0+141806.8 | 190.750170 | 14.301895 | 431.625 | 0.440 | 7 |
| XMMXCS J124305.2+023313.5 | 190.771780 | 2.553772 | 1240.391 | 0.190 | 15 |
| XMMXCS J124310.2+142022.2 | 190.792880 | 14.339511 | 863.184 | 0.340 | 26 |
| XMMXCS J124312.3+131305.4 | 190.801670 | 13.218184 | 390.338 | 0.280 | 5 |
| XMMXCS J124349.6+112025.9 | 190.956770 | 11.340543 | 773.354 | 0.320 | 6 |
| XMMXCS J124412.6+112404.3 | 191.052800 | 11.401196 | 749.124 | 0.220 | 11 |
| XMMXCS J124423.6+113516.0 | 191.098520 | 11.587794 | 686.653 | 0.480 | 8 |
| XMMXCS J124453.1-002627.9 | 191.221250 | -0.441086 | 435.418 | 0.170 | 18 |
| XMMXCS J124454.1-003331.1 | 191.225430 | -0.558641 | 1339.641 | 0.190 | 28 |
| XMMXCS J124926.2+051221.9 | 192.359520 | 5.206089 | 894.236 | 0.570 | 6 |
| XMMXCS J124928.8-060010.7 | 192.370020 | -6.002997 | 351.930 | 0.300 | 18 |
| XMMXCS J125047.4+263352.9 | 192.697640 | 26.564700 | 416.542 | 0.440 | 16 |
| XMMXCS J125313.8+155544.6 | 193.307570 | 15.929056 | 1025.031 | 0.260 | 42 |
| XMMXCS J125403.2+310149.4 | 193.513370 | 31.030396 | 413.588 | 0.480 | 11 |
| XMMXCS J125612.4+474303.2 | 194.051770 | 47.717556 | 4119.872 | 0.200 | 50 |
| XMMXCS J125704.5+270632.7 | 194.268840 | 27.109105 | 336.255 | 0.280 | 11 |
| XMMXCS J125727.7+475213.7 | 194.365560 | 47.870474 | 1990.491 | 0.130 | 22 |
| XMMXCS J125749.0+473358.0 | 194.454380 | 47.566114 | 5120.129 | 0.140 | 34 |
| XMMXCS J125800.7+472646.4 | 194.502930 | 47.446243 | 14517.583 | 0.140 | 50 |
| XMMXCS J125808.1+271114.3 | 194.533970 | 27.187321 | 368.386 | 0.390 | 5 |
| XMMXCS J125808.7+344432.7 | 194.536270 | 34.742430 | 1288.836 | 0.170 | 9 |
| XMMXCS J125813.7+474638.0 | 194.557340 | 47.777235 | 342.206 | 0.460 | 22 |
| XMMXCS J125836.5+474344.5 | 194.652140 | 47.729051 | 833.486 | 0.370 | 5 |
| XMMXCS J125932.8+274937.2 | 194.887020 | 27.827027 | 12675.608 | 0.100 | 33 |
| XMMXCS J125938.8+350005.6 | 194.911810 | 35.001577 | 1040.516 | 0.120 | 11 |
| XMMXCS J125950.0+344658.9 | 194.958360 | 34.783055 | 1332.168 | 0.100 | 10 |
| XMMXCS J125950.4+274920.6 | 194.960220 | 27.822392 | 5428.498 | 0.470 | 13 |
| XMMXCS J125956.2+345652.0 | 194.984380 | 34.947781 | 508.346 | 0.100 | 6 |
| XMMXCS J130009.8+281016.2 | 195.041100 | 28.171169 | 548.584 | 0.130 | 8 |
| XMMXCS J130020.6+275526.7 | 195.085990 | 27.924107 | 1891.141 | 0.100 | 7 |
| XMMXCS J130348.5+534607.3 | 195.952260 | 53.768695 | 726.624 | 0.320 | 50 |
| XMMXCS J130749.6+292549.3 | 196.956740 | 29.430371 | 7307.049 | 0.250 | 47 |
| XMMXCS J130802.4+213115.9 | 197.010190 | 21.521083 | 23031.925 | 0.100 | 50 |
| XMMXCS J130852.3+213652.5 | 197.218120 | 21.614596 | 6256.827 | 0.180 | 50 |
| XMMXCS J130902.9+211532.2 | 197.262380 | 21.258973 | 12852.924 | 0.350 | 44 |
| XMMXCS J130933.6+573928.0 | 197.390320 | 57.657789 | 566.587 | 0.200 | 28 |
| XMMXCS J130937.9+212932.1 | 197.408240 | 21.492266 | 10830.035 | 0.200 | 29 |
| XMMXCS J131058.3+572042.1 | 197.743200 | 57.345027 | 417.874 | 0.530 | 19 |
| XMMXCS J131114.8+231317.1 | 197.812020 | 23.221429 | 576.589 | 0.270 | 10 |
| XMMXCS J131122.5+232908.7 | 197.844000 | 23.485774 | 2535.066 | 0.160 | 44 |
| XMMXCS J131139.3+232017.7 | 197.913990 | 23.338270 | 695.093 | 0.100 | 9 |
| XMMXCS J131154.4+352242.3 | 197.976680 | 35.378421 | 754.049 | 0.180 | 47 |
| XMMXCS J131158.1+233416.7 | 197.992150 | 23.571324 | 1208.864 | 0.500 | 7 |
| XMMXCS J131302.5+351946.6 | 198.260620 | 35.329629 | 319.504 | 0.320 | 36 |
| XMMXCS J131626.3+415134.5 | 199.109640 | 41.859592 | 79241.442 | 0.100 | 25 |
| XMMXCS J131934.2-144619.2 | 199.892890 | -14.772012 | 661.642 | 0.150 | 5 |
| XMMXCS J131937.1-145446.1 | 199.904680 | -14.912807 | 485.480 | 0.140 | 14 |
| XMMXCS J132053.8+335521.6 | 200.224520 | 33.922687 | 678.987 | 0.200 | 50 |
| XMMXCS J132324.5+432317.4 | 200.852320 | 43.388190 | 870.657 | 0.100 | 6 |
| XMMXCS J132434.4+053419.6 | 201.143620 | 5.572135 | 633.323 | 0.230 | 50 |
| XMMXCS J132959.5+583423.1 | 202.497970 | 58.573103 | 319.985 | 0.270 | 19 |
| XMMXCS J133434.9+375700.2 | 203.645450 | 37.950070 | 874.775 | 0.320 | 36 |
| XMMXCS J133443.6+380828.1 | 203.682070 | 38.141146 | 3548.495 | 0.250 | 21 |
| XMMXCS J133457.3+375021.8 | 203.738770 | 37.839408 | 696.338 | 0.360 | 30 |
| XMMXCS J133514.4+374908.8 | 203.810030 | 37.819115 | 358.514 | 0.320 | 21 |
| XMMXCS J133529.0+374519.3 | 203.871220 | 37.755386 | 39923.883 | 0.290 | 50 |
| XMMXCS J133604.9+514530.9 | 204.020450 | 51.758608 | 1015.107 | 0.530 | 27 |
| XMMXCS J133620.1+242014.5 | 204.083880 | 24.337380 | 366.116 | 0.140 | 17 |
| XMMXCS J133817.8+242450.5 | 204.574430 | 24.414054 | 368.244 | 0.450 | 17 |
| XMMXCS J134305.1-000056.6 | 205.771410 | -0.015748 | 1374.531 | 0.550 | 25 |
| XMMXCS J134921.9+261449.8 | 207.341450 | 26.247170 | 1204.352 | 0.100 | 23 |
| XMMXCS J134937.0-035948.7 | 207.404450 | -3.996882 | 415.310 | 0.100 | 5 |
| XMMXCS J135047.9+600702.7 | 207.699650 | 60.117426 | 623.321 | 0.400 | 6 |
| XMMXCS J135358.8+335003.1 | 208.495390 | 33.834209 | 566.679 | 0.370 | 38 |
| XMMXCS J135442.1+052848.2 | 208.675580 | 5.480074 | 368.469 | 0.110 | 6 |
| XMMXCS J140154.6+620008.9 | 210.477890 | 62.002478 | 732.847 | 0.330 | 5 |
| XMMXCS J140354.4+431608.7 | 210.976710 | 43.269086 | 1304.789 | 0.100 | 5 |
| XMMXCS J140355.2+540839.6 | 210.980130 | 54.144343 | 348.190 | 0.130 | 6 |
| XMMXCS J140615.8+283047.8 | 211.565980 | 28.513296 | 372.561 | 0.200 | 11 |
| XMMXCS J140919.5+262550.3 | 212.331360 | 26.430643 | 935.123 | 0.100 | 5 |
| XMMXCS J140938.5+260639.9 | 212.410800 | 26.111086 | 713.404 | 0.450 | 10 |
| XMMXCS J141534.9+282334.6 | 213.895430 | 28.392969 | 703.108 | 0.280 | 21 |
| XMMXCS J141643.6+105306.1 | 214.181960 | 10.885041 | 314.602 | 0.100 | 8 |
| XMMXCS J141832.0+251105.4 | 214.633730 | 25.184837 | 6336.790 | 0.290 | 50 |
| XMMXCS J141857.7+250815.0 | 214.740520 | 25.137517 | 698.683 | 0.460 | 26 |
| XMMXCS J142023.3+462056.7 | 215.097220 | 46.349091 | 729.648 | 0.540 | 6 |
| XMMXCS J142041.3+462253.6 | 215.172210 | 46.381560 | 1366.782 | 0.550 | 35 |
| XMMXCS J142115.1+030745.9 | 215.313100 | 3.129434 | 550.423 | 0.300 | 7 |
| XMMXCS J142207.1+193253.9 | 215.529900 | 19.548325 | 455.965 | 0.330 | 34 |
| XMMXCS J142213.4+194121.5 | 215.555890 | 19.689333 | 399.431 | 0.100 | 14 |
| XMMXCS J142232.8+193824.7 | 215.636680 | 19.640204 | 732.631 | 0.120 | 12 |
| XMMXCS J142244.4+194804.9 | 215.685190 | 19.801368 | 792.197 | 0.140 | 16 |
| XMMXCS J142510.1+415719.3 | 216.292160 | 41.955386 | 318.924 | 0.100 | 5 |

Continued on Next Page...

Table H.2 – Continued

| XCS name | R.A (J2000) | Dec (J2000) | Soft Counts | Redshift | Ngal |
|---|---|---|---|---|---|
| XMMXCS J142730.8+262900.6 | 216.878360 | 26.483511 | 759.361 | 0.350 | 14 |
| XMMXCS J142946.1+415221.8 | 217.442430 | 41.872729 | 378.605 | 0.380 | 6 |
| XMMXCS J142954.4+421848.6 | 217.476940 | 42.313513 | 335.144 | 0.210 | 6 |
| XMMXCS J143024.2+421939.8 | 217.600910 | 42.327724 | 360.447 | 0.170 | 8 |
| XMMXCS J143102.2+421431.3 | 217.759260 | 42.242040 | 779.533 | 0.410 | 35 |
| XMMXCS J143118.8+415842.4 | 217.828400 | 41.978450 | 567.748 | 0.370 | 23 |
| XMMXCS J143120.8-005344.6 | 217.837000 | -0.895733 | 768.773 | 0.360 | 44 |
| XMMXCS J143425.6+190414.6 | 218.606980 | 19.070723 | 1233.140 | 0.280 | 11 |
| XMMXCS J143456.4+192655.4 | 218.735210 | 19.448739 | 1306.048 | 0.290 | 32 |
| XMMXCS J143610.3+363152.5 | 219.043120 | 36.531251 | 4050.092 | 0.170 | 22 |
| XMMXCS J143613.2+363810.4 | 219.055220 | 36.636240 | 1429.292 | 0.490 | 14 |
| XMMXCS J143656.6+364646.7 | 219.236070 | 36.779646 | 49854.907 | 0.130 | 50 |
| XMMXCS J143934.8+002216.4 | 219.895080 | 0.371237 | 498.959 | 0.120 | 50 |
| XMMXCS J144010.3+000845.6 | 220.043320 | 0.146014 | 782.036 | 0.220 | 50 |
| XMMXCS J144103.1+352501.8 | 220.262940 | 35.417178 | 377.895 | 0.480 | 6 |
| XMMXCS J144125.1+353655.9 | 220.354850 | 35.615540 | 307.692 | 0.320 | 10 |
| XMMXCS J144154.6-003256.1 | 220.477600 | -0.548936 | 21151.935 | 0.130 | 50 |
| XMMXCS J144216.7+353138.9 | 220.569900 | 35.527479 | 769.128 | 0.260 | 8 |
| XMMXCS J145009.3+090429.1 | 222.539090 | 9.074751 | 669.104 | 0.600 | 8 |
| XMMXCS J145317.4+033443.0 | 223.322540 | 3.578627 | 890.822 | 0.330 | 15 |
| XMMXCS J145847.6+493456.8 | 224.698570 | 49.582451 | 306.554 | 0.440 | 18 |
| XMMXCS J150234.6+473846.9 | 225.644510 | 47.646386 | 463.133 | 0.310 | 5 |
| XMMXCS J150333.6+472426.6 | 225.890170 | 47.407413 | 425.778 | 0.320 | 5 |
| XMMXCS J150824.8-001533.7 | 227.103500 | -0.259362 | 468.315 | 0.100 | 23 |
| XMMXCS J151051.6+670631.4 | 227.715020 | 67.108737 | 1510.097 | 0.400 | 30 |
| XMMXCS J151537.8+560512.1 | 228.907700 | 56.086702 | 2037.294 | 0.280 | 8 |
| XMMXCS J151553.3+070857.7 | 228.972160 | 7.149388 | 531.571 | 0.400 | 5 |
| XMMXCS J151603.2+560607.8 | 229.013460 | 56.102177 | 859.478 | 0.310 | 13 |
| XMMXCS J151803.1+671917.5 | 229.513260 | 67.321542 | 46825.364 | 0.460 | 50 |
| XMMXCS J152035.3+671804.9 | 230.147270 | 67.301372 | 18622.863 | 0.400 | 50 |
| XMMXCS J152312.5+084206.7 | 230.802440 | 8.701887 | 905.613 | 0.170 | 14 |
| XMMXCS J152535.8+515121.5 | 231.399260 | 51.855990 | 2924.192 | 0.400 | 33 |
| XMMXCS J152620.3+512246.5 | 231.584910 | 51.379591 | 1311.921 | 0.450 | 12 |
| XMMXCS J152713.8+513102.5 | 231.807700 | 51.517375 | 47267.599 | 0.140 | 50 |
| XMMXCS J152715.8+514442.6 | 231.815870 | 51.745195 | 2351.729 | 0.120 | 11 |
| XMMXCS J153132.0+324344.2 | 232.883630 | 32.728969 | 581.629 | 0.110 | 7 |
| XMMXCS J153132.6+240345.6 | 232.886200 | 24.062687 | 849.934 | 0.100 | 10 |
| XMMXCS J153135.3+323931.5 | 232.897090 | 32.658767 | 1773.102 | 0.100 | 5 |
| XMMXCS J153206.6+325427.8 | 233.027540 | 32.907736 | 20425.362 | 0.100 | 50 |
| XMMXCS J153237.6+325617.7 | 233.156840 | 32.938267 | 583.784 | 0.100 | 8 |
| XMMXCS J153240.3+325632.8 | 233.168130 | 32.942446 | 1005.998 | 0.100 | 22 |
| XMMXCS J153256.5+325624.9 | 233.235530 | 32.940254 | 6372.533 | 0.100 | 46 |
| XMMXCS J153301.6+322840.8 | 233.256910 | 32.478013 | 926.199 | 0.100 | 16 |
| XMMXCS J153323.4+323021.4 | 233.347840 | 32.505954 | 2657.069 | 0.120 | 25 |
| XMMXCS J153358.1+233427.8 | 233.492180 | 23.574394 | 14901.052 | 0.180 | 50 |
| XMMXCS J153510.7+544056.5 | 233.794630 | 54.682372 | 2182.701 | 0.120 | 50 |
| XMMXCS J153543.1+232917.4 | 233.929860 | 23.488172 | 3221.006 | 0.100 | 50 |
| XMMXCS J153644.9+543729.0 | 234.187220 | 54.624748 | 329.039 | 0.340 | 10 |
| XMMXCS J154233.1+535921.3 | 235.638160 | 53.989256 | 518.348 | 0.640 | 10 |
| XMMXCS J154405.4+534715.8 | 236.022770 | 53.787733 | 326.664 | 0.450 | 13 |
| XMMXCS J154443.1+483352.1 | 236.179800 | 48.564480 | 1145.130 | 0.100 | 15 |
| XMMXCS J154454.6+483241.3 | 236.227640 | 48.544812 | 2209.602 | 0.110 | 11 |
| XMMXCS J154541.5+483144.1 | 236.423130 | 48.528925 | 13282.744 | 0.100 | 50 |
| XMMXCS J154546.1+483801.1 | 236.442110 | 48.633643 | 1774.682 | 0.130 | 5 |
| XMMXCS J154636.3+485044.9 | 236.651370 | 48.845813 | 4060.822 | 0.110 | 37 |
| XMMXCS J154636.7+483603.8 | 236.653160 | 48.601073 | 1865.319 | 0.170 | 12 |
| XMMXCS J154931.5+255220.0 | 237.381570 | 25.872240 | 892.130 | 0.100 | 7 |
| XMMXCS J154932.2+213302.1 | 237.384360 | 21.550590 | 476.923 | 0.690 | 5 |
| XMMXCS J155004.1+255152.7 | 237.517450 | 25.864656 | 1959.500 | 0.140 | 26 |
| XMMXCS J155011.8+261256.6 | 237.549430 | 26.215724 | 1393.535 | 0.180 | 36 |
| XMMXCS J155022.8+260548.0 | 237.595120 | 26.096684 | 1492.043 | 0.170 | 50 |
| XMMXCS J155146.2+551721.9 | 237.942890 | 55.289416 | 366.959 | 0.390 | 5 |
| XMMXCS J155204.2+552413.8 | 238.017530 | 55.403853 | 655.929 | 0.100 | 8 |
| XMMXCS J160129.7+083901.6 | 240.373870 | 8.650461 | 1079.236 | 0.220 | 18 |
| XMMXCS J160413.8+325146.7 | 241.057760 | 32.862974 | 31428.697 | 0.130 | 50 |
| XMMXCS J160434.1+174345.7 | 241.142370 | 17.729364 | 60712.334 | 0.100 | 28 |
| XMMXCS J160434.5+323757.1 | 241.143840 | 32.632545 | 2117.795 | 0.110 | 11 |
| XMMXCS J160451.0+173430.0 | 241.212610 | 17.575010 | 313.754 | 0.480 | 6 |
| XMMXCS J160456.3+254437.2 | 241.234780 | 25.743684 | 799.278 | 0.540 | 18 |
| XMMXCS J160539.7+323607.7 | 241.415740 | 32.602160 | 1378.391 | 0.140 | 11 |
| XMMXCS J160543.5+260530.8 | 241.431410 | 26.091901 | 811.340 | 0.350 | 10 |
| XMMXCS J160549.9+253827.5 | 241.458070 | 25.640979 | 618.469 | 0.100 | 11 |
| XMMXCS J160612.9+272106.6 | 241.553830 | 27.351852 | 424.550 | 0.260 | 8 |
| XMMXCS J160620.9+601856.8 | 241.587150 | 60.315800 | 1411.407 | 0.530 | 18 |
| XMMXCS J160637.1+254403.6 | 241.654680 | 25.734355 | 495.104 | 0.270 | 16 |
| XMMXCS J160637.5+255915.7 | 241.656490 | 25.987707 | 691.147 | 0.650 | 7 |
| XMMXCS J160730.3+270401.9 | 241.876260 | 27.067216 | 753.603 | 0.100 | 9 |
| XMMXCS J160952.1+544658.6 | 242.467320 | 54.782957 | 17588.854 | 0.100 | 50 |
| XMMXCS J160957.2+542352.7 | 242.488660 | 54.397988 | 829.566 | 0.260 | 6 |
| XMMXCS J161040.3+540556.9 | 242.667970 | 54.099146 | 590.067 | 0.330 | 33 |
| XMMXCS J161057.3+544148.0 | 242.738770 | 54.696670 | 1407.311 | 0.350 | 13 |
| XMMXCS J161136.1+541629.8 | 242.900720 | 54.274965 | 1951.358 | 0.340 | 50 |
| XMMXCS J161137.7+544240.7 | 242.907360 | 54.711329 | 3123.877 | 0.100 | 27 |
| XMMXCS J161237.6+540817.5 | 243.156810 | 54.138206 | 535.133 | 0.150 | 9 |
| XMMXCS J161554.3+121930.0 | 243.976320 | 12.325011 | 627.855 | 0.340 | 38 |
| XMMXCS J161657.7+345305.0 | 244.240560 | 34.884725 | 795.220 | 0.580 | 8 |
| XMMXCS J161754.9+060539.9 | 244.478980 | 6.094426 | 70850.207 | 0.240 | 50 |
| XMMXCS J161755.5+350328.7 | 244.481630 | 35.057990 | 780.325 | 0.330 | 7 |
| XMMXCS J163015.6+243423.8 | 247.565120 | 24.573281 | 1075.567 | 0.100 | 28 |
| XMMXCS J163141.4+340440.0 | 247.922760 | 34.077787 | 550.424 | 0.140 | 16 |
| XMMXCS J165651.1+353007.8 | 254.213210 | 35.502176 | 570.372 | 0.570 | 5 |
| XMMXCS J165705.8+353255.6 | 254.274180 | 35.548788 | 646.373 | 0.210 | 8 |
| XMMXCS J165725.5+351729.9 | 254.356550 | 35.291661 | 719.020 | 0.110 | 5 |
| XMMXCS J170933.1+590201.0 | 257.387970 | 59.033631 | 1733.197 | 0.140 | 6 |
| XMMXCS J170942.5+585443.6 | 257.427350 | 58.912129 | 324.667 | 0.190 | 16 |
| XMMXCS J171015.8+585129.5 | 257.566160 | 58.858196 | 37761.788 | 0.110 | 50 |
| XMMXCS J171149.5+584705.3 | 257.956600 | 58.784825 | 2072.685 | 0.210 | 28 |
| XMMXCS J171218.2+584912.3 | 258.075890 | 58.820111 | 353.666 | 0.220 | 10 |
| XMMXCS J171231.3+585310.3 | 258.130780 | 58.886211 | 1708.845 | 0.360 | 23 |
| XMMXCS J171351.9+434402.5 | 258.466500 | 43.734039 | 1169.582 | 0.490 | 5 |
| XMMXCS J171410.8+434126.2 | 258.545170 | 43.690626 | 942.119 | 0.480 | 6 |
| XMMXCS J171420.2+434034.1 | 258.584270 | 43.676155 | 588.421 | 0.500 | 7 |
| XMMXCS J171521.4+572451.9 | 258.839190 | 57.414441 | 6506.194 | 0.100 | 15 |
| XMMXCS J171934.0+590403.0 | 259.892070 | 59.067526 | 567.326 | 0.500 | 8 |
| XMMXCS J171953.7+263005.9 | 259.973950 | 26.501662 | 23355.409 | 0.150 | 31 |
| XMMXCS J172006.1+583810.7 | 260.025620 | 58.636318 | 762.187 | 0.570 | 6 |
| XMMXCS J172106.3+583857.6 | 260.276590 | 58.649335 | 685.027 | 0.750 | 5 |
| XMMXCS J172123.5+585951.5 | 260.348140 | 58.997656 | 595.985 | 0.110 | 12 |
| XMMXCS J172151.9+584830.0 | 260.466480 | 58.808351 | 1481.799 | 0.100 | 8 |
| XMMXCS J172214.4+342344.2 | 260.560380 | 34.395638 | 363.774 | 0.110 | 16 |
| XMMXCS J172228.7+340753.8 | 260.619680 | 34.131632 | 819.759 | 0.210 | 20 |
| XMMXCS J172303.1+342319.0 | 260.763260 | 34.388630 | 839.934 | 0.100 | 8 |
| XMMXCS J172345.1+341734.0 | 260.937980 | 34.292779 | 355.062 | 0.160 | 10 |
| XMMXCS J172414.1+341742.7 | 261.059080 | 34.295218 | 494.844 | 0.380 | 5 |

Continued on Next Page...

Table H.2 – Continued

| XCS name | R.A (J2000) | Dec (J2000) | Soft Counts | Redshift | Ngal |
|---|---|---|---|---|---|
| XMMXCS J173334.3+604553.8 | 263.393220 | 60.764949 | 872.028 | 0.460 | 7 |
| XMMXCS J173353.9+604950.9 | 263.474640 | 60.830808 | 489.357 | 0.310 | 7 |
| XMMXCS J173411.7+605429.3 | 263.549100 | 60.908152 | 805.314 | 0.470 | 8 |
| XMMXCS J173424.7+603637.1 | 263.602960 | 60.610332 | 644.083 | 0.190 | 9 |
| XMMXCS J173429.2+605814.8 | 263.621990 | 60.970785 | 540.398 | 0.330 | 6 |
| XMMXCS J173632.8+604353.1 | 264.136970 | 60.731427 | 909.321 | 0.470 | 7 |
| XMMXCS J173711.0+660316.7 | 264.296120 | 66.054652 | 503.092 | 0.380 | 10 |
| XMMXCS J200758.0-110256.9 | 301.991660 | -11.049159 | 308.757 | 0.280 | 13 |
| XMMXCS J211430.2+061540.2 | 318.625840 | 6.261170 | 312.525 | 0.230 | 6 |
| XMMXCS J211506.8+060823.7 | 318.778420 | 6.139918 | 515.542 | 0.370 | 12 |
| XMMXCS J211510.7+055757.4 | 318.794710 | 5.965971 | 1067.326 | 0.180 | 22 |
| XMMXCS J211511.6+055832.6 | 318.798430 | 5.975725 | 1365.580 | 0.180 | 20 |
| XMMXCS J213037.9+045522.6 | 322.658310 | 4.922968 | 559.974 | 0.600 | 20 |
| XMMXCS J213341.1-003842.7 | 323.421340 | -0.645205 | 655.493 | 0.220 | 16 |
| XMMXCS J215437.6-091534.2 | 328.656840 | -9.259518 | 776.701 | 0.110 | 7 |
| XMMXCS J215807.6-302250.4 | 329.532060 | -30.380677 | 474.637 | 0.390 | 13 |
| XMMXCS J215850.5-302451.1 | 329.710790 | -30.414202 | 601.156 | 0.400 | 9 |
| XMMXCS J223546.8+335243.7 | 338.945080 | 33.878825 | 316.525 | 0.350 | 5 |
| XMMXCS J223615.1+335639.0 | 339.063220 | 33.944182 | 548.044 | 0.510 | 7 |
| XMMXCS J223633.6+343000.2 | 339.140010 | 34.500080 | 634.337 | 0.120 | 10 |
| XMMXCS J231932.9+081809.2 | 349.887150 | 8.302559 | 5467.971 | 0.100 | 29 |
| XMMXCS J232125.0+194513.5 | 350.354550 | 19.753756 | 4666.836 | 0.330 | 13 |
| XMMXCS J232813.5+144112.0 | 352.056570 | 14.686683 | 3862.003 | 0.130 | 7 |
| XMMXCS J232841.5+143931.7 | 352.173040 | 14.658823 | 26574.822 | 0.100 | 9 |
| XMMXCS J235001.8+362521.7 | 357.507530 | 36.422718 | 682.011 | 0.150 | 18 |

Table H.2: XCS300 DR3 redshifts produced using SDSS DR7

| Cluster | z | nH ($10^{20}$ cm$^{-2}$) | $T_X$ (keV) | $L_{500}$ ($10^{44}$ erg s$^{-1}$) | Z (Solar) | $r_c$ (arcmin) | $\beta$ |
|---|---|---|---|---|---|---|---|
| XMMXCS J120930.2+392756.2 | 0.22198 | $1.04^{+15.00}_{-1.04}$ | $1.06^{+0.31}_{-0.38}$ | $0.05^{+0.02}_{-0.05}$ | $0.18^{+0.20}_{-0.15}$ | $0.10^{+0.01}_{-0.02}$ | $0.67^{+0.00}_{-0.00}$ |
| XMMXCS J144940.6+084738.3 | 0.38804 | $0.71^{+18.07}_{-0.71}$ | $0.96^{+0.43}_{-0.53}$ | $0.17^{+0.02}_{-0.17}$ | $0.07^{+0.22}_{-0.07}$ | $0.26^{+0.05}_{-0.04}$ | $0.67^{+0.00}_{-0.00}$ |
| XMMXCS J125047.3+263356.4 | 0.45184 | $0.61^{+0.00}_{-0.00}$ | $1.76^{+0.89}_{-0.57}$ | $0.45^{+0.83}_{-0.12}$ | $0.30^{+0.00}_{-0.00}$ | $0.10^{+1.90}_{-0.00}$ | $0.55^{+0.40}_{-0.20}$ |
| XMMXCS J033225.3-275836.9 | 0.12400 | $0.89^{+0.00}_{-0.00}$ | $0.65^{+0.07}_{-0.06}$ | $0.01^{+0.00}_{-0.00}$ | $0.30^{+0.00}_{-0.00}$ | $1.29^{+0.05}_{-0.04}$ | $0.67^{+0.00}_{-0.00}$ |
| XMMXCS J015719.5+375635.8 | 0.24000 | $6.87^{+3.91}_{-3.44}$ | $3.79^{+2.03}_{-1.13}$ | $0.96^{+1.41}_{-0.68}$ | $0.00^{+0.28}_{-0.00}$ | $1.96^{+0.04}_{-1.86}$ | $0.67^{+0.28}_{-0.32}$ |
| XMMXCS J111729.8+174452.9 | 0.54800 | $0.10^{+2.60}_{-0.10}$ | $3.05^{+2.10}_{-1.52}$ | $1.85^{+0.80}_{-1.06}$ | $0.39^{+1.24}_{-0.39}$ | $0.15^{+0.04}_{-0.04}$ | $0.67^{+0.00}_{-0.00}$ |
| XMMXCS J121334.9+025350.7 | 0.40900 | $0.61^{+2.01}_{-0.61}$ | $5.49^{+1.56}_{-1.13}$ | $2.25^{+0.44}_{-0.36}$ | $0.31^{+0.36}_{-0.30}$ | $0.78^{+0.11}_{-0.10}$ | $0.84^{+0.09}_{-0.10}$ |
| XMMXCS J003427.6-431855.8 | 0.40000 | $2.74^{+1.11}_{-1.04}$ | $3.43^{+0.34}_{-0.32}$ | $2.16^{+0.10}_{-0.10}$ | $0.40^{+0.15}_{-0.13}$ | $0.19^{+0.01}_{-0.01}$ | $0.42^{+0.01}_{-0.01}$ |
| XMMXCS J134807.0+261645.0 | 0.56181 | $0.00^{+1.75}_{-0.00}$ | $7.09^{+4.67}_{-2.40}$ | $1.35^{+0.07}_{-0.34}$ | $0.16^{+0.60}_{-0.16}$ | $0.19^{+0.01}_{-0.01}$ | $0.67^{+0.00}_{-0.00}$ |
| XMMXCS J112349.4+052955.1 | 0.67928 | $4.43^{+0.00}_{-0.00}$ | $3.39^{+1.77}_{-0.90}$ | $1.55^{+1.10}_{-0.42}$ | $0.30^{+0.00}_{-0.00}$ | $0.10^{+1.90}_{-0.00}$ | $0.37^{+0.58}_{-0.02}$ |
| XMMXCS J083025.8+524129.1 | 0.99000 | $5.90^{+1.60}_{-1.42}$ | $6.44^{+1.25}_{-1.04}$ | $11.59^{+0.47}_{-0.56}$ | $0.21^{+0.14}_{-0.14}$ | $0.77^{+0.01}_{-0.01}$ | $0.67^{+0.00}_{-0.00}$ |
| XMMXCS J172814.0-142813.9 | 0.40530 | $26.62^{+13.82}_{-9.84}$ | $5.15^{+4.16}_{-1.86}$ | $4.80^{+0.64}_{-1.13}$ | $0.34^{+0.45}_{-0.34}$ | $0.50^{+0.06}_{-0.05}$ | $0.35^{+0.00}_{-0.00}$ |
| XMMXCS J123144.3+413729.5 | 0.19100 | $2.04^{+4.73}_{-2.04}$ | $3.14^{+1.63}_{-1.16}$ | $0.33^{+0.17}_{-0.13}$ | $0.40^{+0.63}_{-0.37}$ | $0.43^{+0.13}_{-0.10}$ | $0.53^{+0.10}_{-0.07}$ |
| XMMXCS J054710.3-511155.0 | 0.28200 | $4.92^{+0.00}_{-0.00}$ | $2.15^{+0.33}_{-0.23}$ | $0.48^{+0.04}_{-0.04}$ | $0.30^{+0.00}_{-0.00}$ | $0.12^{+0.01}_{-0.01}$ | $0.42^{+0.01}_{-0.01}$ |
| XMMXCS J073603.7+433911.9 | 0.38000 | $5.72^{+0.00}_{-0.00}$ | $3.58^{+1.15}_{-0.75}$ | $1.29^{+0.18}_{-0.17}$ | $0.30^{+0.00}_{-0.00}$ | $0.35^{+0.04}_{-0.04}$ | $0.67^{+0.06}_{-0.05}$ |
| XMMXCS J130545.0+175318.9 | 0.55763 | $2.06^{+0.00}_{-0.00}$ | $3.49^{+2.88}_{-1.31}$ | $0.67^{+0.09}_{-0.11}$ | $0.30^{+0.00}_{-0.00}$ | $1.19^{+0.12}_{-0.10}$ | $0.67^{+0.00}_{-0.00}$ |
| XMMXCS J100141.8+022538.2 | 0.12412 | $2.47^{+0.00}_{-0.00}$ | $1.49^{+0.14}_{-0.13}$ | $0.14^{+0.09}_{-0.12}$ | $0.30^{+0.00}_{-0.00}$ | $1.73^{+0.19}_{-1.63}$ | $0.67^{+0.28}_{-0.32}$ |
| XMMXCS J083454.8+553420.3 | 0.29282 | $4.38^{+1.26}_{-1.25}$ | $4.29^{+0.89}_{-0.61}$ | $14.57^{+0.56}_{-0.67}$ | $0.23^{+0.17}_{-0.15}$ | $0.21^{+0.00}_{-0.00}$ | $0.67^{+0.00}_{-0.00}$ |
| XMMXCS J022045.1-032555.8 | 0.33000 | $2.49^{+0.00}_{-0.00}$ | $2.17^{+0.78}_{-0.45}$ | $0.36^{+0.12}_{-0.06}$ | $0.30^{+0.00}_{-0.00}$ | $0.12^{+0.03}_{-0.04}$ | $0.67^{+0.00}_{-0.00}$ |
| XMMXCS J132053.9+335522.9 | 0.18200 | $0.10^{+1.51}_{-0.10}$ | $4.47^{+1.88}_{-1.28}$ | $0.70^{+0.24}_{-0.54}$ | $0.58^{+0.81}_{-0.52}$ | $2.00^{+0.18}_{-1.90}$ | $0.80^{+0.04}_{-0.09}$ |
| XMMXCS J005655.6-221358.7 | 0.11600 | $1.50^{+0.00}_{-0.00}$ | $1.76^{+0.42}_{-0.24}$ | $0.11^{+0.02}_{-0.02}$ | $0.30^{+0.00}_{-0.00}$ | $0.10^{+0.00}_{-0.00}$ | $0.41^{+0.01}_{-0.01}$ |
| XMMXCS J003548.2-432230.6 | 0.55000 | $2.82^{+0.00}_{-0.00}$ | $2.39^{+0.95}_{-0.73}$ | $0.55^{+0.07}_{-0.06}$ | $0.30^{+0.00}_{-0.00}$ | $0.10^{+0.01}_{-0.01}$ | $0.52^{+0.04}_{-0.03}$ |
| XMMXCS J130534.8+175659.5 | 0.51261 | $3.52^{+4.40}_{-3.18}$ | $3.87^{+2.15}_{-1.41}$ | $1.84^{+0.60}_{-0.50}$ | $0.13^{+0.40}_{-0.13}$ | $0.62^{+1.38}_{-0.08}$ | $0.67^{+0.04}_{-0.32}$ |
| XMMXCS J091821.8+211447.5 | 0.69000 | $3.98^{+0.00}_{-0.00}$ | $6.83^{+6.47}_{-2.63}$ | $3.91^{+2.59}_{-2.96}$ | $0.30^{+0.00}_{-0.00}$ | $0.10^{+0.05}_{-0.00}$ | $0.50^{+0.45}_{-0.15}$ |
| XMMXCS J145009.4+090429.9 | 0.49674 | $2.09^{+0.00}_{-0.00}$ | $3.19^{+0.93}_{-0.63}$ | $0.99^{+0.09}_{-0.09}$ | $0.30^{+0.00}_{-0.00}$ | $0.47^{+0.02}_{-0.02}$ | $0.35^{+0.00}_{-0.00}$ |
| XMMXCS J040646.7-711630.7 | 0.22900 | $8.31^{+2.91}_{-2.45}$ | $3.52^{+0.78}_{-0.69}$ | $2.73^{+0.22}_{-0.30}$ | $0.38^{+0.39}_{-0.27}$ | $0.47^{+0.03}_{-0.02}$ | $0.35^{+0.00}_{-0.00}$ |
| XMMXCS J101339.2-450640.0 | 0.11930 | $11.68^{+0.00}_{-0.00}$ | $1.27^{+0.08}_{-0.08}$ | $0.21^{+0.28}_{-0.19}$ | $0.30^{+0.00}_{-0.00}$ | $0.10^{+1.90}_{-0.00}$ | $0.35^{+0.60}_{-0.00}$ |
| XMMXCS J232124.6+194515.9 | 0.41000 | $5.83^{+1.69}_{-1.55}$ | $3.53^{+0.58}_{-0.46}$ | $3.28^{+1.19}_{-2.71}$ | $0.18^{+0.16}_{-0.14}$ | $0.49^{+1.51}_{-0.39}$ | $0.60^{+0.35}_{-0.25}$ |
| XMMXCS J223934.0-060019.1 | 0.17300 | $3.88^{+0.00}_{-0.00}$ | $1.72^{+0.53}_{-0.30}$ | $0.16^{+0.04}_{-0.03}$ | $0.30^{+0.00}_{-0.00}$ | $0.10^{+0.03}_{-0.03}$ | $0.36^{+0.02}_{-0.02}$ |
| XMMXCS J022610.7-045812.0 | 0.05000 | $2.55^{+0.00}_{-0.00}$ | $0.64^{+0.21}_{-0.13}$ | $0.00^{+0.01}_{-0.00}$ | $0.30^{+0.00}_{-0.00}$ | $0.69^{+0.03}_{-0.59}$ | $0.92^{+0.03}_{-0.05}$ |
| XMMXCS J100115.3+250612.4 | 0.67000 | $2.77^{+0.00}_{-0.00}$ | $2.54^{+1.40}_{-0.78}$ | $0.55^{+0.09}_{-0.10}$ | $0.30^{+0.00}_{-0.00}$ | $1.47^{+0.05}_{-0.05}$ | $0.67^{+0.00}_{-0.00}$ |
| XMMXCS J022827.3-042536.3 | 0.43300 | $2.65^{+0.00}_{-0.00}$ | $4.22^{+2.21}_{-1.22}$ | $0.69^{+0.50}_{-0.11}$ | $0.30^{+0.00}_{-0.00}$ | $0.46^{+0.19}_{-0.15}$ | $0.95^{+0.56}_{-0.56}$ |
| XMMXCS J232221.3+193855.8 | 0.26000 | $4.64^{+0.00}_{-0.00}$ | $2.12^{+0.68}_{-0.41}$ | $0.29^{+0.06}_{-0.05}$ | $0.30^{+0.00}_{-0.00}$ | $2.00^{+0.07}_{-0.07}$ | $0.35^{+0.01}_{-0.01}$ |
| XMMXCS J130553.5+181439.6 | 0.44645 | $2.04^{+0.00}_{-0.00}$ | $1.50^{+0.71}_{-0.38}$ | $0.35^{+0.13}_{-0.10}$ | $0.30^{+0.00}_{-0.00}$ | $0.71^{+0.12}_{-0.11}$ | $0.95^{+0.60}_{-0.60}$ |
| XMMXCS J145015.1+270832.2 | 0.40698 | $2.50^{+0.00}_{-0.00}$ | $3.01^{+2.43}_{-0.88}$ | $0.52^{+0.11}_{-0.11}$ | $0.30^{+0.00}_{-0.00}$ | $0.23^{+0.05}_{-0.05}$ | $0.67^{+0.00}_{-0.00}$ |
| XMMXCS J094034.7+355952.5 | 0.29427 | $1.46^{+0.00}_{-0.00}$ | $1.44^{+0.64}_{-0.31}$ | $0.11^{+0.04}_{-0.03}$ | $0.30^{+0.00}_{-0.00}$ | $0.18^{+0.12}_{-0.06}$ | $0.67^{+0.00}_{-0.00}$ |
| XMMXCS J000429.1+633127.1 | 0.37400 | $72.61^{+0.00}_{-0.00}$ | $1.94^{+0.45}_{-0.27}$ | $3.51^{+0.69}_{-0.96}$ | $0.30^{+0.00}_{-0.00}$ | $2.00^{+0.00}_{-1.90}$ | $0.72^{+0.23}_{-0.37}$ |
| XMMXCS J003603.7+851321.4 | 0.57000 | $7.84^{+0.00}_{-0.00}$ | $5.33^{+2.25}_{-1.40}$ | $3.23^{+0.25}_{-0.32}$ | $0.30^{+0.00}_{-0.00}$ | $2.00^{+0.00}_{-0.00}$ | $0.67^{+0.00}_{-0.00}$ |
| XMMXCS J005558.3-373301.2 | 0.16200 | $2.53^{+0.65}_{-0.63}$ | $5.22^{+0.43}_{-0.44}$ | $2.22^{+0.77}_{-0.49}$ | $0.36^{+0.11}_{-0.11}$ | $0.74^{+0.30}_{-0.21}$ | $0.67^{+0.00}_{-0.00}$ |
| XMMXCS J130650.1-233129.4 | 0.27000 | $9.01^{+0.00}_{-0.00}$ | $3.17^{+1.42}_{-0.83}$ | $1.24^{+1.39}_{-0.72}$ | $0.30^{+0.00}_{-0.00}$ | $1.22^{+0.78}_{-1.12}$ | $0.67^{+0.28}_{-0.32}$ |
| XMMXCS J093709.1+611612.5 | 0.20789 | $2.67^{+0.00}_{-0.00}$ | $1.34^{+0.45}_{-0.27}$ | $0.08^{+0.04}_{-0.04}$ | $0.30^{+0.00}_{-0.00}$ | $0.10^{+0.03}_{-0.03}$ | $0.42^{+0.08}_{-0.05}$ |
| XMMXCS J130514.7-102311.5 | 0.70000 | $3.32^{+0.00}_{-0.00}$ | $2.30^{+0.66}_{-0.51}$ | $0.88^{+0.16}_{-0.15}$ | $0.30^{+0.00}_{-0.00}$ | $0.21^{+0.07}_{-0.07}$ | $0.35^{+0.02}_{-0.02}$ |
| XMMXCS J161554.2+121928.5 | 0.35019 | $4.54^{+0.00}_{-0.00}$ | $3.75^{+1.97}_{-1.16}$ | $1.49^{+0.26}_{-0.29}$ | $0.30^{+0.00}_{-0.00}$ | $1.49^{+0.13}_{-0.11}$ | $0.67^{+0.00}_{-0.00}$ |
| XMMXCS J140615.7+283049.2 | 0.54600 | $0.10^{+2.12}_{-0.10}$ | $6.44^{+7.10}_{-2.45}$ | $2.40^{+1.23}_{-1.12}$ | $0.60^{+1.42}_{-0.60}$ | $0.35^{+1.65}_{-0.08}$ | $0.67^{+0.06}_{-0.06}$ |
| XMMXCS J123019.4+110118.5 | 0.24546 | $2.17^{+0.00}_{-0.00}$ | $1.89^{+0.68}_{-0.33}$ | $0.05^{+0.01}_{-0.01}$ | $0.30^{+0.00}_{-0.00}$ | $0.25^{+0.04}_{-0.07}$ | $0.95^{+0.45}_{-0.22}$ |
| XMMXCS J103131.2+311315.9 | 0.37290 | $0.10^{+1.33}_{-0.10}$ | $5.18^{+2.92}_{-1.62}$ | $1.97^{+0.33}_{-0.74}$ | $0.97^{+1.49}_{-0.87}$ | $0.34^{+0.27}_{-0.18}$ | $0.39^{+0.09}_{-0.07}$ |
| XMMXCS J143252.1-441909.5 | 0.10360 | $10.70^{+1.56}_{-1.44}$ | $4.29^{+0.41}_{-0.41}$ | $4.75^{+0.75}_{-0.42}$ | $0.48^{+0.17}_{-0.15}$ | $0.14^{+0.02}_{-0.02}$ | $0.35^{+0.01}_{-0.01}$ |
| XMMXCS J062210.7+781831.0 | 0.12910 | $8.90^{+7.91}_{-5.67}$ | $3.39^{+3.18}_{-1.55}$ | $0.50^{+0.07}_{-0.15}$ | $0.36^{+1.15}_{-0.36}$ | $1.91^{+0.04}_{-0.03}$ | $0.67^{+0.00}_{-0.00}$ |

Continued on Next Page...

Table H.3 – Continued

| Cluster | z | nH ($10^{20}$ cm$^{-2}$) | $T_X$ (keV) | $L_{500}$ ($10^{44}$ erg s$^{-1}$) | Z (Solar) | $r_c$ (arcmin) | $\beta$ |
|---|---|---|---|---|---|---|---|
| XMMXCS J015241.1-133855.1 | 0.82000 | $1.60^{+0.00}_{-0.00}$ | $5.78^{+4.76}_{-2.04}$ | $3.37^{+0.37}_{-0.45}$ | $0.30^{+0.00}_{-0.00}$ | $0.10^{+0.00}_{-0.00}$ | $0.36^{+0.01}_{-0.01}$ |
| XMMXCS J223924.4-054718.5 | 0.24200 | $3.98^{+0.00}_{-0.00}$ | $2.73^{+0.31}_{-0.26}$ | $1.15^{+1.96}_{-0.68}$ | $0.30^{+0.00}_{-0.00}$ | $0.17^{+1.83}_{-0.07}$ | $0.51^{+0.44}_{-0.16}$ |
| XMMXCS J221559.4-173815.5 | 1.45700 | $0.10^{+2.67}_{-0.10}$ | $8.10^{+8.38}_{-3.49}$ | $3.99^{+0.57}_{-1.29}$ | $0.00^{+0.59}_{-0.00}$ | $0.11^{+0.01}_{-0.01}$ | $0.67^{+0.00}_{-0.00}$ |
| XMMXCS J074921.2-674951.4 | 0.27400 | $9.87^{+9.99}_{-6.82}$ | $3.24^{+2.28}_{-1.32}$ | $0.84^{+0.23}_{-0.46}$ | $0.73^{+1.52}_{-0.70}$ | $0.56^{+0.12}_{-0.12}$ | $0.67^{+0.07}_{-0.07}$ |
| XMMXCS J104422.4+213024.7 | 0.65463 | $2.10^{+0.00}_{-0.00}$ | $3.92^{+0.42}_{-0.37}$ | $2.47^{+0.10}_{-0.10}$ | $0.30^{+0.00}_{-0.00}$ | $0.27^{+0.01}_{-0.01}$ | $0.63^{+0.02}_{-0.02}$ |
| XMMXCS J092114.4+370129.8 | 0.42975 | $1.56^{+0.00}_{-0.00}$ | $0.82^{+0.28}_{-0.15}$ | $0.08^{+0.05}_{-0.03}$ | $0.30^{+0.00}_{-0.00}$ | $1.11^{+0.70}_{-1.01}$ | $0.66^{+0.29}_{-0.31}$ |
| XMMXCS J004753.1+852716.9 | 0.33000 | $7.71^{+0.00}_{-0.00}$ | $5.82^{+3.34}_{-1.63}$ | $0.57^{+0.43}_{--0.14}$ | $0.30^{+0.00}_{-0.00}$ | $0.10^{+1.90}_{-1.71}$ | $0.67^{+0.00}_{-0.00}$ |
| XMMXCS J235708.5-241453.7 | 0.51000 | $1.85^{+0.00}_{-0.00}$ | $5.31^{+6.10}_{-1.97}$ | $2.19^{+0.48}_{-0.52}$ | $0.30^{+0.00}_{-0.00}$ | $0.31^{+0.15}_{-0.10}$ | $0.35^{+0.01}_{-0.01}$ |
| XMMXCS J160129.7+083856.6 | 0.18753 | $3.80^{+0.00}_{-0.00}$ | $1.93^{+1.78}_{-0.47}$ | $0.34^{+0.29}_{-0.10}$ | $0.30^{+0.00}_{-0.00}$ | $0.44^{+0.17}_{-0.18}$ | $0.75^{+0.22}_{-0.21}$ |
| XMMXCS J120934.4+392234.8 | 0.54702 | $0.00^{+4.17}_{-0.00}$ | $4.70^{+2.60}_{-1.66}$ | $0.75^{+0.04}_{-0.57}$ | $0.44^{+0.81}_{-0.44}$ | $0.10^{+0.01}_{-0.01}$ | $0.40^{+0.55}_{-0.02}$ |
| XMMXCS J233949.7-121307.1 | 0.19000 | $2.98^{+0.00}_{-0.00}$ | $1.30^{+0.14}_{-0.16}$ | $0.13^{+0.06}_{-0.03}$ | $0.30^{+0.00}_{-0.00}$ | $0.12^{+0.06}_{-0.06}$ | $0.45^{+0.04}_{-0.02}$ |
| XMMXCS J131455.1-163838.3 | 0.61000 | $5.07^{+0.00}_{-0.00}$ | $3.62^{+2.69}_{-1.16}$ | $0.97^{+0.23}_{-0.18}$ | $0.30^{+0.00}_{-0.00}$ | $0.10^{+0.04}_{-0.04}$ | $0.51^{+0.06}_{-0.03}$ |
| XMMXCS J025006.5-310400.2 | 0.80000 | $1.92^{+0.00}_{-0.00}$ | $5.34^{+3.58}_{-1.82}$ | $3.12^{+0.35}_{-0.40}$ | $0.30^{+0.00}_{-0.00}$ | $0.13^{+0.03}_{-0.02}$ | $0.35^{+0.01}_{-0.01}$ |
| XMMXCS J011952.1-441519.9 | 0.11800 | $0.50^{+8.60}_{-0.50}$ | $1.36^{+0.93}_{-0.41}$ | $0.04^{+0.09}_{-0.03}$ | $0.14^{+0.32}_{-0.13}$ | $0.29^{+1.71}_{-0.33}$ | $0.41^{+0.54}_{-0.08}$ |
| XMMXCS J022457.7-034852.6 | 0.61000 | $2.49^{+0.00}_{-0.00}$ | $4.09^{+1.55}_{-1.02}$ | $3.02^{+0.39}_{-0.35}$ | $0.30^{+0.00}_{-0.00}$ | $0.12^{+0.04}_{-0.07}$ | $0.39^{+0.02}_{-0.02}$ |
| XMMXCS J140439.3-341235.3 | 0.83000 | $5.52^{+0.00}_{-0.00}$ | $4.13^{+2.65}_{-1.31}$ | $2.26^{+0.25}_{-0.39}$ | $0.30^{+0.00}_{-0.00}$ | $2.00^{+0.02}_{-0.02}$ | $0.67^{+0.00}_{-0.00}$ |
| XMMXCS J004333.8+010107.8 | 0.18600 | $2.50^{+0.00}_{-0.00}$ | $1.48^{+0.32}_{-0.30}$ | $0.21^{+0.05}_{-0.04}$ | $0.30^{+0.00}_{-0.00}$ | $0.24^{+0.08}_{-0.08}$ | $0.35^{+0.01}_{-0.01}$ |
| XMMXCS J151424.7+363710.1 | 0.37200 | $1.35^{+0.00}_{-0.00}$ | $5.44^{+5.78}_{-2.25}$ | $5.55^{+1.05}_{-1.19}$ | $0.30^{+0.00}_{-0.00}$ | $1.51^{+0.12}_{-0.10}$ | $0.67^{+0.00}_{-0.00}$ |
| XMMXCS J010607.9+005013.2 | 0.27700 | $2.84^{+2.79}_{-2.34}$ | $3.42^{+1.63}_{-0.91}$ | $2.81^{+0.23}_{-0.46}$ | $0.58^{+0.78}_{-0.39}$ | $2.00^{+0.07}_{-0.07}$ | $0.67^{+0.00}_{-0.00}$ |
| XMMXCS J224113.3+032833.0 | 0.25000 | $5.25^{+0.00}_{-0.00}$ | $1.67^{+1.40}_{-0.44}$ | $0.18^{+0.07}_{-0.06}$ | $0.30^{+0.00}_{-0.00}$ | $0.10^{+0.01}_{-0.01}$ | $0.67^{+0.00}_{-0.00}$ |
| XMMXCS J014449.9-043231.5 | 0.18000 | $2.84^{+0.00}_{-0.00}$ | $1.36^{+0.19}_{-0.14}$ | $0.08^{+0.01}_{-0.01}$ | $0.30^{+0.00}_{-0.00}$ | $2.00^{+0.00}_{-0.00}$ | $0.67^{+0.00}_{-0.00}$ |
| XMMXCS J022539.3-031124.4 | 0.14000 | $2.93^{+1.56}_{-1.45}$ | $3.67^{+0.83}_{-0.60}$ | $2.24^{+0.14}_{-1.48}$ | $0.13^{+0.22}_{-0.13}$ | $2.00^{+0.00}_{-0.15}$ | $0.35^{+0.02}_{-0.00}$ |
| XMMXCS J161132.8+541635.5 | 0.37900 | $1.37^{+0.00}_{-0.00}$ | $6.86^{+4.92}_{-2.16}$ | $2.16^{+0.41}_{-0.27}$ | $0.30^{+0.00}_{-0.00}$ | $0.37^{+0.02}_{-0.05}$ | $0.95^{+0.37}_{-0.10}$ |
| XMMXCS J084958.1+445947.4 | 0.54645 | $2.68^{+0.00}_{-0.00}$ | $2.59^{+1.20}_{-0.69}$ | $0.82^{+0.11}_{-0.10}$ | $0.30^{+0.00}_{-0.00}$ | $0.51^{+0.12}_{-0.09}$ | $0.35^{+0.01}_{-0.01}$ |
| XMMXCS J030614.6-000537.0 | 0.44000 | $6.51^{+0.00}_{-0.00}$ | $2.73^{+0.93}_{-0.58}$ | $0.68^{+0.58}_{-0.28}$ | $0.30^{+0.00}_{-0.00}$ | $0.10^{+1.90}_{-0.00}$ | $0.43^{+0.52}_{-0.08}$ |
| XMMXCS J031833.0-030258.1 | 0.37000 | $4.77^{+0.00}_{-0.00}$ | $5.80^{+0.70}_{-0.54}$ | $6.73^{+0.43}_{-0.41}$ | $0.30^{+0.00}_{-0.00}$ | $0.53^{+0.03}_{-0.02}$ | $0.68^{+0.02}_{-0.02}$ |
| XMMXCS J120801.1+433928.2 | 0.26569 | $0.10^{+4.32}_{-0.10}$ | $3.02^{+1.27}_{-1.17}$ | $1.28^{+0.70}_{-0.52}$ | $0.55^{+0.76}_{-0.51}$ | $0.15^{+0.04}_{-0.07}$ | $0.67^{+0.00}_{-0.00}$ |
| XMMXCS J022722.1-032145.3 | 0.32900 | $2.61^{+0.00}_{-0.00}$ | $2.93^{+1.29}_{-0.72}$ | $0.42^{+0.06}_{-0.06}$ | $0.30^{+0.00}_{-0.00}$ | $0.31^{+0.03}_{-0.03}$ | $0.95^{+0.06}_{-0.06}$ |
| XMMXCS J092018.9+370618.0 | 0.18512 | $1.57^{+0.00}_{-0.00}$ | $2.48^{+0.07}_{-0.07}$ | $2.04^{+0.04}_{-0.04}$ | $0.30^{+0.00}_{-0.00}$ | $0.16^{+0.00}_{-0.00}$ | $0.55^{+0.00}_{-0.00}$ |
| XMMXCS J133514.4+374908.0 | 0.59500 | $0.10^{+3.20}_{-0.10}$ | $4.02^{+3.77}_{-1.76}$ | $0.69^{+0.08}_{-0.27}$ | $0.01^{+0.28}_{-0.01}$ | $0.25^{+0.07}_{-0.05}$ | $0.58^{+0.09}_{-0.06}$ |
| XMMXCS J133459.5+375024.5 | 0.38200 | $0.10^{+3.56}_{-0.10}$ | $3.99^{+2.25}_{-1.24}$ | $0.27^{+0.06}_{-0.09}$ | $0.75^{+0.98}_{-0.63}$ | $0.61^{+0.24}_{-0.18}$ | $0.67^{+0.00}_{-0.00}$ |
| XMMXCS J003646.4-432020.6 | 0.25000 | $2.82^{+0.00}_{-0.00}$ | $1.28^{+0.55}_{-0.29}$ | $0.14^{+0.06}_{-0.05}$ | $0.30^{+0.00}_{-0.00}$ | $1.00^{+0.44}_{-0.13}$ | $0.35^{+0.11}_{-0.06}$ |
| XMMXCS J130526.8+181156.4 | 0.42202 | $2.05^{+0.00}_{-0.00}$ | $4.04^{+1.05}_{-0.81}$ | $2.07^{+0.35}_{-0.43}$ | $0.30^{+0.00}_{-0.00}$ | $1.29^{+0.52}_{-0.30}$ | $0.45^{+0.18}_{-0.08}$ |
| XMMXCS J110954.1+482705.2 | 0.49513 | $1.23^{+0.00}_{-0.00}$ | $6.91^{+3.04}_{-1.75}$ | $2.66^{+0.42}_{-0.39}$ | $0.30^{+0.00}_{-0.00}$ | $0.15^{+0.03}_{-0.03}$ | $0.38^{+0.02}_{-0.01}$ |
| XMMXCS J093259.4+551545.0 | 0.52000 | $2.02^{+0.00}_{-0.00}$ | $2.32^{+2.36}_{-0.74}$ | $0.39^{+0.10}_{-0.10}$ | $0.30^{+0.00}_{-0.00}$ | $0.30^{+0.05}_{-0.04}$ | $0.67^{+0.00}_{-0.00}$ |
| XMMXCS J112245.6+013332.7 | 0.12973 | $7.83^{+14.01}_{-7.83}$ | $0.90^{+0.21}_{-0.16}$ | $0.07^{+0.02}_{-0.06}$ | $0.15^{+0.48}_{-0.10}$ | $2.00^{+0.13}_{-0.12}$ | $0.67^{+0.00}_{-0.00}$ |
| XMMXCS J124235.3-112412.9 | 0.06800 | $3.55^{+0.00}_{-0.00}$ | $1.05^{+0.12}_{-0.11}$ | $0.03^{+0.00}_{-0.00}$ | $0.30^{+0.00}_{-0.00}$ | $1.83^{+0.07}_{-0.06}$ | $0.67^{+0.00}_{-0.00}$ |
| XMMXCS J005656.6-274032.0 | 0.56000 | $1.86^{+0.00}_{-0.00}$ | $3.02^{+1.52}_{-0.77}$ | $1.55^{+0.30}_{-0.41}$ | $0.30^{+0.00}_{-0.00}$ | $0.10^{+0.05}_{-0.06}$ | $0.48^{+0.05}_{-0.02}$ |
| XMMXCS J054732.7-511014.4 | 0.07600 | $7.77^{+17.33}_{-7.77}$ | $0.63^{+0.13}_{-0.15}$ | $0.01^{+0.00}_{-0.01}$ | $0.13^{+1.09}_{-0.10}$ | $1.35^{+0.11}_{-0.09}$ | $0.67^{+0.00}_{-0.00}$ |
| XMMXCS J083147.8+525036.1 | 0.46000 | $3.90^{+0.00}_{-0.00}$ | $5.21^{+1.84}_{-1.23}$ | $0.84^{+0.08}_{-0.08}$ | $0.30^{+0.00}_{-0.00}$ | $1.02^{+0.07}_{-0.06}$ | $0.35^{+0.01}_{-0.01}$ |
| XMMXCS J051549.8+794000.9 | 0.61000 | $8.05^{+0.00}_{-0.00}$ | $5.01^{+3.57}_{-1.66}$ | $1.10^{+0.14}_{-0.19}$ | $0.30^{+0.00}_{-0.00}$ | $0.89^{+0.04}_{-0.04}$ | $0.67^{+0.00}_{-0.00}$ |
| XMMXCS J133804.0+482105.9 | 0.08807 | $1.67^{+0.00}_{-0.00}$ | $0.53^{+0.10}_{-0.10}$ | $0.02^{+0.00}_{-0.00}$ | $0.30^{+0.00}_{-0.00}$ | $0.32^{+0.03}_{-0.03}$ | $0.35^{+0.00}_{-0.00}$ |
| XMMXCS J084859.0+445149.6 | 1.26100 | $2.72^{+0.00}_{-0.00}$ | $5.36^{+2.03}_{-1.31}$ | $2.22^{+0.27}_{-0.27}$ | $0.30^{+0.00}_{-0.00}$ | $0.70^{+0.03}_{-0.04}$ | $0.95^{+0.07}_{-0.06}$ |
| XMMXCS J115043.3+545639.0 | 0.22806 | $1.13^{+0.00}_{-0.00}$ | $2.13^{+0.41}_{-0.28}$ | $0.49^{+0.45}_{-0.04}$ | $0.30^{+0.00}_{-0.00}$ | $1.38^{+0.17}_{-0.17}$ | $0.67^{+0.10}_{-0.32}$ |
| XMMXCS J210849.1-051640.2 | 0.31900 | $5.64^{+0.00}_{-0.00}$ | $4.77^{+2.69}_{-1.39}$ | $1.55^{+0.79}_{-0.52}$ | $0.30^{+0.00}_{-0.00}$ | $0.21^{+0.13}_{-0.08}$ | $0.35^{+0.06}_{-0.07}$ |
| XMMXCS J233402.4+485108.5 | 0.06230 | $14.08^{+0.00}_{-0.00}$ | $5.51^{+0.48}_{-0.46}$ | $0.35^{+0.69}_{-0.03}$ | $0.30^{+0.00}_{-0.00}$ | $0.34^{+0.02}_{-0.01}$ | $0.52^{+0.01}_{-0.01}$ |
| XMMXCS J034808.5+241603.0 | 0.12130 | $11.92^{+4.96}_{-4.19}$ | $2.68^{+0.77}_{-0.60}$ | $0.18^{+0.02}_{-0.03}$ | $0.60^{+0.62}_{-0.37}$ | $0.24^{+0.01}_{-0.01}$ | $0.67^{+0.00}_{-0.00}$ |
| XMMXCS J120943.5+391435.1 | 0.35511 | $0.00^{+1.61}_{-0.00}$ | $6.38^{+7.73}_{-2.53}$ | $0.61^{+0.78}_{-0.43}$ | $0.99^{+1.89}_{-0.98}$ | $0.10^{+1.90}_{-0.00}$ | $0.51^{+0.44}_{-0.16}$ |
| XMMXCS J022616.3-023954.2 | 0.06000 | $2.67^{+0.00}_{-0.00}$ | $0.61^{+0.04}_{-0.04}$ | $0.02^{+0.01}_{-0.00}$ | $0.30^{+0.00}_{-0.00}$ | $0.46^{+0.10}_{-0.08}$ | $0.70^{+0.11}_{-0.08}$ |
| XMMXCS J222818.8-050746.8 | 0.75000 | $5.15^{+0.00}_{-0.00}$ | $1.20^{+0.70}_{-0.35}$ | $0.63^{+0.42}_{-0.30}$ | $0.30^{+0.00}_{-0.00}$ | $0.10^{+0.03}_{-0.03}$ | $0.42^{+0.05}_{-0.04}$ |
| XMMXCS J223939.4-054327.4 | 0.24300 | $5.53^{+2.35}_{-2.07}$ | $2.65^{+0.53}_{-0.49}$ | $0.91^{+0.16}_{-0.15}$ | $0.34^{+0.27}_{-0.20}$ | $0.77^{+0.10}_{-0.09}$ | $0.80^{+0.10}_{-0.08}$ |
| XMMXCS J063945.9+821849.6 | 0.40000 | $4.93^{+0.00}_{-0.00}$ | $4.60^{+2.20}_{-1.10}$ | $0.80^{+0.17}_{-0.37}$ | $0.30^{+0.00}_{-0.00}$ | $0.23^{+0.05}_{-0.13}$ | $0.41^{+0.54}_{-0.02}$ |
| XMMXCS J045506.0-532342.5 | 0.40000 | $4.07^{+0.00}_{-0.00}$ | $3.01^{+1.09}_{-0.67}$ | $0.67^{+0.11}_{-0.09}$ | $0.30^{+0.00}_{-0.00}$ | $2.00^{+0.06}_{-0.06}$ | $0.35^{+0.01}_{-0.01}$ |
| XMMXCS J122929.0+015126.0 | 0.46022 | $1.79^{+0.00}_{-0.00}$ | $10.00^{+5.41}_{-2.84}$ | $2.66^{+3.25}_{-1.09}$ | $0.30^{+0.00}_{-0.00}$ | $0.44^{+1.56}_{-0.03}$ | $0.67^{+0.28}_{-0.32}$ |
| XMMXCS J223228.7+391518.3 | 0.27100 | $11.75^{+0.00}_{-0.00}$ | $3.54^{+3.18}_{-1.06}$ | $1.56^{+0.68}_{-0.73}$ | $0.30^{+0.00}_{-0.00}$ | $1.92^{+0.10}_{-0.43}$ | $0.95^{+0.43}_{-0.25}$ |
| XMMXCS J111515.3+531949.1 | 0.46647 | $0.92^{+0.00}_{-0.00}$ | $8.11^{+2.59}_{-1.82}$ | $18.42^{+1.97}_{-1.80}$ | $0.30^{+0.00}_{-0.00}$ | $0.45^{+0.02}_{-0.02}$ | $0.67^{+0.00}_{-0.00}$ |
| XMMXCS J233231.0+485406.9 | 0.11100 | $13.93^{+0.00}_{-0.00}$ | $1.70^{+1.35}_{-0.40}$ | $0.07^{+0.07}_{-0.03}$ | $0.30^{+0.00}_{-0.00}$ | $0.10^{+0.02}_{-0.02}$ | $0.95^{+0.10}_{-0.08}$ |
| XMMXCS J135358.8+335003.4 | 0.46897 | $1.25^{+0.00}_{-0.00}$ | $2.41^{+0.81}_{-0.79}$ | $1.21^{+0.93}_{-0.16}$ | $0.30^{+0.00}_{-0.00}$ | $0.12^{+1.88}_{-0.01}$ | $0.47^{+0.48}_{-0.12}$ |
| XMMXCS J200312.6-324754.9 | 0.21510 | $10.15^{+4.37}_{-3.76}$ | $2.95^{+0.80}_{-0.58}$ | $0.70^{+2.14}_{-0.40}$ | $0.41^{+0.37}_{-0.28}$ | $0.10^{+1.90}_{-0.00}$ | $0.57^{+0.38}_{-0.22}$ |
| XMMXCS J000259.0-295504.8 | 0.15560 | $1.31^{+0.00}_{-0.00}$ | $1.34^{+0.32}_{-0.23}$ | $0.04^{+0.03}_{-0.02}$ | $0.30^{+0.00}_{-0.00}$ | $0.10^{+0.08}_{-0.08}$ | $0.40^{+0.10}_{-0.05}$ |
| XMMXCS J121743.8+472915.4 | 0.27900 | $1.25^{+0.00}_{-0.00}$ | $7.43^{+8.56}_{-2.54}$ | $2.35^{+3.38}_{-0.80}$ | $0.30^{+0.00}_{-0.00}$ | $0.83^{+0.13}_{-0.37}$ | $0.95^{+0.60}_{-0.40}$ |
| XMMXCS J121205.5+131743.3 | 0.44875 | $1.72^{+6.93}_{-1.72}$ | $1.71^{+1.34}_{-0.73}$ | $0.64^{+0.15}_{-0.49}$ | $0.01^{+0.21}_{-0.01}$ | $0.10^{+0.01}_{-0.01}$ | $0.35^{+0.01}_{-0.01}$ |
| XMMXCS J003551.3-431217.8 | 0.38000 | $2.78^{+0.00}_{-0.00}$ | $1.72^{+0.78}_{-0.34}$ | $0.18^{+0.04}_{-0.03}$ | $0.30^{+0.00}_{-0.00}$ | $0.22^{+0.07}_{-0.05}$ | $0.37^{+0.03}_{-0.03}$ |
| XMMXCS J232152.7+195333.2 | 0.30000 | $4.62^{+0.00}_{-0.00}$ | $2.55^{+1.94}_{-0.87}$ | $0.35^{+0.07}_{-0.06}$ | $0.30^{+0.00}_{-0.00}$ | $0.13^{+0.05}_{-0.05}$ | $0.35^{+0.01}_{-0.02}$ |
| XMMXCS J022205.0-043240.6 | 0.32000 | $2.64^{+0.00}_{-0.00}$ | $1.96^{+1.12}_{-0.46}$ | $0.23^{+0.32}_{-0.08}$ | $0.30^{+0.00}_{-0.00}$ | $1.96^{+0.11}_{-1.86}$ | $0.95^{+0.60}_{-0.50}$ |
| XMMXCS J223633.7+342959.3 | 0.05900 | $8.62^{+0.00}_{-0.00}$ | $0.64^{+0.05}_{-0.05}$ | $0.02^{+0.00}_{-0.00}$ | $0.30^{+0.00}_{-0.00}$ | $0.18^{+0.02}_{-0.02}$ | $0.67^{+0.00}_{-0.00}$ |
| XMMXCS J131524.8-163227.9 | 0.49000 | $4.98^{+0.00}_{-0.00}$ | $3.30^{+2.33}_{-1.05}$ | $22.24^{+6.36}_{-5.24}$ | $0.30^{+0.00}_{-0.00}$ | $1.37^{+0.41}_{-0.24}$ | $0.67^{+0.00}_{-0.00}$ |
| XMMXCS J003439.3-120716.0 | 0.25500 | $2.46^{+0.00}_{-0.00}$ | $5.30^{+5.01}_{-1.87}$ | $0.48^{+0.10}_{-0.11}$ | $0.30^{+0.00}_{-0.00}$ | $0.41^{+0.04}_{-0.04}$ | $0.67^{+0.00}_{-0.00}$ |

Continued on Next Page...

Table H.3 – Continued

| Cluster | z | nH ($10^{20}$ cm$^{-2}$) | $T_X$ (keV) | $L_{500}$ ($10^{44}$ erg s$^{-1}$) | Z (Solar) | $r_c$ (arcmin) | $\beta$ |
|---|---|---|---|---|---|---|---|
| XMMXCS J122118.7+275732.3 | 0.76000 | $1.88^{+0.00}_{-0.00}$ | $1.90^{+1.02}_{-0.52}$ | $0.45^{+0.17}_{-0.12}$ | $0.30^{+0.00}_{-0.00}$ | $0.86^{+0.88}_{-0.25}$ | $0.43^{+0.17}_{-0.17}$ |
| XMMXCS J133604.6+514531.5 | 0.46291 | $1.09^{+0.00}_{-0.00}$ | $2.09^{+1.30}_{-0.64}$ | $0.51^{+0.09}_{-0.08}$ | $0.30^{+0.00}_{-0.00}$ | $2.00^{+0.03}_{-0.03}$ | $0.67^{+0.00}_{-0.00}$ |
| XMMXCS J101931.6+080345.2 | 0.17200 | $2.90^{+0.00}_{-0.00}$ | $2.54^{+1.27}_{-0.68}$ | $0.56^{+0.31}_{-0.22}$ | $0.30^{+0.00}_{-0.00}$ | $0.30^{+0.15}_{-0.08}$ | $0.36^{+0.06}_{-0.05}$ |
| XMMXCS J095957.8+251630.4 | 1.05000 | $2.70^{+0.00}_{-0.00}$ | $3.70^{+0.75}_{-0.61}$ | $2.04^{+0.17}_{-0.18}$ | $0.30^{+0.00}_{-0.00}$ | $0.10^{+0.00}_{-0.00}$ | $0.53^{+0.01}_{-0.01}$ |

Table H.3: XCS Spectral and surface brightness fitting results.

# Appendix I

# A description of the XCS Spectral and Surface brightness fitting

## I.1 Spectral fitting

The spectral fitting was carried out using version 12.5.0ac of the XSpec X-ray spectral fitting package. The models were simultaneously fitted to the spectra for the available observations and cameras using the maximum likelihood Cash statistic. The spectral bins were grouped such that there was a minimum number of counts per bin. This minimum number of counts was based on the number of counts in the spectrum and varied from 1 for spectra with 250 counts and below up to 5 for spectra with 850 counts and above, scaling as a powerlaw with an index of 0.75 for values in between. This scaling of the minimum number of counts per bin was derived from simulations of spectral fitting EPIC data and is designed to minimise the bias in the derived parameters while also minimising the errors. Data between 0.3 and 7.9 keV were used for the fitting in order to maximise the signal-to-noise.

Four different models were fitted to the data. All the models included a photoelectric absorption component (WABS) to simulate the absorption from the neutral gas in our galaxy and a hot plasma component (MEKAL) to simulate the X-ray emission from the intracluster medium (ICM). The first model involved fitting these components with the hydrogen column and ICM metallicity frozen (at the galactic radio column for the hydrogen column and the canonical value of 0.3 for the metallicity). The second model was the same as the first except that the hydrogen column and metallicity were allowed to vary. The third model included an extra powerlaw component to simulate a potential contaminating point sources, and the fourth model had two MEKAL components rather than one in order to simulate the case where there is a significant cool core in the cluster. The best fitting model was used to derive the luminosity and temperature of the cluster.

### I.1.1 Background Subtraction

The background subtraction from the spectral fitting was done using an in-field method, since XCS clusters do not have large angular sizes. The background spectra were taken from an annulus around the source (in the case of sources very near the edge of the field of view an ellipse perpendicular to the direction of the centre of the field of view with a circular region centred on the cluster excluded, was used instead). The outer edge of the annulus in 1.5 times the maximum radius identified for the source by XAPA and the inner edge is at 1.05 times that radius.

## I.2 Surface brightness fitting

The surface brightness fitting was performed by simultaneously fitting a model to the individual images for each camera and observation of the source. The model was convolved with the 1-dimensional "Extended Accuracy" XMM-Newton point spread function model, multiplied by the exposure map and have a background map added before being compared with the data. The maximum likelihood Cash statistic was used for the comparison and the MINUIT package of minimisation algorithms was used to find the best fit. The main function used the characterise the shape of the clusters was a a 1-dimensional King profile consisting of a core with a powerlaw decline outside that. Three different models were fitted to the data. First a simple King model with $\beta$ frozen at the canonical value of $\frac{2}{3}$. Second a King model with $\beta$ allowed to vary. Thirdly a King model by with an inner powerlaw cusp where inside a certain radius (usually of the order of the core radius) the surface brightness increase as a powerlaw into the centre. The best fitting model was used to calculate the scaling of the luminosity from the extraction region to $r_{500}$.

### I.2.1 Background Subtraction

The same background regions were used for the surface brightness fitting as were used for the spectral fitting. However in addition to . Since the background can be considered as two components, an 'X-ray' component that is focused (and so vignetted) by the telescope mirrors and a 'particle' component that is not. In reality the 'X-ray' component includes soft protons that are focused by the mirrors and the 'particle' component includes high energy photons that are created as the result of particle collisions with the telescope structure. These need to be treated separately as their spatial variation is different. To calculate the 'particle' component which should be approximately constant across the field of view the number of counts and effective exposure time is measured for two regions with significantly different off-axis angles. The comparison of these quantities allows the 'particle' background rate to be calculated. Using the total rate estimated from the annular background region and the exposure map, background map can then be constructed consisting of the sum of the constant 'particle' background and the spatially varying X-ray background.